Head Office: Università degli Studi di Padova

Department: Industrial Engineering

Ph.D. COURSE IN: Industrial Engineering

CURRICULUM: Materials Engineering

SERIES: 31st cycle

Lithography-based additive manufacturing of ceramics

from siloxane preceramic polymers

Coordinator: Prof. Paolo Colombo

Supervisor: Prof. Paolo Colombo

Ph.D. student: Johanna Eva Maria Schmidt

Abstract

Additive manufacturing is a fabrication approach which offers the possibility to build complex 3D structures from a virtual model without requiring moulds or costly post-processing steps to accomplish the final structures. Digital Light Processing (DLP) and 2-Photon-Lithography (2PL), two lithography-based techniques, represent additive manufacturing processes, which offer the highest degree of achievable complexity and resolution in their printed structures. Both techniques print their 3D structures by using light to polymerise photosensitive materials. Photocurable preceramic polymer resins offer the possibility to be shaped by both DLP and 2PL printing and are subsequently transformed into ceramic material through pyrolysis, while maintaining their predetermined printed structure.

This work is divided into four parts and presents complementary approaches at the material and production level to build highly complex 3D ceramic macro- and micro-structures, all based on the printing of a photosensitive siloxane preceramic polymer.

In the first part the photosensitive polysiloxane is blended with other preceramic siloxane resins, offering no photosensitivity but a high ceramic yield upon pyrolysis. Complicated structures with cm-sized dimensions and resolution as low as 30 µm are shaped via DLP printing and turned into SiOC macro-structures with complete shape maintenance. The blending of two siloxanes offers the possibility to control and alter the ceramic yield, shrinkage, resolution and free-carbon content of the structures, while at the same time exhibiting no diminished printing capability. Detailed sinter- and mechanical properties of one of the blends was investigated in detail and at all scales and demonstrated that, while the overall shape of ceramic structures are preserved during pyrolysis, different shrinkages as well as a change in aspect ratio depending on the structural configuration can occur and has to be taken into consideration.

The photosensitive polysiloxane, already used for macro-fabrication to gain SiOC structures, was also used in 2PL printing to fabricate structures of the same complexity at the microscale. SiOC ceramics with homogenous shrinkage and feature sizes as low as 800 nm were built with the help of a new printing configuration and printed support structures.

The third part of this work describes a complementary approach at the processing level, when SiOC ceramic structures are fabricated with a new hybrid additive manufacturing approach, combining DLP and 2PL printing. The advantages of DLP, the free standing and easy handling of macro-dimensional structures, are joined with the resolution capability of 2PL printing. Precisely positioned 3D structures with sub-µm sized features on top of cm-sized structured components were printed.

In the final part the polymer processing capability of preceramic polymers and their transformation into a reactive ceramic phase upon pyrolysis is exploited. Instead of producing pure SiOC ceramics, the photocurable siloxane preceramic polymer is combined with alumina powders to develop a new ceramic phase, mullite, upon sintering. The phase transformation at low sintering temperatures developed the new mullite phase within the 3D structure, fabricated due to the photosensitive capabilities of the siloxane via DLP printing.

Due to the complementary approach in this work, 3D ceramic structures have been fabricated at the macroscale (DLP), microscale (2PL) and multi-scale (Hybrid additive manufacturing; DLP + 2PL) on basis of a photosensitive preceramic polymer. Different ceramic materials, SiOC and mullite, have been produced from the polysiloxane thanks to its transformation capability into SiOC ceramic and reactive SiO_2 phase at high temperatures. Through the addition of passive and active fillers complex, dense, pore- and crack-free ceramic structures with no sign of delamination and complete maintenance of shape have been developed with varying properties.

Acknowledgements

Table of Contents

List of Tables

List of Figures

1 General Introduction

Advanced materials and manufacturing technologies for a direct fabrication of 3D functional structures are attracting consistent attention within both academia and industry communities, mainly for prototyping and complex tool fabrication. Traditionally ceramics have been manufactured via processing routes like powder pressing, tape or slurry casting using moulds or dies and are given its final shape and structure through various stages of pre- and post-processing. These machining steps, although now highly developed and refined, take away material through cutting, drilling, polishing etc. to get to the desired shape. To shape a ceramic comes with its own problems like danger of damage to the brittle sample, tool abrasion and wear as well as machinery cost which is especially high, around 80 % of overall manufacturing cost, in this class of hard and brittle materials.[1] Besides the request for near-net-shaped ceramics, which meet the required geometry to eliminate post-processing costs, there is a demand for more and more complex ceramic structures with undercuts or designed, non-stochastic porosity as well as small features. Parts with high structural complexity are very hard or impossible to achieve with the traditional subtraction of material and would require a lot of time and costly machining steps,[1] whereas in additive manufacturing the cost and time of production is uncorrelated to the structural complexity or is in fact cheaper and faster for highly complex and porous structures, where less material needs to be used.[2] Therefore, the need to change the fabrication process arouse. With additive manufacturing ceramic structures are built by adding material instead of subtracting, eliminating the need for other shaping processes, the cost for models and moulds or post-processing steps. The fast time from the design to the actual product and the flexibility in changing the geometry makes additive manufacturing cost efficient for customized products and small series production. While traditional manufacturing processes are still cost efficient for larger scale productions, additive manufacturing complements them, for example in producing parts of complex geometries, small batches, flexible production, spare parts, prototypes or customized products.

1.1 Additive Manufacturing of Ceramics

Additive manufacturing or three-dimensional (3D) printing describes different methods to directly shape parts from a material feeding source through a pattern-generating device on a computer-controlled translation stage.[3] The state of the material feeding source can be either solid (Powder based 3D Printing, Selective Laser Sintering, Laminated Object Manufacturing) or liquid (Slurry based 3D Printing, Powder-Based Selective Laser Sintering, Stereolithography, Direct 3D Printing, Direct Ink Writing). Ink deposition nozzle(s) or laser-writing optics are used to generate the patterns of a virtual model from a CAD-file (computer-aided design). Depending on the deposition process of the material and the way to consolidate it, there is a distinction between direct and indirect additive manufacturing techniques (see Figure 1).

The first category consists of Direct Inkjet printing (DIP) and Direct Ink writing (DIW), also named Robocasting or Fused Deposition Modelling (FDM). In DIP a water or organic based ceramic suspension, with ceramic loading < 30 vol%, is stabilised with different additives to control viscosity, ink spreading or drying and is loaded in a printing head.[1, 4] The print head deposits directly either continuous or individual, drop-on-demand, drops of ink onto the printing platform. Structures show good sintering activity as the ink is a ceramic suspension, therefore has high powder packing density, and uses sub-micrometre powders which leads to good mechanical properties.[1] Resolution and accuracy is not only affected by the extrusion parameters like extrusion rate or nozzle speed but also by the ink parameters such as solid content, particle size and viscosity. In DIW, the ceramic suspension has the viscosity of a paste and is extruded through a nozzle in the form of a continuous filament. The exact control of the rheological properties of the ceramic paste is necessary to prevent the sagging of the printed filament and the deformation of the part after extrusion. The extrusion nozzle can take different cross sections to create circular, square, hollow or other geometric filaments and its size, which can range from about 100 – 2000 μm, affects the resolution of the printed product.[1, 4] The texture of the structure is that of stacked filaments which affects the final surface quality.

To the second category, indirect additive manufacturing, belong 3D printing techniques which are inscribing patterns in a spread layer of powder, liquid or solid sheet material via laser optics or print heads. After the successful inscription within one layer the platform moves in z-direction in a predefined slicing distance and the next layer of material is coated onto the inscribed lower layer. In this way the whole 3D structure is being build up. In Powder based 3D Printing (P-3DP) as well as Selective Laser Sintering/Melting (SLS/SLM) a coater deposits a new sheet of flowable powder on a printing platform. The structure is selectively inscribed via a print head, which distributes droplets

of a liquid binder to glue the powder particles together, or via a laser beam, which locally sinters/melts the powder particles. Negative aspect of these types of 3D printing is the large particle size (30 – 100 µm) necessary for the flowability of the powder during layer deposition which leads to a theoretical powder bed density of as low as 25 – 50 % and prevents therefore sintering to high density.[1, 4] Additionally, for SLS the short interaction time of the laser with the powder limits the diffusion of the material which also leads to a poor densification. The high level of residual porosity is the reason for the low mechanical properties of structures fabricated via P-3DP or SLS/SLM.[1, 4] On the other hand, there are no limitations regarding the complexity of the parts geometry as the powder bed acts as additional support during the fabrication. The great speed and relatively low cost equipment for P-3DP makes it possible to build affordable, big parts in a relative quick time frame,[1] while SLS and SLM are the only additive manufacturing processes which are sintering the ceramic powder during printing, making ready to use ceramic parts.[4] By using a liquid ceramic suspension for the layer spread instead of a layer of flowable powder the powder packing density in the layer can be increased, potentially exceeding 60 % theoretical density in Slurry based 3D Printing (S-3DP) and Slurry-Based SLS (S-SLS).[4] A solid material source is used in Laminated Object Manufacturing (LOM), where paper, tapes or other flat shapes are laminated together at low to medium temperature and pressure after a laser cuts out the respective shape from the material sheet. Structures fabricated by this method are quite affordable as not only the machine investment but also material and processing expenses are low. Green tapes from extrusion process or tape casting can directly be used to produce the laminates and the lamination process operates better at lower applied pressure and temperature were additionally delamination and distortion can be reduced. The still occurring delamination together with interfacial porosities, defects and differential shrinkage are responsible for the poor quality of the tape interfaces and result in considerably low and anisotropic mechanical properties.[1, 4] High mechanical properties, similar to the ceramic pieces obtained by casting processes, and the highest level of accuracy and printing detail can be achieved with stereolithography (SLA).[4-6] Achievable resolutions, typically around 50 µm in lateral and 10 – 250 µm in horizontal direction, are the highest one from all the additive manufacturing techniques and are only excelled by 2-photon-lithography (2PL), a lithography-based process to gain resolutions < 1 µm. SLA and 2PL are based on a similar mechanism in which a photocurable liquid reacts upon light exposure and photopolymerises in the illuminated areas, building the solid structure. They will be explained in detail in the following sub-chapters.
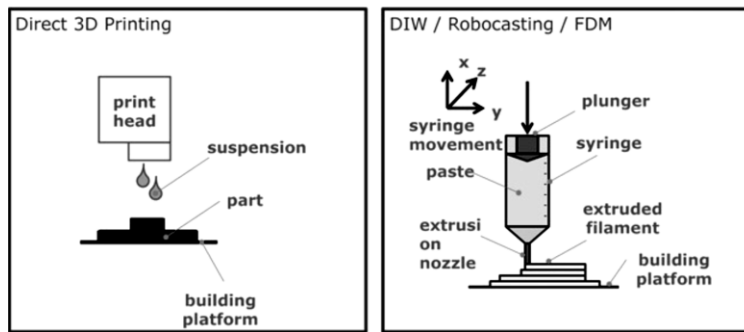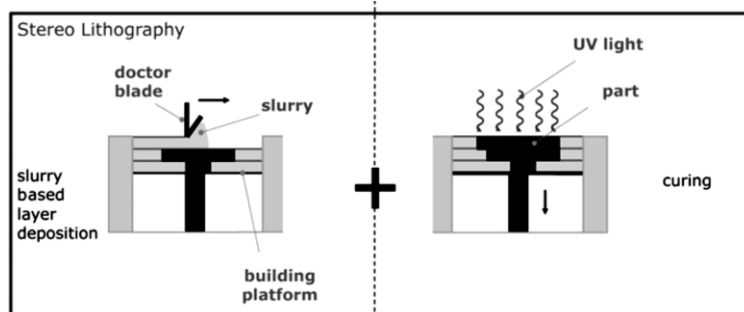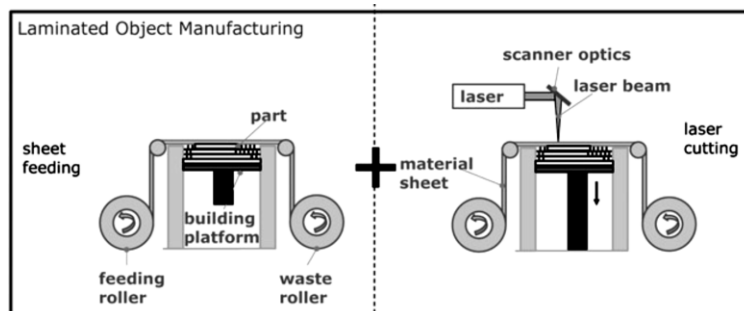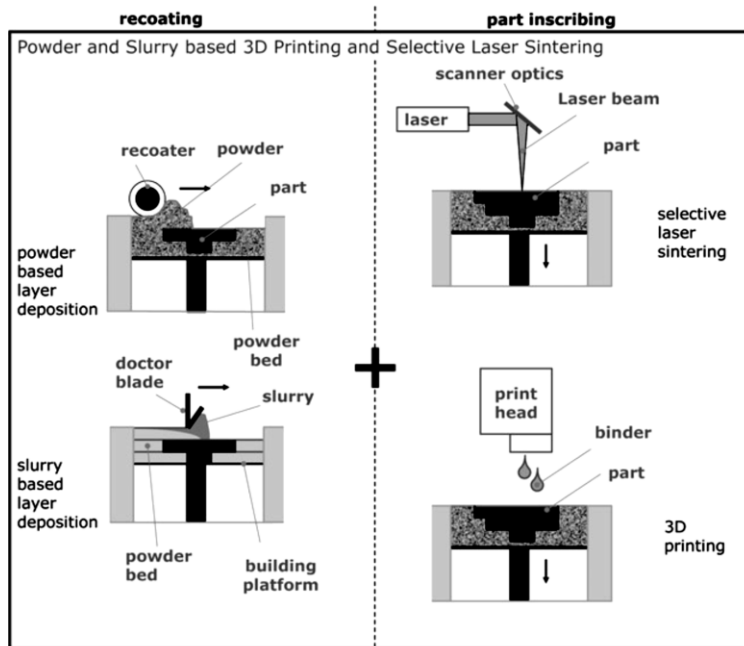
Figure 1 Schematic of additive manufacturing methods.[4]

In general, additive manufacturing of ceramics is much more difficult than the 3D printing of polymers since ceramic powders, for instance, negatively affect the viscosity of suspensions as well as printing accuracy, and usually have a low packing density, which can lead to not-fully dense parts after sintering and detrimental mechanical properties. While the 3D printing process of polymers already culminates in the finished end-product, the ceramic parts still have to undergo two additional steps, debinding and sintering. This is often the most difficult part of the 3D printing of ceramics as the whole organic part has to be burned out in a controlled way and the ceramic sintering process optimised to reach a high density in the finished ceramic with homogenous shrinkage and no defect formation like wrapping, pore and crack formation or delamination.

1.1.1 Stereolithography and Digital Light Processing

Additive manufacturing (AM) techniques started only around 30 years ago in 1986 with the release of the first stereolithography (SLA) machine by 3D Systems.[7] It is a laser-based technology in which light triggers a chemical reaction, leading to the photoinduced polymerisation of a liquid photosensitive resin, containing typically vinyl or acrylate groups.[4] A schematic representation of the chemical radical polymerisation reaction can be seen in Figure 2. During exposure, the intensity of the light source causes the excitation of photoinitiators, molecules which have a low photodissociation energy and are added to the photocuring liquid in small concentrations. Upon photon absorption a chemical bond in the photoinitiator is cleaved (photodissociation) and free radicals are created. Those radicals attack the unstable double bonds of the monomers or oligomers and form a covalent bond with one of the electrons of the double bond while the other electron in turn remains unbound, creating a radical in those organic compounds. In this way, the polymerisation process is initiated. A continuous double-bond breaking and free radical formation in the subsequent monomers leads to the growth of the polymer chain. If monomers with more than one double bond are used, an interconnected, branched solid 3D network of a highly cross-linked polymer forms. The chain reaction is terminated when two radicals, either from the initial initiator or from the radical chain in any step of the growth process, meet and react with each other to form a stable covalent bond.

Photoinitiator dissociation

Initiation

Propagation

Termination

Figure 2 Schematic drawing of free radical polymerisation using the example of a photoinitiator I which builds free radicals upon light exposure and polymerises an organic molecule R with acrylate groups.

This free radical polymerisation starts in certain locations upon light exposure. These locations are patterns belonging to a virtual CAD-file, which can be modelled digitally (Figure 3a). Arbitrarily complex 3D structures can be designed with the help of different software construction programs. If necessary, support structures have to be added to the design (see Figure 3b) in order to remove overhangs and ensure the printability of the structure as the printing resin is liquid and presents no support capabilities. The added support structures have to be removed from the structure after printing. The designed virtual model is transformed into a printable stl-file, which is being sliced in

layers of a defined thickness and composes, stacked together, the entire structure (Figure 3c). Every layer is printed one after another to successively fabricate the whole 3D structure via stereolithography (Figure 3d).

| a) Virtual model | b) Addition of support structures if necessary | c) Slicing |

d) Printing of stl-file
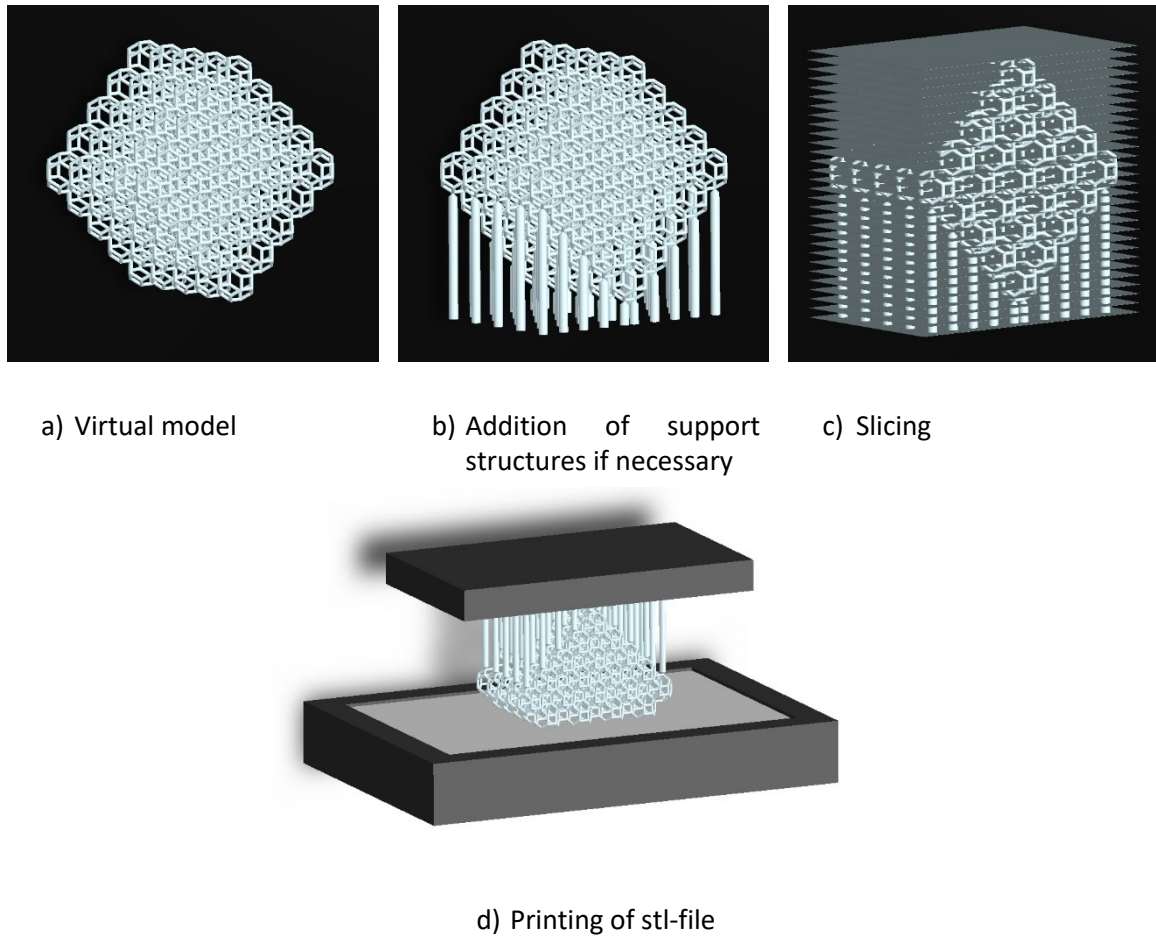
Figure 3 Stereolithography operation process; from model (a) to printed structure (d).

In SLA, a UV laser beam is the light source causing the free radical photopolymerisation. It scans the surface of the resin in a series of points and lines and selectively hardens the photosensitive material corresponding to a cross section of the product. SLA builds the 3D part in z-direction layer-by-layer, enabling the fabrication of components with high resolution and a good surface quality.[4, 8] Digital light processing (DLP) is a more time efficient variant of this technique, in which a projector is used to flash a single image of each 2D layer across the entire printing platform, and therefore exposes and cures the entire cross-sectional slice of the photopolymerisable resin at once. Because an entire layer is exposed with a single pattern, faster build speeds are achieved, independent of layer complexity or filling,[4] in contrast to SLA where the scanning time for each layer depends on the area which needs to be polymerised.[9] Since the entire printing area is illuminated in DLP at the same time, multiple objects, closely located together over the entire build area, with different structures can be done simultaneously, which significantly increases productivity, as one complete print can produce several different objects at once within the same time frame. Although DLP represents

the lithography-based process with faster printing times, the surface quality of SLA fabricated objects is superior, because in DLP the layers are not written as points and lines, but each layer is composed of squared pixels from the projectors digital screen. Those squared pixels result in a layer formed from small rectangles which gives the surface a very pronounced step-by-step profile and has a negative effect on curved edges also within one slice.[10] The layer-by-layer print of SLA and DLP leaves behind a horizontal stepwise profile in both lithography methods. This profile can be smoothened in z-direction by reducing the layer thickness, which can typically be set in SLA and DLP printers between 10 to 250 µm.[9] By printing thinner layers more detail and more accuracy in the print can be achieved but this comes at a cost of build time, because more layers have to be re-coated and illuminated.

There are two methods in stereolithography for how to project the light into the printing resin and in which direction growth of the final structure is achieved, both shown in Figure 4. In the bottom-up method (Figure 4a) the structure is printed upside down. The light shines from the bottom through a transparent window and transparent, non-sticky PDMS vat layer into the printing resin and exposes a thin layer of liquid between the PDMS and the building platform. After the appropriate exposure time, the platform lifts the solidified layer in positive z-direction a distance of the previously determined layer thickness. Liquid resin from the surrounding bath fills the empty spaces through gravitational force and is subsequently again exposed when the new layer is being polymerised. During printing, the structure is built while partially submerged in the liquid, preventing any contact between resin and oxygen which avoids oxygen inhibition of the polymeric chain growth.[9] As the parts are only partially submerged in the liquid, only small amounts of slurries are needed to build the part, which makes this the preferred method in research laboratories, where new materials are tested in small quantities. Another advantage of this method is the consistent resolution in z-direction as the layer thickness remains constant and precise, being the distance between previously printed layers and bottom of the vat. A huge disadvantage on the other hand is that the object has to adhere very well to the building platform as it rises vertically, which might require a large amount of support structures. As the resin is cured between two solid surfaces, already printed layers and PDMS vat layer, it faces two attachment choices. The PDMS is chosen as the material for the vat layer since it is not only transparent but also non-sticky, which limits the attachment-appeal for the freshly polymerised material slices.[11-13] Still, a certain amount of force is required to separate newly cured layers from the bottom surface. This separation force is higher the larger the exposed, dense area is, and limits therefore wall thicknesses and can lead to manufacturing defects, delamination and failures of the whole part as subsequent layers will connect to once detached material and also remain at the bottom of the vat.[13] Furthermore, due to the separation forces in every layer, the PDMS vat layer will deteriorate over time as the exposure of the

2D patterns creates so called "ghost-interfaces" in the transparent layer, which means that it has to be replaced.

The other method, top-down shown in Figure 4b, builds the structure from top to bottom. The light shines from above inside the printing resin, illuminates the photosensitive slurry from the top and polymerises the illuminated pattern at the interface between air and liquid. This exposure to air might cause oxygen inhibition of the polymerisation and therefore slows down the printing process as it requires a higher exposure time.[9] The building platform moves in negative z-direction and lowers the structure into the liquid resin, which covers the already printed part before the next layer exposition. One obvious advantage of this projection method is that no part of the printing equipment is consumable, like the PDMS layer in the bottom-up method, and therefore doesn`t need to be replaced. Furthermore, the 2D patterns in each layer are not build between two solid faces, PDMS layer and already printed part, but at the top of the structure, at the interface between air and previously solidified layers. They therefore don`t have to be detached from another solid face (PDMS vat) which means they can also only attach to the printed object, and therefore there is no danger of parts failure in the middle of a print due to failed separation from the vat. Less support structures might be necessary than with the bottom-up method as the structure sits on top of the building platform and doesn`t hang from it, which reduces consumed resin, takes lesser time for file preparation and reduces the amount of structures which have to be removed after printing. Negative aspect in this method is that the layers thickness is not constant and not so easily controlled, as surface tensions might cause ripples on the surface. Moreover, high viscosity liquids might require a long time to coat the previously illuminated area and form a new liquid layer to be exposed, or could lead to incomplete covering of the surface of the object being printed. Another disadvantage is the large quantity of printing liquid that is needed, as the structure is at all times completely submerged inside the printing bath. This makes this projection method not favourable for research facilities testing new materials but rather for businesses which want to print tall parts with large, dense areas, which would require a high detachment force from the PDMS layer in the bottom-up projection method.[13]

| a) Bottom-up | b) Top-down |
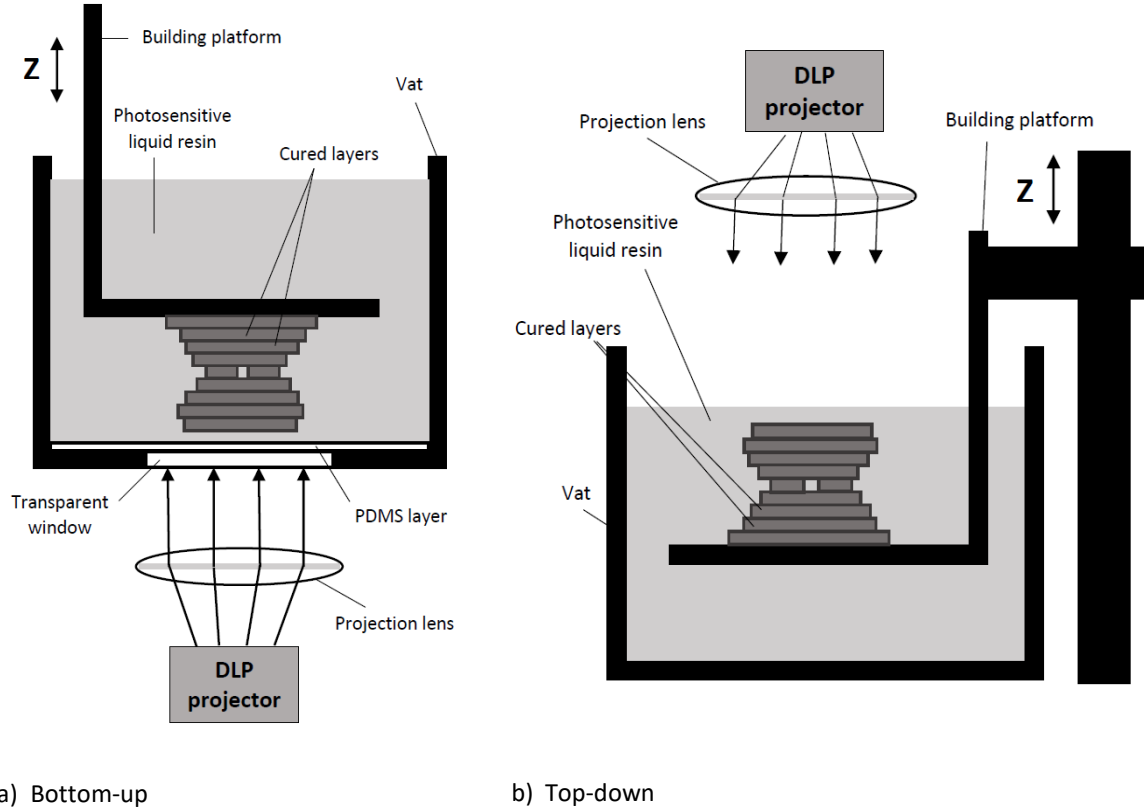
Figure 4 Schematic drawing of stereolithography projection method.

For printing ceramics and glasses, the photosensitive resin is filled with fine glass or ceramic particles, which become entrapped in the hardened polymer after the photosensitive material is polymerised during the light exposure. The finished photopolymerised green samples are subsequently debindered to remove the organic content and sintered to dense ceramics.[4, 6, 14-16] Stereolithography of ceramics and glasses is not trivial due to the presence of these glass or ceramic particles. The solid loading content has to be maximised, typically the resin is filled up to $40 - 60$ vol%,[1, 14, 17] in order to avoid cracking during debinding and to achieve a dense glass or ceramic after sintering. Contrary to this objective, a high solid loading will increase the viscosity, which has to be kept at a suitable low level for printing.[1, 9, 14, 17-19] The change in viscosity η by introducing a solid volume fraction ϕ in a pure liquid ϕ_0 was modelled by Griffith et al.[17] using a modified Krieger-Dougherty equation.

$$\eta = \eta_0 \left(1 - \frac{\beta\phi}{\phi_0}\right)^{-2.5\phi_0} \tag{1}$$

The dispersion quality of the particles is represented in β and equals 1 for perfectly colloidally dispersed particles where the slurry reaches the lowest possible viscosity, while it is significantly greater than 1 for fine powders as dispersion progressively gets more difficult. The maximum possible solid fractions, according to above model, reaches 0.7 for powders with wide particle size distribution when the viscosity of the system changes to that of a wet solid paste.[17] As the viscosity

has to be kept at a suitable level for printing, typically below 5 Pa*s,[1, 18, 19] and rises sharply for suspensions in the 40 – 60 vol% range, indicated to be necessary to achieve dense ceramics,[1, 14, 17] special dispersants have to be used in order to keep the printing resin fluid enough to recoat the printing vat for the next layers.[1, 4, 15, 17, 18] Furthermore, the particles have to be stabilized against sedimentation during the printing process to avoid an inhomogeneous distribution of the glass or ceramic particles inside the printed structure and an accumulation of them in the remaining printing liquid.

Additionally, in contrast to pure polymer resins, the ceramic particles not only dilute the active photosensitive monomers in the slurry, but also cause light absorbance and scattering due to their interaction with the incoming light.[1, 9, 14, 15] The penetration depth of light will be decreased, as photons are absorbed and redirected from the forward beam, and the shape of features, especially those of high aspect ratios, can be broadened and rounded as the scattered photons widen the beam.[1, 9, 15, 16] While absorption and scattering are always present in a glass or ceramic particle filled resin, the amount of it depends on the solid volume fraction, the particle size, particle size distribution, and the difference in refractive index between the solid phase and the liquid.[1, 9, 14, 17] The penetration depth, or cure depth D_{cure}, is the distance the UV beam can travel inside the particle filled slurry and still have enough intensity I_{cure} left to polymerise the photosensitive polymer in the resin. This can be modelled, and includes the factors which influence the cure depth through absorption and scattering, the ceramic volume fraction ϕ, the particle size d and the efficiency factor Q which is proportional to the square of the refractive index difference between ceramic and UV curable monomers.[17]

$$D_{cure} \approx \left(\frac{d}{Q}\right) \left(\frac{1}{\phi}\right) ln\left(\frac{I_0}{I_{cure}}\right) \qquad (2)$$

The above equation shows how the intensity of the initial beam, I_0, decreases with increasing ceramic volume fraction, decreasing particle size and increasing refractive index difference, which leads to a reduced penetration depth. The smaller the difference in refractive index between the glass or ceramic and the photosensitive liquid, acrylates or vinyls in general, the more UV-transparent those slurries get, which reduces the scattering and absorption significantly. Therefore, those glasses and ceramics like fused silica (n = 1.45), quartz (n = 1.56) or alumina (n = 1.70), which show a relatively small refractive index contrast to acrylates like poly(ethylene glycol) diacrylate (PEGDA; n = 1.47) or trimethylolpropane ethoxylate triacrylate (TMPETA; n = 1.471), are easier to print than ceramics with high refractive index contrast like silicon nitride (n = 2.05), zirconia (n = 2.20) or silicon carbide (n = 2.55), as they require a high energy dose for a notable z-penetration depth.[9, 15, 17, 20]

Despite those problems in printing ceramics, SLA and DLP still offer a high precision 3D printing method of ceramic materials, compared to other additive manufacturing techniques like direct ink writing or powder-based 3D printing. The printing method offers a high printing accuracy with resolutions smaller than any other additive manufacturing technique for ceramics. As stereolithography is just a shaping step to give the end-form, the structures have to be post-processed. Once printing is complete, the parts are removed from the building platform and post-cured to complete the polymerisation of all the acrylate groups, since the exposure time of the printer is selected to be just long enough to give the final shape, but quick enough to limit exposure and therefore printing time, which leaves some acrylates unreacted. Post-curing increases the mechanical properties of the parts, stabilises them and therefore increases its durability.[21] Any support structures, which had to be added during the print to avoid overhangs (see Figure 3b), have to be mechanical removed before the structures are debindered and sintered to ceramic material. After sintering, dense struts inside the structure are obtained with SLA/DLP, which are beneficial for the mechanical properties, which themselves are similar to those obtained by using traditional shaping techniques.[6]

1.1.2 Two Photon Lithography

Continuing advances in research and development in the field of three-dimensional advanced manufacturing techniques have pushed resolution limits down to the micro- and nano-scale. The straightforward realization of miniaturized parts provides a solution to the growing demand for high densities of integration, less power consumption, better performance and reduction in fabrication cost. Moreover, further opportunities come from the unique spectrum of properties that small-scale topological and structural features can provide. Microscale lattice materials, metamaterials, photonic crystals, nano-electro-mechanical (NEMS) and micro-electro-mechanical systems (MEMS) are just some examples of functional systems taking advantage of small-scale feature size effects in 3D.[22-29]

The concept of multiphoton effects was first predicted by later Nobel Prize winner Maria Göppert more than eighty years ago, but it took around 30 years more to develop lasers with enough light source intensity to proof the concept. The first commercially available femtosecond laser, based on Kerr lens mode-locking, was introduced in the 1990s, starting the development of those type of lasers just three decades ago.[30, 31] The femtosecond laser utilises the concept of simultaneous multi-photon absorption in atoms to reach electron transition states, which cannot be accomplished with single-photon absorption. The excited energy levels S1 and S2 in Figure 5 are therefore not the same, which means the multi-photon absorption can be used to accomplish tasks not possible with single-photon absorption. Since the virtual state (dashed line in Figure 5b) has an incredibly short lifetime, in the range of femtoseconds, a second photon is needed to reach the excited state for the electron before the decay of the virtual state. The probability for both absorptions to happen increases with laser intensity, and is therefore restricted to the focus of the laser beam, which leads to a strongly confined interaction region (see Figure 5c). Because of their high spatial resolution and the ability to selectively excite specific molecules, femtosecond pulsed lasers can be used for multi-photon microscopy. Other applications include laser ablation of materials due to plasma generation inside the material for nano- and micromachining, surface patterning of, for the wavelength of the applied laser, transparent materials e.g. inside various types of glasses, or for the creation of structures with resolutions below the micrometre.[30, 31]
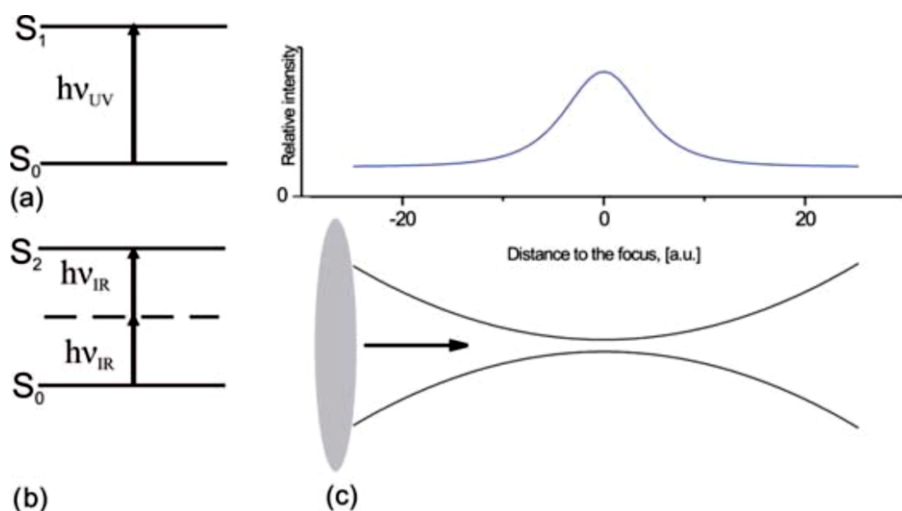
Figure 5 Atom excitation with both single-photon (a) and two-photon absorption (b); intensity distribution along the propagation direction of the focused laser beam. [30]

Two-photon lithography (2PL) is a laser-assisted technology for the intrinsic-3D fabrication of structures at the micro- and mesoscale and was first demonstrated by Maruo et al. in 1997.[32] The setup of 2PL can be seen in Figure 6. A femtosecond pulsed laser with very high peak intensities is tightly focused into a volume of photosensitive polymeric liquid to induce a localized chemical polymerisation reaction based on the same radical polymerisation mechanism as in stereolithography (see Figure 2). By exploiting two-photon absorption, the exposed volume is confined to the focal region, leading to a polymerised small element (voxel) whose ellipsoid shape dimensions range from the nm-range (in width) to a few μm (in height). Different to stereolithography, were the laser (SLA) or the projected digital light (DLP) is absorbed at the surface of the photosensitive material, in 2PL the laser radiation is polymerising in the focal voxel within the photoresist, and passes through the rest of the resin without interaction since the absorption threshold is not exceeded (see Figure 6). The laser beam is initially focused at the substrate glass/resin interface, and material is polymerised successively along the trace of the focal voxel. The whole structure is being fabricated, according to 3D design, by keeping the focus fixed and moving the substrate through a piezoelectric scanning stage in every direction. This controlled movement of the voxel within the liquid volume allows the fabrication of 3D structures of high resolution, below the micrometre range.[30, 33-36]
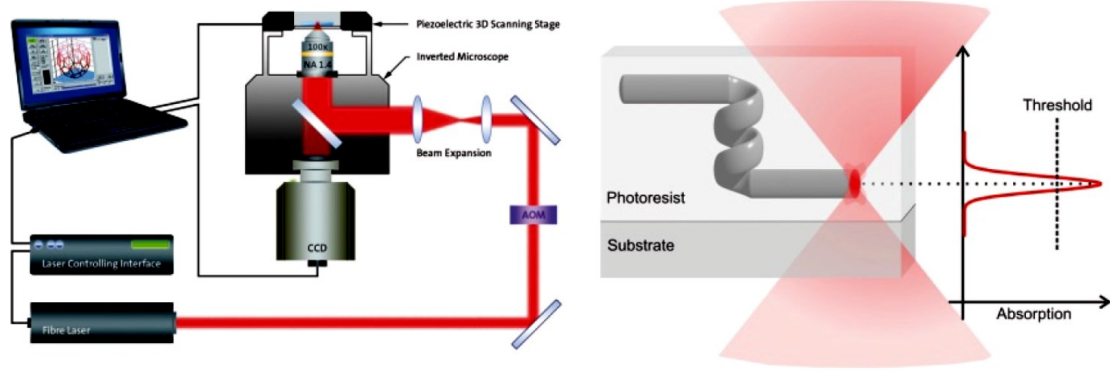
Figure 6 2-Photon Lithography setup.[36]

The resolution itself depends on the size of the voxel, which in turn depends on the exposure dose. The structural resolution as a function of laser intensity can be seen in Figure 7. It shows that structures are being written in those areas where the intensity exceeds the polymerisation threshold. Higher intensity broadens the voxel size and increases the line width and depth of the structural features as illustrated in Figure 7. Areas of exposure dose below the threshold remain unaffected and maintain their liquid state. In areas above a certain intensity value, more than two photons may be absorbed simultaneously, which can induce multiphoton ionization, optical breakdown and plasma formation. While useful for nanomachining e.g. during refractive eye surgery,[31] the formation of bubbles and explosions in the focused voxel destroys already printed structures and leaves this area unusable for 2PL. This demonstrates that the line width and depth of the structural features can be tuned by adjusting the exposure dose of the laser radiation within certain boundaries.[30]
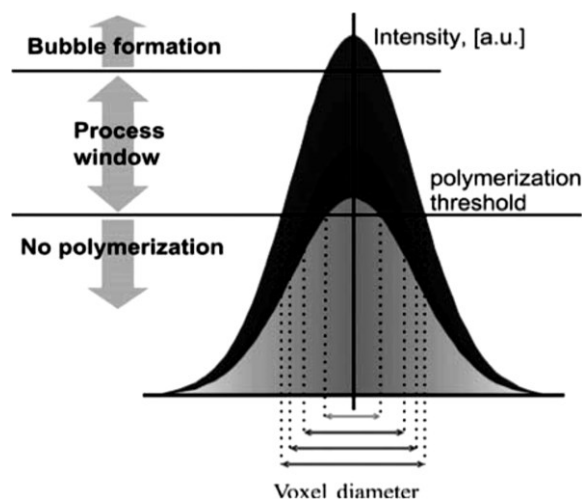
Figure 7 Intensity distribution of the exposure dose at the cross-section of the focal spot. [30]

The following processing steps is again equal to SLA or DLP printing, when the finished structures are cleaned of all excess fluid of unpolymerised resin, revealing the fabricated structures. After development, the structures remain attached to their glass substrate on which they were printed.

1.2 Preceramic Polymers

Preceramic polymers are a special class of inorganic polymers, which combine the processability properties of polymers with the capability of transforming into ceramic materials, also called polymer-derived-ceramics, after high-temperature treatments in inert or oxidative atmospheres. The main attraction of using preceramic polymers to fabricate ceramics is that shaping and forming is done in the polymeric state, thus avoiding the high cost of ceramic machining[1] and the problems occurring with tool wear and brittle fracture.[37] In fact, preceramic polymers can be shaped with a variety of polymer forming technologies, like extrusion, injection molding, infiltration, coating, spinning or pressing among others.[37, 38] After forming, the preceramic polymers are treated like any other ceramic component and will be debindered, to decompose organic groups, and then sintered to ceramic material; the entire process is termed "pyrolysis". While the organic groups of the preceramic polymers burn away with gas release and shrinkage during debinding, the inorganic backbone remains behind. Likewise to the decomposition of purely organic polymers, organic moieties such as methyl, phenyl, vinyl or Si-H, Si-OH, Si-NH$_x$ groups in the preceramic polymers will be eliminated and removed from the remaining part through continuous gas flow.[37] The velocity of the burn-out depends on the heating rate and will induce, if is it too rapid, typically > 2 °C/min, defect formation like cracks or pores, which will catastrophically decrease the mechanical properties and can lead to total collapse of the structure. The ceramic conversion is being completed at rather low temperatures, of around 1000 – 1300 °C, compared to powder-based ceramic technologies.[8, 37-40] Although most of the shrinkage occurs during debinding below 600 °C, the transformation into ceramic material is accompanied with an additional significant shrinkage when "transient porosity" is eliminated and the structure further densifies with increasing temperature.[41, 42]

Besides the possibility of shaping the ceramic in their polymeric state and transforming them to ceramic material at low temperature, unique ceramic materials, like SiC, Si$_3$N$_4$, BN, SiOC, SiCN, SiBCN ceramics, can be manufactured from preceramic polymers with a composition only realizable via the molecular route.[38, 40, 43] They can be classified according to the number of different atoms in their ceramic material. The most well-known ceramic materials developed from preceramic polymers are Si$_3$N$_4$, SiC, BN, and AlN, belonging to the binary system, SiCN, SiOC, and BCN, which are counted to the ternary system, and SiCNO, SiBCN, SiBCO, SiAlCN, and SiAlCO which belong to the quaternary system.[37] The most frequently used preceramic polymers contain silicon atoms in their backbone, and are classified according to the nature of the group sharing a covalent bond to the Si atom in the inorganic polymeric chain (group X see Figure 8). The repeating units Si-X of poly(organocarbosilanes) (X = CH$_2$), poly(organosiloxanes) (X = O), poly(organosilazanes) (X = NH) and poly(organosilylcarbodiimides) (X =(C=N=C)) are detailed in Figure 8, together with the ceramic materials, SiC, Si$_x$O$_y$C$_z$ and Si$_x$C$_y$N$_z$, those preceramic polymers yield after pyrolysis.[37]
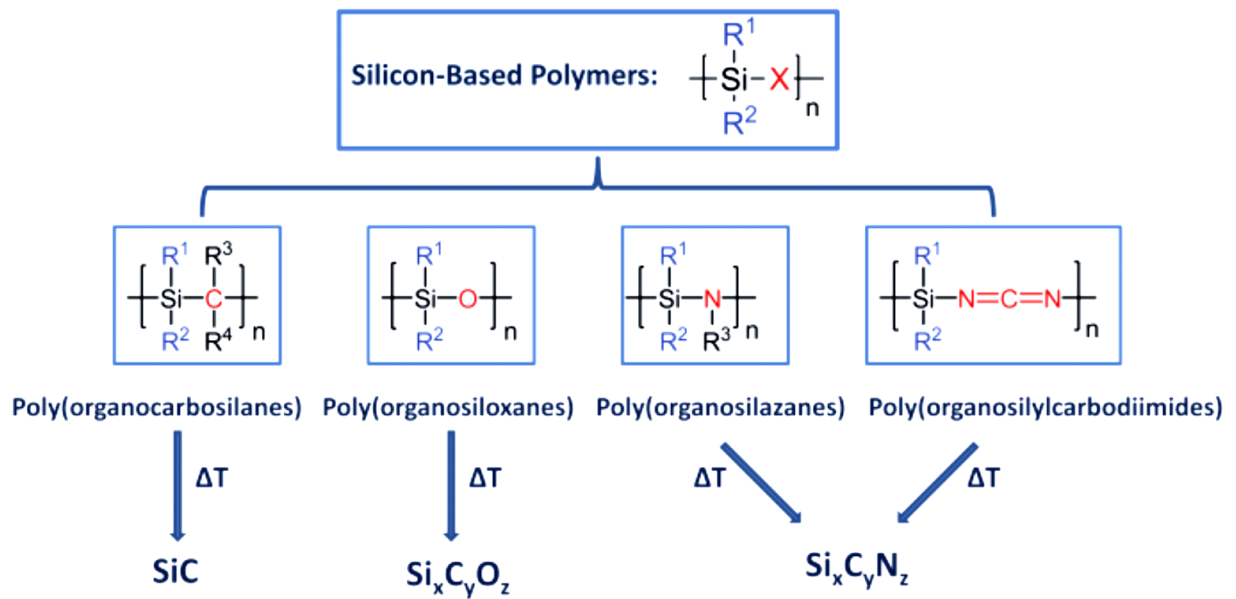
Figure 8 Classes of preceramic polymers grouped by the nature of their connection to the silican atom in their inorganic chains and their respective ceramic material they are converted to upon pyrolysis.[37]

While the group X characterises the nature of the preceramic polymer and its polymer-derived-ceramic material, the organic groups R^1 and R^2, sharing the other covalent bond with the silicon atom, can be used to modify the properties of both the original polymeric material and the ceramic end-product. If they represent certain functional groups, they can be used to shape the polymer by forming a network under certain circumstances like heat or UV exposure or by combination with other functional groups in presence of catalysts. The amount of C-C connections, which are not converted into gaseous species during burn-out, will be responsible for the amount of carbon in the ceramic material, which will change the atomic ratio between the remaining atoms. Important parameters, like electrical conductivity, stability against crystallisation and high-temperature resistance depend on the ceramic composition and the amount of free carbon in the ceramics and can be modified and controlled over the nature of the organic groups R^1 and R^2, connected to the Si atom.[37, 39]

The role of free carbon in the polymer-derived-ceramic system is particularly strong in SiOC ceramics. Those silicon oxycarbide glasses are amorphous solid material and are obtained by pyrolysing polysiloxanes, which are described more in detail below. The ideal composition of silicon oxycarbide glasses exhibits only Si-O and Si-C bonds, with no Si-Si, C-O or C-C bonds, and has the structural composition of $SiC_xO_{2(1-x)}$ in which one tetravalent carbon atom is substituted by two divalent oxygen atoms.[44] However, the amount of carbon in the system depends on the organic side groups R (see Figure 8) and varies significantly by having methyl, vinyl, propyl or phenyl etc. side groups. Depending on the number of carbon atoms and its molecular connections in the side group, the residual carbon content after pyrolysis will change, leading by high carbon content to the formation

of a free carbon phase. Therefore, SiOC ceramics can be described as consisting of a silicon oxycarbide matrix with the general formula of $SiC_xO_{2(1-x)}$, forming SiC and SiO_2 phases, and a second phase of dispersed free carbon, which shows itself in the black colour of these amorphous glasses.[44, 45] While the carbon remains homogeneously dispersed in the amorphous material at lower temperature, it forms structural units or locally enriched regions of turbostratic graphite above 1000 °C.[37] The structure of the amorphous network together with its properties changes depending on the amount of free carbon in the ceramic system. In fact, superior mechanical, chemical and electrical properties are shown in SiOC amorphous systems with high carbon content, in which the elastic modulus, hardness, density, glass transition temperature, electrical conductivity and chemical durability increases.[37, 44, 46, 47] So are for example polymer-derived SiOC ceramics insulators at low pyrolysis temperature < 600 °C, while the conductivity increases to semiconducting levels with temperatures above 800 °C. Metallic-like conductivity can be reached in SiOC ceramics if a continuous network of free carbon is formed, either at temperatures above 1400 °C or in high carbon containing SiOCs, like those yielded from polysiloxanes containing phenyl-groups, also at lower temperatures such as 1100 °C.[37] Furthermore, chemical properties depend on the pyrolysis temperature, since it affects the complete removal of hydrogen, present in residual C–H bonds, from the system and therefore the oxidation rate and affects e.g. phase separation in SiOC in lower chemical durable SiO_2 rich areas, SiC and carbon regions.[37] Mechanical properties depend not only on their general composition, but also on their density, which is, as mentioned above, depending on pyrolysis temperature as well as on the amount of free carbon in the system, which increases the elastic modulus and hardness. These examples point out the significant influence of the free carbon phase on the properties of SiOC ceramics, which can be controlled over the organic side group and easiliy decreased as well as increased. In fact, more carbon can be dissolved in silica to produce carbon-enriched silicon oxycarbide, than is possible by other synthetic approaches or conventional solid state reactions, which shows the importance of choosing the preceramic polymer-derived approach in fabricating SiOC ceramics.[37]

The properties of polymer-derived-ceramics in general depend on their composition, microstructure, density, shape, ceramic yield, surface finish, number of defects and pyrolysis temperature. Depending on its application those characteristics, determining the electrical, optical, mechanical or chemical properties, are optimised and can further be changed by adding fillers, to increase e.g. electrical and magnetic properties by adding metallic fillers.[37]

In order to effectively use a preceramic polymer, it has to meet certain requirements. The functional groups R have to have enough latent chemical reactivity to be efficient in the curing and cross-linking step, producing a strong connected network, which can maintain its given shape during the

subsequent pyrolysis treatment. The overall preceramic polymer has to possess appropriate rheological properties in the liquid state or malleability or solubility, if they are in solid state, to apply them in their respective shaping process. Additionally, they have to have a sufficient high molecular weight to avoid the volatilization of low-molecular components in order to possess high ceramic yields.[37, 48] Lower ceramic yield preceramic polymers, typically linear polymers, possess a high shrinkage, which should not only be avoided from an engineering viewpoint as it is accompanied with a huge loss of material, but can also cause significant problems such as residual stress, distortion or fracture of the structure.[49] Therefore, polymeric structures which are branched or contain rings or cages are preferred to decrease the weight loss during pyrolysis, as the removal of those large molecular structures would require multiple chemical bond breakings and is also sterically hindered.[48, 50]

2 Materials and Methods

2.1 Ink Preparation

The photosensitive preceramic polymer the majority of this work is based on was a liquid photo-curable siloxane of proprietary composition (TEGO RC 711, Evonik Industries, Germany). Photoinitiator Irgacure 819, Ciba Specialty Chemicals, Switzerland and photoabsorber E133, Squires Kitchen, England were used in the DLP printing process. For 2-photon-lithography (2PL) fabrication 4,4'-Bis(diethylamino)benzophenone (BDEBP), Sigma Aldrich, was used as photoinitiator. The samples produced at collaboration partner Lithoz GmbH were printed using a photoinitiator of proprietary composition and the light penetration depth was controlled by using an azo dye. No catalysts were added for promoting the crosslinking of the preceramic polymers in any printing process.

For the fabrication of SiOC macro- and micro-ceramics, two high ceramic yield silicone resins were used, Silres 601 and H44, Wacker Chemie A.G., Germany. A list of further preceramic polymers and solvents tested but not selected in this work can be found together with all used chemicals in Table S1. Toluene was employed as the solvent for the preparation of the blends, and diphenylether for the cleaning of the printed parts (both from Sigma Aldrich). The solid polysiloxanes Silres 601 and H44 were dissolved in toluene in a constant weight ratio of polysiloxane/solvent of 3/1 with a magnetic stirrer at 60 °C within 2 hours. TEGO RC 711 was then added to the dissolved preceramic polymer solutions in the desired amount.

For the fabrication of mullite, two alumina powders with different particle sizes were used to react, during firing, with the silica source deriving from the preceramic polymer, forming mullite: nano-sized γ-Al_2O_3 (Aluminium oxide C, Degussa, Germany, mean particle size = 15 nm, specific surface area = 100 m^2/g) and micro-sized γ-Al_2O_3 (Puralox TH 100/150, SASOL, Germany, mean particle size = 2–6 µm).The alumina particles were dispersed in phenoxyethanol, before the liquid RC 711 was added. The ratio between RC 711 and Al_2O_3 was determined from the molar composition of mullite and the ceramic yield of RC 711 in air, and adjusted for the micrometre-sized alumina mixture to develop mullite without SiO_2 surplus through XRD characterisation. A small amount of dispersing agent, 0.24 wt% phosphoric acid polyester, was added to the printing formulations to adjust the rheology.

After the respective material formulation, the printing resins for DLP were equipped with 2 wt% Irg 819 and 0.75 wt% photoabsorber E133 in respect to RC 711 content, the resins for 2PL fabrication with 1 wt% BDEBP according to RC 711 content and the blends printed at Lithoz GmbH with their proprietary photoinitiator and azo dye as photoabsorber. All bottles containing the photosensitive

resins were wrapped in aluminium foil to prevent light illumination from the surrounding environment, and homogenized at 60 °C overnight.

2.2 Printing Processes and Heat Treatment

For macrofabrication, the homogeneous resins for the production of SiOC macrostructures were printed using DLP printer 3DLPrinter-HD 2.0 (Robofactory, Italy) operating in the visible light range (the wavelength was limited to the 400-500 nm range by applying an optical filter). The printer operates according to the bottom-up method (Figure 4a). It proved to be essential for the success of the printing, that the glass printing platform was cleaned after every printing step with acetone and occasionally polished to remove any polymeric smear layer, which was detrimental for the attachment of the printed object to said printing platform. Additionally, the PDMS layer of the vat was regularly replaced due to the formation of "ghost-interfaces" left over from the printing process, which lessened the transparency of the chamber and the non-sticky property of the PDMS material, essential to prevent attachment to the bottom of the chamber during printing. The layer of the printing chamber was self-made from PDMS Sylgard 184 (DOW CORNING, USA). The liquid two component material was mixed in ratio of base to catalyst of 10 to 1 and thoroughly mixed. Entrapped air bubbles were removed by vacuum drawing in exsiccator and the liquid material subsequently spread in a flat sheet on a plastic dish, surrounded by the reusable PDMS walls of the printing vat. The material was solidified at 60 °C over night in a drying furnace, connected to the previously made solid PDMS walls and was, after hardening, removed from the plastic dish to be used as the new printing vat. Typically, and if not otherwise indicated, structures were prepared with a set layer height of 50 μm and default lateral resolution of equally 50 μm by 50 μm. The stl-files of all printed structures, which were used during the course of this work, are represented in Table S2 and overall dimensions as well as strut sizes of lattice structures are indicated. All structures were cleaned after printing using diphenylether in an ultrasonic bath for 6 min and blow dried using compressed air. A list of further tested solvents and their suitability to remove uncured resin, while leaving the polymerised structure intact, can be seen in Tables S3 and S4. After the removal of the uncured liquid, the partially cured structures were illuminated for 15 min in an UV furnace (365 nm, Robofactory, Italy), to complete the formation of the acrylic network. The fully cured structures were dried at 60 °C in a drying furnace overnight, to remove all traces of cleaning solvent from the surface of the parts.

Mullite parts and parts for the hybridisation experiment were printed at Lithoz with DLP printer CeraFab 7500 (Lithoz GmbH, Austria; wavelength of 455 to 465 nm) at a set layer height of 25 μm and post-cured for 2 min with an UV lamp (Intensity ~20 mW/cm²). Afterwards the structures were cleaned in phenoxyethanol and blow dried with compressed air. Additionally, the mullite structures were dried at 120 °C for 38 h.

To fabricate microstructures, two-photon lithography was carried out using a Nanoscribe GT Photonic Professional device. The system is equipped with an erbium-doped femtosecond laser source, with a center wavelength of 780 nm and power of about 150 mW at a pulse length between 100 fs and 200 fs. A 63 x 1.4NA oil immersion objective of 360 μm working distance was used. Nanoscribe GT was calibrated to about 50 mW power in the sample plane, for a power scaling value of 1.0 (returned by the acousto-optic modulator calibration) and 100 % laser power. An estimate of the effective power during a fabrication process was provided by multiplying 50 mW by laser power and power scaling values. The laser beam was focused through a glass substrate (a coverslip) into the photosensitive polymer solution; in this configuration, the maximum structure height is limited by the objective working distance and by the substrate thickness (equal to about 150 μm). All substrates, onto which polysiloxane structures were fabricated, required a previous functionalization with a (3-methacryloxypropyl)trimethoxysilane solution, in order to provide methacrylate surface groups for covalent binding of the acrylate siloxane to the glass surface. This step guarantees stable linkage between the 3D solid and the glass substrate during development and during pyrolysis, which is necessary for handling the fabricated micro- objects. After 3D laser writing, removal of the unpolymerised solution was likewise performed with diphenyl ether using a pipette to promote solvent flow on the glass substrate and the just fabricated structure. Once cleaned, samples were dried at 60 °C on a heating plate for at least 1 h to remove any trace of cleaning solvent from the surface.

The heating schedules were selected on the basis of DTA results. The polysiloxane blends, 2PL and hybrid structures were pyrolysed in an alumina tube furnace (Lindberg, Riverside, MI and Carbolite CTF 17/300) at 1000 °C for 1 h in nitrogen (99.99 %) with a heating rate of 2 °C/min to fabricate SiOC ceramics. The SiOC samples were placed in a crucible with a lid on top during heat treatment, to build "heat walls" from all sides, which ensured a uniform heating and therefore a uniform shrinkage of the structures. Open spots between lid and crucible guaranteed that gaseous organic moieties can escape from the inside during pyrolysis, causing no problems to the structure.

The mixtures yielding mullite ceramics were sintered at temperatures in the range 1200-1400 °C in air. The processing cycle in air consisted of the debinding (heating at 1 °C/min to 190 °C with a holding time of 2 h, and then to 500 °C at 1 °C/min for 1 h) to decompose the polymer network, and the firing (heating at 5 °C/min to the final temperature for 1 h) to develop the ceramic 3D printed mullite structures.

2.3 Characterisation

Morphological characterization of the printed structures was performed on all scales by camera (Nikon D7500, AF-S Micro Nikkor 40mm Lens, Nikon, Tokyo, Japan), stereo-microscopy (STEMI 2000-C, Zeiss, USA) and scanning electron microscopy (SEM, Quanta 450, FEI, USA and SEM, Zeiss 1550 VP FE SEM, Carl Zeiss AG, Oberkochen, Germany, on metal-coated samples), which was also used to perform EDX analysis on the samples. To investigate the shrinkages of all fabricated components, large dimensional values of the overall macro-structures were measured with manual caliper, while the dimensions of the small-scale structure or individual beam elements were obtained from SEM images and ImageJ software, both performed at multiple locations. Thermo-gravimetric analyses (TGA, STA 409/429 Netzsch, Verona, Italy) were carried out with printed samples at a heating rate of 5 °C/min in flowing nitrogen or in air atmosphere. The optical absorbance of the preceramic polymers, the photoinitiators and photoabsorber (dissolved in toluene at a 0.1 wt% concentration) was investigated by UV-Vis spectrometry (V-650, JASCO International Co., Japan). XRD spectra were collected on the same amount of ground samples with a diffractometer (AXS D8, Bruker Italia, Italy), with Cu-Kα radiation and θ-2θ configuration. The crystalline phases were identified supported by data from PDF-2 database (ICDD-International Centre for Diffraction Data, Newtown Square, PA, USA) and Match! program package (Crystal Impact GbR, Bonn, Germany). The true density of the heat-treated printed samples was characterised by means of a helium pycnometer (Accu-Pyc 1330, Micromeritics, USA).

The compressive strength of mullite samples were evaluated at room temperature with an Instron 1121 UTM (Instron, Danvers, MA, USA), operating with a cross-head speed of 0.5 mm/min. The mechanical properties of the entire SiOC trusses as well as the beam elements were determined using Instron 5982 (Instron, Danvers, MA, USA) with two different set-ups, illustrated in Figure 9. The printed and pyrolysed SiOC samples were cut on top and bottom using a diamond wafer blade in an Isomet 5000 saw (Buehler Inc.) to ensure a planar contact area. The cut was made through the truss nodes to minimize partial truss cells at the loading surface, which could lead to inhomogeneous loading and additional contact stresses, leading to early failure. Additionally, the testing set-up for uniaxial compression was modified with spherical washers on either side of the tested sample, to allow some degree of rotation and get completely parallel contacts during the compression test, illustrated in Figure 9A. The uniaxial compression strength of the SiOC trusses was tested at a constant displacement rate of 0.1 mm/min. The E-Moduli of the samples was taken from stress-strain curves of the mechanical compression tests with compliance adjustment.
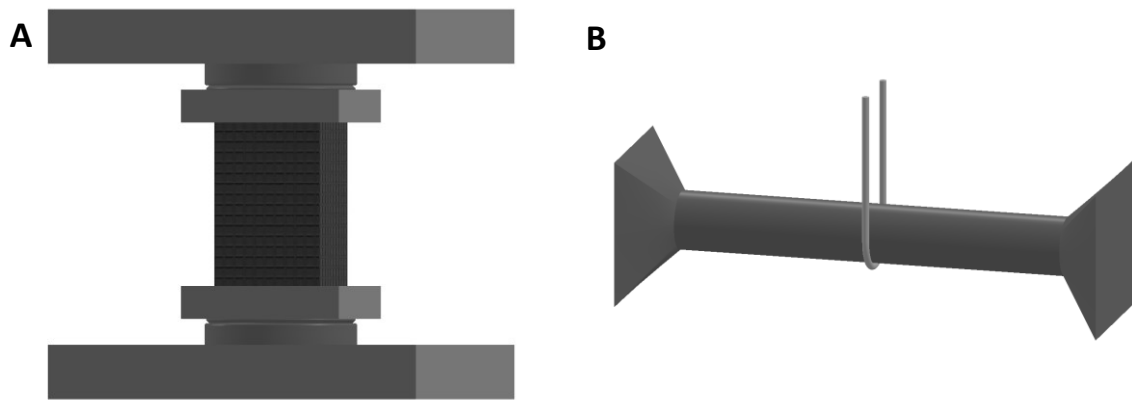
Figure 9 Schematic drawing of set-up of compression test of lattice structures (A) and flexural tests of individual beams (B).

An illustration of the flexural tests on individual beams, adapted from the work of Brezny et al.,[51] investigating the strength of single struts in alumina and zirconia replica-foams, can be seen in Figure 9B. The samples were mounted in a small-scale bench vice and oriented so that the tested struts were arranged perfectly horizontal to the loading direction. A low carbon steel wire with a diameter of 0.014 in. was looped around the centre of the single struts and attached to a tensile fixture on the load frame. A three-point-bending test was performed on the individual beams by pulling the wire at a constant displacement rate of 1.0 mm/min.

2PL printed microsamples were mechanically tested by using a nano-indentation rig (Alemnis Gmbh, CH) developed for in-situ testing inside an SEM. The samples were mounted on top of a rotational stage to align them to the flat diamond punch, which was applying the compression load onto the samples at a controlled displacement rate of 5 nm/s.

To test the reliability of the 3D printed ceramic samples, the compressive strengths have been analysed according to DIN EN 843-5 with the maximum-likelyhood method to determine the Weibull parameters, the Weibull-modulus m and the characteristic strength.

3 Digital Light Processing of SiOC Ceramic Components at the Macroscale

Preceramic polysiloxanes can be used to fabricate SiOC ceramic structures when pyrolysed in inert atmosphere. A common practice, when not satisfied with the performance and properties of the ceramic structures, is to integrate a suitable filler material inside the preceramic polymer. Previous work demonstrates that there exist two categories of filler material, active and passive fillers.[37, 42, 52-56] The active fillers, which are usually metallic or intermetallic powders can react during pyrolysis with the decomposed organic moieties, the gas atmosphere or also with the ceramic phase generated from the preceramic polymer. The so called "inert" or passive fillers, on the other hand, which up to now have been ceramic powders, are integrated in the preceramic polysiloxane matrix but, different from the active fillers, do not react with the transformed ceramic phase from the preceramic polymer or the decomposition gases upon heating. They are staying inert through the pyrolysis and maintain their state and composition during ceramic phase transformation of the preceramic polymers. They are therefore simply decreasing the amount of decomposition gasses by increasing the ceramic residue after heat treatment, and therefore influencing the shrinkage of the produced compound and decreasing the susceptibility to crack or pore formation. In following, the material and structure of SiOC parts were influenced by adding different secondary high ceramic yield polysiloxanes as passive fillers to a photosensitive low ceramic yield preceramic polysiloxane for a volumetric/geometrical effect, while maintaining a pure SiOC phase after pyrolysis. In this way the parameters of not only the printing resin, but also the final SiOC ceramic structures, shaped via Digital Light Processing, were altered in a wide range of values and carefully characterised, particularly regarding shrinkage and mechanical properties at all scales.

3.1 Achieving Variable Properties in SiOC Ceramics through Physical Blend Formulation

Additive manufacturing using photocurable preceramic polymers is one method to answer the increased demand of ceramic structures with complicated morphology by fabricating ceramic parts with high resolution and good surface quality. Introduced here is a new method, which was partially published in Schmidt & Colombo,[57] to fabricate SiOC ceramic structures by utilizing a simple physical blend between two different preceramic polysiloxanes. Blends consist of one polysiloxane which provides the necessary photosensitive acrylate groups and a second one which is non-photocurable but has a high ceramic yield. Different blend ratios have been realized and respectively optimized concerning the printing additives and setting times to fabricate exact replications of highly complex polysiloxane structures by Digital Light Processing. An image of all stl-files printed in this chapter can be seen in Table S2A. After pyrolysis, a uniform, homogenous shrinkage was observed yielding dense, pore- as well as crack-free SiOC ceramics. By adjusting the ratio between the different polysiloxanes, parameters such as the ceramic yield, shrinkage, chemical composition and resolution after pyrolysis were tailored in a wide range of values.

3.1.1 Stereolithography of Preceramic Polymers

Preceramic polymers have been successfully employed as feedstock for a variety of different AM techniques.[56] Besides the chance to fabricate materials which are only realisable over the molecular route[38, 40, 43] the use of preceramic polymer also lacks some of the disadvantages which are present when using a ceramic particle filled resin for stereolithography. As the preceramic polymers themselves are converted by pyrolysis into ceramics[37, 40] with decomposition of organic moieties and associated shrinkage, no ceramic particles are inside the printing resin and therefore no light scattering and absorption[1, 9, 14, 15] from the particles are present. Also, the refractive index of preceramic polymers (e.g. H44; n = 1,530 - 1,545)[58] matches those of other polymers, including photosensitive acrylate containing ones, which would make a mixture of both UV transparent, exhibiting no photoabsorption caused by the material. [9, 15, 17, 20]

Obviously, in order to process preceramic polymers by SLA/DLP, they need to possess photocurable moieties (like acrylate or vinyl groups). There exists a small number of commercially available silicon-containing polymers possessing photo-reactive groups (produced by companies such as Merck, Bluestar Silicones, Evonik and Starfire Systems). However, they often display very low ceramic yields, due to the decomposition of their photocurable acrylic side groups during heat treatment[20, 59] and the fact that they generally possess a linear polymeric chain, which generates volatile low molecular weight fragments during pyrolysis[48, 50]. For UV-curing of ceramic material specially developed preceramic polymers can offer suitable ceramic yields (around 60 – 80 wt% from Starfire Systems[60]) and have been used in soft lithography for the production of microreactors[61] or other micro components.[11, 62] Although they exhibit good soft lithography characteristics, the necessary UV exposure time, of the order of several minutes,[11, 61, 62] excludes them for the use in 3D Stereolithography, since in the available printing time frame no crosslinking between the preceramic chains on their own takes place using a SLA/DLP printer.[20, 63]

As no commercial resins are available which possess the necessary high photo-sensitivity, and therefore short crosslinking times, to be used with SLA/DLP printers, while also having a suitable high ceramic yield for the production of ceramic components, three different approaches can be followed to create such a material combining those two characteristics.

1) Chemical modification of a commercially available, high ceramic yield preceramic polymer by grafting of photocurable moieties;

2) Building up a preceramic polymeric structure starting from the photoinduced reaction of two distinct (often oligomeric) precursors;

3) Blending of a photocurable preceramic polymer with a non-photocurable, high ceramic yield preceramic polymer. In this case, no crosslinking reaction between the two different

polymers occurs upon light illumination, and the high ceramic yield preceramic polymer does not need to have specific functional groups.

In the first approach, a single source material is used for generating the 3D network upon light illumination. This has been successfully pursued in a few cases, but it requires a long chemical synthesis and the presence of suitable reactive groups in the preceramic polymer.[8, 59, 64, 65] In the second approach, two components are needed (either two silicon-containing oligomers/polymers[40] or a silicon-containing oligomer/polymer and an organic one[20, 66] have been used so far) possessing different functional groups which crosslink together upon light illumination. Both components are participating during the photoinduced crosslinking reaction via a thiol-vinyl[40, 66] or an acrylate-vinyl[20] copolymerisation, therefore requiring specific functional groups (e.g. vinyl, acrylate, thiol) which limits the selection of the components and also affects their cost.[20, 40, 66]

For the first time, the third approach is demonstrated here, that is a novel way to produce ceramic structures using DLP by generating a physical blend between two preceramic polymers. The primary polymer contains the acrylic groups, which chemically react upon light illumination in free-radical-polymerisation (compare illustration in Figure 2). The preceramic polysiloxane with more than one acrylic group in its polymer chain are forming an interconnected, branched solid 3D network (see illustration in Figure 10). The secondary preceramic polymer, although non-photosensitive, possesses a high ceramic yield, but otherwise leaves a high degree of freedom in selection as no specific functional groups are required, since the polymer is simply imbedded in the highly branched network formed by the photosensitive preceramic polymer. This is a fast and reproducible approach that benefits from the use of commercially available preceramic polymers, requiring no special synthesis procedure nor chemical expertise besides the selection of a suitable co-solvent.

Moreover, it should be pointed out that this innovative method has a significant additional benefit. Specifically, the ceramic yield, and therefore the shrinkage upon pyrolysis, can be varied by simply changing the ratio between the two polymers in the blend. This, in turn, controls the dimension of the structural details of the printed body after pyrolysis. This means that it is possible to achieve a variable, higher resolution with respect to the one achievable in the green state and limited by the equipment employed for the fabrication.
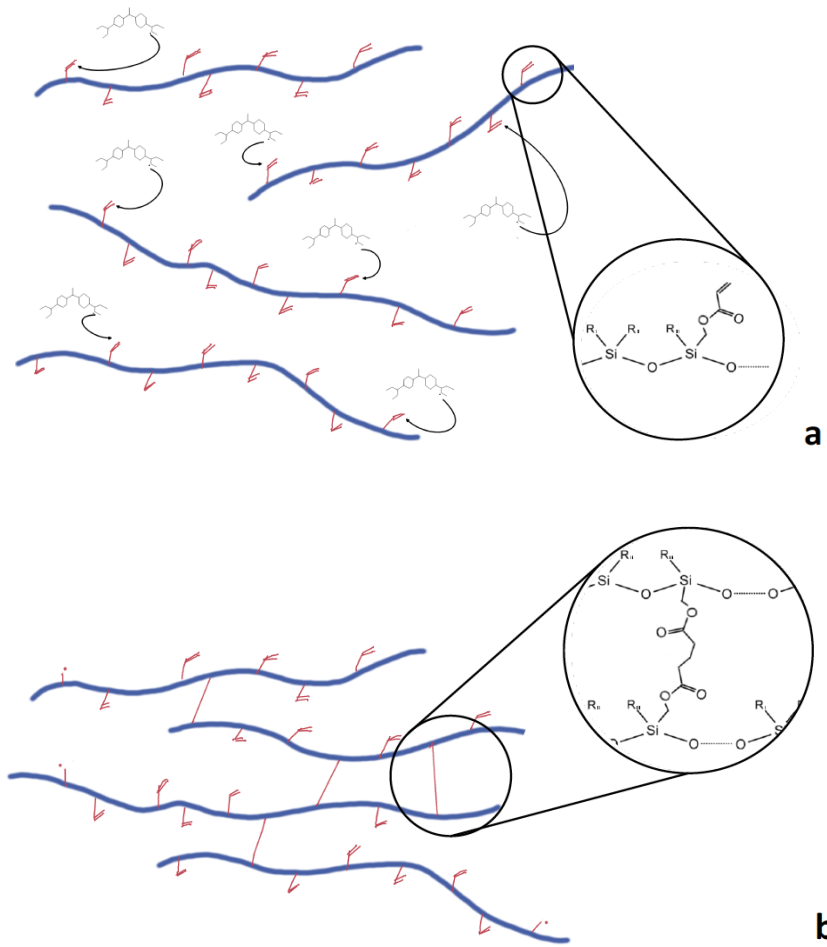
Figure 10 Schematic drawing of the a) photosensitive polysiloxane with acrylate-side groups in its polymeric chain and activation through photoinitiator, b) crosslinking by polymerisation of the siloxane preceramic polymer.

3.1.2 Blend Configuration

The synthesis of the photocurable preceramic blends was based on a physical mixture of two commercially available polysiloxanes, one providing the photocurability and the other the high ceramic yield. Several different polysiloxanes were used and tested in combination with each other and different photoinitiators and solvents in order to fabricate a stable preceramic polymer blend which is photocurable in a small timeframe and produces ceramic components with suitable ceramic yield.

3.1.2.1 Selection of photoinitiator

In order to activate a polymerisation process, a photoinitiator is needed to provide the necessary radical starting groups for the polymerisation chain reaction.[67] The photoinitiator (Irg 819) was selected because it is quite effective within the operational wavelength of the printer (see absorption spectrum of all constituents to the blends in Figure 14 later). An illustration of the photodissociation process and the resulting free radicals from Irg 819 are illustrated in Figure 11. Other photoinitiators like Camphorquinone, Irg 651 or Erythrosin B proved not to be as efficient as Irg 819 and were therefore not used in the following experiments (see Table S5).
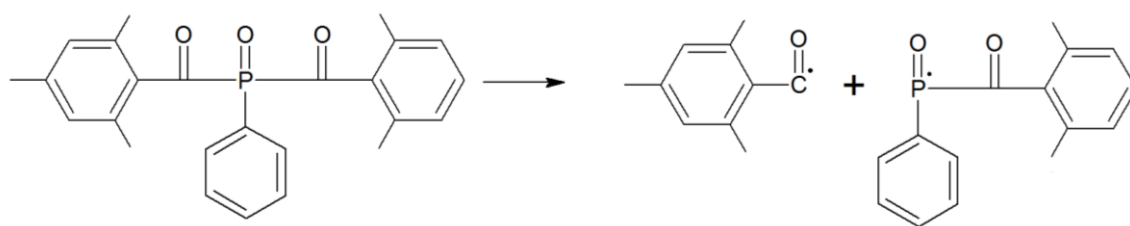
Figure 11 Photoinduced cleavage of Irgacure 819.

An illumination test using a model star shape was conducted to characterize the reactivity of the photosensitive RC 711 with different amounts of Irg 819, in order to select an appropriate amount of photoinitiator suitable for providing a fast polymerisation (see Table 1). No photoabsorber was added in these tests. In the table, the time reported (in seconds) indicates the minimum exposure time of the DLP printer that was necessary for achieving the desired printing quality. It can be observed that, with decreasing amount of photoinitiator, the minimum exposure time, necessary for obtaining a well-defined structure, increases. Further increasing the exposure time did not increase the sharpness of the printed object, but simply led to longer fabrication times required for the printing of the part. A viable exposure time, from the point of view of printing components in the centimetre scale in size using DLP in a reasonable period, is considered to be roughly in the range 1 to 20 s. After these experiments, an amount of 2.0 wt% of Irg 819 with respect to the photosensitive preceramic content was selected, as it reduced the exposure time to 1 s for the production of a model star shape with sharp features with RC 711 (thickness of the printed layer ~150 μm).

Table 1 Optimization experiments for determining the optimal amount of photoinitiator (scale bars = 2 mm) for printing with a short exposure time.

Irg 819: 0.5 wt%	Irg 819: 1.0 wt%	Irg 819: 1.5 wt%	Irg 819: 2.0 wt%
min. exp. time: 4 s	min. exp. time: 2 s	min. exp. time: 1 s	min. exp. time: 1 s
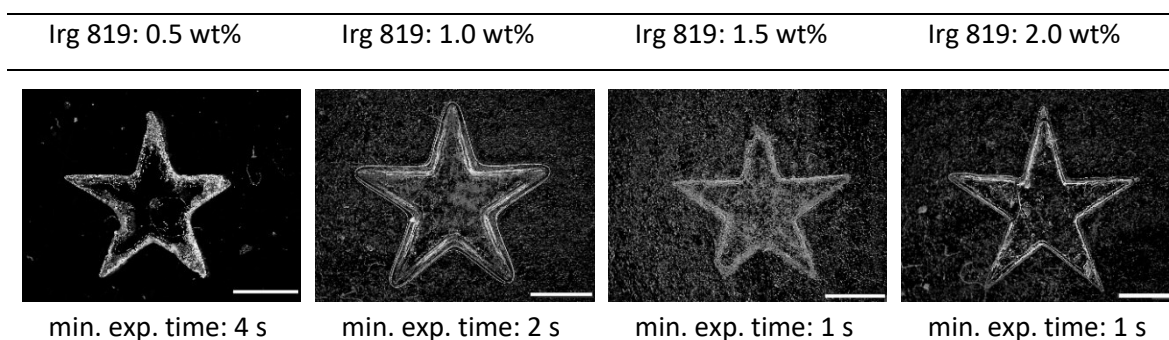
3.1.2.2 Selection of photosensitive polysiloxane

Different photosensitive polysiloxanes were available for characterisation of their photocurable properties and their use in combination with other high ceramic yield polysiloxanes. Table 2 gives an overview of the necessary exposure time of the model star shape (displayed in Table 1) fabricated with different preceramic polymers as well as the ceramic yield of potential candidates for further use in the polysiloxane blends. TGA analyses were only performed for materials which exhibit a minimum exposure time within the reasonable printing time frame < 20 s. If nothing else is indicated 2 wt% of Irg 819 was used as photoinitiator. As it proved to be incompatible with Si-vinyl-EQ, different solvents were used to dissolve Irg 819 before the addition of Si-vinile-EQ.

Table 2 Characterisation of minimum exposure time and ceramic yield of available photosensitive polysiloxanes.

Photosensitive polysiloxanes	Minimal exposure time	Ceramic yield (%)
RC 711	1 s	7.4
RC 711 + 1 wt% Geniosil GF91	–	6.1
RC 711 + 5 wt% Geniosil GF91	–	10.2
UV Poly 110 (UV CATA 102)	15 s	–
UV Poly 110 (2 wt% Irg819)	5 s	8.3
UV Poly 204 (UV CATA 211)	–	–
Si-vinile-EQ (solvent: toluene)	1 min	–
Si-vinile-EQ (solvent: isopropanol)	40 s	–
Si-vinile-EQ (1 wt% Camphorquinone)	20 s	–
AB 108972	10 s	4.7

Table 2 clearly indicates that all polysiloxanes which contain either acrylate (RC 711, UV Poly 110, AB 108972) or vinyl (Si-vinile-EQ) groups can be polymerised by free-radical-polymerisation using the operational wavelength of the available DLP printing equipment. Only UV Poly 204 is a cationic

photoresist, based on epoxy-silicone copolymer technology, and is therefore not usable in the DLP printer. Si-vinile-EQ shows the by far highest minimal exposure dose, which is not surprising considering that polymers containing vinyl-groups are rather inefficient in radical polymerisation compared to acrylic-groups.[66] From all the available photosensitive polysiloxanes RC 711, UV Poly 110 and AB 108972 show exposure times below 20 s, with RC 711 having by far the lowest exposure time of 1 s. The ceramic yield of all of these commercially available photosensitive polysiloxanes proved to be quite small, as expected,[20, 48, 50, 59] and show values beneath 10 wt%. Considering that UV Poly 110 only shows an increase of ceramic yield of less than 1 wt% while it takes five times the exposure time to fabricate the same model star shape, and that AB 108972 is the worst one of the three options in both minimal exposure time and ceramic yield, RC 711 was selected as the photosensitive polysiloxane in the future blend compositions.

Tests were also performed to increase the ceramic yield of RC 711 by addition of a catalyst, Geniosil GF91, a promoter of autocatalytical condensation reaction between the silanol groups within RC 711, to form a better-connected network of Si-O-Si groups. The addition of 5 wt% of Geniosil proved to improve the ceramic yield, but the increase was minimal, of only ~ 3 wt% and the addition of the photoinitiator to the RC 711/Geniosil solution showed a quick solidification within 10 min even without UV light exposure. It was therefore discarded as a way to improve the ceramic yield.

To get an idea about the effectiveness of the selected RC 711 polysiloxane compared to other photocurable polysiloxanes, functionalised MK, modified with vinyl groups,[8] was synthesised and the model star shape was fabricated. A high amount of 5 wt% photoinitiator yielded a minimal exposure time of 15 s with the available printing equipment. Printing tests later confirmed a limitation in printable height due to the low polymerisation degree of the printed functionalised MK, which yields a very soft structure unable to be built in height within the exposure range (1 – 20 s) of the available DLP printer.

3.1.2.3 Combination of polysiloxanes

Several combinations of RC 711 siloxane with different silicone resins with high ceramic yield but no specific functional groups were selected and tested if they would form a stable solution. Different solvents were used in order to select a combination that would provide the formation of a homogenous, stable system without macroscopic phase separation. Table 3 lists the blending tests between RC 711 and the secondary polysiloxane with the respective solvent, performed at a ratio of RC 711 to secondary polysiloxane of 5/5.

Table 3 Testing of different available polysiloxane materials regarding phase separation with RC 711 (ratio between secondary polysiloxanes and RC711 is 5/5) and min. exp. time of model star shape of stable blends.

Preceramic polymer	Solvent (ratio)	Phase separation	Min. exp. time
MK	Dowanol (3/1,3)	Yes	
	Phenoxyethanol (3/2)	Yes	
	Benzylalcohol (3/2)	Yes	
	Toluene (3/1)	Yes	
	Isopropanol (3/1)	Yes	
	Hydroxyethyl Methacry-late (3/2)	Yes	
MK *(PEGDA instead of RC 711)*	Toluene (3/1)	Yes	
	Dowanol (3/1,3)	Yes	
Silres 601	Dowanol (2/1)	Yes	
	Phenoxyethanol (3/1.5)	Yes	
	Benzylalcohol (2/1)	Yes	
	Dimethylsulfoxid (2/1)	Yes	
	Cyclohexanone (3/2)	Yes	
	Divinylbenzene (3/1)	No	20 s
	Isopropanol (3/1)	No	2 s
	Diphenylether (3/1)	No	2 s
	Toluene (3/1)	No	2s
Dow Corning 3074	Liquid	Yes	
H62C	Liquid	Yes	
DOW 217	Toluene (3/2)	No	3 s
Silres 610	Toluene (3/1)	Yes	
H44	Toluene (3/1)	No	2 s

Due to the very high ceramic yield of MK (85 wt%) several combinations with solvents and RC 711 were tested but all resulted in macroscopic phase separation. Even when trying to substitute the preceramic polymer RC 711 with another photosensitive polymer (Poly(ethyleneglycol)diacrylate; PEGDA) precipitation of a second phase took place. Tests were also performed with Silres 601 which show no phase separation with the solvents divinylbenzene, isopropanol, diphenylether and toluene. The minimal exposure time of 20 s rules out the use of divinylbenzene as a possible solvent,

which might be due to the double bonds in divinylbenzene interfering with the polymerisation of the acrylate groups of RC 711. The printing resins containing isopropanol, diphenylether and toluene as solvents show a necessary light exposure of a minimum of 2 s to produce the model star shape, which makes all three of them suitable for printing with the available DLP printing equipment. The solvents show that the same quantity is needed to completely dissolve Silres 601, while maintaining a suitable viscosity for printing. The low vapour pressure of diphenylether of only 0.08 hPa[68] actually favours the use of this solvent over isopropanol and toluene, which have high vapour pressures of 42.6 hPa and 29.1 hPa at 20 °C respectively.[69] However, printing tests with diphenylether as the solvent showed that difficulties in printing and a limitation in height of the object, which can be printed, exist. The material printed using diphenylether as a solvent was much softer than the one printed using toluene, and therefore it was unable to bear the load of the structure being printed, resulting in only very small structure being printable. This is probably due to a higher amount of solvent remaining trapped in the printed structure, acting as a plasticiser. The difference with what was observed with toluene might be related to a different affinity between the polymeric chains and the two different solvents. On the other hand, printing tests with isopropanol as solvent showed a substantial evaporation of isopropanol during printing, when the resin was introduced in the open chamber, which quickly changes the viscosity of the solution during printing, making isopropanol unsuitable to be used as solvent. As the combination with RC 711 with toluene as the solvent resulted in no evaporation of toluene during printing, despite its high vapour pressure, and no difficulties in printing were apparent, toluene was selected as the solvent to produce the blend mixtures. Tests on other available preceramic polymers, some in liquid form (Dow Corning 3074, H62C) others dissolved in toluene as solvent (DOW 217, Silres 610, H44), were performed as well. This resulted in three secondary preceramic polymers in total, in this limited number of available preceramic polymer, which form a stable solution with RC 711 by using toluene as solvent. The three selected preceramic polymers, containing phenyl (DOW 217, Silres 601) and phenyl-methyl (H44) side groups, are all in solid form and show ceramic yields of 69.8, 66.8 and 76.5 wt% respectively. As none of the selected preceramic polymers showed a significant increase in viscosity due to potential toluene evaporation over time, toluene was confirmed as the solvent of choice for the physical blends.

The solid polysiloxanes DOW 217, Silres 601 and H44 were dissolved in toluene in a constant weight ratio of polysiloxane/solvent indicated in Table 3. The ratio indicates the minimal amount of solvent needed to achieve an adequate viscosity necessary for printing. RC 711 was then added to the dissolved preceramic polymer solutions, as well as Irg 819 to initiate the photoinduced polymerisation. The resulting blends enabled the formation of a homogenous mixture with RC 711, providing not only compatibility but also long-term stability without precipitation of any secondary phase in the

course of several months. It should be noted that the investigation of the specific reasons for the phase separation with some combination of materials was beyond the scope of this work, which mainly aimed at validating the general processing approach of printing using a mixture of two different preceramic polymers. Also, the secondary preceramic polymers and the solvents used to try to dissolve them without phase separation upon blending with RC 711 is by no means complete. It is likely that those or other preceramic polymers with different combinations of solvents are equally forming a stable solution with a photosensitive preceramic polymer as well.

Initial pyrolysis tests were performed for blends with a ratio of DOW 217, Silres 601 and H44 to RC 711 of 5/5 to see if the structure of the printed product would be preserved after heat treatment and to finalise the selection of the appropriate preceramic polymers. Structures consisting of an arrangement of Kelvin cells (tetrakaidecahedron) were printed with the indicated blends and pyrolysed in nitrogen (see Figure 12). The picture in Figure 12A shows that a combination of RC 711 with DOW 217 exhibits bloating during pyrolysis and distortion of shape as material is flowing out of shape. It indicates that the polymerised RC 711 cannot contain the foaming DOW 217 in its polymerised network during heat treatment, allowing it to distort the structure and form bubbles. Further evidence of bloating and loss of shape of pyrolysed RC 711/DOW 217 blends can be seen in Figure S1. Geniosil was again added as a crosslinking agent, to test for the formation of connections within DOW 217, which could prevent the bubble formation during pyrolysis. Besides the already overserved reactions between Geniosil and the photoinitiator, which resulted again in a gelled solution, leaving not enough time for printing before the setting point, TGA results show a comparable ceramic yield of 45.8 % compared to 44.4 % without catalyst, indicating no further crosslinking in the material solution, and still foaming being present during pyrolysis.

Differently, the combination with Silres 601 and H44 show in the images in Figure 12B,C that the blends formed with these two secondary preceramic polymers are not only stable in the liquid state and printed polymeric condition but also maintain their shape after pyrolysis and form a homogenous ceramic.
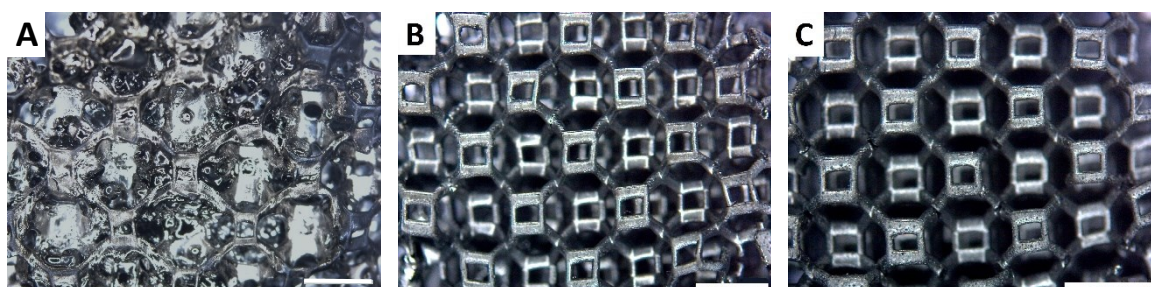
Figure 12 Pyrolysed Kelvin cell structure fabricated with blends of DOW 217 (A), Silres601 (B) and H44 (C) to RC 711 with ratio of 5/5 showing the bubble formation in A and preservation of shape in B and C; scale bars = 2 mm.

After the pyrolysis experiments, DOW 217 was discarded for the use as a secondary preceramic polymer to contribute a high ceramic yield to the preceramic polymer mixture.

Homogenous blend formation and preservation of shape after pyrolysis show Silres 601 and H44 as suitable candidates for the formation of the physical blends between two preceramic polymers, one contributing photosensitivity and the other a high yield of ceramic material to the properties of the physical blends. Following, those two were selected and four different weight ratios of RC 711 to Silres 601 or H44, ranging from 9/1 to 3/7, were tested and structures manufactured, using pure RC 711 as well (see Table 4).

Table 4 Composition of selected preceramic polymeric blends.

Weight ratio RC 711/Silres 601 or RC 711/H44	1	9/1	7/3	5/5	3/7
RC 711 content (wt%)	100	87.1	63.6	42.9	24.3
Silres 601 or H44 content (wt%)	-	9.7	27.3	42.9	56.8
Toluene content (wt%)	-	3.2	9.1	14.2	18.9

The use of the two different preceramic polymers, containing different functional side groups, produces SiOC ceramic structures possessing a different amount of free carbon.[39, 45] The chemical composition of Silres 601 and H44 has been analysed by Scheffler et al.[45] and show that Silres 601, containing only phenyl side groups, possesses more carbon than the phenyl-methyl containing H44 (contribution of SiO_2, SiC and C in the SiOC ceramics Silres 601 and H44 can be seen in Table S6). The chemical nature of the repeating unit in the three utilized preceramic polymers RC 711, Silres 601 and H44, and their different organic functional side-groups, are schematically illustrated in Figure 13.

a) RC 711   b) Silres 601   c) H44
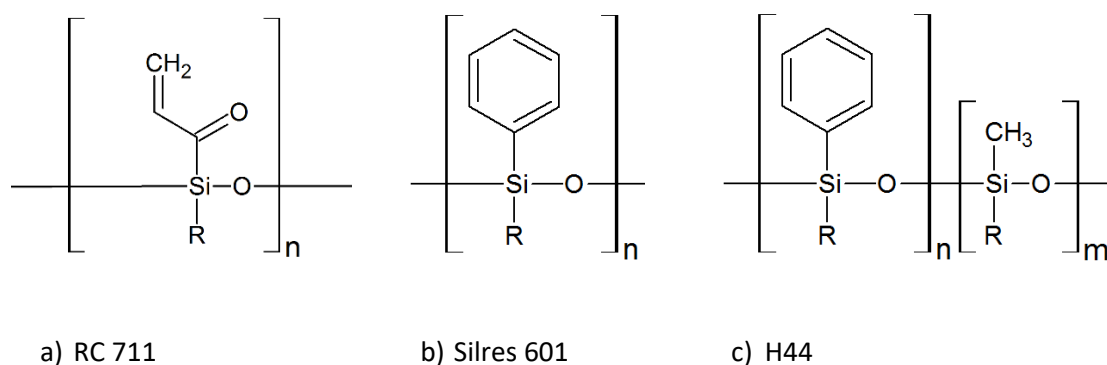
Figure 13 Schematic drawing of the repeating unit with their different organic, functional side-groups of the selected preceramic polysiloxanes.

3.1.3 Optimisation of 3D Printing Process

Printing tests confirmed that even only 24 wt% of RC 711 (see Table 4, ratio between RC711/Silres 601 or RC 711/H44 = 3/7) was sufficient to build the continuous acrylic network necessary for the formation of 3D printed structures (in the green state), entrapping up to 56.8 wt% of light-insensitive, high ceramic yield secondary polysiloxane. During printing, the highly acrylated, photosensitive RC 711 provided the reactive end groups capable of forming a continuous polymer network which acts as a partial frame incorporating the silicone resin chains. While Silres 601 and H44 on its own are photoinsensitive, they became entrapped by the polymerised network during printing, decreasing the weight loss of the blends upon pyrolysis, due to their high ceramic yield. After printing, the parts had to be cleaned to remove all extra fluid without damaging the actual structure. After testing several solvents (Table S3 and S4), diphenylether was selected to be used in the cleaning process since it successfully removed the uncured resin and no macro- or microcracks formed during cleaning of the porous structures, leaving no residual pattern on the surface which could be observed. Interestingly, the washing with the solvent did not extract the unpolymerised silicone resin from the printed structure, leading to dense, pore free polymeric structures (see later, Figure 23D,G). This indicates that the physical blend between the silicone resin and a photopolymerised photocurable siloxane occurs at the molecular level, without the creation of macroscopic phase separated islands in the printed material. After heating, a continuous pore-free ceramic SiOC structure was generated. Its chemical composition, and especially the amount of free carbon, changed according to the amount of RC 711 and the type of secondary polysiloxane (Silres 601 or H44) used, due to their different chemical side groups.[45]

3.1.3.1 Optimization of photoabsorber amount

During the printing process, the structures are partially submerged in the liquid polymeric blend contained in a vat, since the printer operates in the bottom-up projection method (compare Figure 4a). In order to increase the resolution in the z printing direction (perpendicular to the vat surface), and limit the penetration of light to the layer thickness chosen in the set-up of the printing parameters, a photoabsorber has to be added to the solution as it absorbs photons and therefore reduces the cure depth.[8, 15]

The photoabsorber E133 was selected (see Figure S2), as it has an absorbance peak within the operational wavelength of the printer (in the range of 400 to 500 nm, Figure 14). From Figure 14 it can also be observed that the absorbance of blends containing the two preceramic polymers (Silres 601 and H44) followed the same trend, with H44 absorbing slightly more light. Solutions containing a very limited amount of photoinitiator (0.1 wt%) and photoabsorber (0.1 wt%) had a much higher

absorbance than the preceramic polymers used in this work in the wavelength interval of interest, which makes the slightly higher light absorption of H44 negligible. Compared to pure RC 711, H44 and Silres 601 show similar absorbance values and have, as all three of them are of a polymeric nature, roughly the same refractive index[15, 17] which leaves the blends UV transparent and therefore leads to no scattering or absorbance due to refractive index contrast.[1, 9, 14, 17]
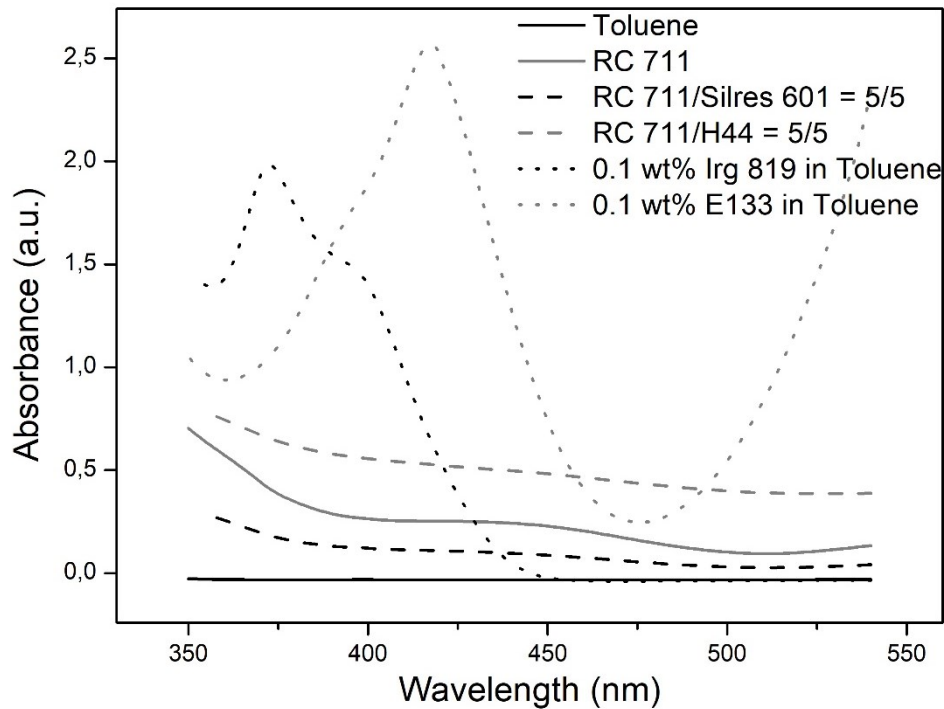
Figure 14 Absorbance of the solvent toluene, photoinitiator Irg 819, photoabsorber E133, the pure RC 711 silicone and an example of one polymeric blend (RC 711/Silres 601 or H44 in a 5/5 ratio).

In order to define the necessary amount of photoabsorber that would limit the overexposure of printed structures, leading to an accurate layer thickness (in our experiments, the layer thickness was set to 50 microns), different tests were conducted on pure RC 711 and the different blends indicated in Table 4 by printing a model scaffold structure, see Figure 15. The amount of photoinitiator used was 2 wt% with respect to the amount of RC 711 in all the blends (optimised according to Table 1), and the exposure time was in the range 1 to 14 seconds (see later); it should be noted that the change in exposure time is only slightly affecting the penetration depth of the light, outweighed by the influence of the amount of photoabsorber and depending on the composition of the blend. The feature to be evaluated was the degree of definition, that is the appropriate thickness, of the horizontal struts. To better visualize the details, a 4-layer (200 μm) horizontal strut size was selected in the design of the sample scaffold.
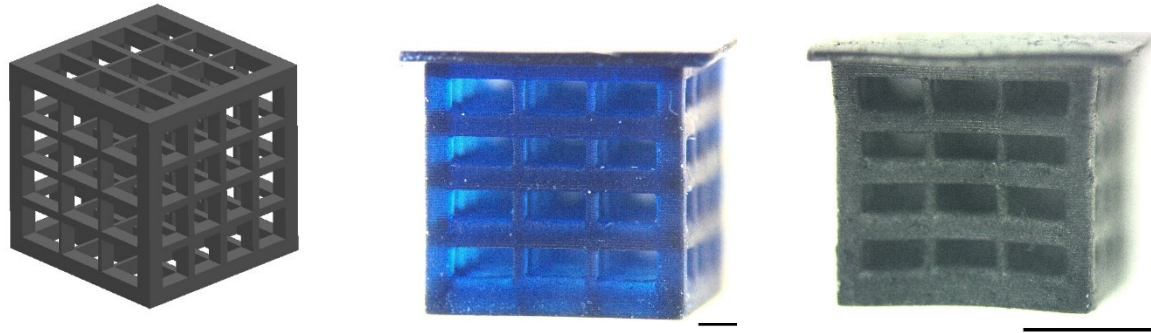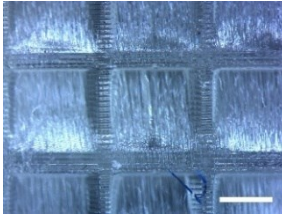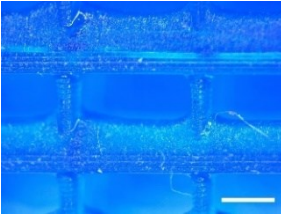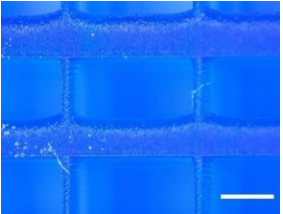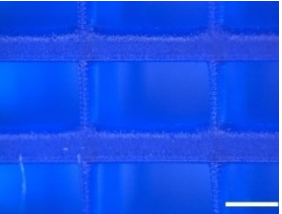
| CAD model scaffold | Printed scaffold | Pyrolysed scaffold |

Figure 15 Printing history: from CAD model to SiOC ceramic scaffold (sample produced using a RC 711/H44 = 9/1 blend; scale bars = 1 mm).

While it was important to avoid overexposure of the print, to ensure that a part with the desired dimensions was generated, the amount of photoabsorber had to be limited to ensure that the cure depth was not smaller than the imposed layer thickness, in order to print the full layer and avoid delamination by ensuring good inter-layer cohesion.[15, 70] Table 5 reports light microscope images of the side view of the scaffold printed using pure RC 711 with different amounts of E133. It can be observed that the lack of photoabsorber led to fully closed features due to the unhindered light penetration through the horizontal struts. The addition of the photoabsorber E133 enabled to build a proper scaffold structure, with defined horizontal struts and opening of the side walls. However, when the amount of photoabsorber was limited, additional material was also photocured on the top of the horizontal struts (the light illuminated the samples from the bottom of the images). Table 5 shows that an amount of 0.75 wt% E133 in RC 711 was necessary to fully replicate the struts in the stl-file and avoid overexposure at the set layer height of 50 μm.

Table 5 Optimization of photoabsorber E133 to reduce the overexposure and provide an exact replica of a model scaffold structure (pure RC 711; scale bars = 0.5 mm).

0.00 wt%	0.25 wt%	0.50 wt%	0.75 wt%

The same optimization test for the amount of photoabsorber was also carried out for all the polymeric blends (see Table 4). Starting from the blends with RC 711 to Silres 601 and H44 of 5/5 an amount of 1.5 wt% E133 according to RC 711 content was necessary to limit the z-penetration depth to the desired amount (see Table S7). This equals an amount of 0.75 wt% of photoabsorber with

respect to the preceramic siloxane content (acrylic siloxane plus silicone resin) for both secondary preceramic polysiloxanes, confirming that the limited difference in absorbance among the different silicones was not relevant (compare Figure 14). This amount of E133 in respect to the overall siloxane content was confirmed in all polymeric blends (see Table S8), providing printing solutions for all mixtures with complete and accurate replication of the designed struts without overexposure.

3.1.3.2   Optimization of exposure time

After the optimization of photoinitiator and photoabsorber, the necessary amount of exposure time for each polymeric blend for achieving well defined components was determined. The model scaffold structure shown in Figure 15 was printed with all eight blends, plus pure RC 711, using different amounts of exposure time. Table 6 reports, as an example, the optimization process carried out for pure RC 711 (2 wt% photoinitiator and 0.75 wt% photoabsorber, both with respect to RC 711 content). The stereomicroscope images taken perpendicularly to the top of the printed samples show that, in order to photocure even the smallest features in the selected model (horizontal strut width of 100 μm), a minimum amount of light exposure time was necessary. For pure RC 711, this proved to be 3.5 s per layer, as a shorter exposure time did not allow to obtain continuous horizontal struts with the required thickness, while a longer exposure time did not further modify their size. Note that this optimal time is longer than the one reported in Table 1 (1 sec), due to the presence of the photoabsorber in the mixture and the smaller area of the strut in comparison to the model star shape. An effect of the size of the sample was also observed since the larger struts in the stl file were already printed at lower exposure time, leading to an increase of exposure time needed for printing with decreasing feature size. To reduce the exposure time, more photoinitiatior could be added if desired, but was considered unnecessary as the exposure time didn't exceed 1 – 20 s, which was deemed an acceptable printing time.

Table 6 Optimization of exposure time for pure RC 711 samples printed at different exposure times (scale bars = 0.5 mm).

2 s	3 s	3.5 s	4 s
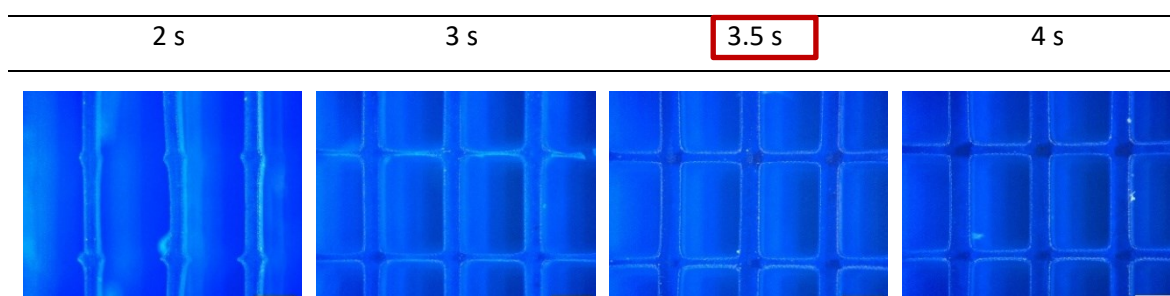
This optimization process was repeated for all the polymeric blends to determine the influence of their composition on the exposure time per layer (see Table S9). The amount of photoabsorber was kept constant in these experiments, at 0.75 wt% with respect to the total content of siloxanes, and the amount of photoinitiator was 2 wt% with respect to the RC 711 amount. Figure 16 summarizes the optimisation process carried out in Table S9 and shows that, with decreasing amount of RC 711, an increase of exposure time was necessary to provide the same resolution of at least 100 μm on the printing plane for all blends. The exposure time steadily increased from 3.5 s for pure RC 711 to a maximum of 14 s per layer for the RC 711/Silres 601 = 3/7 or 13 s for the RC 711/H44 = 3/7 blends. This trend was very similar for both secondary preceramic polymers (Silres 601 and H44), despite their slight difference in light absorption (Figure 14). The increase in absorbance of the blends containing H44 was rather small and did not appear to have a significant influence on the minimum exposure time.
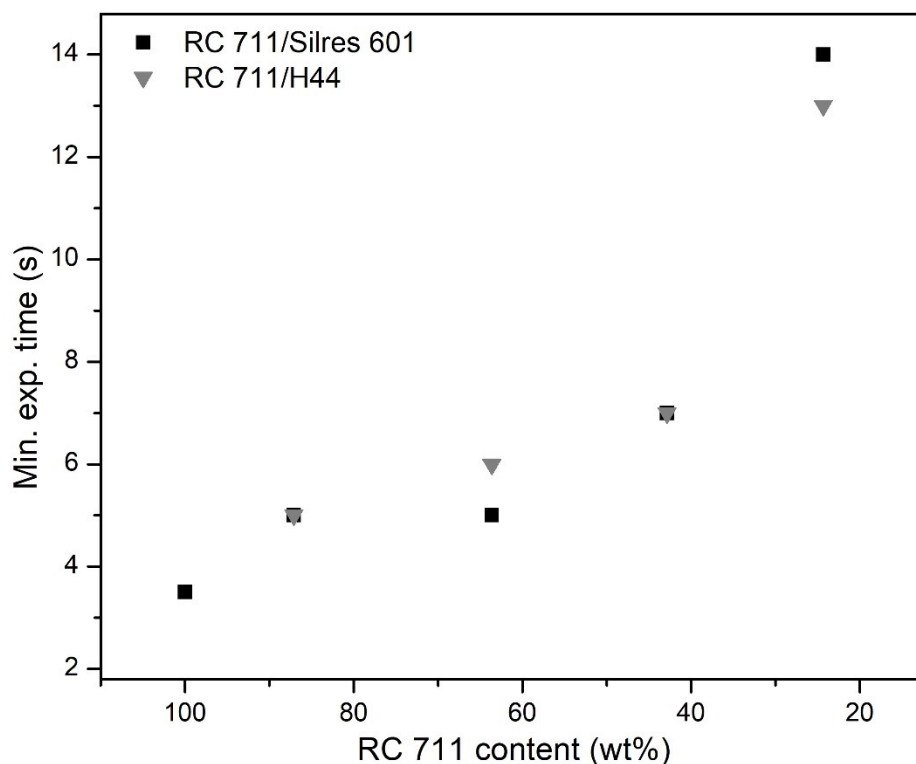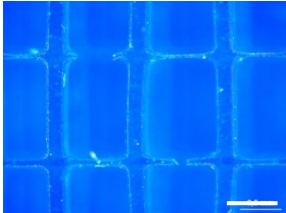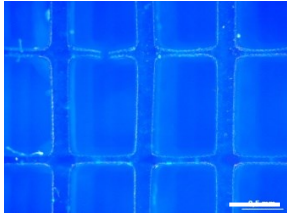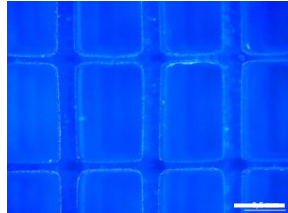
Figure 16 Minimum required exposure time of all the prepared blends to fully polymerise one layer with features of 100 μm in size in the printing plane.

While the printing blends proved to be stable against phase separation for several month, a test was conducted about the photosensitivity of the printing solution after a longer storage time. Table 7 shows the exposure optimisation of pure RC 711 solution, containing the standard 2 wt% Irg 819 and 0.75 wt% E133. After preparation, the solution was stored, wrapped in aluminium foil to prevent external light exposure, for 6 weeks before it was used to print the model cube structure.

Table 7 Determination of necessary exposure time of long-stored RC 711, scale bars = 0.5mm.

3 s	4 s	5 s

The results show that the exposure time for RC 711 increases from 3.5 s to 5 s, which indicates a slight reduction in the effectiveness of the printing solution with time. However, since the photo-sensitivity is not greatly reduced over the rather long time-frame of 6 weeks, it also shows that the printing solution can be stored for some time and still be used for 3D printing.

3.1.4 Transformation into Ceramic Material

Thermo-gravimetrical analyses showed that the decomposition process of the blends was a combination of the behaviour of the constituent polysiloxanes. In Figure 17, the curves for the pure siloxanes and for only one of the tested compositions (ratio RC 711/Silres 601 and RC 711/H44 = 5/5) are shown, as an example. The pure photocurable polymer (RC 711, tested on a printed sample produced following the same processing schedule adopted for all the samples in this work) had a very limited ceramic yield, due to the linear nature of the main polymeric chains.[48, 50] For the pure silicone resins (Silres 601 and H44), the limited low temperature weight loss associated with thermal crosslinking, followed by the typical decomposition occurring with gas release in the polymer-to-ceramic transition region (~400 to 800 °C), all well described in the literature,[37] were visible. The same features were retained in all the blends, indicating that the simple mixture of the polymers did not modify their pyrolysis behaviour.
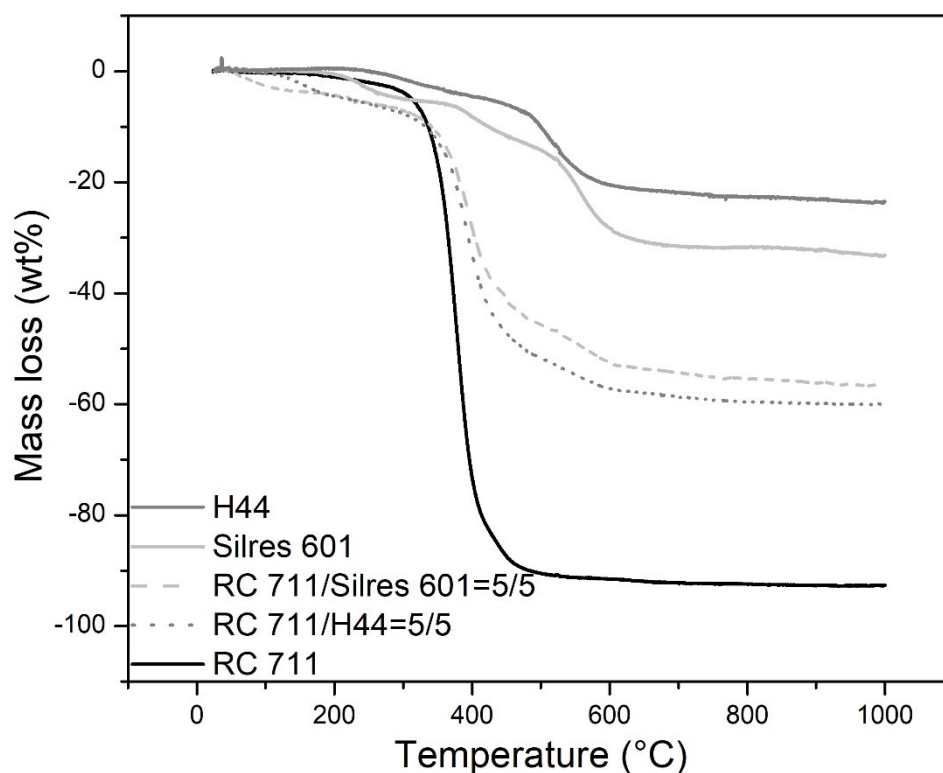
Figure 17 TGA curves of the pure constituents of the blends (RC 711, Silres 601 and H44) and of the blends with a 5/5 ratio.

3.1.4.1 Influence of blend composition on the ceramic yield

Printed structures were used to measure the ceramic yield, which remained, considering measuring accuracy, within the area of theoretical ceramic yield of the blends of RC 711 and Silres 601 or H44 respectively (see Figure 18). The theoretical values were calculated considering the measured ceramic yield of the pure polysiloxanes at 1000 °C (7.4 wt% for RC 711, 66.8 wt% for Silres 601 and

76.5 wt% for H44). The upper and lower lines of the shaded graph areas correspond to the theoretical yield considering, respectively, total or no evaporation of the toluene solvent before TGA measurement. The data suggest that, in some cases, some residual toluene was still present after printing, curing and drying.

The fact that the measured ceramic yield of the printed structures was within the upper and lower limits of the theoretical ceramic yield demonstrates that the material that was solidified by photocuring maintained the expected composition. This proves, in particular, that the preceramic siloxanes (H44 and Silres 601) were homogeneously dispersed in the liquid and, more importantly, that they became efficiently entrapped by the photocurable polymer in the solid structure during printing. That is, they were not expelled from the polymeric solid during the curing of the acrylated siloxane nor during the pyrolysis.

The data confirmed that with increasing amount of Silres 601 or H44, respectively, the ceramic yield of the blends increased steadily from 7.4 wt% (pure RC 711, after photocuring) up to 47.6 wt% (RC 711/Silres 601 = 3/7) and 60.2 wt% (RC 711/H44 = 3/7). The ceramic yields of the different blends displayed in Figure 18 are spanning an entire region, which incorporates all values of printed ceramic samples previously reported based on the different approaches (approach 1[8, 59] and approach 2[20, 40]). This demonstrates that this simple processing approach is very competitive and can provide a suitably large ceramic residue after pyrolysis.
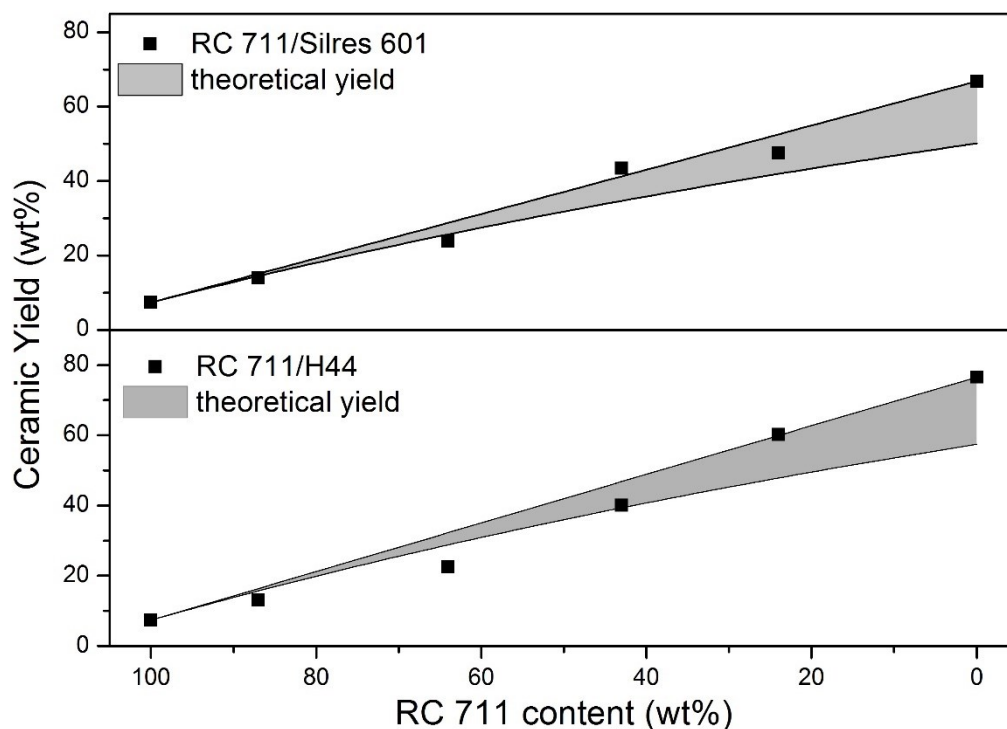
Figure 18 Region of theoretical ceramic yield, with upper and lower limit depending on the complete removal or presence of residual solvent in the printed structures, and experimentally measured values (data taken at 1000 °C).

3.1.4.2 Influence of blend composition on shrinkage

Besides for the optimization of photoabsorber and exposure time, the model scaffolds also served the purpose to determine the shrinkage upon pyrolysis of all the blends. Ten cubes for each composition were printed, and their dimensions in the x,y and z direction were measured before and after pyrolysis and then compared to the nominal values of the CAD file ($4.5 \times 4.5 \times 4.5$ mm^3). All the samples of the different blends showed a complete retention of their shape after heating to high temperature. It should be pointed out that this is a non-obvious finding, because it means that the photocured, acrylic polymer constituted a continuous network even at a low concentration, encasing the non-photosensitive preceramic polymer and preventing it from flowing during pyrolysis (even in the absence of a crosslinking catalyst).[8] We should also observe that the silicone resins possess silanol groups, and therefore can thermally crosslink by condensation during pyrolysis. It is the fact that the acrylic polymer decomposes above 300 °C (see Figure 17) that probably enabled to have the presence of a supporting network during thermal crosslinking of the preceramic polymers. Moreover, the decomposition of the acrylic polymer allows for the creation of a continuous network of pores, which enables the elimination of the gases generated by the decomposition of the silicone resins during pyrolysis. In turn, this enables the fabrication of dense, crack-free SiOC components with a thickness not achievable when directly pyrolysing a component made solely of

a pure silicone resin. Furthermore, these experiments prove that the proposed approach of a simple physical mixing of two preceramic polymers, one photocurable and mostly sacrificial and the other one with high ceramic yield, is viable for the fabrication of ceramic components via DLP.

The data collected on the green samples, after evaporation of the solvent, and the pyrolysed samples indicate that the printed parts underwent a uniform and homogenous shrinkage in all directions. In Figure 19A the x, y and z drying, pyrolysis and total shrinkage values for a blend of RC 711/H44 = 7/3 are shown as an example. Figure 19B reports the values of the average linear shrinkage after drying and pyrolysis (averaged considering the values corresponding to the 3 spatial directions), for both blends, as a function of their RC 711 content. The printed scaffold of pure RC 711 shows a shrinkage of only 1.7 % compared to the original stl-file. The change in dimension after printing for the pure preceramic polysiloxane results from a combination of polymerisation shrinkage (liquid to solid transition) with possible expansion due to swelling and heating during printing and post-curing in UV chamber.[21, 71] The amount itself is not very pronounced, and depends on printing parameters (exposure time in DLP, scan velocity and laser power in SLA) and the necessary post-curing, which fully polymerises the uncured photosensitive groups retained within the printed structure to improve its mechanical property and durability.[21] While the polymerisation shrinkage occurs in all resins containing RC 711, it is negligible compared to the drying shrinkage of the physical blends. The drying shrinkage of the blends is increasing with decreasing amount of acrylic polymer due to the fact that, in order to dissolve a higher amount of solid preceramic polymer silicone resin, a higher amount of toluene solvent was necessary (see Table 4). The data indicates that, within the error margin, an equal increase of the drying shrinkage with the decrease of RC 711 occurred for both preceramic polymer blends. This is attributable to the fact that a constant ratio between both Silres 601 and H44 to toluene (3/1) was used, and suggests that the different molecular nature of the silicone resins had no effect on the evaporation of the solvent.

The average pyrolysis shrinkage (computed with respect to the dimensions of the dried samples) decreased with increasing amount of preceramic polymers, either Silres 601 or H44, present in the blend, because of their much higher ceramic yield with respect to RC 711. Unexpectedly, blends containing Silres 601 had a lower pyrolysis shrinkage than those with H44, despite the latter having the higher ceramic yield. This indicates that the relationship between shrinkage upon pyrolysis and ceramic yield is less straightforward than one could imagine, and must be related to additional factors such as the molecular architecture of the preceramic precursor and the degree of thermal crosslinking occurring during heating (related to the number of silanol and ethoxy groups present in the silicone resins).[45] The detailed investigation of this aspect was, however, beyond the scope of this work.
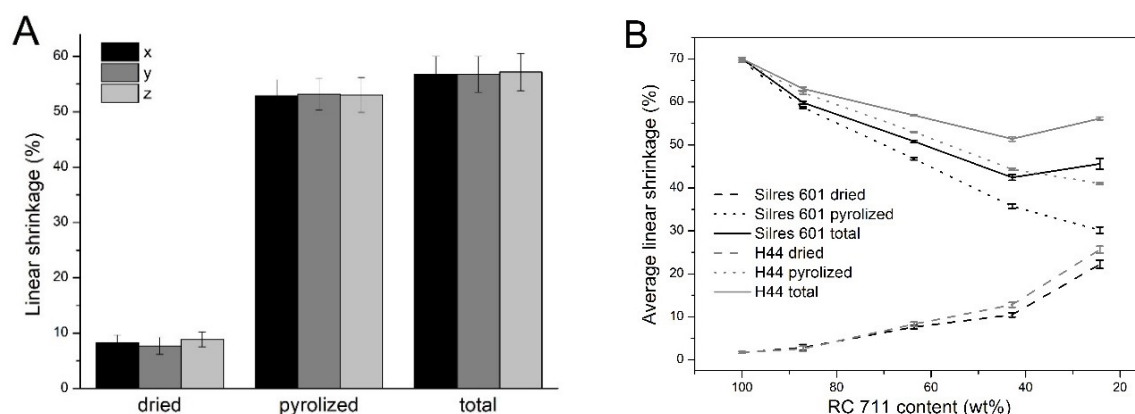
Figure 19 Linear drying, pyrolysis and total shrinkage in x, y, z direction of RC 711/H44 = 7/3 (A); Average drying, pyrolysis and total shrinkage of blends according to their RC 711 content (B).

The total linear shrinkage values were computed from the dimensions after pyrolysis with respect to those of the model CAD structure, and comprise the sum of the drying and pyrolysis shrinkages. These shrinkages had an opposite trend with decreasing amount of RC 711, leading to a not very pronounced minimum in the curves for both preceramic systems, occurring for a blend ratio of 5/5 (see Table 4). Of all the systems, pure RC 711 had a maximum total average linear shrinkage of 70.1 ± 0.5 %, while the smallest values reached were 42.4 ± 3.8 % for RC 711/Silres 601 = 5/5, and 51.4 ± 3.3 % for RC 711/H44 = 5/5.

It should be noted that the features that had a size of 100 µm in the CAD file, and of 98, 88, and 87 µm in the printed scaffolds after drying (for pure RC 711 and for the RC 711/Silres 601 = 5/5 and RC 711/H44 = 5/5 blends), after pyrolysis possessed a dimension of ~30 µm (RC 711), 58 µm (RC 711/Silres 601 = 5/5) and 49 µm (RC 711/H44 = 5/5), respectively. This demonstrates that, although structures manufactured with RC 711 had the highest shrinkage and lowest ceramic yield, they also exhibited the highest resolution. Therefore, the proposed processing approach provides an additional degree of freedom with respect to the size of the features that could be produced using the DLP printer, as a function of the composition of the blends (content of RC 711).

Furthermore, the selection of the pyrolysis temperature will also play a role in determining the final size of the component, as shrinkage depends also on the heating schedule employed.[41, 42] Figure 20A shows, that the shrinkage of RC 711 is only 62.5 ± 1.3 % at 800 °C compared to the 70.1 ± 0.5 % it has at 1000 °C. Combined with an increase in density from 1.8 to 2.0 g/cm^3 this means that the siloxane material is further densifying with an increase in temperature of 200 °C, while at the same time shrinking another 8 % when all the "transient porosity" is eliminated.[41] While the SiOC shows another increase in density to 2.1 g/cm^3, which could be related with rearrangements at the molecular and nanoscale level,[47] the shrinkage value drops to 66.5 ± 0.7 % at 1200 °C. This expansion

at higher temperature could be associated to the atomic rearrangement and the partial crystallisation of the material which until 1000 °C remains amorphous but starts to contain some β-SiC nano-sized crystals after treatment at 1200 °C (Figure 20B).
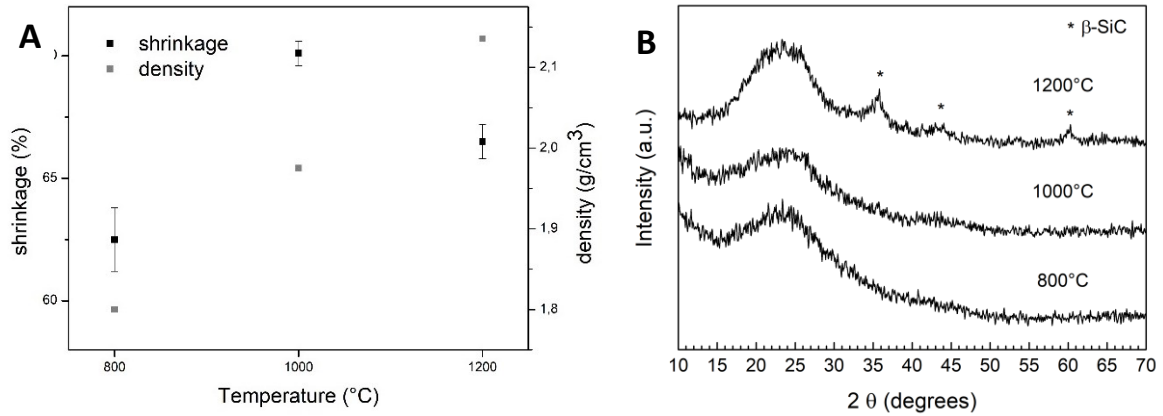
Figure 20 Shrinkage and Density values (A) and XRD patterns (B) of printed RC 711 samples treated at 800, 1000 and 1200 °C.

This variation in shrinkage depending on the selected blend mixture and employed pyrolysis temperature means that the resolution of the pyrolysed structures can be increased independently on the resolution of the used printing equipment. Therefore, features with a size below the capability of 3D printers, typically around 50 μm in the polymeric state, can be achieved.

3.1.5 Fabrication of Complex Architectures

The optimization of blend composition and printing parameters that was carried out enabled to fabricate components with complex architectures. Structure based on the Kelvin cell (a tetrakaidecahedron), which is one of the most efficient ways of partitioning space with cells of uniform volume generating a lightweight, strong network, are reported here.

Figure 21 shows SEM images of the dried and pyrolysed parts produced using the optimized RC 711 solution. The presence of discrete layers, typical of DLP printed structures, is evident (the height of the layer was set at 50 μm), but the horizontal features are rather smooth, also after pyrolysis. No deformation (warping) was observable, confirming the occurrence of isotropic, homogeneous shrinkage upon heating. A similar result was obtained when using the blends. Figure 22 reports, as an example, SEM images for samples printed with Silres 601 and H44 in the blends in the ratio of 5/5 with RC 711. It is evident that 42.9 wt% of photosensitive material in the blend was sufficient to print exactly the same structures with the same resolution (before pyrolysis) and complexity as when using the material consisting solely of the photosensitive polysiloxane.
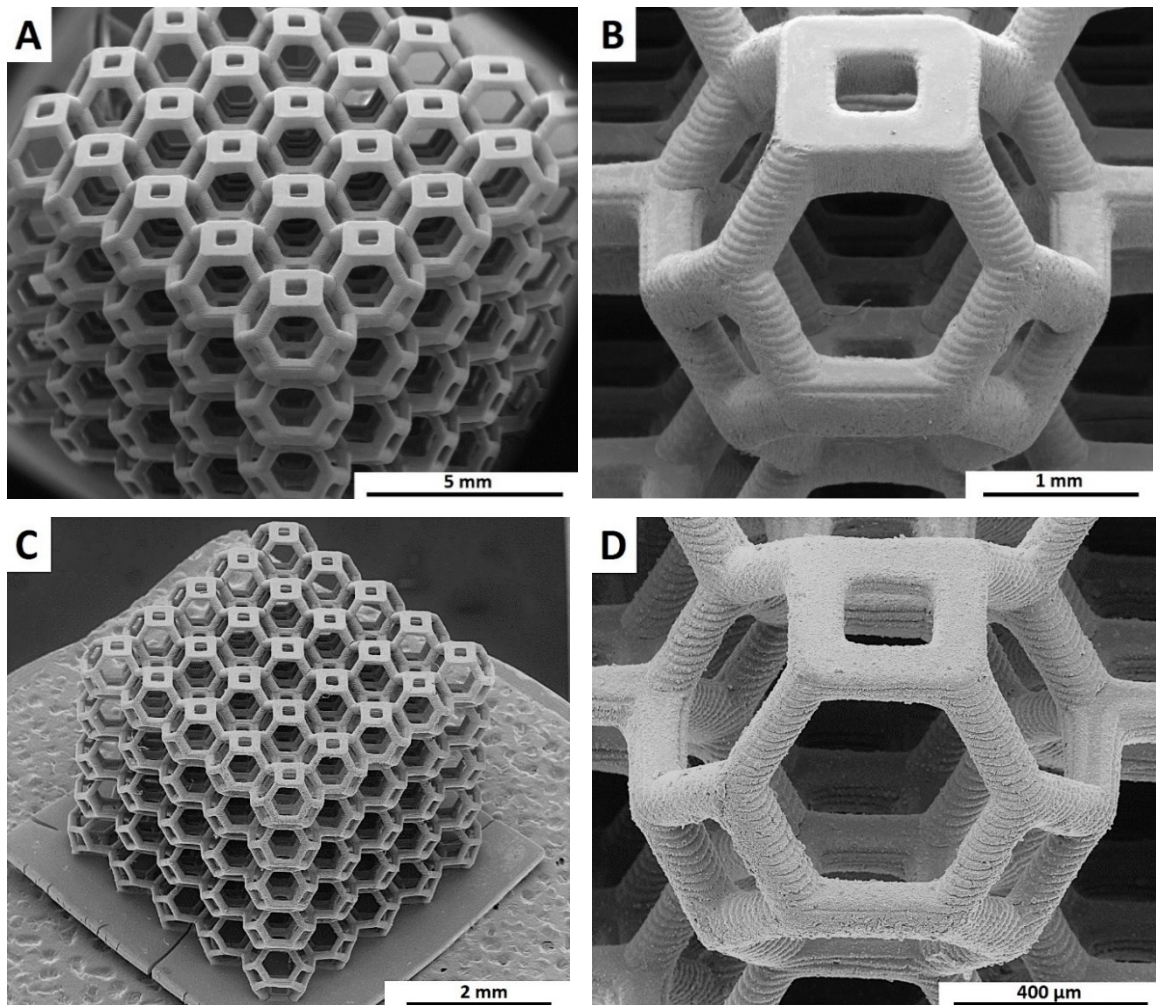
Figure 21 SEM images of the dried (A, B) and pyrolysed (C, D) Kelvin cell structure printed with the optimized solution of RC 711.
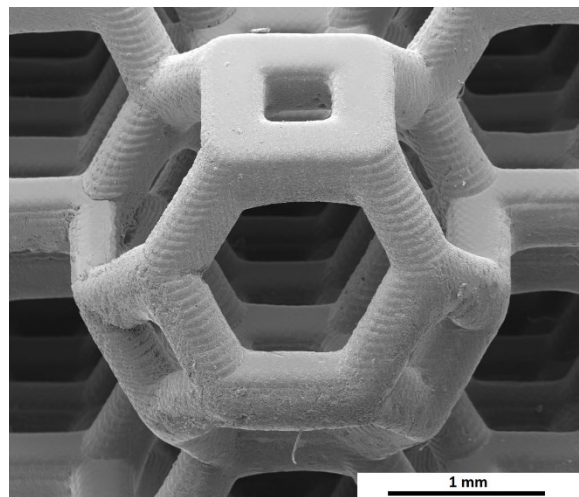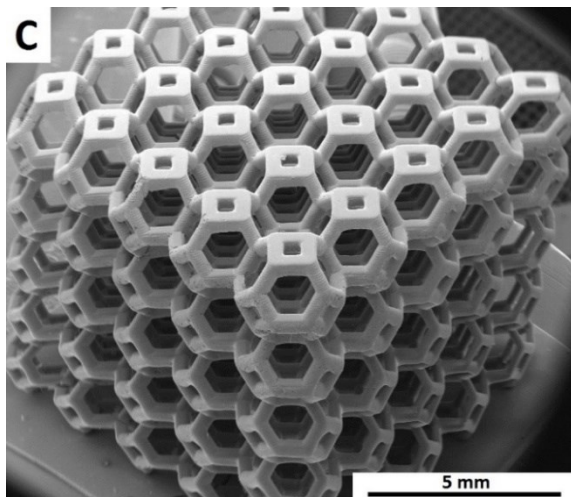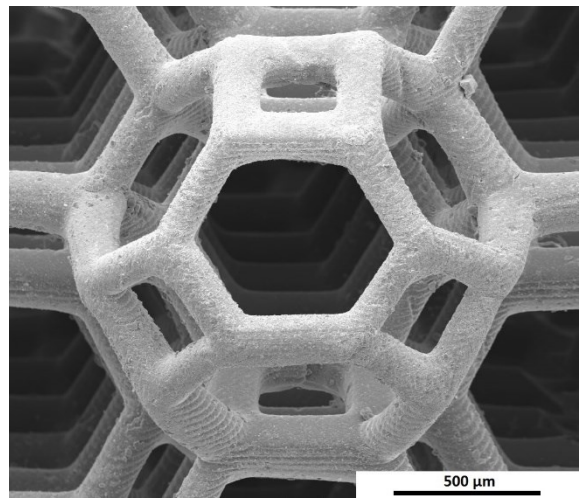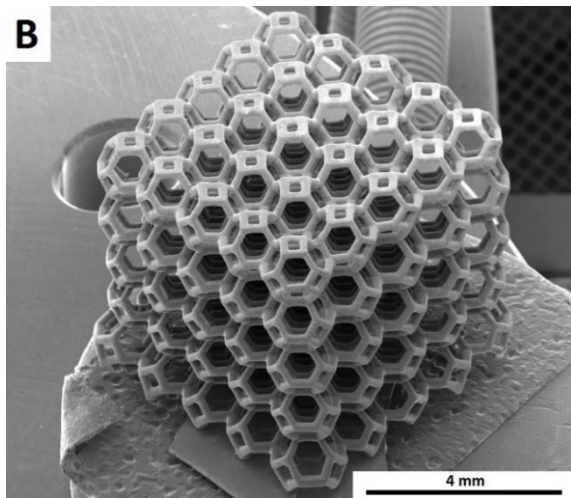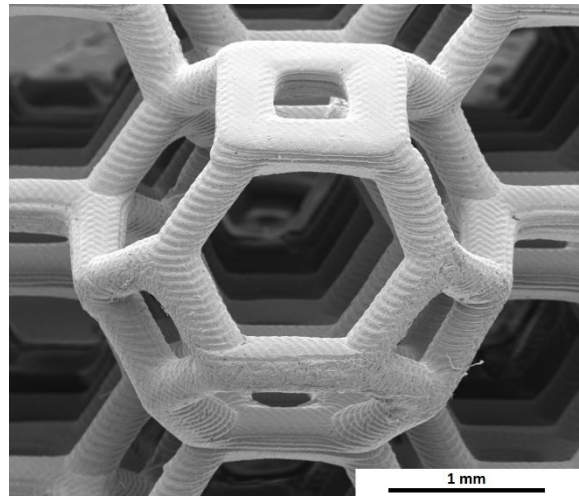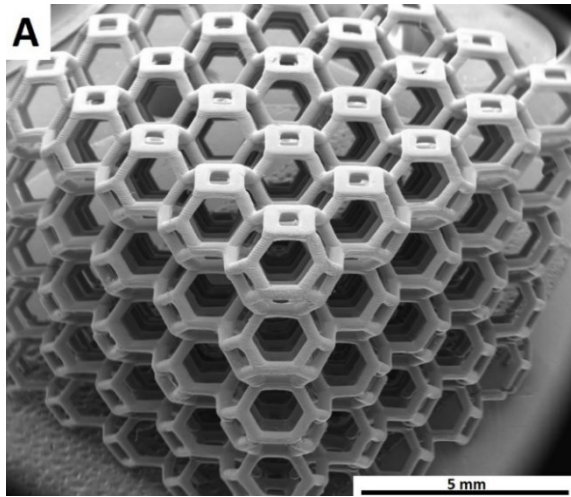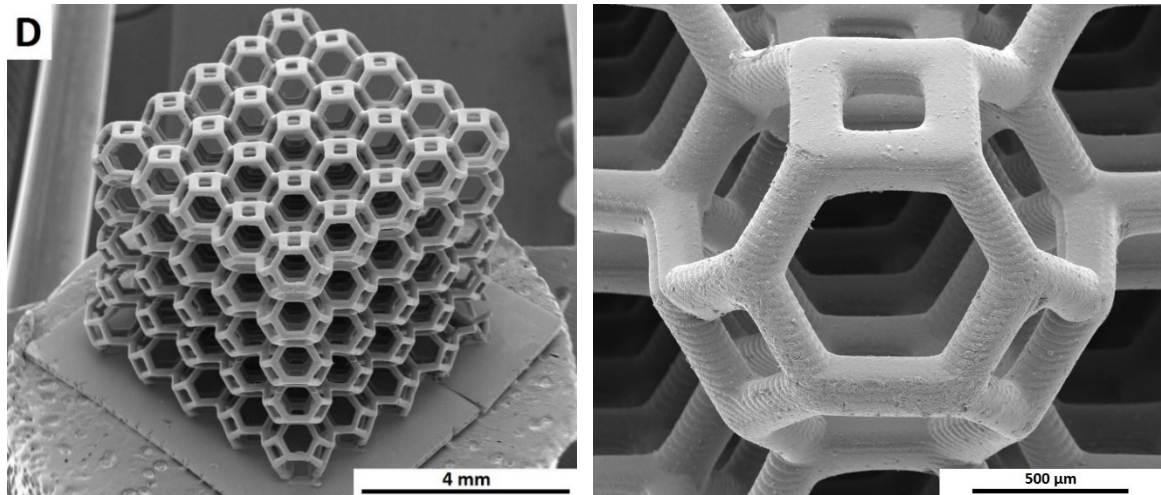
Figure 22 SEM images of the dried (A: Silres 601; C: H44) and pyrolysed (B: Silres 601; D: H44) Kelvin cell structure printed with the optimized blends (ratio preceramic polymer/RC 711 = 5/5).

3.1.6 Microstructure of 3D Printed Siloxanes and SiOCs

The microstructures of the 3D printed Kelvin cell structures displayed in Figure 21 and 22 were analysed in Figure 23. In the printed polymeric state all the materials, pure RC 711 as well as the mixtures with Silres 601 and H44, ratio with RC 711 equals 5/5, show a smooth surface (Figure 23 A,D,G). No distinction between the two polysiloxanes used within one blend can be observed. The printed struts present themselves as one unit of material, besides the fact that only RC 711 has formed the polymeric network incorporating Silres 601 and H44 in a scale not detectable via SEM. The same occurs in the pyrolysed state (Figure 23 B,C,E,F,H,I). No sign of separation between SiOC material originating from RC 711 and Silres 601 or H44 can be observed. The parts are transformed into one undistinguished SiOC material. Actually, pure pyrolysed RC 711 exhibits the roughest surface (Figure 23 B,C) whereas the blend with H44 shows the smoothest one (Figure 23 H,I) with smaller surface features, showing no sign of materials separation even below the μm range.
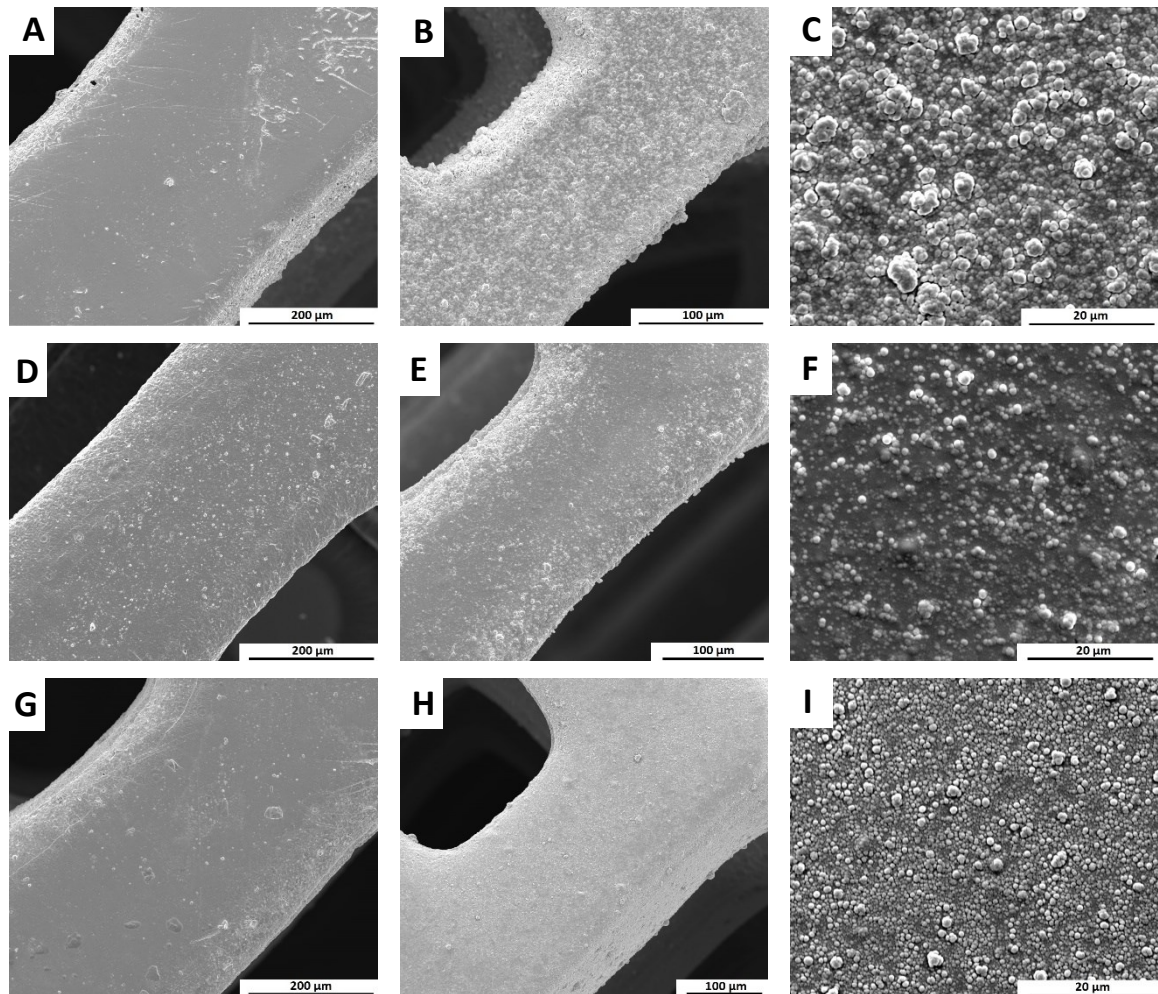
Figure 23 Microstructures analysed from the Kelvin cell structures in Figure 21 and 22 of RC 711 (printed A, pyrolysed B and C), RC 711/Silres 601 = 5/5 (printed D, pyrolysed E and F) and RC 711/H44 = 5/5 (printed G, pyrolysed H and I).

Apart from the smoothness of the surface of the materials within one layer, all printed parts show the representative step-wise production of the DLP printing technique across layers. The slicing of

the stl-file (illustrated in Figure 3c) to print an object layer-by-layer is visible and produces the rough surface in z-direction (see Figure 24A). It was already previously noted that the resolution of the pyrolysed structures can be increased independently on the resolution of the printing equipment through the pyrolysis of the polysiloxanes with their respective shrinkage and temperature control. This leads to the fabrication of smaller features below the DLP equipment's resolution limit (see chapter 3.1.4.2). Likewise, the step-like surfaces of the parts in z-direction can be smoothed, when the parts are transformed into SiOC ceramic, through the shrinkage of the material, which lowers the step-sizes significantly (Figure 24B). This, together with a control of the slicing thickness, can lead to the production of 3D printed parts via DLP with almost no distinguishable steps but a smooth transition within an object even in z-direction, which can be seen in the pyrolysed SiOC structure printed with a slicing of 25 µm instead of the usual 50 µm (Figure 24C).
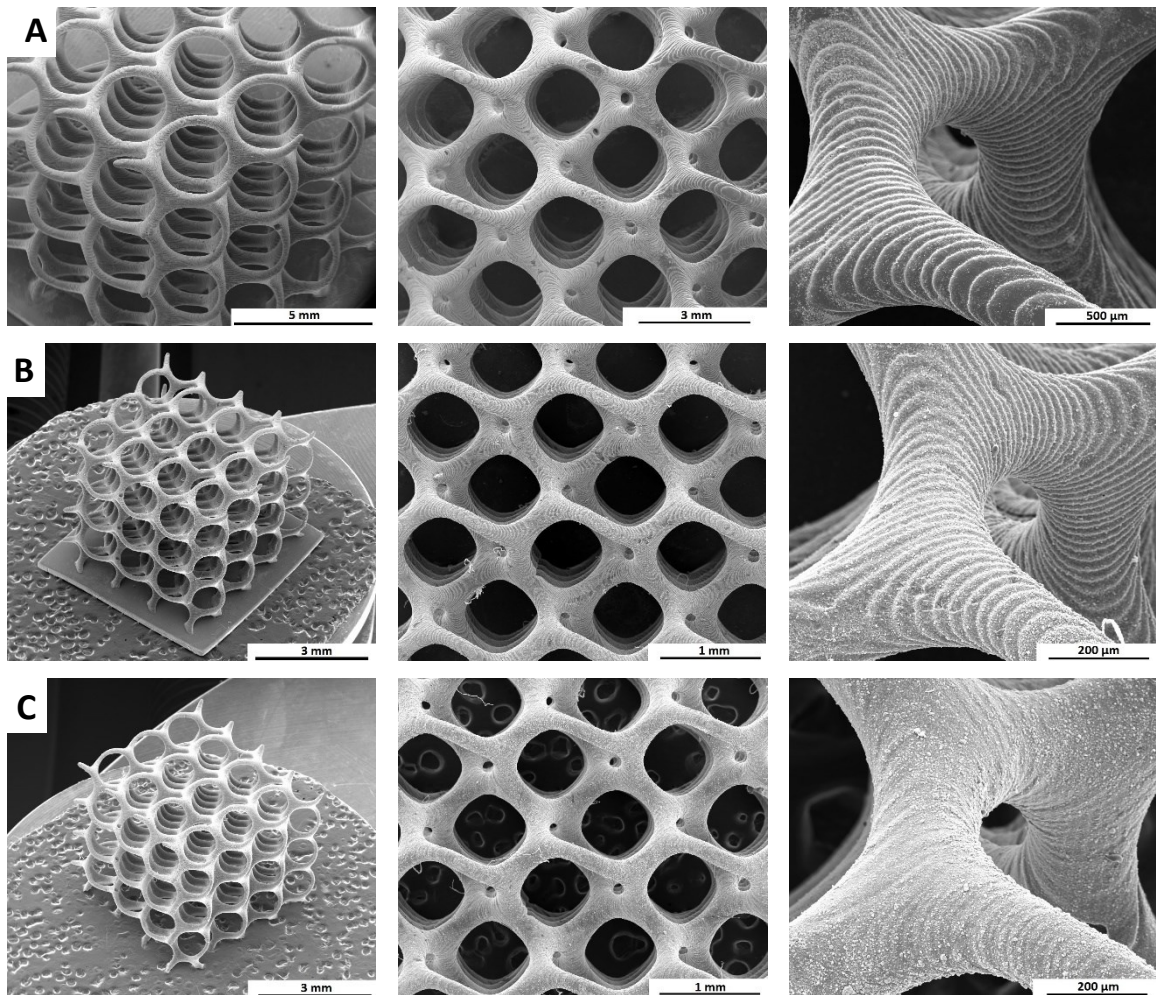
Figure 24 Representation of surface smoothening in z-direction through pyrolysis and slicing thickness; parts are RC 711 printed with 50 µm slicing (A) and pyrolysed with 50 µm (B) and 25 µm (C) slicing.

It should be noted that during pyrolysis, besides the retention of shape and homogenous shrinkage, the polymeric and ceramic structures in Figure 21 – 24 show neither before nor after pyrolysis pores, microcracks or bubbles on the surface of the components, and no delamination between the

printed layers was observed, testifying that optimal printing conditions were achieved. The fracture surface of a pyrolysed sample (see Figure 25) demonstrates also the absence of surface or internal cracks and the lack of (macro) porosity within the SiOC ceramic. The fracture side shows the typical fracture behaviour of brittle material[72] with a point of fracture origin (mirror), mist region and hackle lines and brittle fracture propagation throughout the whole strut. Noticeable is also that the cracks, exemplarily shown in two broken struts in Figure 25, are not propagating along the slicing direction within the x-y plane, but rather through different planes (slices) in the z direction. This shows that the original layers in the printed object are no preferential points of weakness along which a fracture could propagate through the material, and that the adhesion between different layers is optimal.
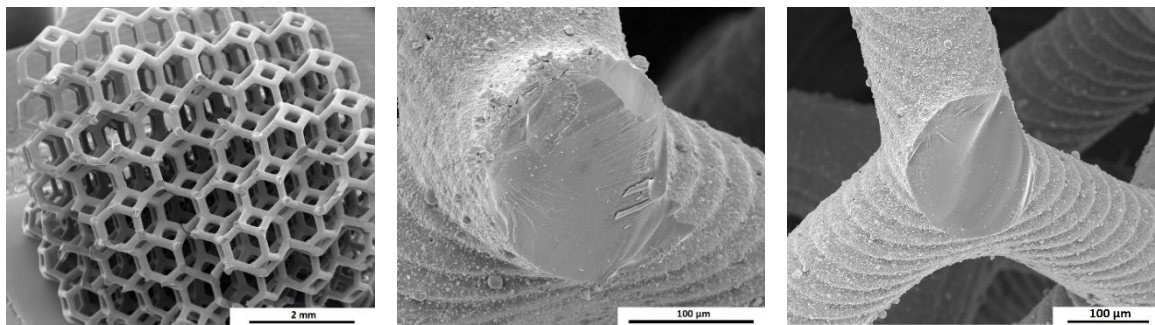
Figure 25 Fracture surfaces of a pyrolysed SiOC printed structure (RC 711/H44 = 5/5).

The elimination of the sacrificial acrylic network and other organic groups of the preceramic polymers during the transformation into a SiOC ceramic led to a dense and homogeneous structure, showing no internal or surface microcracks nor porosity, no delamination nor weakness in case of a fracture along the original slices or segregation of the different polysiloxanes, within a printing blend, on the surface and inside the material.

3.1.7 Conclusion

A novel approach has been developed for the additive manufacturing via DLP of dense, crack and pore free SiOC ceramic structures with a high degree of complexity, by simply mixing high ceramic yield preceramic polymers with a photocurable acrylic siloxane. All precursors are commercially available, and no chemical synthesis was required.

Two silicone resins (Silres 601 and H44) dissolved in toluene were found to lead to homogenous stable solutions upon mixing with a photosensitive acrylic preceramic polymer (RC 711). An optimization of the system, in terms of amount of photoinitiator, photoabsorber and exposure time, enabled to obtain a range of blends that were printable in conditions suitable for the manufacture of parts in a limited amount of time.

The composition of the blends, particularly the ratio between the preceramic polymer and the acrylic polymer, controlled the ceramic yield and related shrinkage occurring upon pyrolysis. Different blends were realized, demonstrating that a RC 711 content as low as 24 wt% was sufficient for producing well defined parts; a maximum ceramic yield of 60.2 wt% was obtained. Thus, the composition of the blends can be exploited as an additional design tool for controlling the dimension of the features obtainable in the printed ceramic parts, independently on the resolution of the printing equipment employed. For example, starting from a design feature size of 100 μm, a dimension down to 30 μm could be produced in the final ceramic component. The SiOC structures after pyrolysis showed a complete retention of shape and homogenous shrinkage. The use of two different preceramic polymers, containing either phenyl (Silres 601) or phenyl-methyl (H44) groups, produced SiOC ceramic structures possessing a different amount of free carbon,[45] and therefore potentially different functional properties e.g. electrical conductivity, mechanical properties or chemical durability can be achieved.[37, 44, 47]

3.2 Analysis of Multi-scale Sinter- and Mechanical Properties of SiOC Trusses

Preceramic polymer resins have previosuly been used via stereolithography to produce highly complex structures which were subsequently transformed into SiOC or SiC ceramics.[8, 20, 40, 56, 57] However, analyses were restricted to characteristics of the printing resin itself, printing parameters, ceramic yield, overall linear shrinkage and compressive strength of the ceramic components. For the first time lattice structures, of much larger scale than previously produced, were printed in different geometrical arrangements and the shrinking behaviour upon pyrolysis as well as the mechanical properties of not only the whole SiOC lattice but of the individuel beam elements themselves were analysed in detail. Furthermore, a new hybrid structure was designed to incorporate two different geometrical configurations with different strut thicknesses within one structure, taking advantage of the possibility to control each individual strut and its positioning via additive manufacturing. The easiest configuration was chosen for the moment, a combination of two different geometrical arrangements in parallel.

In particular, a specific formulation of the developed physical blends was chosen and coupled with the additive manufacturing approach, which allowed for a precise control of the architecture of the porous ceramic components and provided better properties compared to parts with stochastic porosity together with the possibility of a detailed analysis of each uniform element. The ongoing work was carried out in collaboration with Professor Katherine Faber and Neal Brodnik (California Institute of Technology (CalTech, USA) and will be partially published.[73]

3.2.1 Multi-Scale Shrinkage Analysis

The preceramic printing resin used was the physical blend of RC 711/H44 in ratio 5/5 (see Table 4). Four different structures with overall dimensions of 30 x 30 x 60 mm^3, consisting of 7 x 7 x 14 unit cells, were designed; two Kelvin cell structures, with different strut diameters, one octet cell structure and a hybrid structure, combining Kelvin 2 and octet cells in parallel (see Figure S2B). The dimensions of the elements of the respective unit cells of all structures can be seen in Table 8; the significance of the chosen beam diameters will be explained later (chapter 3.2.2).

Table 8 Characterisation of respective unit cells of Kelvin cell and octet structures.

	Kelvin 1	Kelvin 2	Octet
Unit cell size (mm)	4.2	4.2	4.2
Beam length (mm)	1.5	1.5	3.0
Diameter (mm)	0.60	0.70	0.34

The characteristics of the utilised preceramic printing resin were investigated in chapter 3.1. As in all developed physical blends, the added amount of photoinitiator provided a fast curing solution with no overexposure in the printed parts since the z-penetration depth of the light was controlled using an optimised amount of provided photoabsorber. The preceramic blend was stable throughout the whole printing process and the silicone resin chains of the non-photosensitive H44 were entrapped in the continuous polymer network formed by the acrylated, photosensitive RC 711 during light exposure. The ceramic yield of 40.1 wt% is made up of the ceramic yields of pure RC 711, 7.4 wt%, and pure H44, 76.5 wt%, and is consistent with the theoretical value for this blend mixture (see Figure 18), confirming a homogeneous distribution not only in the liquid but also in the solid structure with no repulsion of the non-photosensitive silicone chains during printing.

The large Kelvin cell, exemplarily shown for the Kelvin 2 configuration, and octet structures of 30 x 30 x 60 mm^3, were printed with this preceramic resin and are shown in Figure 26. As already previously investigated, no sign of delamination or crack formation was visible in the printed state of all of the fabricated preceramic structures, including the newly printed Kelvin and octet ones. Likewise, crack-free ceramic SiOC structures were generated after pyrolysis which maintained their overall shape. An accurate copy of the stl file (shown in Table S2B) was produced with complete shape retention since the shrinkage in x, y and z direction after pyrolysis of every structure proved to be the same (see Table 9). A detailed analysis of the average linear shrinkage of the respective structures as well as the individual unit cell elements are shown in Table 10.
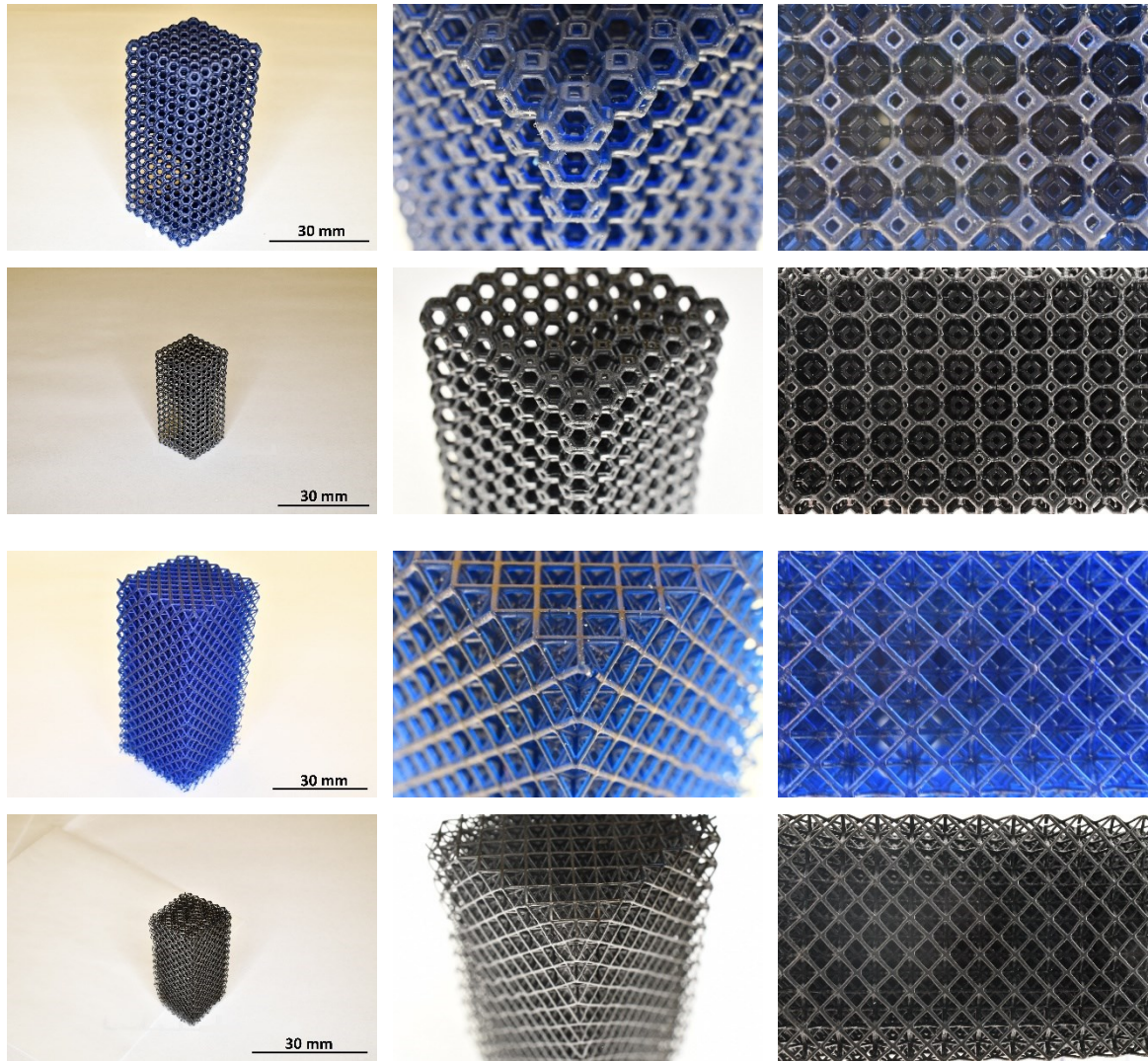
Figure 26 Kelvin cell and octet structure before and after pyrolysis.

Table 9 Linear shrinkage in x, y and z-direction of Kelvin cell and octet structures.

	Kelvin 1	Kelvin 2	Octet
x - direction (%)	45.4 ± 1.6	43.7 ± 0.7	49.5 ± 1.4
y - direction (%)	44.8 ± 1.7	43.3 ± 0.8	48.8 ± 1.4
z - direction (%)	45.2 ± 0.8	43.4 ± 0.7	49.3 ± 1.3

Table 10 Analysis of linear shrinkage of Kelvin 1,2 and octet structure and respective unit elements.

	Kelvin 1	Kelvin 2	Octet
Overall structure (%)	45.1 ± 1.4	43.5 ± 0.8	49.2 ± 1.4
Beam diameter (%)	36.9 ± 1.7	37.5 ± 1.0	44.6 ± 1.3
Beam length (%)	44.9 ± 1.6	42.0 ± 0.8	67.0 ± 1.0
Beam volume (%)	77.9 ± 2.4	77.3 ± 0.7	90.0 ± 0.8

The linear shrinkages of the overall structures, their unit cell elements, beam diameter, length and volume, was investigated for the two Kelvin cell structures, with different beam thicknesses of 0.6 and 0.7 mm, as well as for the octet structure (Table 10). It is notable that even though the linear shrinkages are isotropic for each structure and at all scales, the shrinkages are not the same, neither within one structure nor between different structural geometries fabricated with the same material.

While the shrinkage of the beam diameter of both Kelvin cells is around 37 % the beam length is shrinking a notable 5-8 % more, close to the overall shrinkage of the whole structure. The volume of the beams is decreasing by roughly 77 % each. The shrinkage analysis of the octet structure confirms the different shrinkages and their trend, although in general much larger shrinkage values are found in the octet compared to the Kelvin structure in all shrinkage categories. Here, the individual beam volume is shrinking by a remarkable 90 %. The beam length in the octet configuration shrinks 22 % more than the beam diameter and the whole structure reflects this with a 49 % size reduction, a significant increase in overall shrinkage compared to the Kelvin cell structures.

The aspect ratio between beam diameter and length for the SiOC ceramic structures are compared to the initial aspect ratios of their respective designs. In all three structures the aspect ratio of the pyrolysed SiOC struts is decreasing compared to the nominal value set by the stl-design. While this reduction in aspect ratio is comparatively small for the Kelvin structures, with values of 14.7 ± 9.3 % for Kelvin 1 and 7.7 ± 2.5 % for Kelvin 2 design, it is highly pronounced in the octet structure, decreasing by 67.0 ± 8.6 %.

It is clear that the aspect ratio of the unit elements after pyrolysis is different from the original design. The remarkable aspect of this is, that in spite of the different shrinkages in beam thicknesses and length, which results in the notable change in aspect ratio compared to initial values, the structure as a whole has a homogenous shrinkage in all directions. The shape is maintained over the complete structure despite its large size.

However, this is not the case in the hybrid structure, where the non-anticipated difference in linear shrinkage of the same material in Kelvin and octet part of the hybrid structure resulted in a bent configuration, shown Figure 27. The slight curving in printed state towards the higher shrinking octet part, which comes from the drying of the structure when the solvent toluene is removed (see Figure 19B), gets more pronounced after pyrolysis when more than 6 % difference in shrinkage occurs. Despite its bent geometry, also the hybrid structures, like the Kelvin and octet structures, show no cracks within the structure, nor any sign of delamination or strut separation, even at the interface between the two geometrically different parts. The link of the material with itself proves

to be strong enough to account for the internal stresses, which arise due to the different shrinking properties of the two sides within the same structure.
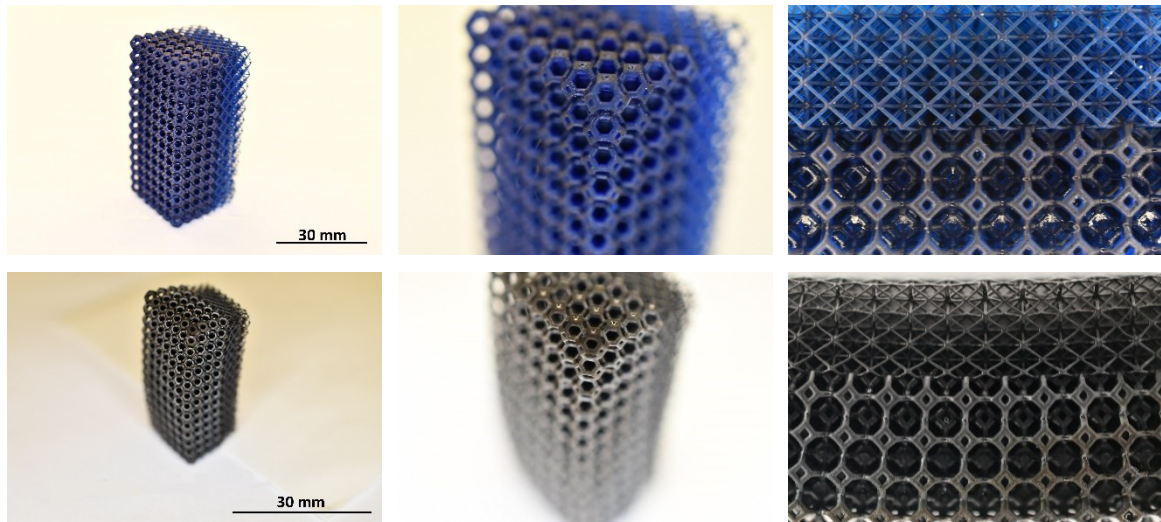
Figure 27 Hybrid structure, constituent of halve Kelvin 2 and octet structure, before and after pyrolysis.

The linear shrinkage values reported in Table 10 show that the shrinkage behaviour in a shaped specimen is not as straight forward as commonly assumed. Typically linear shrinkage values in x, y and z-direction, or overall volume shrinkage is reported to analyse the size change ceramics undergo during sintering, concentrating on the isotropic or directional contraction of the material without considering the structural configuration of said material. Following the common trend, the linear shrinkage of the used preceramic polymer blend was already previously investigated on model cube structres, exhibiting a homogenous shrinkage of 51.5 ± 3.3 %, and compared to other material blends, printed in the same cubic structure, focusing as well on different material shrinkages (see chapter 3.1.4.2). The shrinkage analysis in this study was far more detailed and points out that while a structure shows a uniform shrinkage in all directions, different structures as well as their constituent elements within the structure can exhibit different shrinking values, which change their geometry non-uniformly. Especially in technical applications, where a precise size and shape of ceramic parts is particulary important, the investigation of not only the overall shrinkage behaviour but also of the essential elements becomes important. Compared to commonly used manufacturing techniques to fabricate porous ceramics, like via replica, self-foaming or pore former technique, additive manufacturing allows precise control over strut size and beam length of each unit cell in lattice structures, which allowes to investigate the shrinkage of individuel ceramic beams during pyrolysis.

The experiments revealed that the shrinkages in the two Kelvin cell structures, depite having different strut thicknesses, are similar for the overall structure as well as the unit cell elements. In contrast, the octet structure shrinks around 6 % more than the Kelvin ones and shows also a

remarkable difference in the strut shrinkage with an additional decrease of 13 % in strut volume, more than 22 % in beam length and 7 % in thickness. The alike shrinking characteristics of the Kelvin structures and the significant difference to the octet structure points out that the shrinkage behaviour is dependent on the geometric arrangements of the struts rather than on the thickness of them. It seams that the architecture of a scaffold puts constraints on the materials ability to freely move during the transformation from preceramic polymer into ceramic material and the involving size change due to polymer burn out and densification. If the nodes are considered as rigid points, where the struts intersect and the contraction of struts is non-uniform, then the difference in geometrical arrangement of the nodes between the Kelvin and octet structures, will influence the free shrinkage movement of the individuel cells, resulting in a different overall size change between the Kelvin and octet structures.

The aspect ratio of the individuel beams changes in comparison to the original structural design for both geometrical different structures. While this change is not as pronounced in the Kelvin structures it is highly significant in the octet one, where the shrinkage in beam diameter versus beam length is off by more than 20 %. The original aspect ratio of the Kelvin cells (0.40 and 0.47) is much higher than the one in the octet structure with 0.11 (see beam values in Table 8). The shrinkage during pyrolysis seams to affect the structure with an already high aspect difference more than the one where the discrepancy between beam thickness and length is rather small. The long and slender octet beams are much more susceptible to a different shrinkage. It seams that during pyrolysis the material not only uniformly contracts due to the burn out of polymeric groups, but rather, that a local material transport takes place. The material tries not only to densify but also to minimse the surface energy by tightening the materials in the struts. The higher contraction in length than in thickness results in a decrease in aspect ratio, which decreases the strut surface and therefore limits its surface energy.

Despite the difference in cell element shrinkage and its invovling change in aspect ratio, the overall shrinkage of both Kelvin and octet structures are uniform in every direction due to the globally isotropic truss structure. This is not the case in the hybrid structure where the Kelvin and octet parts are arranged in parallel and lead to a non-homogeneous shrinking structure due to the difference in Kelvin and octet shrinkage. This demonstrates that, while a structure consisting of two different geometrical arrangements can be produced via additive manufacturing and that the interface between the two parts represents no weak point even during fracture (see later Figure 29), special attention must be placed on the shrinkage analysis of the consistuent parts and elements, which exceeds the normal linear shrinkage analysis used up to now. It was demonstrated that the shrinkage behaviour of a constrained net-shape part produced via stereolithography is nontrivial

and has to be carefully investigated and considered when using additive manufacturing to produce large parts for technical applications.

3.2.2 Mechanical Characterisation of Overall Structure and Single Struts

3.2.2.1 Analytical Analysis

Lattice structures with different geometrical arrangements are mechanical behaving in a different way. In order to compare them within one study, the differences in beam geometry and arrangement must be properly analysed. The analytical investigation of the truss systems allows to relate the failure strength and elastic moduli for different lattice structures with varying porosities and geometrical truss arrangements. While in this study the calculation of uniaxial compression test is straightforward via the engineering stress and strains using the outer dimension of the overall truss structure, the relation between the effective elastic moduli of the different trusses can be analytical analysed and expressed in terms of beam size and their respective structural arrangement. This is especially important in the hybrid lattice structure and its constituent lattice parts, the Kelvin and octet part, which are failing in two different dominant failing mechanism via bending or stretching. Note, that both in this analysis and the equations used by Zhu et al.[74] and Deshpande et al.[75] to calculate the E-modulus of the Kelvin cell and octet structures, the beams in each cell within one structure are all of equal length, diameter and moment of inertia. Due to the differences in geometrical arrangement of their respective strut system, the beams in the octet cell are twice as long as those in the Kelvin cell, for a defined unit cell size of same size (see Table 8).

Kelvin cell structures exhibit bending-dominant failure mechanism. When they are loaded in one of their primary directions, their beams at 45° angle in respect to the loading direction are deforming by bending and then subsequently fracture. Zhu et al. developed calculations to express the elastic modulus of open cell foam structures with tetrakaidecahedral (truncated octahedral) cells, Kelvin cell structures, which are failing in a bending-dominant way.[74] Since the Kelvin cells are symmetrical in all (100) family directions, the moduli in all those primary directions is the same, and can be expressed as

$$E_{001} = \frac{6\sqrt{2}E_S I}{L^4\left(1+12\frac{I}{AL^2}\right)}$$

(3)

While E_S is the elastic modulus of the bulk solid material, I the moment of inertia of the beams along the bending axis, L the length and A the cross-sectional area of a single beam.

On the other hand, octet cell structures are deforming in a stretching dominant way, when loaded equally along their primary (001) axis. The beams perpendicular to the loading direction are carrying the tension and will fail first, which leads to a fracture path propagating at 45° angle to the load axis. Based on the relative density $\bar{\rho}$ of the octet lattice, depending on the radius R and length L of

a single beam, Deshpande et al.[75] are specifying the elastic modulus of octet trusses, which are equally dependent on E_S, as

$$E_{001} = \frac{\bar{\rho}}{5} E_s \tag{4}$$

$$\bar{\rho} = 6\sqrt{2}\pi \left(\frac{R}{L}\right)^2 \tag{5}$$

For the designed hybrid structure several conditions were placed on its configurations to properly characterise the mechanical behaviour. First, the cell sizes of both the Kelvin and octet lattice had to be uniform in order to exchange one cell with another without breaking up the periodical arrangement (see same cell size in Table 8). And second, the E-Moduli of both respective lattice parts were set equal, so that during the mechanical compression tests the stiffness and therefore the force impacting both sides of the hybrid structure would be the same. Starting from the equations by Zhu and Deshpande and the fact that both structures are printed from the same material, therefore having the same elastic modulus of the bulk solid, an equation for the design of the hybrid structure was developed.

$$\frac{4}{5}\left(\frac{L_k^4}{R_k^4} + 3\frac{L_k^2}{R_k^2}\right) = \left(\frac{L_o^2}{R_o^2}\right) \tag{6}$$

This equation sets the length and the radius of the cylindrical beams of the Kelvin cell, L_K and R_K, and the octet cell, L_O and R_O, in relation. Since the Kelvin and octet cells are periodic regular structures and have the same unit cell size, the beams of the octet lattice are exactly twice the length of those of the Kelvin cell structure, $2L_k = L_o$. Substituting this relation in equation 6, simplifies the design condition of the hybrid structure to following form.

$$\left(\frac{L_k^2}{R_k^2} + 3\right) = 5\left(\frac{R_k^2}{R_o^2}\right) \tag{7}$$

By defining a particular unit cell size, equal for both structures, and the beam radius for one of the structures, Kelvin or octet, the beam radius of the other structure is fully defined by equation 7, when designing a hybrid structure of uniform stiffness. Taking equation 7 in consideration the beam dimensions of Kelvin 2 and octet cell structures in Table 8 are chosen.

Finally, the flexural strength of the individual beam elements was determined through a test setup inspired by Brezny et al.[51] and illustrated in Figure 9B. The strength of the truss beams, which are the cylindrical rods in three-point flexure as described in ASTM C 1684,[76] can be calculated as

$$\sigma = \frac{8PL}{\pi D^3} \tag{8}$$

The wire loop underneath the beam in Figure 9B is exerting the load P on the cylindrical strut of length L and diameter D. While this test setup allows to test the flexural strength of the individual struts in the lattice structures, the large compliance of the testing fixture prevents an accurate determination of the elastic modulus of the single beams.

3.2.2.2 Compressive Frakture Behaviour of Truss Structures

Preliminary compression tests were performed on printed lattice structures to determine the best testing conditions. The samples were embedded in epoxy resin VariDur 3003 and samplekwick (Buehler Inc.), or sandwiched between cork, aluminium-foil, rubber and neoprene layers as well as cut to achieve planar and smooth surface areas and applied with an oil layer to minimise friction. Experiments with test samples confirmed that the highest strength was reached on cut samples, where fracture initiation in this testing condition didn`t always originate at the contact point to the metal compression plate, but within a flaw inside the structure. Therefore, the actual test lattices were cut to get planar contact areas (see Figure S3). This had the additional advantage that some of the eccentricity of the hybrid structures at the outer ends due to its bent configuration was removed, while the middle, more homogenous part, was preserved. Unfortunately, complete avoidance of load peaks at the sample surface was not guaranteed and fracture originating from the contact point to the metal compression plate was still observed in a few Kelvin structures, showing therefore slightly smaller strength values. However, it was impossible to determine the origination of the fracture point in the octet samples, as the fracture propagated at an 45° angle towards the compression direction (see Figure 29), therefore intersecting at one side always with the interface due to the sample height. If the crack started at the contact point to the compression plate or in the middle of the samples was impossible to determine, as the fracture happened instantaneous, within or even in-between a frame of the taken fracture video and was also often not at the observed sample side. Therefore, the strength data of all samples, disregarding the fracture origination point, was taken into consideration, as it was intended to compare the fracture strength between the different samples.

Table 11 lists the experimentally identified porosity, strength and E-modulus of all configurations. The thicker beams, while maintaining the cell size, in the Kelvin 2 configuration in contrast to the Kelvin 1 design decreased the porosity by roughly 4 % but lead to an increase in strength by 2.3 MPa. The octet structure exhibits a large porosity of 91 % and shows the smallest strength value of 3.8 %. Since the hybrid structure consists of halve Kelvin 2 and halve octet design, its porosity,

strength and E-modulus values is a combination of both, but tends to be closer to the one from the Kelvin 2 structure.

Table 11 Mechanical characterisation of lattice structures.

	Kelvin 1	Kelvin 2	Octet	Hybrid
Porosity (%)	85.3 ± 0.5	81.5 ± 1.2	91.1 ± 0.4	84.3 ± 0.1
Strength (MPa)	7.7 ± 1.1	10.0 ± 1.8	3.8 ± 0.7	9.4 ± 0.4
E-modulus (GPa)	2.0 ± 0.7	3.1 ± 0.6	0.9 ± 0.1	2.7 ± 0.1

A specimen of each structural configuration has been exemplarily chosen to display in Figure 28 the fracture behaviour of the manufactured SiOC ceramic lattice structures. The stress-strain curves show the typical linear elastic behaviour followed by brittle fracture of a ceramic material. Besides having several small local peak loads, especially in the octet samples, the structures showed catastrophic failure after fracture peak load was reached.
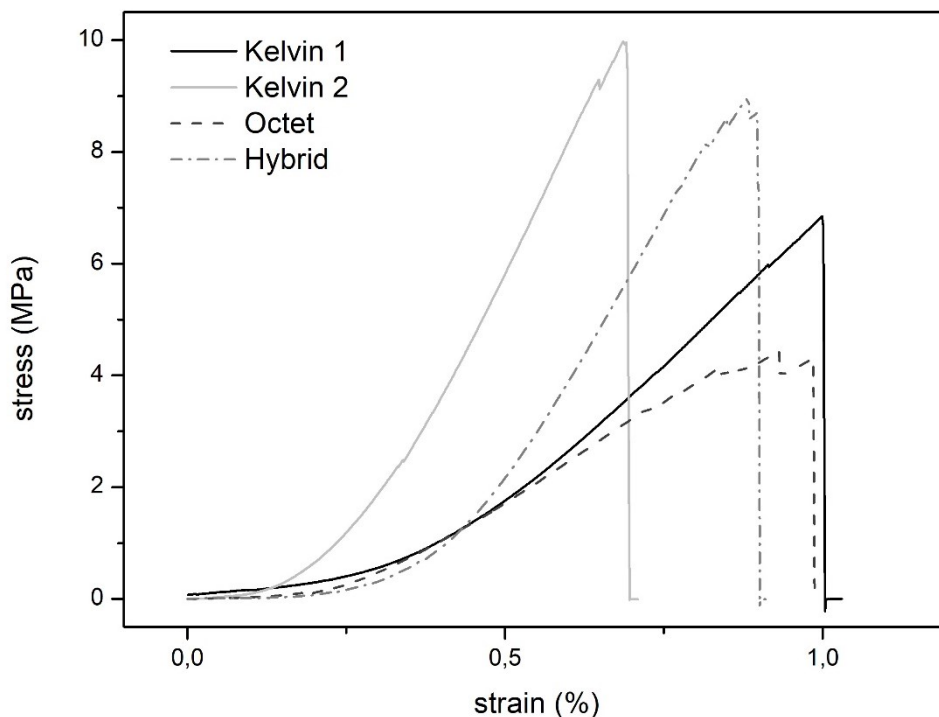
Figure 28 Selected stress-strain curves for all tested configurations, exemplarily chosen to display the fracture behaviour.

The fracture behaviour of the Kelvin, octet, and hybrid structure was analysed and the fracture pattern characterised by means of SEM (see Figure 29). In the Kelvin structures, the fracture path proceeds horizontal to load direction. The beams at 45° angle towards the printed z-direction,

which equals loading direction, are breaking, showing the expected bending-dominant fracture behaviour. This is different from the octet structure, where the fracture path is angled at 45° to loading direction, while much of the fracture is in the beams parallel to it, demonstrating the stretching-dominant failure of octet structures. The hybrid structure combines the different fracture characteristics, fracture path and broken beam orientation, which occur in their respective parts of the structure. The interface proved to be well connected, even during fracture. Instead of representing a weak point, the fracture path progresses from one side of the structure into the other side with changing fracture behaviour, generally ignoring the interface. Note, that although fracture videos were taken throughout the whole compression experiments, the fracture itself happens catastrophically (see Figure 28) and instantaneous, making it impossible to observe from which side, Kelvin or octet, the fracture is originating in the hybrid structures.

Fractography of all structures show a dense and, away from the fracture, crack-free SiOC material with no internal porosity and a density of 2.1 g/cm^3. The individual layers of which the structures are made of during the stepwise printing process show no influence in the fracture behaviour. This shows, that the transition between the layers represent no crack-initiation points nor weak planes the crack might follow.
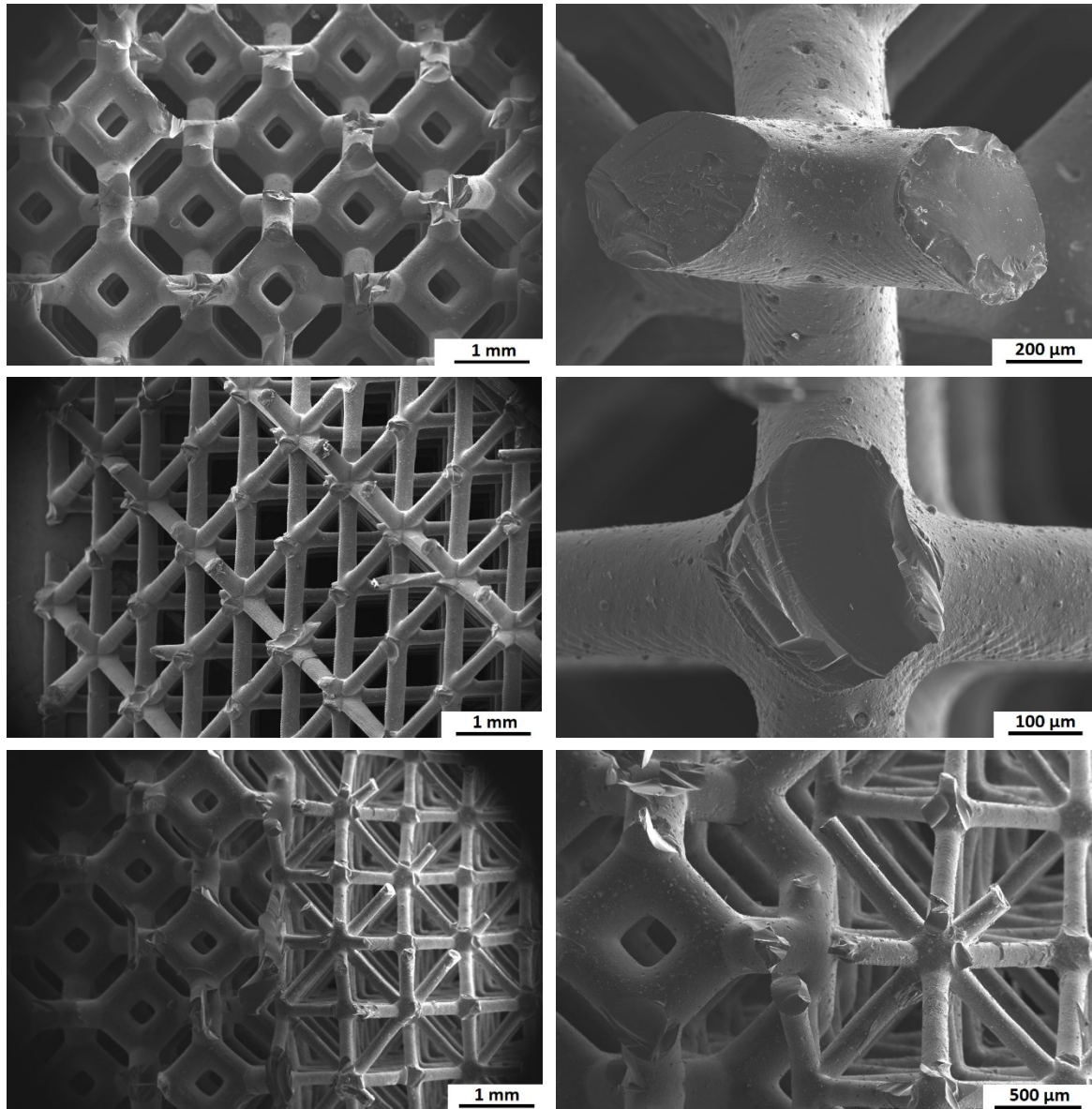
Figure 29 Fracture pattern of Kelvin cell, octet, and hybrid structure.

Although the octet structure shows by far the lowest compressive strength of the produced lattice structures, this is mainly attributed to the fact that it has by far the largest porosity (see Table 11), which negativly affects the mechanical properties of porous structures.[77] A comparison of the strength over relative density for all lattice structures in Figure 30 shows that although the compressive strength of the octet structure is by far the lowest, it`s not unreasonable low considering the respective relative density. In fact it seams that all fabricated structures, the two Kelvin cells, the octet and the hybrid structures, have a realitvely linear relation between strength and relative density.
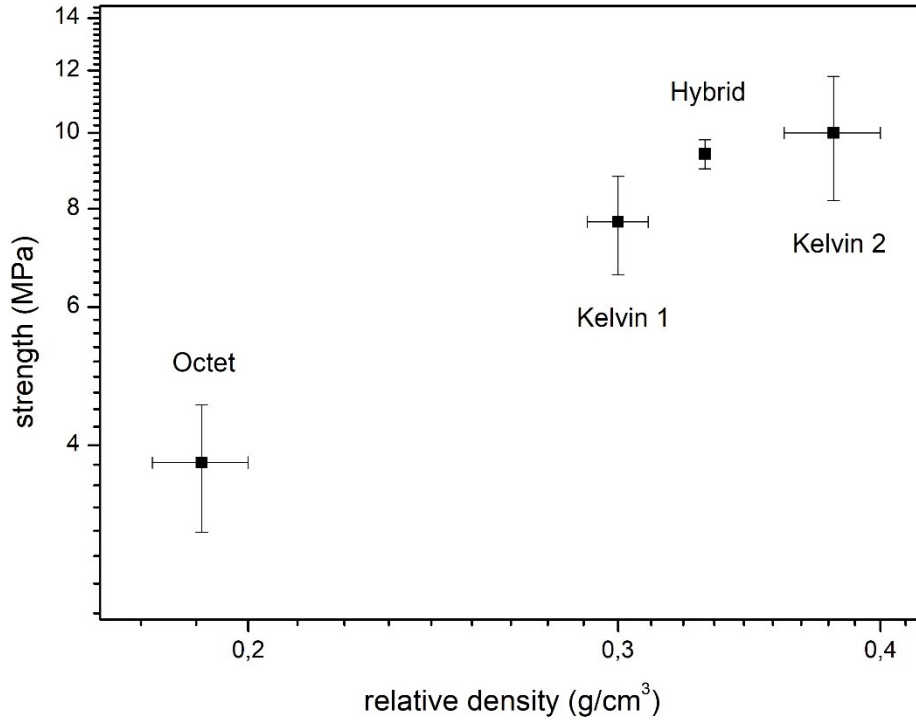
Figure 30 Compressive strength over relative density for all printed SiOC lattice structures; logarithmic scaling.

It should be noted, that this is not an expected behaviour due to the different beam deformation modes of the respective structures during fracture. In fact, the critical failure strength σ^*_{cr} of a open-cell foam is dependent on the failure strength of the solid material σ_s, was well as on the relative density of the solid ρ_s and porous structure ρ^* and can be desdribed as

$$\frac{\sigma^*_{cr}}{\sigma_s} \sim \left(\frac{\rho^*}{\rho_s}\right)^n \tag{9}$$

Where the exponent n is dependent on the modus of fracture and is equal to 3/2 for bending-dominant and equal to 1 for stretching-dominant fracture behaviour.[78] This would mean, that even so the relative densities of Kelvin and octet structures are different from one another, the failure strength of the octet structure, representing a streching-dominand lattice, is expected to be relatively speaking greater than the failure strength of the Kelvin cell structures, representing bending-dominand lattice structures, and not to scale linearly (see Figure 30).

Compared to other truss structures in literature, it should be noted that the strength values of the lattices reported in this study are higher than those of other cellular materials[78] and those of SiOC foams, which are produced via direct foaming and are of comparable density.[79] While this is true, the compressive strength is lower than those reported in Eckel et al.[40] for SiOC printed microlattices and honeycombs. It is suspected that this is due to a drastic difference in specimen

dimensions, since the samples tested in Eckel et al. were sheets with single-cell thicknesses, while the lattice structures here show dimensions of 7 x 7 x 14 cells.

3.2.2.3   Evaluation of Individual Beam Strength

The strength of the individual struts in the structures were tested in flexure, in the configuration illustrated in Figure 9B. Two different kind of fracture behaviour has been observed during the adapted three-point bending experiment. While images extracted from the video files taken in situ during the experiment can be seen in supplementary information Figure S4, Figure 31B,C displays the fracture types in detail. While the images in Figure 31A show the Kelvin and octet struts before breaking, the images in Figure 30B display the fracture of the beams while the nodes remain unaffected and Figure 31C shows strut failure, where the node was affected and partially taken out with the struts. Both behaviours were observed in the tested samples but no significant difference in strength values between the two fracture modes was observed (see supplementary information Table S10).

The struts and cell nodes adjacent to the loaded beams remain unaffected during the experiment, providing a rigid support of the tested beams. The strength of the individual Kelvin struts is very similar with 0.47 ± 0.16 GPa for the Kelvin 1 and 0.54 ± 0.15 GPa for the Kelvin 2 structure. The octet shows a four times larger strength with a value of 1.93 ± 0.27 GPa.
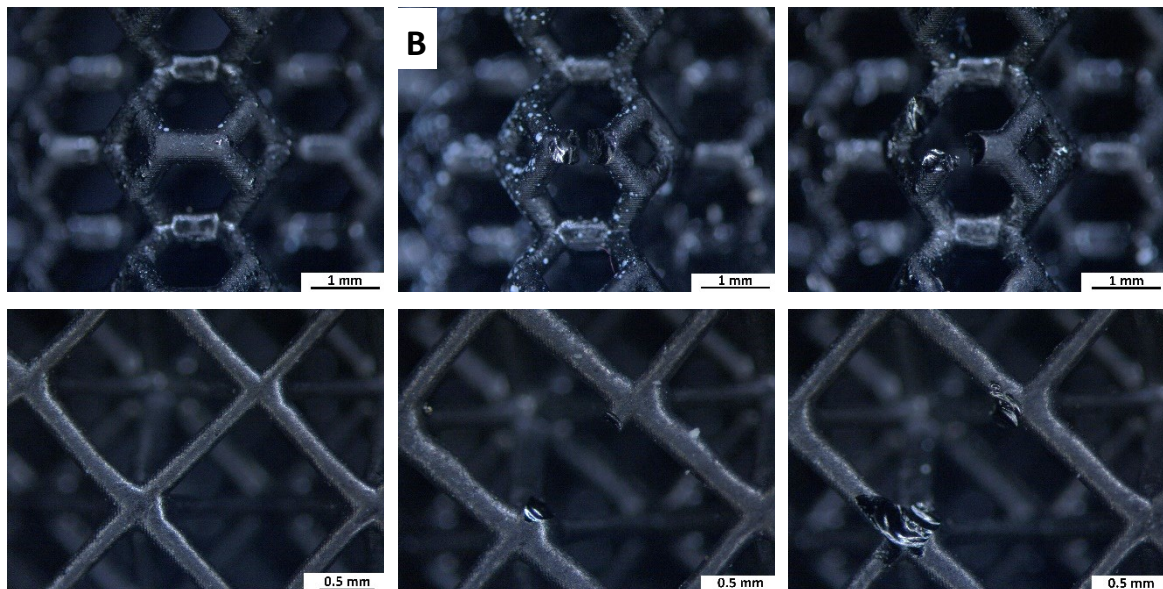
Figure 31 Fracture analysis of Kelvin and octet strut failure; left to right: unbroken strut (A), fracture with node intact (B), fracture with node affected (C).

The strength of the unit elements of the truss structures, Kelvin and Octet, were analysed using similar methods as Brezny et al.[51] It should be noted that in contrast to Brezny, the struts in this

study were not from a replica foam but from a structure fabricated via additive manufacturing. This means that all the beams are of the same size, positioned in the same orientation (horizontal to loading direction), exhibit no change in strut thickness over the whole length of the beam and have no internal pores (as is the case in ceramic replica foams). Sincce these predetermined errors from Brezny are no longer present in this study, the measured failure strength of the ceramic struts is far more reliable.

When comparing the flexural strength of the individual struts to to their respective truss structures, a different behaviour can be seen. While the strut strength of the two Kelvin structures is remarkably similar, the Kelvin lattices are exhibiting different structural strength. Additionally while the octet struts are about four times as strong as the Kelvin ones, the octet lattice structure shows due to it`s high porosity the lowest strength. This significant difference in strut strengths is likely due to the size effect. The slender octet struts are thin enough to have a greatly reduced possible defect size, which therefore impoves the strength of the beams.

While the size effect can explain the greater strength of the slender octet struts, it doesn´t explain the lower specific strength of the octet structure (see Figure 30) despite having struts showing a remarkable greater strength, which should logically make a structure stronger. This is not the case here and possible explanation factors are some degree of load eccentricity during compressive loading and a deviation in strut failure from bending to tensile mode. Even so all possible steps were taken to minimise load eccentricity during testing of the overall Kelvin and octet structures, it can still occur due to some amount of local shrinkage variation, which, although small, is inevitable during pyrolysis and may affect the strength, especially in structures sensitive to small variations, like the octet structure since it`s composed of very slender beams. This may lead to some degree of shearing in the lattice structure, which could lead to a reduction of strength not present in the testing of the individual struts but in the overall structure. This also would affect the octet structure more than the Kelvin ones, since deformation by shearing is very similar to deforamtion by bending but completely different from deformation by stretching. The octet structure is, due to its more slender beams, more susceptible to possible load eccentricity and additional the possible shearing is more pronounced in stretching than in bending-dominant lattice structure. This could explain the comparatively rather low strength of the octet structure despite its greater strut strength. Another factor which may have contributed to the remarkable difference in the strength in the struts between octet and Kelvin is a deviation from the expected flexural bending failure. As described in chapter 2.3 the struts are loaded over a looped wire, which pulls on the struts connected to rigid nodes. Equal to Brezny[51] a three-point bending test was assumed to be as close to the fracture test as possible and therefore the flexural strength of the struts have been caluclated according to

equation 8.[76] Equally to the fracture of the overall structure also the failure of the struts was dramatic and instantaneous. Although observed in situ via video camera (see Figure S4) it was impossible to observe the actual breaking mechanism. Considering the fracture images in Figure 31 it could be that in addition to bending of the struts some degree of tensile load was exhibited, which could have caused a pull-out of the strut rather than failure via bending. This could lead to a different fracture mode and therefore another calculation of the fracture strength of the individual struts, which might change the relation between the strength and beam length and thicknesses and thus in turn change the difference in strength of octet versus Kelvin struts. An analysis of the exact failure mechanism would however require additional testing and was beyond the scope of this study.

3.2.2.4   Investigation of E-Moduli

The experimentally measured elastic moduli were compared to their values gained by analytical methods to compare if the theoretical calculations can be applied and the expected stiffness relations are met. Since all structures are fabricated via Digital Light Processing with the same preceramic polymer blend and transformed in the same pyrolysis process, the elastic modulus of the solid SiOC ceramic material is the same. Given this fact, the expected stiffness ratio between two different structures can be described as

$$\text{Stiffness Ratio} = \frac{E_{001}^{\text{Design 2}}}{E_{001}^{\text{Design 1}}} \tag{10}$$

While the actual stiffness ratio can be gained from the experimentally measured elastic moduli of the respective structures, the equations $3 - 5$ allow an analytical expression of the expected stiffness ratio from the measured pyrolysed strut dimensions.

The elastic moduli of Kelvin cell structures can be described according to Zhu et al.[74] with equation 3. According to the analytical stiffness ratio between the two Kelvin designs, it is expected that the Kelvin 2 structure is about twice as stiff as the Kelvin 1 structure. However, the experimental values show a ratio of only about 1.5 instead. This deviation from the analytical value is likely due to the lack of slenderness of the Kelvin cell struts. Since the strut thicknesses were designed in such a way to match the expected higher stiffness in the octet structure, for the use in the hybrid structure according to equation 7, the aspect ratio was necessarily per design already relatively low. This together with the anisotropic beam shrinkage, which further decreased the aspect ratio of the Kelvin beams, resulted in an aspect ratio in the order of 4:1, while the analytical calculation of the stiffnesses assumes much more slender beams in their structures, meaning an aspect ratio of

typically 10:1 or more. This lack in slenderness can lead to some deformation not only in the beams themselves but also in the nodes of the structures, which would cause a change in the stiffness and the stiffness ratio of the structures.

While the analytical stiffness ratio of the two Kelvin designs is not that different from the measured ones and the deviation can be explained by the lack of slenderness in the Kelvin beams, the behaviour, particularly the elastic modulus, of the octet structure is far from expected. The Kelvin 2 and octet structures were designed to be printed with the exactly same elastic modulus, based on equation 7. Due to the discrepancy in shrinkage (see Table 10) the measured beam dimensions would not only leave the two structures with a different elastic moduli, but would also assume that the octet structure shows a higher stiffness than either of the Kelvin structures. This is obviously not the case since Kelvin 2 is around 3 times as stiff as the octet (see Table 11), which together with the different behaviour in strength of the octet struts and overall octet structure, indicates an unusual behaviour in the octet lattice strucutres. Some assumptions to this behaviour, like e.g. load eccentricity during fracture testing, can be drawn, as previously stated, but more thorough investigation of this unusual behaviour is beyond the scope of this study.

3.2.2.5 The hybrid structure

As already previously stated, the stiffness of the Kelvin 2 and octet structure does not match one another (see Table 11), although designed that way according to equation 7. This means that also in the hybrid structure the two respective parts are exhibiting different stiffness values. Despite this difference in elastic moduli, originating from the different shrinkages of the structures and their individual elements (Table 10), which obviously changes the elastic moduli of the design to the actual SiOC ceramic, together with some degree of load eccentricity leaving errors in the measured elastic moduli, a relative anaylsis of the expected and measured stiffness can still be performed. Since the Kelvin and octet part are arranged in parallel, the hybrid structure shows an isostrain configuration. The rule of mixture together with the experimental modulus measurements of the respective Kelvin 2 and octet structures allows to calculate the modulus of the hybrid structure as

$$E_{hybrid} = v_{Kelvin}E_{Kelvin} + v_{octet}E_{octet} \qquad (11)$$

with 4/7 being the volume fraction of the Kelvin cells and 3/7 being the one of the octet cells in the hybrid structure as designed. According to equation 11 the hybrid structure should show an elastic modulus of about 2.2 GPa, which is slightly lower than the experimentally determined 2.7 GPa. This slight deviation towards the elastic modulus of the Kelvin design (see Table 11) can be explained due to the non-uniform shrinkage in the hybrid structure. Since the octet part is shrinking with a

greater value than the Kelvin one, the volume fraction of the Kelvin part exceeds the 4/7 predetermined in the hybrid design. Additionally, the bent configuration of the hybrid strucutre results in the Kelvin part having to bear a larger percentage of the load. This non-uniform shrinkage of the same material printed in two different configurations explains why the elastic modulus of the hybrid structure is closer to the value of the Kelvin part of its structure than the rule of mixture predicts.

The strength of the hybrid structure was measured taken the compressive load and the overall area of the structure subjected to the load into account. A value of 9.4 MPa was measured as the compressive strength of the hybrid structure (see Table 11). However, since the stiffness of the two respective parts of the hybrid structure is different from one another, the two parts are subjected to different percentages of the overall load, since the force is predominantly loaded on parts exhibiting higher stiffnesses. This means that the Kelvin part, having the higher elastic modulus, is also bearing a higher percentage of the load and vice versa. In order to investigate the actual stress sustained by the two parts of the hybrid structure, the stresses faced by the Kelvin and octet part, σ_K or σ_O, can be expressed via the elastic moduli of their respective structures, E_K or E_O, as well as the stress and elastic modulus of the overall hybrid strucutre, σ_H and E_H, assuming the isostrain loading condition due to the parallel design of the hybrid struture.

$$\sigma_K = E_K * \frac{\sigma_H}{E_H} \tag{12}$$

$$\sigma_O = E_O * \frac{\sigma_H}{E_H} \tag{13}$$

According to equation 12 and 13 the actual load bearing on the Kelvin part of the hybrid structure is 10.8 MPa, while it is 3.1 MPa for the octet part. Both values are remarkable close to the values of their respective structures within their standard deviations (see Table 11), which is logical since it means, that the hybrid structure is failing when one of its parts exceeds the critical failure load of its respective designed structures. Applying the rule of mixture to the failure stress, likewise to the elastic modulus calculation a smaller value of 7.5 MPa than the actual 9.4 MPa of the overall hybrid structure was calculated. This again is due to the non-uniform shrinkage of the hybrid structure, in which the Kelvin part occupies a larger volume percentage than the predetermined 4/7. This means that just as in the elastic modulus calculation the measured strength of the hybrid structure is closer to the value of its Kelvin than its octet part exceeding the analytical prediction.

3.2.3 Conclusion

Additive manufacturing techniques, especially stereolithography, allow for a precise control over the architecture of produced parts. A simple alteration of a computer model (CAD-file) can be performed to obtain the desired geometric arrangement of struts and alter their dimensions. This precise control over the architecture allows for a detailed investigation of the properties of lattice structures at all scales. Large dimensional lattices in different geometrical arrangements and beam thicknesses were manufactured with the exactly same preceramic polymer blend material.

It was demonstrated that the shrinkage behaviour is not a straight-forward approach, depending only on the utilised material. Instead, even so the overall shape of the structure was completely maintained during printing, the shrinkage of the unit cell elements was different from one another as well as the shrinkage of the overall structure, depending on their geometrical strut arrangement. This is an important point, which should be taken carefully in consideration when designing structures for technological applications in order to avoid possible different shrinkages of component parts, as was the case in the hybrid structure.

Even so the unexpected un-even shrinkages in the hybrid structure lead to a bent configuration and a different stiffness in its respective parts, Kelvin and octet, the printing of such a structure was an important first step in realising carefully constructed hybrid truss structures. Truss systems have previously been designed to create large structures with a variety of properties, which normal solids cannot exhibit, like high acoustic dampening, negative coefficients of thermal expansion or highly nonuniform mechanical response.[80, 81] Often reffered to as metamaterials those architectured trusses have been fabricated via additive manufacturing but mostly from polymeric materials, with a few exceptions of metal or ceramics, and the mechanical catacterisation has generally been limited to the elastic region with limited consideration of failure mechanics.[80-83] Additionally, the printed truss structures were limited to one particular geometry and strut dimension without incorporating two different truss structure within one lattice material. If such a material, with identical elastic moduli in the ceramic phase could be made, as was intended, the different deformation modes in the truss segments could produce a structure with the same stiffness, but controlled failure in the weaker part of the structure. The cells of this weaker part would then be expected to fail first and, if specifically placed in certain positions within the structure, the fracture path could be designed and controlled, already in the initial step of the manufacturing process, the design of the stl file. A predictable failure with conotrolled fracture path could be of great advantage in fracture research as well as in technological applications.

Additionally, it was shown, that the interface between two segments with different architectural design, porosity and mechanical properties is strong and not subjected to delamination, micro-

crack appearance or represents a weak point during fracture. A continuous ceramic structure could be designed with controlled reinforced parts, which can be of particular advantage in load bearing applications with non-uniform stress impact application.

4 Expanding SiOC Ceramic Structures to the Microscale through Two Photon Lithography

Shaping ceramic materials at the nanoscale in 3 dimensions (3D) is an engineering challenge, that can offer new opportunities in a number of industrial applications, including metamaterials, nano-electromechanical systems, photonic crystals and damage-tolerant lightweight materials. 3D fabrication of sub-micron ceramic structures can be performed by 2 Photon laser writing of a preceramic polymer. However, polymer conversion to a fully ceramic material has proven so far unfeasible, due to a lack of suitable precursors, printing complexity and high shrinkage during ceramic conversion. In following ceramic structures have been achieved through an appropriate engineering of both the material and the printing process, enabling the fabrication of preceramic 3D shapes and their transformation into dense and crack-free SiOC ceramic components with highly complex, 3D sub-micron architectures. The research work, which was carried out in collaboration with Professor Giovanna Brusatin and Dr. Laura Brigo (DII, University of Padova) and partially published in,[84] allows for the manufacturing of structures with any 3D specific geometry (see Figure S2C) with fine details down to about 800 nm and height up to 100 μm. The rapidly printed structures were converted into ceramic objects possessing sub-micron features, offering unprecedented opportunities in different application fields.

4.1 2-Photon Lithography of Ceramic Materials

By fabricating components based on ceramic materials instead of the typical polymers or metals, the range of properties would be expanded for instance in the direction of higher refractoriness, increased chemical durability, better wear and oxidation resistance, higher elastic modulus, improved dimensional stability with temperature, etc. So far, only very few examples of ceramic sub-micron fabrication have been reported.[49, 64, 65, 83, 85-88] They were produced via two-photon lithography (2PL), a laser-assisted technology for the intrinsic-3D manufacturing of structures at the micro- and meso-scale of a photosensitive material, a photoresist that is typically in a liquid state.

Standard photoresists compositions for 2PL are mainly based on purely organic acrylates. In one example, the acrylic polymer resist was transformed into glassy carbon by pyrolysis at 900 °C and, due to the high shrinkage, sub-micron shapes not taller than a few µm were fabricated.[85] Alternatively, in a multi-step process hollow TiN ceramic structures were obtained by 2PL of a standard photoresist followed by atomic layer deposition of titanium tetrachloride with N_2/H_2 gas mixture and subsequent O_2 plasma etching.[86, 87] Using the same approach Meza et al.[83] also fabricated hollow alumina nanolattices via deposition of trimethyl aluminium on the surface of the polymeric nanolattice followed by the subsequent removal of the polymer. In all cases a commercial acrylate polymer photoresist, IP-Dip (Nanoscribe Gmbh), was used to fabricate the nanolattices and either turned into glassy carbon at 900 °C[85] or coated via atomic layer deposition to produce ceramic TiN[86, 87] or alumina[83] nanolattices consisting of a network of hollow tubes.

Differently from photosensitive organic resins, preceramic polymers (precursors for SiOC, SiCN, or SiC materials) are a unique class of polymers that combine the processability properties of polymeric materials with the capability of transforming into ceramics at high-temperature in inert or oxidative atmospheres.[37] The use of preceramic polymers as photoresists in 2PL printing allows the fabrication of ceramic materials at the sub-micron scale with dense struts. However, shaping preceramic polymers at that scale, while generating complex 3D ceramics architecture, has been so far unfeasible: scarce examples reported in literature present limitations like poor definition and lack of small, resolved features of the printed 3D components and incomplete pyrolysis,[49, 64, 65, 88] due to lack of suitable precursors, high shrinkage accompanying the heat treatment and pyrolysis temperature below the completion of the polymer-to-ceramic transformation (below 800 °C).[89] Following approach 1 (see chapter 3.1.1), very simple SiCN-based 3D sub-micron structures have been fabricated by 2PL of a acrylate-modified functionalised polyvinylsilazane and subsequent pyrolysis at 600 °C.[64, 65, 88] Likewise, following approach 2, simple 3D microstructures were fabricated through the photoinduced polymerisation of a bifunctional carbosilane with an organometallic photo-hydrosilylation catalyst and turned into SiC-based material at 600 °C.[49] So far dense, but

simple structures have been produced over the preceramic polymeric route[49, 64, 65, 88] and, due to the relatively low pyrolysis temperature, they were not fully converted into a ceramic material.[89] As previously mentioned, complex 3D micro lattices have been produced instead by a photoresist from Nanoscribe itself and turned into either a pure carbon material, which is not resistant to oxidation at high temperature,[85] or a hollow, non-dense, ceramic component.[83, 86, 87]

Therefore, the aim of this work was to fabricate dense and highly complex sub-micron structures of stable, oxidation resistant ceramic material after a complete pyrolysis with structural dimensions of the order of a few hundred µm with resolution of individual features below 1 µm. Following approach 3 to fabricate preceramic polymers using a lithography-based process, the materials from chapter 3.1 developed for macrofabrication via DLP, were used in a 2PL printing process to fabricate microstructures with features below the µm-scale. Unprecedented 3D complex sub-micron architectures are presented, made of dense, pore- and crack-free SiOC ceramic, fabricated by 2PL of a preceramic photosensitive polymer with size up to 100 µm. These micro-structures are fully ceramized without shape distortion during the pyrolysis step at 1000 °C, due to a combination of the functional preceramic polymer, a proper photoinitiator and a new processing configuration for the fabrication of the 3D structures. First examples of the straightforward, fast and versatile 3D fabrication of fully ceramic, dense SiOC sub-micron-sized 3D components with dimensions of several tens of microns and minimum feature dimension down to about 800 nm are presented.

4.2 Optimisation of 2PL Writing Process and Conditions

As starting material for 2PL printing, pure RC 711 was used and, as indicated in Materials and Methods section (chapter 2), a Michler's ketone derivative molecule, BDEBP, was added and completely solubilized overnight. The photoinitiator, while generally used as a single photon radical polymerisation initiator at about 365 nm wavelength (Figure 32), is used to activate radical polymerisation by 2-photon absorption at 780 nm. Thanks to the donor-acceptor-donor structure, upon 2-photon absorption, the carbonyl 4 group of BDEBP is promoted to an excited singlet state, that can undergo an intersystem crossing to the triplet state, from which two radical ions are produced via electron donation by the amine to the carbonyl moieties,[90] thus providing the radicals to start the polymerisation of the polysiloxane. As polymerised resins have a slightly different refractive index from the liquid resin, the patterns written by the 2PL process can be immediately visualised. A sequence of images, showing the 2PL printing process, was extracted from a video, taken during the printing process, and can be seen in Table S11. The lack of added solvent guarantees high stability of the solution during laser writing, avoiding possible evaporation and phase separation. Single photon UV-vis absorbance spectra of resin components are reported in Figure 32 and 2-photon absorption spectrum of BDEBP can be seen in Figure S5.
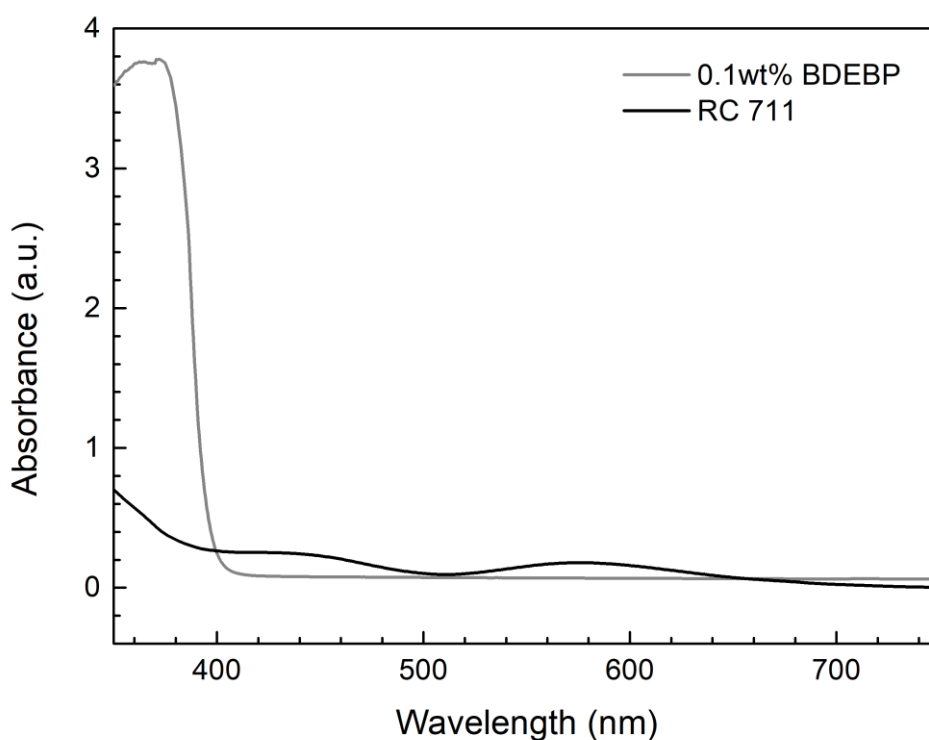
Figure 32 Single photon UV-vis absorbance of the RC 711 preceramic polymer and of the used BDEBP initiator (dissolved in toluene at 0.1 wt% concentration).

Later on, also the mixture with RC 711/H44 = 5/5 of the physical blends was used in 2PL printing. The preparation of the blend is described in chapter 3.1.2.

4.2.1 Printing configuration

Two different configurations were used for the fabrication of the structures (Figure 33). Considering the inverted microscope configuration of Nanoscribe GT, laser beam is initially focused at the lower glass/resin interface in the standard approach and successively moved layer-by-layer inside the printing volume in increasing z-direction. According to the to be printed 3D design the whole structure is polymerised. In practice, power compensation would actually be required for assuring a constant exposure dose at increasingly higher penetration depths within the liquid and through just polymerised layers. Due to the working distance of the used objective, a maximum height of the fabricated structures of ~100 µm on a thin glass slide (150 µm) is possible. It is therefore not possible to use this configuration to fabricate structures onto millimetre-thick, fused silica slides.

Thus, an alternative "inverted" approach was developed to fabricate the structures, which need a support pillar for subsequent pyrolysis on a fused silica glass substrate (Figure 33B). A preceramic polymer solution drop is placed between two glass substrates, separated by a thin PDMS membrane serving as the gasket. The upper fused silica glass slide (arbitrarily thick) serves as the printing platform for the growth of the 3D structures, while the lower coverslip separates the objective immersion oil from the preceramic resin. In this case, the laser beam is initially focused at the upper glass/resin interface, and fabrication proceeds in a layer-by-layer fashion in decreasing z-direction. Thus, shadowing effects from previously polymerised layers are eliminated. The fused silica glass slide can withstand heating temperatures of 1000 °C and is therefore a suitable substrate for the complete pyrolysis of the printed preceramic structures.

A: Writing direction: UP

Liquid resin

Structure

Glass substrate

2 Photon Irradiation

B: Writing direction: DOWN

Fused silica substrate

Structure

Liquid resin

PDMS spacer
(height ~ 135 µm)

Glass substrate
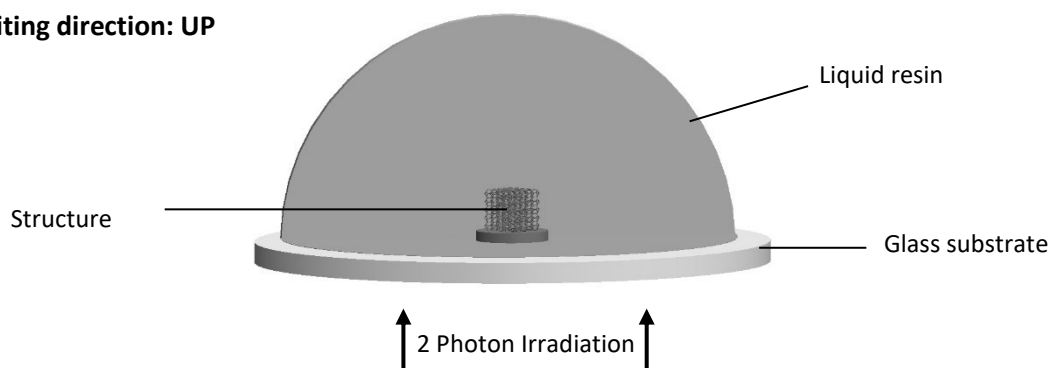
2 Photon Irradiation
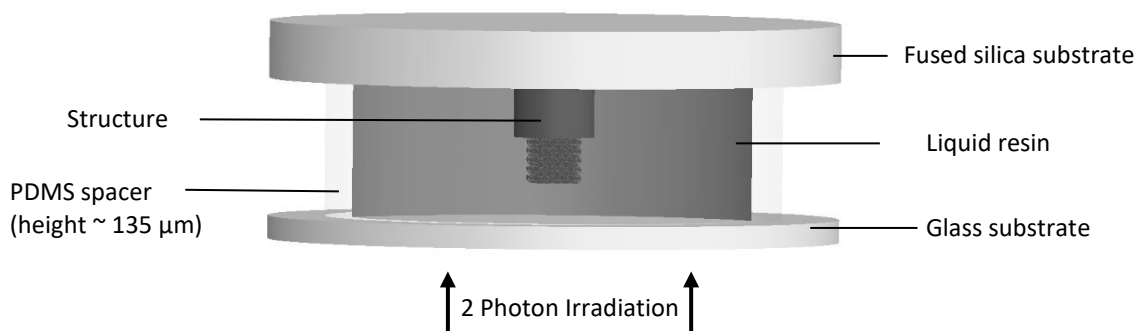
Figure 33 Schematics of the "standard" approach (A: Writing direction: UP) and "inverted" configuration (B: Writing direction: DOWN) for 3D polysiloxane polymer fabrication.

The "standard" approach was used to fabricate the porous polysiloxane structures for observation of their printed, polymeric condition. To fabricate SiOC ceramic structures, the polysiloxane resin was printed on a fused silica substrate in the "inverted" configuration for the pyrolysis step later.

4.2.2   Optimisation of exposure dose

An estimate of the effective power during a fabrication process was provided by multiplying 50 mW by laser power and power scaling values, which determines the intensity within the focal spot. Therefore, the exposure dose can be increased either by increasing the laser power as well as power scaling or by decreasing scan speed, thus increasing exposure time. Such dose is roughly proportional to the square root of the scan speed value. The exposure dose is therefore dependent on three parameters, laser power, power scaling, printing speed, and needs to be adjusted to obtain a sufficient degree of crosslinking of the polymer. Similarly to the DLP process, in which the exposure time (at a fixed projector power) alone determined the exposure dose, an object was chosen and printing tests were performed in order to find the right printing parameters for the RC 711 to print

microstructures. As the polymerisation during 2PL occurs within the focal spot of the intersecting two photons (see Figure 6), only a specific voxel within the printing liquid is illuminated at any one time. Opposite to the DLP process, were the illumination shines through the whole printing bath, if not restricted in the z-direction, no photoabsorber is necessary, since the printing happens only in the tight focal voxel where the polymerisation threshold is exceeded. However, an excessive exposure dose will increase the voxel size and cause polymerisation in the surrounding liquid adjacent to the intended printed voxel. An overabundant excess of exposure dose can even cause explosions in the printing liquid (see Figure 7).[30] A careful control is therefore necessary and fabrication parameters were changed exploring a range of laser power, power scaling and scan speed values, therefore tailoring the final exposure dose.

Exposure tests were performed, similarly to those carried out for DLP printing (see Table 6), through dose matrices by fixing always two of the above-mentioned parameters while changing the third one in controlled increments. The same Kelvin cell, which was printed with RC 711 via DLP (see Figure 21), was used for the exposure dose tests, as it represents an example of a complex, porous and highly detailed architecture, which validates the possibility of generating long overhangs and demonstrate the freedom of 3D design that this technology affords, but at a much smaller scale than DLP printing.

An example of this optimisation process can be seen in Figure 34. In this exemplary dose matrix, the laser power was kept constant at 1.2 and the writing speed at 3000 µm/s. The power scaling was changed from 50 % in 10 % increments up to 100 %. Figure 34 illustrates the point of a tight control of the exposure dose. While the degree of crosslinking was too low at a power scaling of only 50 % (Figure 34A) to form strong enough struts, which are free standing and can support themselves, it was equally too high at 100 % (Figure 34C), causing overexposure of the printed struts. At a laser power of 1.2 and a writing speed of 3000 µm/s, a power scaling of 70 % (Figure 34B) proved to generate the necessary exposure dose for RC 711 for the fabrication of a highly complex structure.
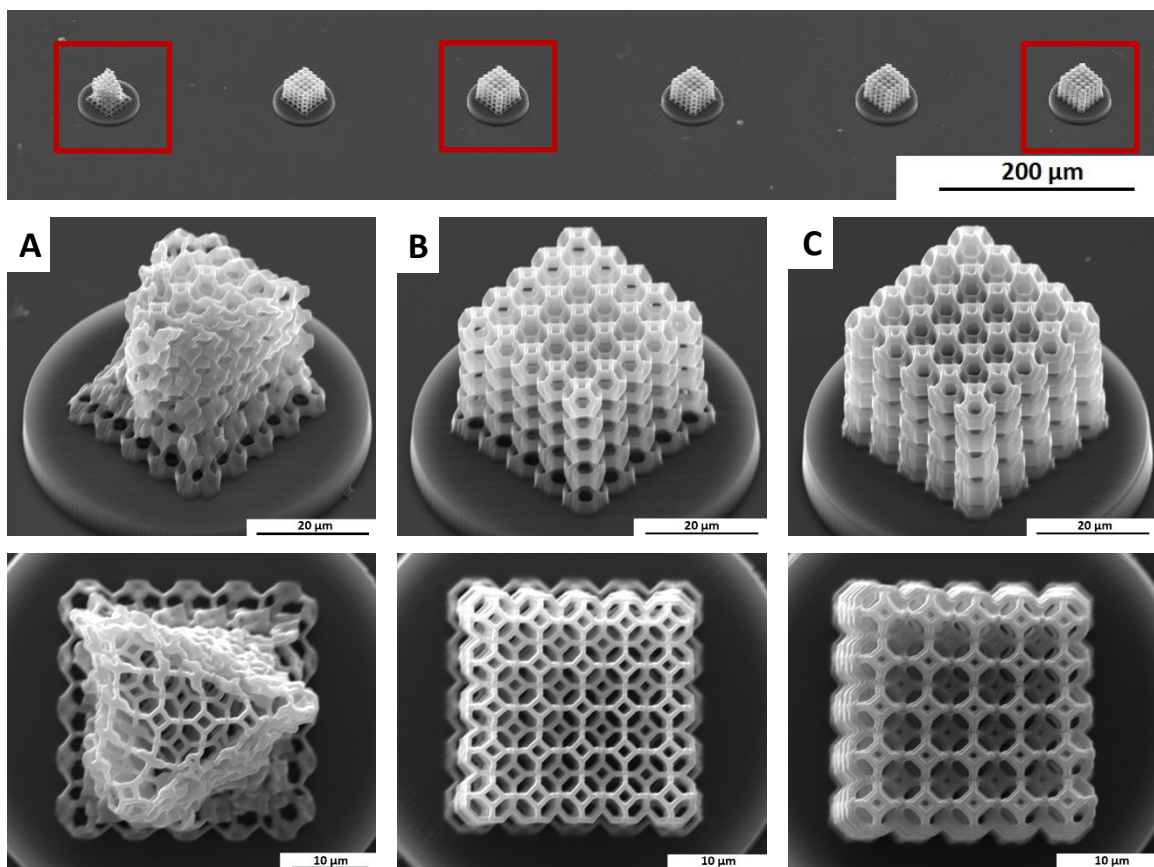
Figure 34 Optimization of process parameters made through dose matrices from underexposed (A) to over-exposed C) fabrications with the preceramic polymer. Writing speed: 3000 µm/s; laser power: 1.2; power scaling in overview: 50 % (left) - 100 % (right); optimised printing condition at 70 % power scaling (B).

As fabrication time is a decisive parameter to develop a promising process technology, the limit of the writing speed of the preceramic RC 711 siloxane was tested. The complex, porous Kelvin cell structure with dimensions of 30 x 30 x 30 µm, fabricated with the optimised writing condition of 1.2 laser power, 70 % power scaling and 3000 µm/s, was already completed in under 6 min, demonstrating the high throughput of RC 711. To push the writing speed and find its ultimate limit, a simple structure was printed, demonstrating a high fabrication speed up to 50000 µm/s (Figure S6). This performance was close to the highest achievable with standard resists from Nanoscribe itself (60000 µm/s) and is very uncommon for non-standard 2-photon laser writing resists. It shows the potential in printing RC 711, not only at the macro- (DLP) but also at the micro-scale, in a time efficient manner.

4.3 Fabrication of Tall and Complex Architecture with non-commercial Photoresist

After demonstrating that the preceramic siloxane can match the writing speed of standard polymeric photoresists, the fabrication possibilities of complex structures were investigated. Figure 35 already shows that highly porous complex structures, like the Kelvin cell structure, can be fabricated with RC 711, exceeding the level of complexity previously shown by other research groups working on 2PL of preceramic polymers.[49, 64, 65, 88]

While highly porous structures, consisting of very small struts like the Kelvin cell structure, can be printed in the standard configuration, tall structures with dense parts constitute a challenge. In fact, when using 2PL frequently encountered drawbacks are the focus distortion and laser power loss, due to shadowing effects when the laser passes through already solidified volumes to move the focus at increasing z coordinates. This is especially common when non-standard resist materials are used, as in the case of RC 711. An example of a failed attempt to print the Pisa Tower, as an example of a complex, tall and bulk structure, can be seen in Figure S7. The polymerised layers of already printed RC 711 presents a barrier to the laser, preventing it from reaching the printing liquid and continuing with the print. The laser power is reduced up to the point where the exposure dose is not high enough anymore to provide a sufficient degree of crosslinking.

In order to print those kinds of structures, the non-standard printing configuration was developed (see Figure 33B). This "inverted" approach made it possible to avoid the shadowing effects and assured a constant exposure dose at increasingly higher penetration depths within the liquid. In this configuration, the resolution of the fabrication was maintained from the bottom to the top of the 3D structure, as the laser focus didn`t have to pass through already polymerised, solid layers. Figure 35 shows examples of the successful fabrication of complex structures using the configuration reported in Figure 33B, with a height up to 0.1 mm, which would have otherwise been limited to about 10 times smaller dimensions, if the standard fabrication configuration would have been used.
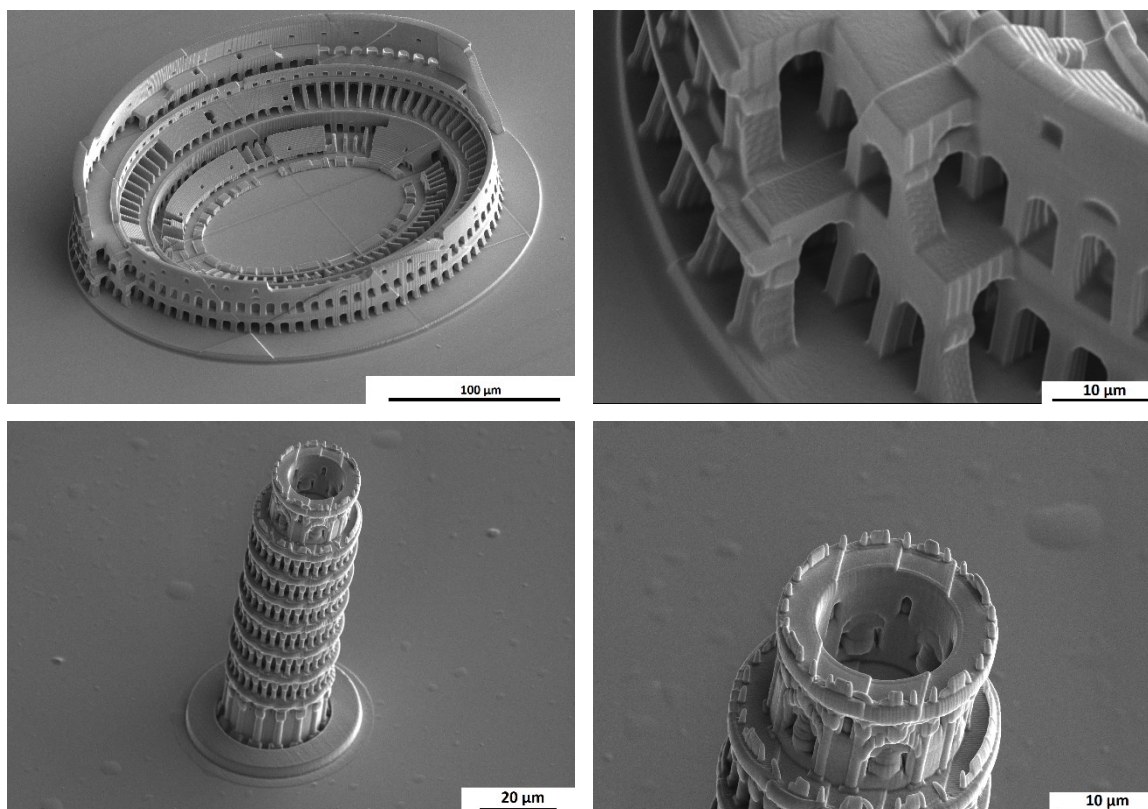
Figure 35 Examples of complex, tall and dense 3D structures produced using the preceramic resist: Colosseum of Rome (top) and Pisa tower (bottom).

With this setup, it was also possible to grow structures on supports of different heights as the need for power compensation, when writing at increasing depths and through dense material, was eliminated (as it would occur in the standard configuration, Figure S7). Furthermore, the support glasses on which the structures were printed could to be exchanged, which made it possible to use fused silica glasses, which were thicker than standard cover slip glass. This is needed for the pyrolysis process, as explained in the following chapter.

4.4   Pyrolysis into SiOC Ceramic

Two important issues arouse with the pyrolysis of the siloxane microstructures and their transformation into a SiOC ceramic, the high temperature and shrinkage during pyrolysis. For complete transformation, a heat treatment at 1000 °C is necessary, which exceeds the softening temperature of standard glass, which renders the normally used cover slips useless for the pyrolysis of RC 711 and makes it necessary to use fused silica glass. And the second problem was the shrinkage of the polysiloxane during pyrolysis coupled with the anchorage of the structure to the glass substrate. Due to the low ceramic yield of RC 711, only 7.4 wt% see Figure 17, the material exhibits a significant shrinkage which leads, because of the retention force due to the anchorage of the structure to the glass substrate, to a complete collapse of the structure (Figure 36).

Noteworthy is that, although the structures had to be handled, transported to different places (printer, furnace, SEM), heat treated, were subjugated to retention forces and exposed to polymer-to-ceramic transformation, the structures remained connected to their glass substrates in printed and pyrolysed state. The connection, which was established during the printing process, remained strong and stable throughout all conditions and also survived the transformation into SiOC ceramic without detaching from the substrate.
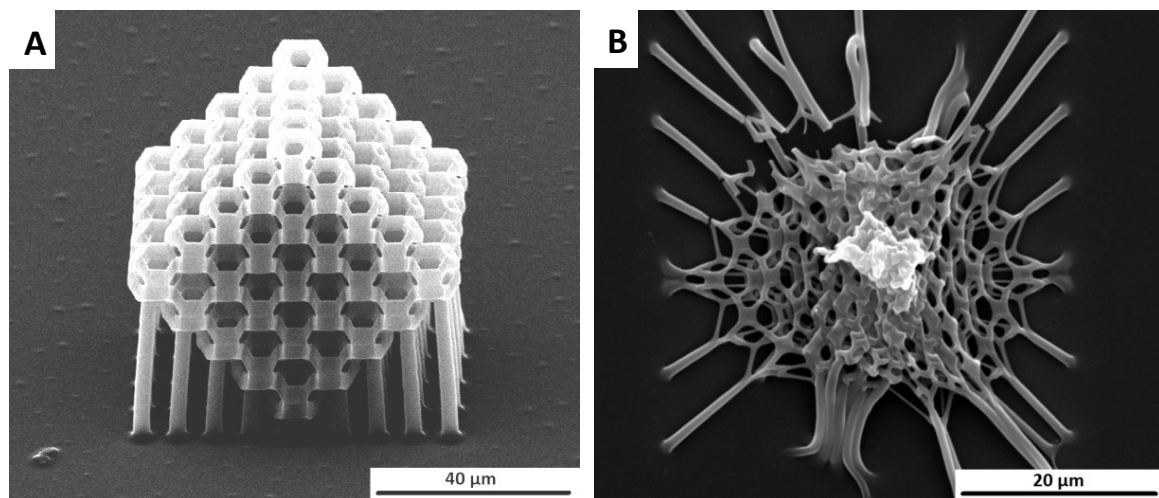
Figure 36 Rotated Kelvin cell Structure printed with RC 711 on glass substrate (A), same structure after pre-pyrolysis at 450 °C (B).

By using the "inverted" configuration in the printing setup (Figure 33B) it was not only possible to grow preceramic structures on arbitrarily thick fused silica glass, which is able to withstand the pyrolysis temperatures of 1000 °C, but also to fabricate them on top of cylindrical supports. These were specifically designed to reduce constraints from the glass substrate during the contraction accompanying the siloxane decomposition. The importance of the presence of a suitable support is shown in Figure 37, where deformation of the 3D structures was observed after pyrolysis when

they were grown on support pillars of insufficient height. The support pillars are disconnecting the actual structure from the glass substrate and are absorbing the inhomogeneous shrinkage, which arouses due the retention force of the structure to the glass substrate, as the glass shows no dimensional change during the heat treatment. It is evident how, in the standard fabrication configuration in which the maximum height would be limited to about 10 µm due the shadowing effect of previously polymerised layers, structures like these could maintain their shape after pyrolysis only by reducing the shrinkage, as when incomplete ceramization is carried out (e.g. by pyrolysis at 600 °C),[49, 64, 65, 88] or by filling the preceramic formulation with powders, to the disadvantage of the structures complexity and the polymerisation efficiency, due to light scattering.[65] The implementation of the "inverted" printing configuration together with the use of fused silica glass and support structures to decouple the structures form the substrate, makes the transformation of RC 711 into SiOC ceramic possible without structural collapse (see last row in Figure 37).
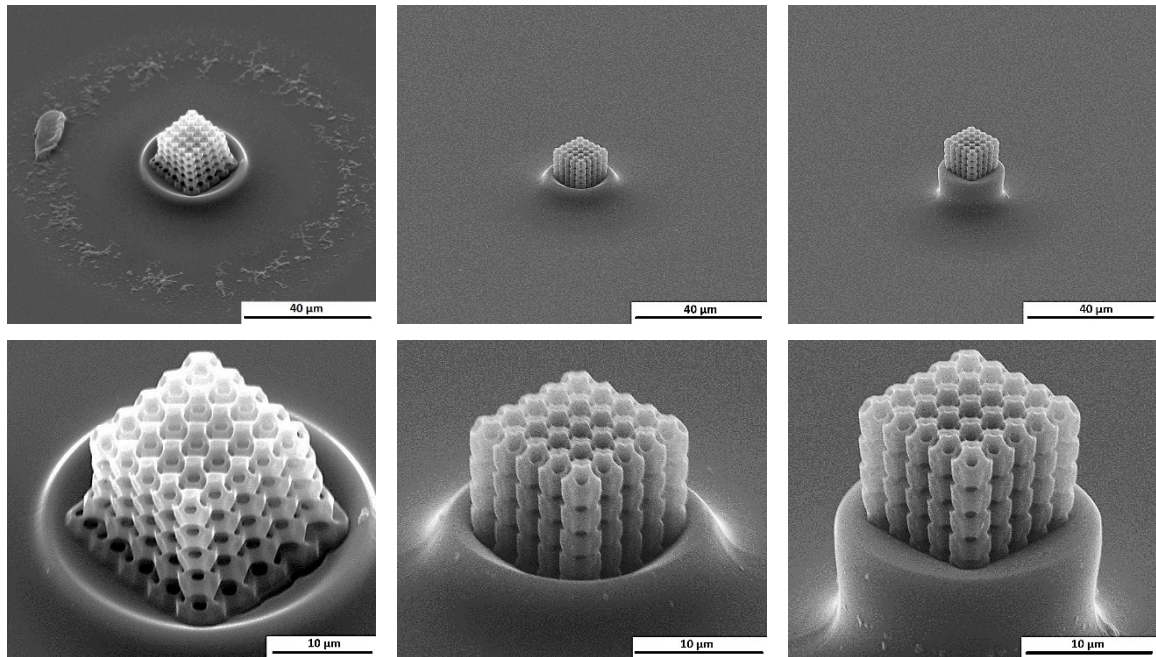
Figure 37 Pyrolysed Kelvin cell structure (scaling 1.8 and pyrolysed at 1000 °C) on support pillars with increasing height, to reduce shrinkage constraints from the glass substrate during pyrolysis; Images in the bottom row represent a magnification of the samples shown in the upper row.

Kelvin cell and diamond structures were fabricated after optimization of process parameters (laser power, power scaling, writing speed) and necessary support heights and converted to SiOC ceramic micro-sized 3D components (Figure 38). After pyrolysis at 1000 °C the actual structures on top of the support pillars show no significant shape distortion in the three dimensions. A complete and crack-free transformation into SiOC ceramic structures with micrometre dimensions and homogenous shrinkage was possible. Remarkably, this was achieved in spite of the overall linear shrinkages of 51 % (Kelvin Cell structure) and 56 % (diamond structure), with respect to the printed structures (Figure 38) that, in terms of volume shrinkage, resulted in a contraction of almost 90 %. The images

in Figure 38 were taken with the same magnification factor before and after pyrolysis, visualising the change in dimension accompanying the ceramic transformation and the complete retention of shape of the overall structure and the sub-µm sized struts. At closer inspection of the pyrolysed Kelvin cell and diamond structure at lowest magnification, the original dimensions of the support base can still be detected.

The lack of evident deformation of the overall architecture or melting during pyrolysis indicated that no softening or bloating occurred during ceramisation. This suggests that a suitably high degree of cross-linking was achieved during the 2-Photon polymerisation. This is an important and key issue when 2PL is used, from which not only the shape preservation during thermal treatment depends, but also the prevention of collapse during the development step, i.e. the chemical treatment used to remove un-crosslinked polymer (see Figure 34A).
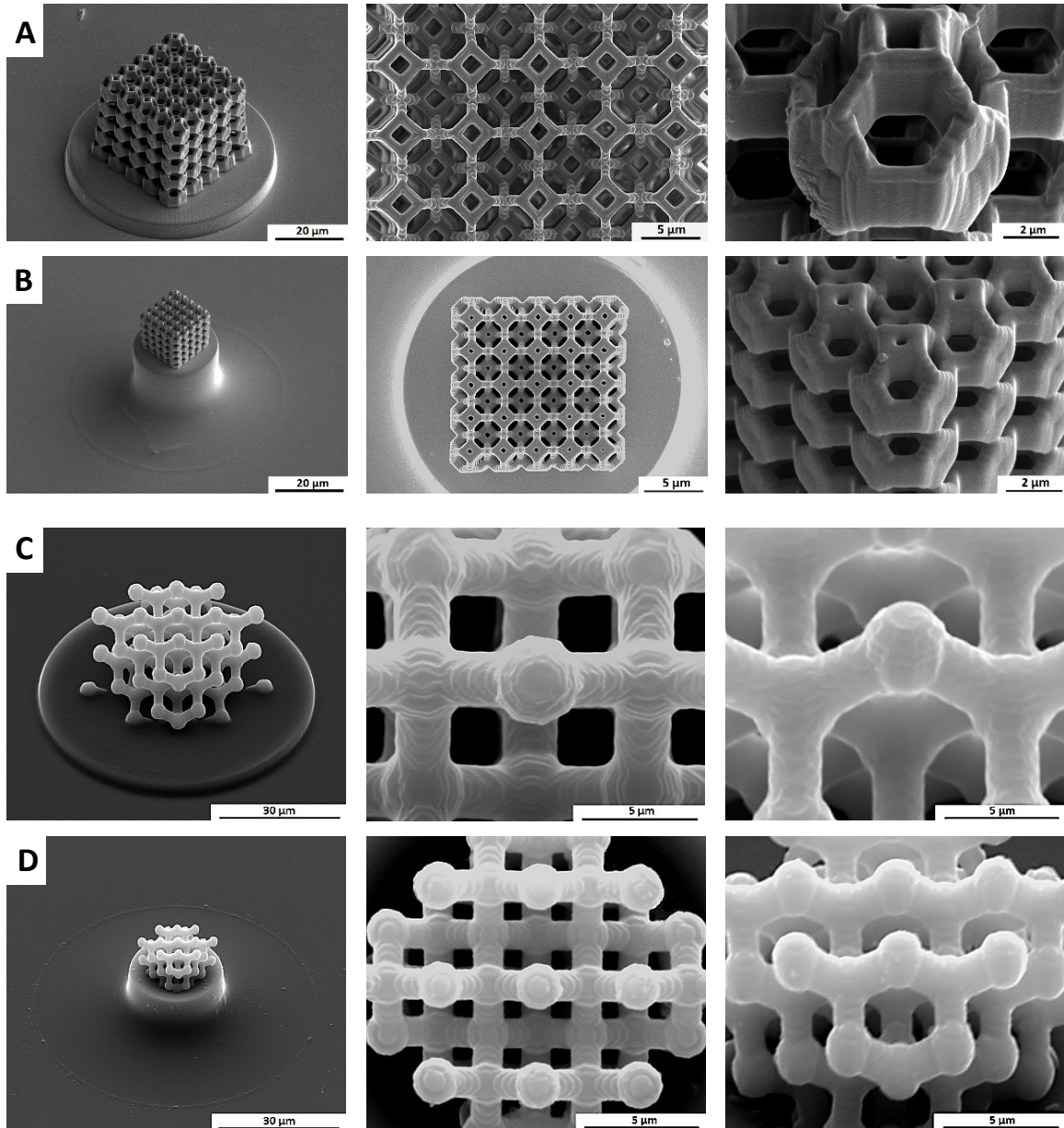
Figure 38 SEM images of a Kelvin cell and diamond structure before (A,C) and after (B,D) pyrolysis at 1000 °C; all SEM before and after pyrolysis were acquired with the same magnification factor within one structure.

Fracture images of a pyrolysed Kelvin structure were taken. Figure 39 shows that RC 711 developed after pyrolysis a dense SiOC ceramic even in micro components, with features elements below the µm scale. A fully dense, crack-free ceramic material is confirmed.
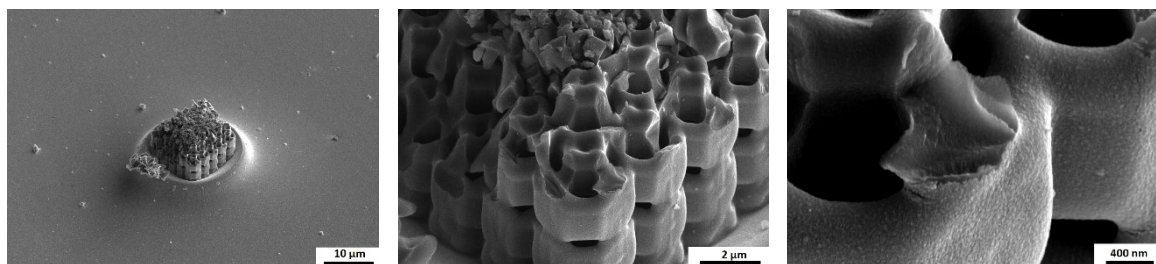
Figure 39 Fracture images of a pyrolysed Kelvin cell structure confirm a fully dense, crack-free ceramic material after pyrolysis at 1000 °C.

4.5   Mechanical Analysis of Micro-sized SiOC Kelvin Cell Structures

Preliminary micro-compression tests have been performed on seven pyrolysed Kelvin cell structures in collaboration with Prof. Saiz from Imperial College London, England. An overview of the tested structures, the stress-strain curves and a structure before and after compression can be seen in Figure 40. Videos were taken during the compression test and one was exemplarily chosen and converted into images. The image sequence of the compression test can be seen in Table S12.
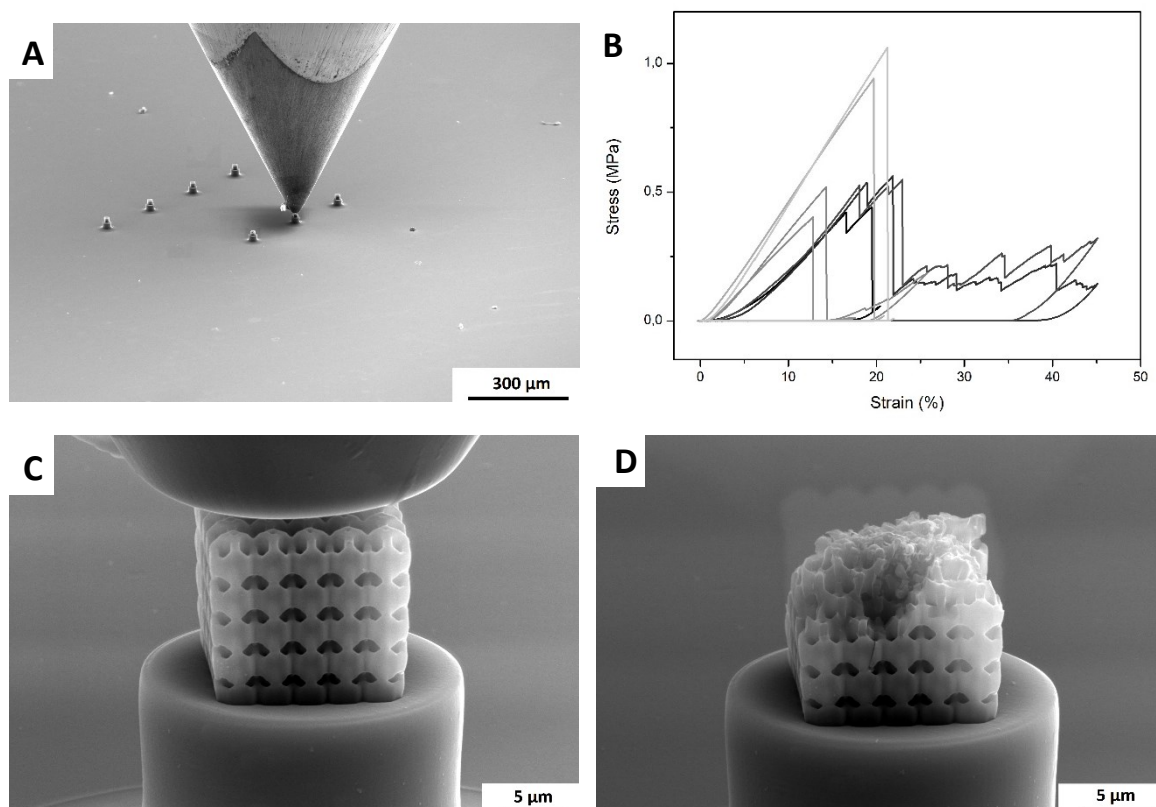
Figure 40 Compression tests on pyrolysed SiOC ceramic microstructures; overview of all tested samples (A), stress-strain compression curves (B), picture of exemplary sample before (C) and after (D) compression.

The fracture data of the SiOC microstructures reports a linear-elastic behaviour until ultimate fracture load followed by brittle failure, typically for ceramic porous structures, for all Kelvin cell structures. The compressive strength reaches values up to 0.64 ± 0.24 GPa at a porosity of around 75 % and density of around 0.5 g/cm^3. The characteristic strength was 0.72 GPa with a Weibull modulus of 2.9 for this brittle, highly porous ceramic material. Porosity and density values have been calculated from pyrolysed Kelvin cell macro-samples printed with exact same geometry from RC 711 via DLP (see Figure 21), as weight measurements could not be performed on the microstructures, together with a powder density of 2.0 g/cm^3 measured by helium-pycnometer. The measured porosity value of 85 % for the macro-samples was reduced by an estimated 10 % due to the overexposure of the tested, preliminary Kelvin cell structures printed via 2PL, evident in Figure 40. The SiOC porous structures were compared to other micro-architected and macroscopically structured lattice

materials,[83, 91-93] carbon-nanotube-based aerogels,[94] carbon and carbon-alumina lattices and honeycombs,[85] as well as to commercial bulk materials. The data was plotted in a compressive strength-density Ashby chart in Figure 41. The compressive strength was higher than that of most bulk materials, while the strength/density ratio well exceeded those of all natural and technical cellular solids and other micro-architected lattices.[83, 85, 91-93] The specific strength was more than ten times higher than the strongest micro-lattice of other ceramic, 2PL printed materials, as the production from preceramic polysiloxane produces ceramic structures with dense (see Figure 41) instead of hollow struts,[83, 91] yielding a structure which is capable of withstanding higher loads. The strength/density value of the produced SiOC Kelvin cells lies between those of the higher strength micro-lattices and the honeycomb structure by Bauer et al.,[85] which are the only other known non-polymeric, dense and fabricated via 2PL micro-architected samples of comparable complexity and accuracy, but has the additional material advantage of being an oxidation-resistant SiOC ceramic instead of only glassy carbon.
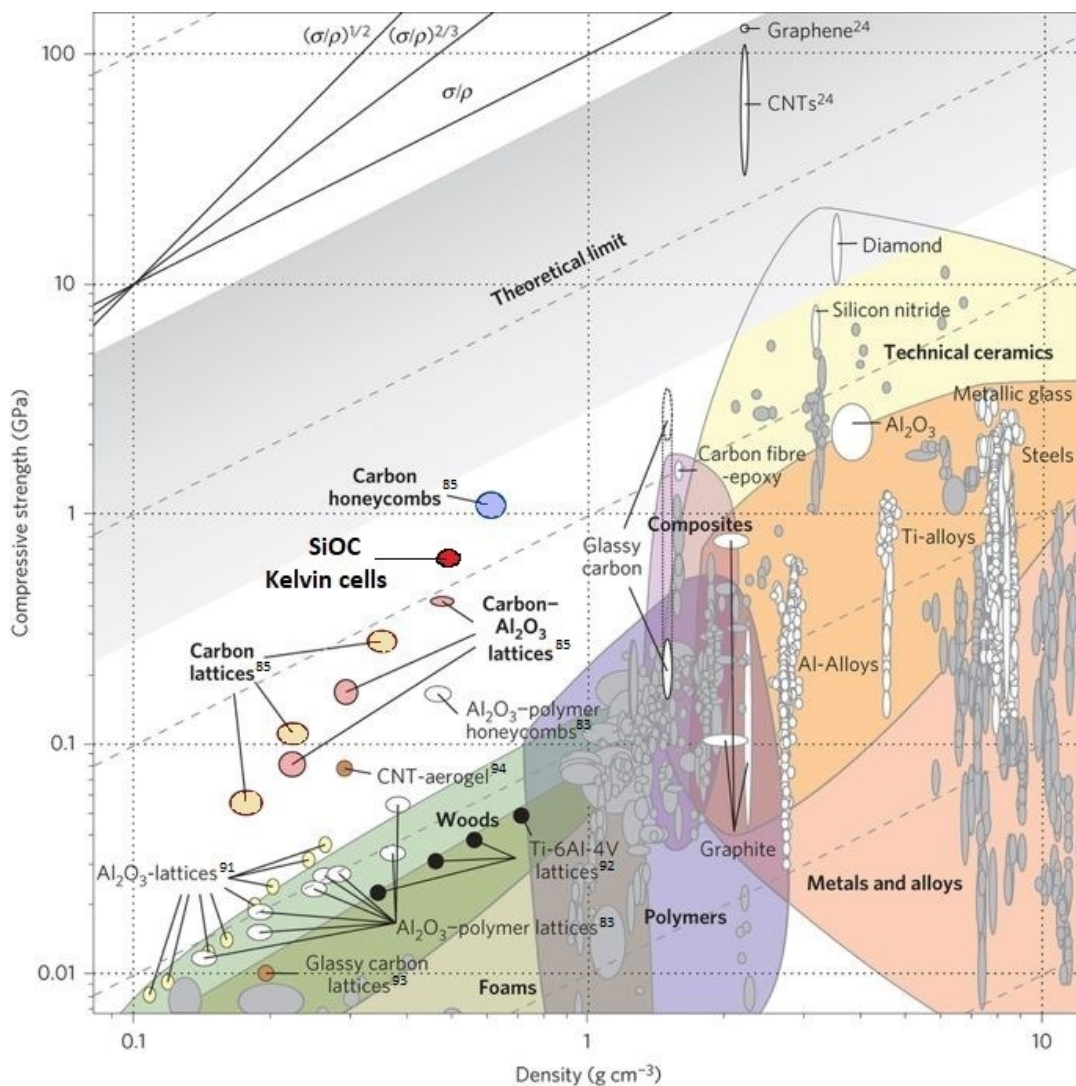
Figure 41 Compressive strength–density Ashby map; Inserted in the chart of Bauer et al. [85] the compressive strength of the pyrolysed SiOC Kelvin cell structures are compared to other micro-structured materials, natural and technical cellular solids, and monolithic bulk materials.

Ceramic is a brittle material were crack initiation starts from the biggest flaw inside a ceramic before it propagates through the material. Griffith[95] proposed as a relationship between the fracture strength of a material σ_f and the critical size of a flaw c

$$\sigma_f \sim \frac{1}{\sqrt{c}} \qquad (14)$$

According to this relation, the fracture strength is indirectly proportional to the flaw size. As the flaw cannot be larger than the structural features in which it is located, structures with micro sized geometries have an arguably higher strength. The exceptionally high strength data of the SiOC microstructures, compared to other porous foams (see Figure 41), supports this proposition. The strength of the SiOC Kelvin micro-structures, with approximately 75 % porosity, exceeds by more than 60 times the one from the SiOC Kelvin macro-structures (see Table 11), exhibiting only a slightly larger porosity of 82 %. Interestingly, the compression strength of the micro-structure is close to the flexural strength of a single Kelvin macro-strut (see chapter 3.2.2.3) and matches an empirical relationship between flexural and compressive strength of plain concrete[96]

$$\sigma_{fl} = 0.7 \sqrt{\sigma_c} \qquad (15)$$

The calculated value of 0.56 coincides to the 0.54 GPa flexural strength of the SiOC Kelvin strut, which shows a comparable strength of a dense, compared to a highly porous, micro-component, structured in the µm-scale via 2PL. This demonstrates the importance of size effects and their arrangement in an ordered architecture, which can be achieved through 2PL printing. As the strength of the dense and crack-free micro-structured SiOC ceramics well exceeds those of previously fabricated hollow ceramic lattice structures[83, 91] or polymer materials in general, lying between the strength/density lines of dense glassy carbon lattices and the honeycomb structure,[85] pyrolysed SiOC structures, printed with 2PL, represent promising candidates for micro-mechanical applications.

4.6 Achievable Resolution Limit of Preceramic Polymer Resist

In order to assess the smallest possible feature dimension and to stretch the upper limit of this technology applied to the preceramic formulation, simple 3D structures were designed. For the resolution tests, woodpile structures were fabricated, as their simple shape allows to investigate the smallest feature dimensions achievable. Woodpile structures were drawn in hand-written Nanoscribe's General Writing Language code as trajectories to be followed by the laser focus inside the polymer solution. A series of woodpile structures of 40 x 40 µm^2 base area, with lateral rod spacing of 5 µm and axial rod spacing in the range of 0.50 – 1.25 µm, were written by tuning laser power values (from 10 to 100 %) at a fixed scan speed of 450 µm/s, for a power scaling of 1.0 (corresponding to 50 mW laser power on the sample). Structures tens of microns in height were produced as successive stacks of the basic four-layer module of a woodpile.

They were printed by moving the laser focus along each pile with a single scan. In this fabrication approach, single line section and 3D size were determined by the voxel shape, which was in turn affected by the used photosensitive material, the writing parameters and settings. As shown in Figure 42, a single pile fabricated after optimization of the process parameters (see Figure S8) possessed an approximatively ellipsoidal cross-section with axes of 0.45 µm and 1.25 µm in the preceramic material (Figure 42B) and smaller, about 0.35 µm and 1.0 µm, for the standard Nanoscribe resist IPL, (Figure 42A). The larger vertical axis in both printed materials reflects the shape of the ellipsoidal voxel, as expected. These single line sections were therefore an indication of the ultimate feature dimension that can be written with these two materials, relatively to this specific geometrical shape. Clearly, optical properties of the preceramic polymer such as refractive index, which was not optimized for 2PL in contrast to the standard resist from Nanoscribe itself, provoked some voxel deformation (defocussing). The minimal size of the written single lines was enlarged when using the preceramic polymer solution. After pyrolysis (Figure 42C), shrinkage in the z axis of the pile section was about 64 %, which resulted in a final dimension of 800 nm, whereas pile width remained almost unmodified. This considerable difference can be explained by a different cross-linking degree of the polymer along the vertical direction of the pile section, due to the weaker light intensity of the voxel along this direction upon defocussing. It is noteworthy to observe that the sizes of the features in the component after pyrolysis were smaller than those in the as printed state, therefore providing resolutions beyond what is allowed by the characteristics of the photosensitive polymer employed in the fabrication, and approaching those achieved with standard photo-resists.
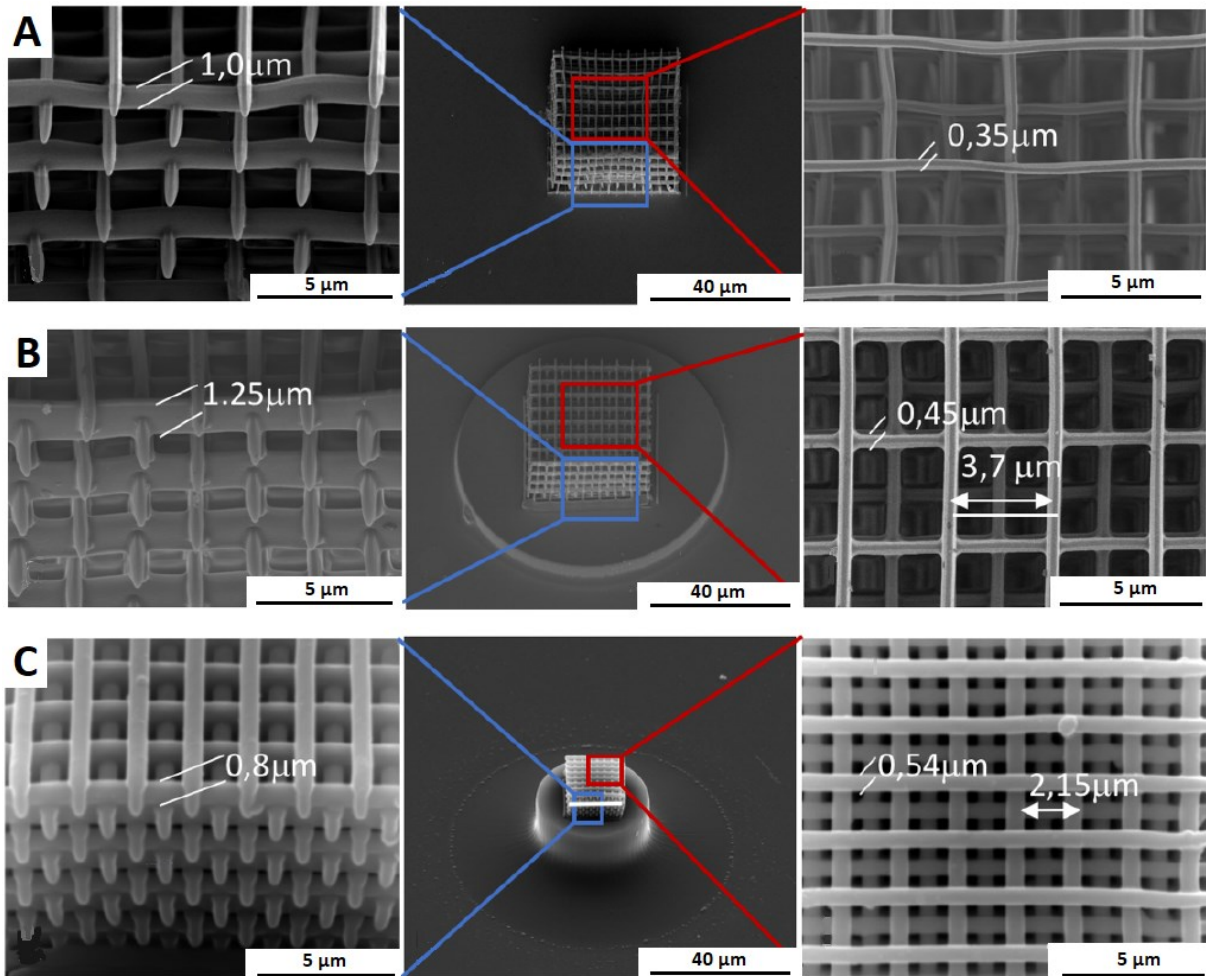
Figure 42 Fabrication of woodpiles using IPL (Nanoscribe) (A), RC 711 in its preceramic polymer state (B) and RC 711 pyrolysed (C).

However, the writing parameters used to design the woodpile structures were single line scans. For normal structures with complex features, not just single line rods, the voxel is scanned multiple times across the features, intersecting with each other, until full polymerisation is achieved. To check the resolution in x-y direction and the possibility of deformation in the printing voxel in z-direction in highly complex structures, Kelvin cell and diamond 3D structures were fabricated. Their dimensions were scaled by a factor between 1 and 3 (Figure 43) to investigate the smallest features dimensions that could be produced. The Kelvin cell structures, after optimisation of their process parameters, were printed at a laser power of 1.2, a writing speed of 2000 µm/s und power scaling of 80 % (36A), 70 % (36B) and 90 % (36C). Likewise, the diamond structures with a scaling of 1 and 3 were both printed with a laser power of 1.0, a writing speed of 3000 µm/s and a power scaling of 40 %.

Printing the same structure in different sizes shows that only a slight variation in exposure dose could be necessary, depending on the size of the to be printed features, but that the overall printing condition stays approximately the same for printing the siloxane material. It also shows that when

printing thicker sized features, the exposure dose can be reduced by reducing laser power, power scaling and increasing writing speed (optimised printing condition of diamond compared to Kelvin cell structure). This is consistent with the performance of the DLP system, when at a reduced exposure time the smallest features were not printed yet, but thicker struts had already polymerised (Table 6).

It also confirms that there is a limitation in resolution, and therefore in the downscaling of a structure. Figure 43C with a scaling of 1.0, is the smallest scaling factor (see Figure S9 for scaling of 0.5) which shows the distinct features of the Kelvin cell, although the struts are slightly warped and connected to each other in some cases. This confirms that a strut diameter of 0.4 µm is just at the border of being too small to being perfectly resolved. By scaling the Kelvin cell by a factor of 2, highly resolved features with strut dimensions of 0.8 µm can be printed in a 36 x 36 x 36 µm^3 volume sized structure. Remarkably, shape complexity and fine features were maintained at all scaling factors, and the provided dimensions of the stl-file (strut in Kelvin cell stl-file: 0.4 µm) transferred in the printed polysiloxane microstructure with remarkable accuracy (slightly thicker struts were obtained at scaling of 2.75).

Focusing on the resolution in z-direction, the oval size of the laser voxel can be seen in the diamond structure (dimensions 23 x 23 x 23 µm^3) in Figure 43E. Images of the smaller magnification in Figure 36D and 36E show the same feature in the diamond structures taken at different magnifications, due to the different scaling factors. The height of the diamond node in Figure 43D is 6.2 µm, matching nearly exactly the node height of the stl-file (2.1 µm), considering the scaling factor of 3, reproducing the intended stl shape perfectly. Differently in the diamond printed with a scaling of 1, where the node size should equal 2.1 µm but exceeds it by nearly 50 % (3.1 µm in Figure 43E). This shows that the size of the diamond node at a scaling factor of 1 is so small that, even in an actual structure printed with multiple line scans, the oval voxel deformation can be detected.
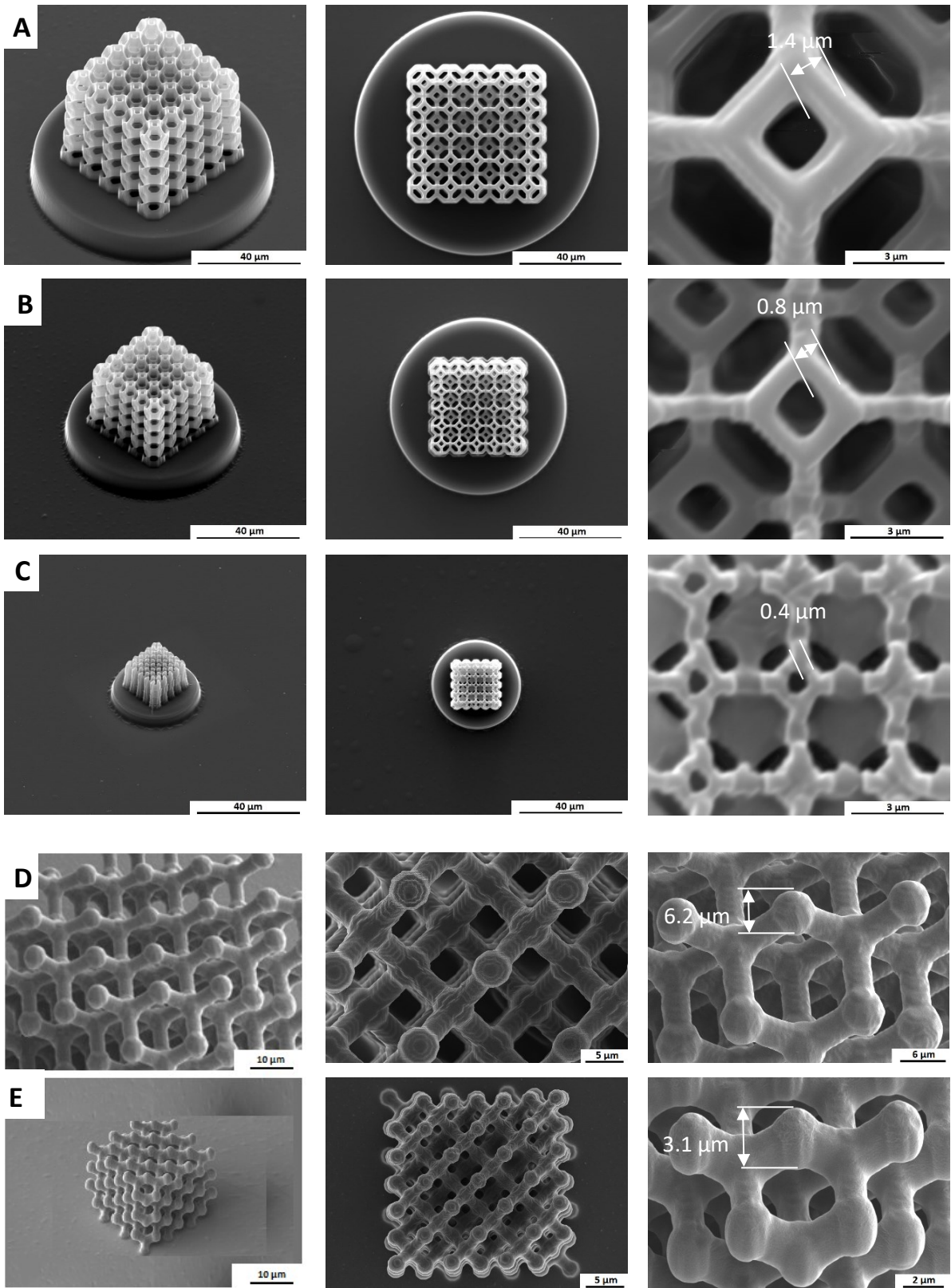
Figure 43 3D fabrication of preceramic structures with different and complex architectures before pyrolysis. SEM images of Kelvin cell (A-C) and diamond structures (D,E).

4.7 2PL Printing of Physical Blend Developed for DLP

So far, it was possible to use the photosensitive RC 711, chosen for DLP printing, also for 2PL printing. The challenge the high shrinkage of this particular polysiloxane presents was overcome by printing in the "inverted" configuration and by growing the actual structures on top of supports. In this way ceramic SiOC micro-structures have been fabricated which can compete regarding printing resolution with that of the standard polymeric Nanoscribe photoresist. Physical blends were developed for DLP printing in order to increase the ceramic yield and reduce the shrinkage (see chapter 3.1). If those systems could be printed by 2PL using a polysiloxane with reduced shrinkage, lower support heights could therefore be employed, also enabling the fabrication of taller structures. Moreover, the variation of the secondary polysiloxane would open the possibilities of varying the properties of the micro-structured SiOC material, due to the change in free-carbon content.[37, 44, 47]

The blend with RC 711/H44 = 5/5 was selected (for composition see Table 4) and, equally to the pure RC 711, 1 wt% photoinitiator BDEBP with respect to the photosensitive RC 711 content was added to the system. By using this blend, it was possible to fabricate structures with 2PL, although the printing window was decisively smaller than that of RC 711. The possible exposure dose variation between not-fully polymerised and too high for printing (see Figure 7),[30] as explosions occurred in the blend resin probably due to an interaction with the solvent in the system, is quite narrow, making it difficult to find the optimised printing condition (see Figure S10 for fabrication of simple, multiple line scans, woodpile structures). Unfortunately, the printed structures, as they have only sizes of a few dozen micrometres, provided not enough material to measure the ceramic yield of the 2PL printed structure via TGA analysis. This would have conclusively proved that the photosensitive RC 711 is incorporating H44 in its printed network, similarly to what happened when printing macrostructures (see Figure 18), hence increasing the ceramic yield of the printed mixture compared to pure RC 711. It was therefore decided to print the same structure with RC 711 and the blend RC 711/H44 = 5/5 and to compare them with each other both in printed and pyrolysed condition. Upon an incorporation of H44 within the polymerised RC 711 network, the shrinkage of the pyrolysed blend structure is expected to decrease by around 20 %, due to the higher ceramic yield of H44 (see Figure 19B).

Figure 44 shows an octet structure printed with RC 711 in polymeric (A) and pyrolysed (B) condition and with RC 711/H44 = 5/5 (polymeric state: C; pyrolysed state: D), SEM pictures taken at the same magnifications. The overall octet structure printed with RC 711 shows dimensions of 36.1 μm in x and y direction in the printed state. Upon pyrolysis, the structure shrinks linearly by 48 % and displays an area of 17.4 x 17.4 μm^2. The blend mixture shows different values of 30.5 μm of the siloxane structure and 14.9 μm in the pyrolysed octet, but the same pyrolysis shrinkage of around 48 %.

The expected decrease of around 20 % was not displayed in the printed structures. In fact, they show the exact same shrinkage upon pyrolysis, suggesting that, although a mixture of RC 711, H44 and toluene as solvent was used in the printing liquid of the mixture, only RC 711 was actually polymerised and formed the material in the printed octet structure. Differently from printing the mixture with DLP, where H44 was entrapped in the polymerised acrylate-network of RC 711, H44 was part of the liquid resin but not of the solid structure, thus not contributing to the reduction in shrinkage. Curiously, it seems that, although the secondary polysiloxane was not part of the printed structure, the solvent was in fact part of the network. The smaller dimensions in printed and pyrolysed condition of the octet, fabricated from the physical blend, show the drying shrinkage associated with the loss of toluene (Figure 19B), and is remarkably close to the value of this particular blend (15 % drying shrinkage in 2PL in contrast to 13 % in DLP for blend of RC 711/H44 = 5/5). It seems that the small molecules of toluene can still be entrapped in the sub-μm sized features, whereas the H44 phase is somehow expelled from the miniscule struts of 1.8 μm thickness in printed condition.
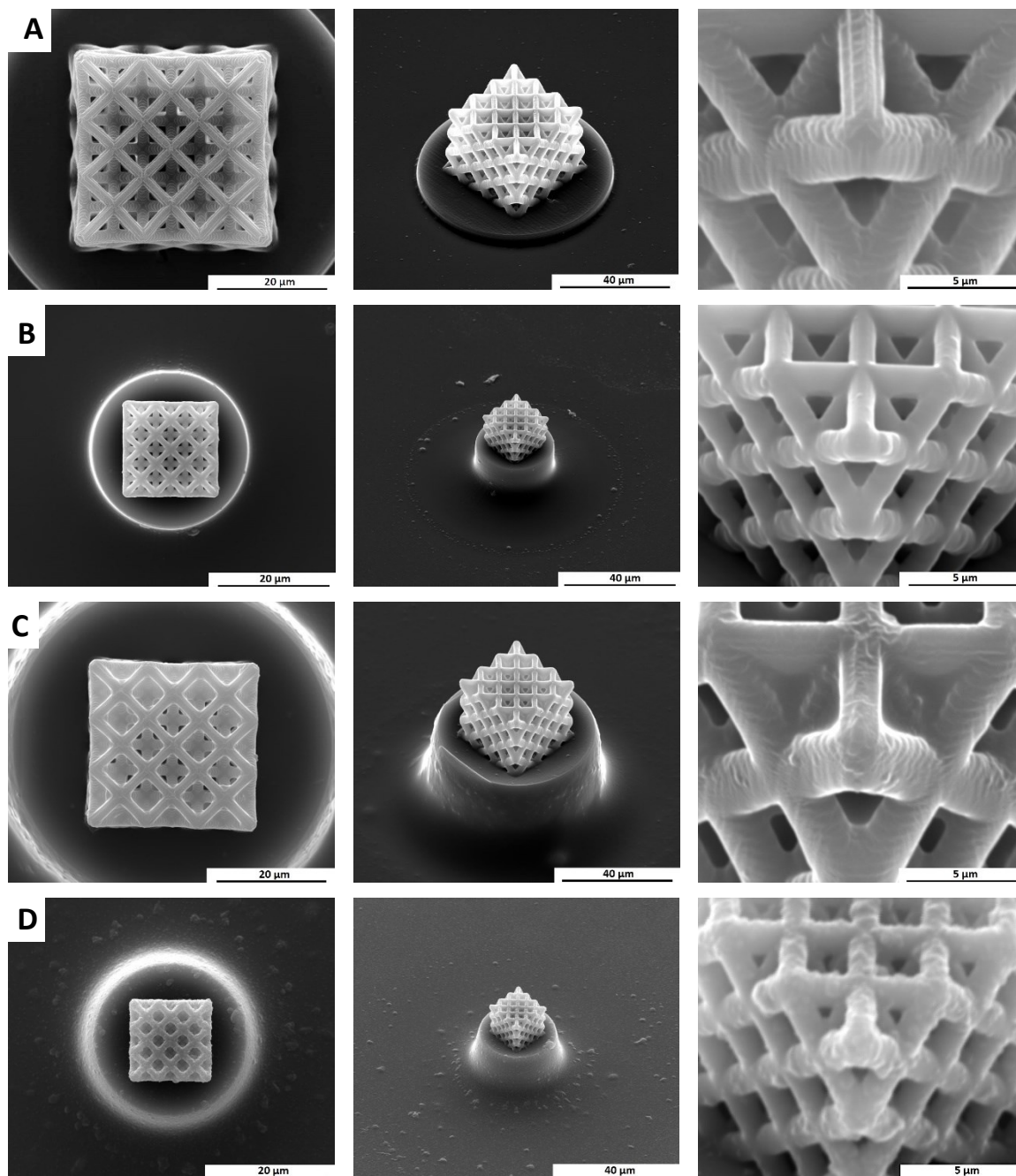
Figure 44 Octet structure fabricated with RC 711 (printed (A) and pyrolysed (B) condition) and with RC 711/H44 = 5/5 (printed (C) and pyrolysed (D) condition) shown with same magnification.

Despite the fact that, apparently, a mixture of RC 711 with additional toluene can be printed and the solvent be trapped inside the printed structure, resulting in even smaller dimensions after pyrolysis (around 15 %), this is not a way to further push the resolution limit, since first of all features smaller than in the octet structure were not able to be printed with the physical blend (see attempts to print Kelvin cell and diamond structures in Figure S11) and, secondly, the print quality after pyrolysis was quite poorly. The octet struts in Figure 44D certainly show the retention of shape after pyrolysis, but irregular and rough surfaces can be observed, compared to the smooth pyrolysed features of pure RC 711 (Figure 44B).

It is possible that in printing larger sized areas, e.g. in bulk samples like a rectangular bar, H44 could be entrapped by the polymerised RC 711 network, since in the stagnant printing liquid it cannot be expelled from the polymerised lines over a "long" distance. However, since the objective was to print highly complex SiOC structures, with a varying degree of shrinkages, ceramic yield, carbon content etc., and the 2PL printing technique was applied to push the printing resolution further than it is possible with DLP systems, limiting oneself to simple, bulk shapes with no intricate features was opposed to this aim, and therefore not further pursued.

4.8 Conclusion

It was demonstrated that the chosen polysiloxane RC 711 can be printed using the 2PL technique, manufacturing highly complicated structures in the μm range. Remarkably, shape complexity and fine features of stl-files were reproduced for even complex, small scale structures, producing features with sizes down to about 800 nm. The resolution, structural complexity and fabrication speed are comparable to that of the polymeric standard photoresists develop from Nanoscribe itself, making it a competitive material. Although the shape deformation of the printing voxel is larger in the polysiloxane, since the optical properties of RC 711 were not optimised for 2PL, the additional shrinkage upon pyrolysis compensates for the enlarged printing voxel. Unfortunately, it was not possible to print, with the 2PL technique, the physical blend mixtures developed for DLP printing system but, since the purpose of using 2PL is to print minimal features in small structures, a high shrinkage, like the one of RC 711, is actual of advantage since it further pushes the resolution limit in the final ceramic component.

It was possible to obtain, from printed RC 711 structures, fully ceramized final shapes with height of a few μm, sacrificing part of the size of the building envelope in the z-direction for support structures to compensate the anchorage to the glass substrate. At the same time, the fabrication depth was dramatically increased by using the newly developed, non-standard printing configuration, as the shadowing effect, which occurs in the standard printing configuration, was eliminated. This allowed to print up to the maximum thickness of 0.1 mm, permitted by this optical set-up, preserving submicron feature details and therefore broadening possible exploitation fields in different technological applications. It is noteworthy that the ceramic SiOC structures, generated after pyrolysis at 1000 °C, are dense, pore- and crack-free and show a homogenous shrinkage with complete shape retention after pyrolysis on their support structure, despite a mass loss larger than 90 %. The polysiloxane, together with the new printing configuration and careful selection of writing parameters produced SiOC ceramics, which outperform currently existing ceramic microstructures in their achievable complexity [49, 64, 65, 88] and the fact that the end-product is a dense (not hollow)[83, 86, 87] ceramic (not glassy carbon)[85] material, which is fully ceramised at 1000 °C.[49, 64, 65, 88]

The availability of ceramic sub-micron shapes with these characteristics can open up new breakthrough opportunities in different fields, where their superior mechanical, thermal and chemical resistance properties allow ceramics to outperform current materials. Just to give some examples, microneedle arrays for transdermal delivery of pharmacologic agents would benefit from the high stiffness and bioinertness of SiOC ceramics, while it would be advantageous to have micro nozzles with improved wear and chemical resistance and better dimensional stability with varying temper-

ature in applications where precisely mixing or dispensing gases or liquids is required. Other examples include components for microfluidics and NEMS or MEMS operating in harsh environments, especially since the mechanical properties exceeds those of natural and technical cellular solids and outperforms other existing micro-architected lattices,[83, 85, 91-93] making the 2PL printed SiOC ceramic a promising candidate for micro-mechanical applications.

5 Hybridization of Lithography-based Technologies for the Fabrication of Multiscale SiOC Ceramic Components

In chapter 3 and 4, developed materials and fabrication techniques to successfully fabricate SiOC ceramics both at the macroscale (DLP) as well as at the microscale (2PL) were introduced. Complex structures with either overall cm-sized dimensions or minimum feature sizes of 800 nm were produced by using a photocurable preceramic polysiloxane (RC 711). Both techniques exhibited certain drawbacks, which are inherent of their respective lithography-based technologies, therefore producing SiOC ceramics with either a limited minimum ceramic resolution of 30 µm (chapter 3.1.4.2), or samples with restricted overall dimensions of around 300 x 300 x 100 µm^3, which remain attached to their glass substrate (chapter 4). A novel approach to fabricate SiOC ceramic structures with a wide range of feature sizes and overall macro-dimensions by additive manufacturing was developed in collaboration with Martin Schwentenwein (Lithoz GmbH, Vienna), as well as Professor Brusatin and Dr. Laura Brigo (DII, University of Padova) and will be partially published.[97] By combining 3D macro-stereolithography (DLP) with 2-photon-lithography (2PL), cm-sized sample geometries with sub-µm surface features were achieved. In this way, the size limitation of 3D-DLP printers can be overcome realizing structures with features well below their resolution limit. Moreover, ceramic patterns in the sub-µm scale can be realized on easily handleable macro-sized samples of the same ceramic composition, freeing 2PL structures from the, until now, unavoidable glass substrates employed in 2PL printing. The hybridisation of lithography-based technologies to fabricate polymer-derived-ceramic components, structured across several length scales and pyrolysed at 1000 °C to obtain dense SiOC ceramics with homogenous shrinkage, is reported here for the first time.

5.1 Limitations of 2PL Produced Ceramic Micro-Structures

Continuing developments in engineering opened up new demands for small-scale functional systems with high degree of complexity. 2-photon-lithography (2PL) enables the fabrication of structures with feature sizes below the micrometre, and has been used to print polymeric micro-structures for use in micromechanical systems, microfluidic devices, micro-optical components, photonic crystals, biomedical devices or scaffolds for tissue engineering.[30, 33, 36, 98-102] The possibility of manufacturing ceramic structures with sub-micrometre features, via 2PL,[49, 64, 65, 83-88] enables these components to exploit the characteristics typical of ceramic materials, such as superior mechanical properties, chemical and thermal resistance with respect to polymers. For example, the danger to break microneedles during skin penetration would be considerably lowered if using a ceramic material with high stiffness and hardness. Furthermore, the chemical and thermal resistance of ceramics would be of advantage in micro nozzles for dispensing gases or liquids, as well as in nano electro-mechanical systems (NEMS) or micro electro-mechanical systems (MEMS) operating in aggressive environments at high temperatures.

2PL has the unchallenged possibility to fabricate micro-components with ultra-high structuring precision in all spatial directions, with extremely high resolution below the micrometre. However, an inevitable part of 2PL processing is that structures are written on top of substrates, which constitute the building platforms of 2PL. Substrates are mainly glass slides, but can also be printed circuit boards or silicon wafers.[36] The presence of the substrate hinders the shrinkage of the fabricated components, as they are fixed on top of the glass slide anchoring the structure to it. For polymeric materials the shrinkage is minimal, as it only originates from the higher mass density of the solid phase with respect to the liquid phase, and it can be avoided or limited by pre-compensation[103] of the designed stl-file or by mechanical stabilisation through a surrounding massive frame.[33] For ceramics, however, the shrinkage originating from sintering or, in this case, the polymer-to-ceramic transformation upon pyrolysis, is significant. While Pham et al. tried to compensate the shrinkage through the addition of silica nanoparticles, with some detrimental consequence to the resolution,[65] others proposed to control it using support structures, fabricated using the same material, to decouple the structures from the substrate.[84, 85, 88] However, even though it is possible to largely accommodate the shrinkage in these ways, both polymeric or ceramic structures remain fixed on top of the glass substrate, as the controlled and undamaged removal of the micro-structures is extremely difficult, due to their minimal size. While structures fabricated with 2PL show the design and resolution needed for their intended purpose, like micro-optical elements, photonic crystals, microstructures for tissue engineering or microneedles,[30, 33, 36, 100-102] their actual use for different applications is restricted as they can hardly be freed from their substrates. Since the intended structures are not able to be formed with one fabrication technology alone, DLP lacking the resolution

and 2PL the required parts dimension and free-standing ability, a hybridisation of both processes was tested to combine the advantages of both techniques within one component.

5.2 Hybrid Additive Manufacturing Processes

Additive manufacturing is like any other manufacturing technique, where the different 3D printing processes have certain advantages and disadvantages. Depending on the application and therefore on the required geometry, dimensions, surface quality, material etc. of the desired part, the available techniques are compared in a competitive manner and the most suitable one selected. Unfortunately, while the selected technique can exhibit the necessary requirements, drawbacks are still existing which will limit the performance of the produced parts. Furthermore, structures with certain features and properties are sometimes needed which cannot be produced by an individual manufacturing technique alone. Hybrid fabrication processes are representing a complementary approach by combining, either in parallel or in series, two different manufacturing processes together, which enables the production of structures with new design possibilities and features of two different manufacturing techniques.[104-118]

Hybrid additive manufacturing processes, in particular, are defined as combining additive manufacturing with one or more secondary process or energy source which are synergistically coupled to enhance part quality, functionality and performance of part and/or process.[104] Up to now, these secondary processes often represent the combination with coupled subtractive machining,[104-107] but can also be combined with other additive manufacturing processes like 2D-nano electron-beam lithography[108] or 3D Direct-Ink-Writing (DIW)[109-112] or secondary energy sources like induction heating[104, 113] or laser-assisted melting.[114] The combination of the two processes are typically applied cyclically, rather than simultaneously, and often do not influence the primary manufacturing process, as the focus is to enhance the functionality of the part and not the manufacturing process itself.[104] The layer-by-layer building nature of additive manufacturing allows for the secondary processes to access the entire build volume of the part, while pausing the 3D printing process, to build or alter, for example, internal embedded features and not only the external surface area, in contrast to post-production machining.[111, 115, 116]

Hybrid (additive) manufacturing has to be separated from hybrid machines, which combine more than one manufacturing process in one machine platform, like the one from DMG MORI SEIKI AG or WFL Millturn GmbH&Co.KG combining laser metal deposition (LMD) with milling or drilling,[117] as hybrid processes refer to the combined process and not the machine platform itself.[104] In hybrid multi-material fabrication[119, 120] two or more materials are fabricated together in one product to fabricate composites, sandwiches, lattices and segmented structures with enhanced functionality by one manufacturing technique (see fabricated examples of multi-material structures produced via DLP in Figure S12). Different to this, hybrid fabrication processes can employ different materials[108-112, 115] but do not have to, as per definition the focus is on the technology combination to

obtain new properties not on material combinations.[104, 114] Via hybrid manufacturing, the advantages of the individual processes are combined and mutually enhanced while overcoming their limitations, resulting in a part that is unachievable by the individual processes. This allows hybridisation to, for example, further reduce available feature sizes, increasing the available resolution of the additive manufacturing techniques,[108] or to obtain parts with better dimensional accuracy and different surface quality.[104-107, 114]

One of the first examples of combining two additive manufacturing techniques with one another was shown by Palmer et al.[110] in the production of electrical interconnects via the combination of DIW and stereolithography. Others followed the example of Palmer, and combined stereolithography techniques (SLA and DLP) with 3D direct-ink-writing to produce embedded electronics and interconnects.[109, 112, 115] Two other additive manufacturing techniques, namely direct-laser-writing (DLW) and electron-beam lithography (EBL) have been combined by Staude et al.[108] to produce 3D metal nanostructures for plasmonic applications with features sizes below 100 nm, not achievable by DLW.

In the following, a new hybrid fabrication approach of two lithography-based technologies for the fabrication of multiscale ceramic components is for the first time reported, by combining Digital Light Processing (DLP) with two-photon lithography (2PL). Ceramic SiOC structures were fabricated in the mm-range size, for easy handling, possessing also features in the sub-µm range, which are impossible to manufacture by stereolithography alone. This complementary combination of the two previously explored (chapter 3 and 4) additive manufacturing techniques, that is their hybridisation, enabled to completely free the micro-structures from a flat glass substrate and, at the same time, eliminated the need to fabricate support structures to accommodate shrinkage during pyrolysis, when processing the same material with both manufacturing techniques. Low viscosity preceramic polymers, which can be converted into ceramic materials by pyrolysis, are ideal precursor materials that allow taking full advantage of polymerisation-based additive manufacturing technologies.

5.3 Hybridisation-Procedure of Lithography-based Technologies

Printable resins were prepared on the basis of photosensitive acrylate polysiloxanes to fabricate SiOC ceramic structures. Modified MK, equipped with photocurable acrylate-groups,[8] and photosensitive RC 711 were both used to fabricate structures via CeraFab 7500 DLP printer, which has a lateral resolution of 40 µm and was set at a layer height of 25 µm. Woodpile structures with dimensions of 2.25 x 2.25 x 1.00 mm^3 were printed to demonstrate the hybrid fabrication approach (see Figure 45a). Much larger components could of course be manufactured with this technology, but the size of the samples was selected in order to be able to fit the macro-sized structures in the building chamber of the 2PL equipment, which in turn can be customized.

Structure

Liquid resin

PDMS spacer
(height ~ 135 µm)

↑ 2 Photon Irradiation ↑

Glass substrate
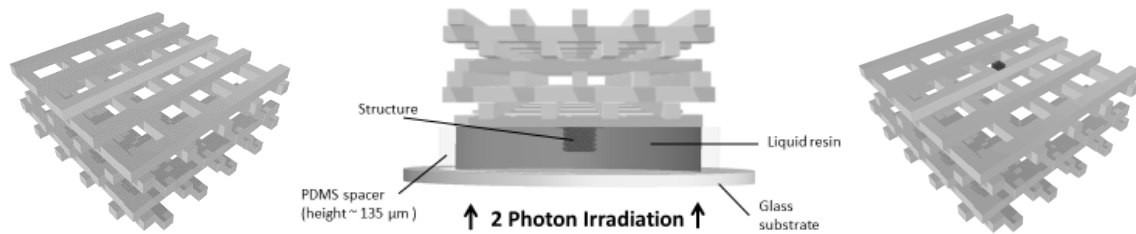
a) DLP printing: macro-sized structure with lateral resolution of 40 µm

b) 2PL printing configuration: fabrication of micro-sized structures with resolution < 1 µm on top of the macro-sized structure

c) Result of combined DLP and 2PL processes: macro-sized structure with mm-sized dimensions and sub-µm features

Figure 45 Hybridisation of stereolithography-based technologies.

After successfully printing mm-sized woodpiles with DLP, the unpolymerised printing resin was removed with diphenylether as solvent, and a structure mounted in the 2PL printer. The adjusted 2PL printing configuration can be seen in Figure 45b. The structure was placed on top of PDMS gaskets, enclosing the liquid RC 711 similar to the inverted configuration in Figure 33B. The 2-photon laser was focused on the liquid-solid interface of the mounted woodpile and then shifted a few layers above said interface, within the already printed macro-sized structure, to ensure that the micro-sized structures were connected to the solid woodpile rods. Small woodpiles with the same geometry, but dimensions of 90 x 90 x 40 µm^3 with rods of only 5 x 5 x 90 µm^3, well beyond the printing resolution of DLP, were printed on the macro-woodpile surfaces, and were grown from top to bottom. Detailed information about the 2PL printing procedure and its optimisation with RC 711 can be found in chapter 4. After the 2PL printing process, the micro-sized structures on top of the macro-sized structure were likewise cleaned with diphenylether, leaving behind the combined woodpiles (Figure 45c). The shape of these specific structures was selected simply with the purpose

of demonstrating a proof-of-concept, that is the manufacturing of a multi-scale, complex structure with overheads, not achievable by employing any other processing methods.

5.4 Realising SiOC Ceramic Material Structured Across Several Length Scales

Two polysiloxanes with different ceramic yields were selected to fabricate via DLP woodpiles with dimensions well above the possible printing volume of 2PL (maximum volume of 300 x 300 x 300 μm^3 with high resolution, in Piezo-Scan-Mode).[36] Modified-MK represents a material with a high ceramic yield of 51.4 wt%[8] while RC 711 only provides a ceramic yield of 7.4 wt% (see Figure 18), due to its different molecular architecture. Differently from RC 711, modified-MK proved to be unsuitable for additive manufacturing with 2PL, because of its extremely narrow processing window and the lack of selectivity of tested developers. Therefore, it was used, together with RC 711, only to fabricate structures via DLP. The surfaces of both macro-sized woodpiles, produced with modified MK and RC 711, were structured by 2PL 3D printing using RC 711.

The successful combination of DLP and 2PL printing technologies can be seen in Figure 46. In both cases, 2PL printed woodpiles were fabricated exactly in the middle of the macro-rods (modified-MK, Figure 46A; RC 711, Figure 46B) and precisely positioned to be aligned along the main axis of the rods. The SEM pictures show no sign of detachment of the microstructures and a good surface integration and adhesion in the green (unpyrolysed) state. The 2PL printed woodpiles remained well connected to the polysiloxane macro-rods during the whole handling of the combined woodpiles, the second cleaning process and SEM imaging. This demonstrates the very stable combination of the two polysiloxanes, which were printed with the two different lithography techniques. The advantages of DLP and 2PL printing were therefore combined, generating resolved features with sizes down to 5 µm, that in principle can be pushed down to the sub-micrometre range (see chapter 4.6), and dimensions in the mm-range, therefore with morphological features not achievable employing a single additive manufacturing technique. Furthermore, this combination makes the use of glass substrates redundant, enabling the fabrication on the same type of material, previously printed at the macro-scale via DLP.
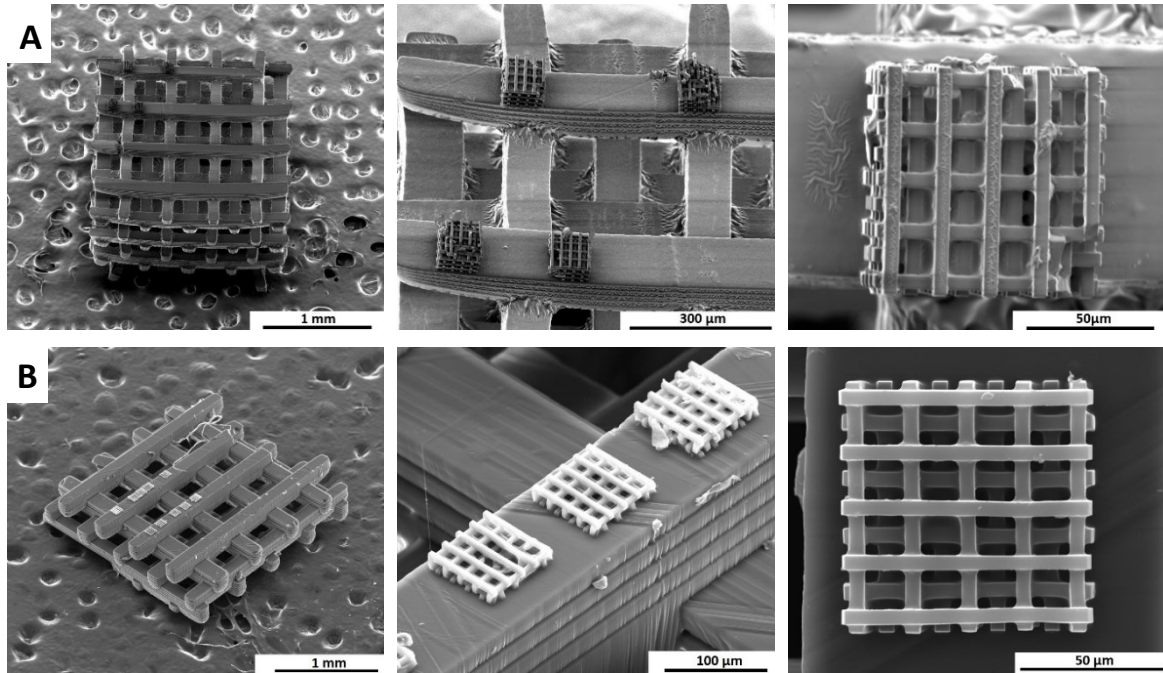
Figure 46 Printed Hybrid-structures: Combination of DLP and 2PL lithography technologies; RC 711 micro-structures on modified-MK (A) and RC 711 (B) macro-woodpiles.

After the printing procedure, both multi-scale woodpiles were converted into SiOC ceramics, by pyrolysis at 1000 °C in nitrogen (Figure 47, 48). Since both materials, modified-MK and RC 711, are preceramic polysiloxanes they have the same temperature treatment, eliminating possible challenges regarding e.g. sintering temperature or atmosphere, which would be faced if different materials would be combined.[120]

Firstly, it is evident from Figure 48 that, in both cases, the overall macro-woodpile structures shrunk homogenously and completely retained their shape. Additionally, the micro-sized woodpiles, fabricated with RC 711, remained strongly connected to both the modified-MK and RC 711 macro-sized structures throughout the entire pyrolysis process. There was no detachment of the microstructures, even when the two combined polysiloxane materials were not the same (Figure 48A). It is worth observing that they even remained attached and well adherent in their original position, despite the shrinkage mismatch and therefore the additional mechanical stress generated on the micro-sized structures during pyrolysis. The 45 % difference in shrinkage between modified-MK (25 % linear shrinkage)[8] and RC 711 (70.4 % linear shrinkage in Figure 19B) caused the inhomogeneous shrinkage of the RC 711 microstructures on top of the modified-MK macro-sized woodpile, observable in Figure 47, leading to their deformation after pyrolysis. A similar effect of constrained/differential shrinkage was obviously also observed when pyrolysing structures deposited on a glass slide, showing that, if the shrinkage mismatch is not compensated through the fabrication of support structures or the presence of fillers, a significant distortion of the printed structures occurs (see Figure 37).[65, 84, 85, 88] This detrimental effect can be limited in the same way as for the production

of ceramic microstructures produced by 2PL, by adding a supporting base structure (see Figure 38). A closer image of pyrolysed RC 711 structures on top of modified-MK woodpile with increasing woodpile height (a-c) and round base support (solid: d, scaffold: e) can be seen in Figure 47. Figure 47b and 47c demonstrate that only the lower part of the woodpile acted as the support and was affected by the differential shrinkage, allowing for the upper part to shrink homogeneously, and that one woodpile height was enough to compensate the shrinkage difference, leaving the additional woodpile section above decoupled from the shrinkage difference with modified-MK (Figure 47b). Additionally, round bases were tested, but the power concentration to fabricate a solid (Figure 47d) and densely scaffolded (Figure 47e) round support base beneath the structure proved to be too high, leading to explosions inside the printing resin due to violation of the intensity limit at the interface between solid macro-woodpile and liquid printing resin.[30] However, by using a porous support base, as it was done by increasing the height of the micro-sized woodpiles, the interaction area at the critical interface is limited, making it possible to fabricate homogenous RC 711 woodpiles on top of modified-MK, by using the lower part as support base (see Figure 48A).
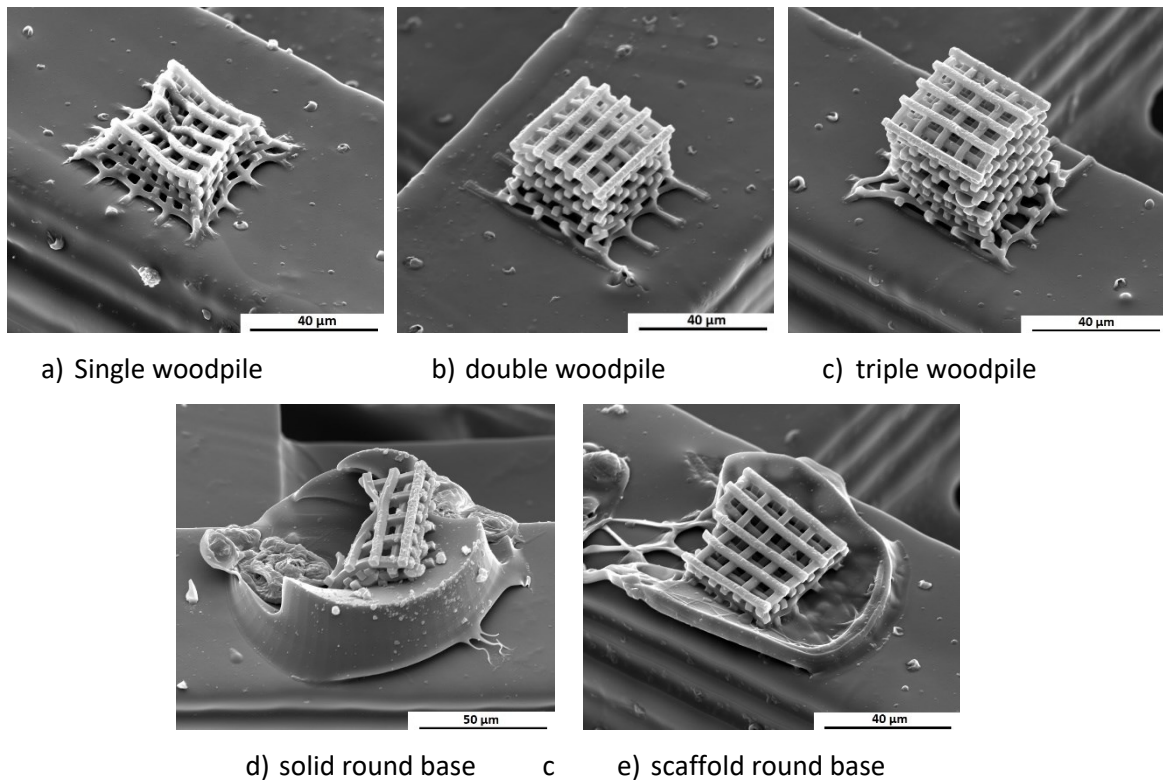

a) Single woodpile   b) double woodpile   c) triple woodpile

d) solid round base   c   e) scaffold round base

Figure 47 RC 711 woodpile structures with different support bases to accommodate the shrinkage difference on modified-MK.
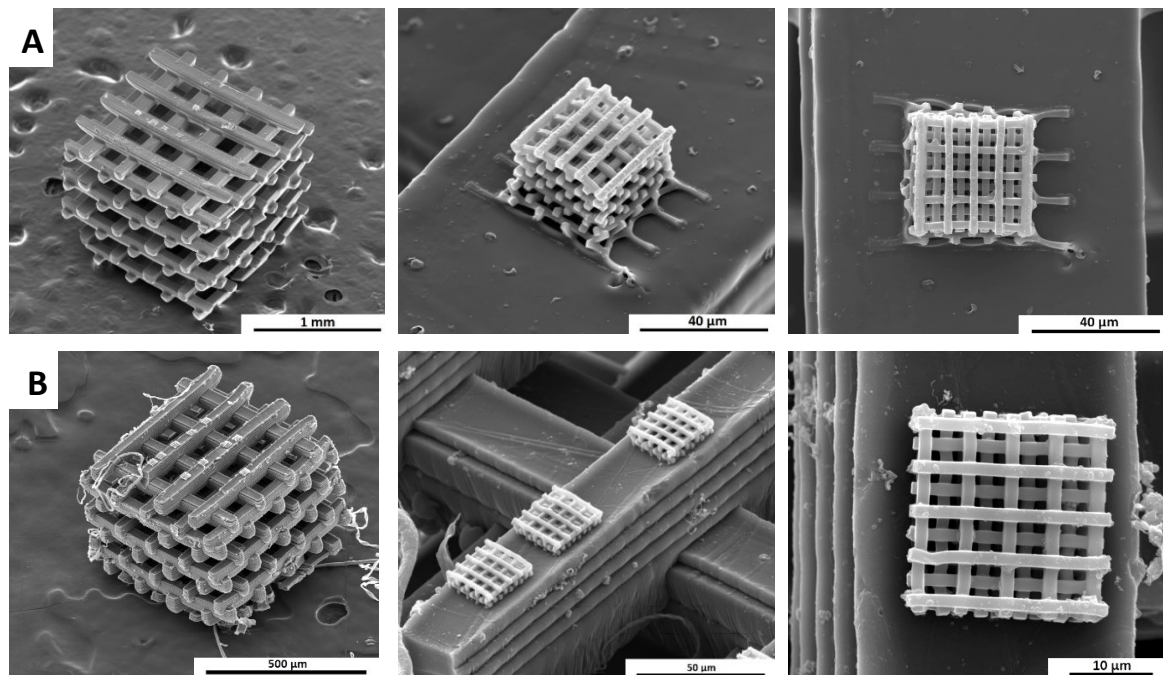
Figure 48 Pyrolysed Hybrid-structures: Combination of DLP and 2PL lithography printing; RC 711 micro-woodpiles on modified-MK (A) and RC 711 (B) macro-woodpiles.

When using the same material (RC 711) for the fabrication of both micro- and macro-sized structures, this problem did not occur, as expected. Figure 48B shows not only that no detachment of the microstructures occurred after pyrolysis, but that it was also possible to obtain a completely homogenous shrinkage throughout the whole combined component, as both structures were printed with the same material, having therefore the same shrinkage upon pyrolysis. This demonstrates that, if no support structures are desired, any shrinkage mismatch between the macro- and micro-sized object could be avoided by using the same material for DLP and 2PL printing. Moreover, if a material is verified to be printable with both DLP and 2PL techniques, any dimensional change after 2PL printing but before pyrolysis, e.g. due to drying/evaporation of volatile solvents after DLP printing (as it occurs also in the physical blends, see Figure 19B), could be prevented by adopting solventless solutions, or high boiling, slow-evaporating solvents. Since printed RC 711 has a negligible shrinkage of 1.7 % compared to the stl-file, which only originates from the liquid-to-solid transition[21, 33, 71, 103] of the preceramic polymer, and is also printable with both lithography-technologies, it presents an ideal candidate for hybrid additive manufacturing combining DLP and 2PL 3D printing.

In both cases, the combined polysiloxane components were successfully transformed into ceramics, leading to SiOC macro-sized structures whose surface was modified by the presence of SiOC micro-sized structures built on it, with ceramized strut sizes with a size of 1.4 µm. The macro-sized woodpiles allowed for the handling of the combined structures, avoiding the use of glass substrates, and enabled the fabrication of microstructures on top of the same material, leading to components with

a homogenous composition. The possible combination of lithography-based additive manufacturing technologies was demonstrated using woodpile structures. Since both fabrication techniques permit the fabrication of much more complex geometries (see chapters 3 and 4) the range of possibilities can be extended further. By combining DLP and 2PL printing, structures made of a bioinert, ceramic material with mm dimensions and sub-μm surface features free of any substrates or additional support structures can be manufactured for potential use, among others, as micro-needles, micro-nozzles or MEMS.

5.5   Conclusion

Digital Light Processing and 2-photon-lithography techniques were combined to realize a SiOC ceramic component structured in three dimensions across several length scales, starting from preceramic polymers. Woodpile structures with overall dimensions in the mm-range were manufactured with a DLP printer using modified-MK and photosensitive RC 711 polysiloxanes. Afterwards, the samples were mounted in a 2PL printer and their surface was additionally structured with RC 711, to fabricate features in the μm range. After pyrolysis, the shrinkage mismatch between modified-MK and RC 711 could be controlled only when structures of adequate height were fabricated, while employing the same material (RC 711) for both the macro-sized and micro-sized components led to a uniform, homogenous shrinkage of the overall sample, with no distortions. After pyrolysis, a dense and crack-free SiOC ceramic multi-scale component was obtained, with no detachment of the microstructures from the macro-woodpiles throughout the whole fabrication process and heat treatment. Due to the size of the sample produced by DLP, the combined sample was easy to handle and allowed for the elimination of the flat glass substrate usually needed for 2PL printing. The use of 2PL enabled the fabrication of precisely positioned microstructures on top of the macrostructure, with features in a size range well beyond the resolution limit of the DLP technology. The hybridisation of vat polymerisation-based additive manufacturing technologies and the use of preceramic polymers, therefore, is a suitable approach for the manufacturing of highly complex structures that can be designed at multiple length scales, and combined with each other to produce hierarchically structured ceramic components.

6 Exploitation of Multi-Functionality of Preceramic Polymers: Mullite Structures from Alumina Filled Polysiloxane

By taking advantage of the multi-functional properties of preceramic polymers, their transformation into ceramic material at low sintering temperatures and the processing capabilities of polymer manufacturing processes, mullite components were fabricated by additive manufacturing.

Up to now, high ceramic yield preceramic polysiloxanes were added to a photocurable siloxane in a physical blend to change the ceramic yield, shrinkage, final resolution and free-carbon content of pure SiOC ceramics after pyrolysis. In doing so, the secondary preceramic polymers are playing the role of passive fillers, which are contributing to the ceramic through their non-sacrificial decomposition. In the following work, which was developed in collaboration with Martin Schwentenwein (Lithoz GmbH, Vienna), and is partially published in,[121] alumina particles are added to the same preceramic polymer RC 711 as active fillers and the solution was shaped into complex structures via Digital Light Processing. Differently from passive fillers, they chemically react with the silica source, that a polysiloxane produces upon sintering in air, and modify therefore the composition of the produced ceramic material in creating mullite as new ceramic phase. Normally, glass and ceramic particles of the desired composition have to be produced first, before they are used in various forming processes. By using the preceramic photosensitive RC 711, the manufacturing procedures to fabricate the ceramic composition and the shaping of the part are combined into one step. Via DLP printing, the photosensitive RC 711 is shaped in the desired structure, incorporating the ceramic particles, suspended in the printing resins, and reacts with them upon sintering in air to form the targeted ceramic phase. Dense and crack-free, highly complex porous mullite ceramics were produced by firing a mixture of a commercially available photosensitive polysiloxane as the silica source, containing alumina powder as active filler, in air at a low sintering temperature (1300 °C).

6.1 Production of Mullite over the Preceramic Polymer Route

Mullite ceramics are of interest for technological applications in areas such as electronics and optics, as well as in high temperature structural components because of their favourable thermal, electrical and mechanical properties.[122-124] For instance, mullite ($3Al_2O_3 \cdot 2SiO_2$) has applications in electrical insulations, due to its low electrical conductivity and low dielectric constant. The high refractoriness of mullite, its low thermal expansion coefficient and subsequent high thermal shock resistance, its high deformation and creep resistance and its durability at high temperatures exceed those of most other metal oxide compounds, making it an ideal ceramic refractory material.[123, 125, 126] Porous mullite structures with suitable amounts of porosity, mechanical strength, permeability, cell size and cell size distribution etc. find their use in areas such as hot gas and molten metal filter applications.[126-128]

Mullite rarely occurs as a natural material, but can typically be fabricated through the reaction sintering of kaolinitic clays with alumina powders at high temperatures,[123, 129, 130] or by heating alumina/silica mixtures in stoichiometric proportions. Synthesis methods for mullite include sol-gel processing,[131-139] co-precipitation,[140] chemical vapor deposition[141] and the sintering of silica-coated alumina powders.[142-144] Recently, a new method was proposed to obtain mullite from the reaction of a preceramic polymer which transforms into a highly reactive silica source upon heat treatment, with Al_2O_3 and/or Al particles.[55, 125, 145-152] This creates a way to fabricate mullite components that is easier than sol-gel processing, where a strict control of the synthesis condition is required, while also providing the benefits of a molecular synthesis approach.[55, 125, 149, 150] The multi-functionality of preceramic polymers – that is, their transformation into a silica source (polymer-derived-ceramic) during sintering in air and the possibility of using any available polymer manufacturing processes (e.g., extrusion, spinning, cold or warm pressing, injection molding, foaming, additive manufacturing) to shape the material – makes this method attractive in terms of processing mullite ceramics with very complex structures. Furthermore, this method can yield phase pure mullite at low processing temperatures.

Until now, highly diluted solutions containing alumina powder and preceramic polysiloxanes dissolved in solvents were prepared to achieve a homogenous mixture of the silica and alumina sources.[55, 125, 147-150] The mixtures were subsequently dried by removing the solvent, and the resulting powder mixture was then cold pressed into monolithic samples.[125, 147-152] Further advances in other polymer shaping processes were achieved by using self-foaming with thermal crosslinking,[145] sacrificial foaming,[146] filament extrusion, injection molding or coating.[55] However, the potential of using additive manufacturing processes to fabricate mullite components with highly complex architectures by the preceramic polymer route had not yet been exploited.

For the first time, the use of digital light processing (DLP), a lithography-based additive manufacturing technique, is presented here to fabricate porous mullite structures from a mixture of alumina powder with the commercially available photosensitive polysiloxane, RC 711. The possibility of shaping photosensitive preceramic polymers via stereolithography and digital light processing into ceramic material by pyrolysis in nitrogen was already successfully demonstrated in the previous chapters yielding dense and crack-free SiOC parts possessing complicated geometrical morphologies, which are only realisable via stereolithography. Additive manufacturing represents a way to easily control the overall microstructure (cell morphology, size and distribution, strut thickness and connectivity), which directly impacts the properties of the component, such as permeability, porosity and mechanical properties. This therefore enables the designed structure to perform its desired functions in a particular application, for example, to meet stringent requirements in filter designs.[126, 127]

6.2 Formulation and Thermal Characterisation of Mullite Printing Resins

When pyrolysed in inert atmosphere RC 711 converts to a silicon oxycarbide (SiOC) ceramic with a ceramic yield of 7.4 wt% (see Figure 17). However, when heated in air, it transforms into silica (SiO_2) with a ceramic yield of 31.8 wt% (Figure 49). Two alumina powders with different particle sizes were reacted during firing with the silica source deriving from the preceramic polymer and thus forming mullite. The ratio between the RC 711 and the Al_2O_3 powders was determined from the molar composition of mullite and the ceramic yield of RC 711 in air and was adjusted with XRD characterisation for the micrometre-sized alumina mixture to develop mullite without SiO_2 surplus (see later Figure 51). Table 12 lists the constituents of the three developed printing formulations, with nano- or micro-sized alumina particles. The weight ratio between the solvent phenoxyethanol (POE) and the alumina powder was optimised to obtain a viscosity suitable for DLP printing, while the weight ratio between RC 711 polysiloxane and the alumina powder was calculated according to stoichiometric proportion (for both particle sizes), and optimised according to XRD data (for the micro-alumina mixture).

Table 12 Weight percentage of components in the nano- and micro-alumina printing formulations.

	Nano-sized alumina (stochiometric), wt%	Micro-sized alumina (stochiometric), wt%	Micro-sized alumina (XRD optimised), wt%
RC 711	14.2	28.5	21.5
Al_2O_3	11.4	23.1	25.3
POE	74.4	48.5	53.2
Weight ratio POE/Al_2O_3	6.5	2.1	2.1

As was previously mentioned, preceramic polymers can play a multi-functional role in the fabrication of a ceramic component, not just by providing a highly reactive silica source upon firing in air at low temperatures, but also by enabling the use of polymeric shaping processes. In order to employ DLP additive manufacturing, preceramic polymers containing specific photocurable functional groups are needed, e.g. acrylate, vinyl or epoxy groups. Commercially available photosensitive preceramic polysiloxanes typically possess either a high ceramic yield but the requirement of a UV exposure time of several minutes,[11, 61, 62] therefore making them suitable for soft-lithography but inapplicable for 3D printing via stereolithography, or they have a low ceramic yield but a high reactivity, suitable for DLP printing, like the selected RC 711 (see chapter 3.1). For every polymer shaping process, the amount of preceramic polymer present has to be sufficiently high to enable the use of the selected plastic forming technology. Previously, preceramic polysiloxanes with a high ceramic yield of greater than 84 wt%[125, 146-152] were used to prepare mullite, in combination with alumina

nano-powder. As the dried mixtures were mainly processed by cold or warm pressing,[125, 147-152] the pre-set amount of reactive filler powders, determined by the stoichiometric requirements, was appropriate for those shaping technologies. The commercially available photosensitive siloxane used in these experiments (RC 711), on the other hand, has a very low ceramic yield of only 31.8 wt% in air. This characteristic of the precursor, while usually being detrimental as it results in a high shrinkage and a high burn-out during pyrolysis and thus leads to micro-crack development in the samples, is in fact advantageous here, as it allows a sufficient amount of photosensitive polysiloxane to be added to ensure good photocurability of the printing solution with the formation of a strong connected network upon UV exposure, while also maintaining the required ratio to develop the mullite composition.

The necessary amount of phenoxyethanol solvent to reach a viscosity suitable for printing resulted in printing solutions of equally low ceramic yields, despite the addition of alumina (Figure 49). Due to the presence of 74 wt% of solvent, the formulation containing the nano-sized alumina possessed the lowest ceramic yield of 15.2 wt%. The use of micro-sized particles enabled a reduction in solvent by more than 20 wt%, resulting in a higher ceramic yield (29.0 wt% for the stochiometric formulation and 34.1 wt% for the adjusted one). It should be noted that since the mass loss of all systems was fully completed at 550 °C, the ceramic yield remained constant for all employed sintering temperatures (1200 – 1400 °C).

The particle filled preceramic solutions had a similar decomposition behaviour to the pure RC 711. All systems showed a high initial mass loss, followed by a lower second one, where the organic burn out takes place. It is notable, that while the full completion of mass loss occurred for all samples roughly at 550 °C, the decomposition onset temperature shifted towards lower temperatures in the particle-filled mixtures. This can be attributed to the presence of residual phenoxyethanol solvent in the UV crosslinked materials, which evaporates at a temperature higher than room temperature, and possibly to the presence of the Al_2O_3 particle fillers, which can alter the crosslinking behaviour of the preceramic polymer (it should be noted that the photocurable siloxane also contains Si-OH groups).[145]
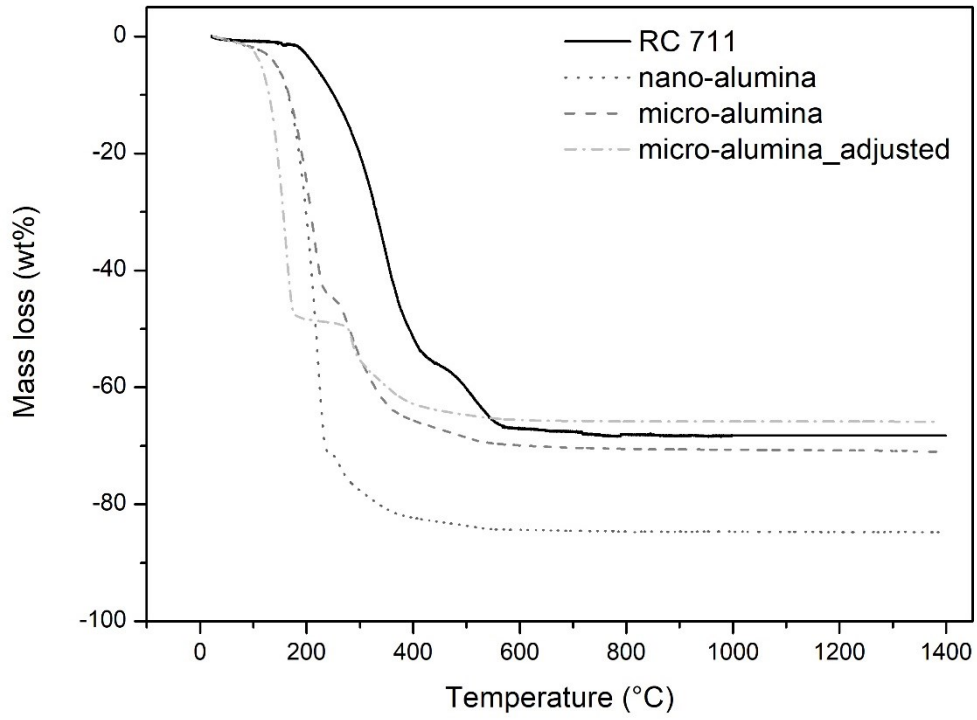
Figure 49 TGA curves of pure RC 711 and of the printing formulations, based on mixtures between the photosensitive RC 711 and nano-sized alumina as well as micro-sized alumina powder, both in the stochiometric and adjusted, silica-free, composition (all after UV-curing).

6.3 Development of Mullite through Reaction between Transformed Silica source and Alumina Fillers

The XRD analyses of the mixtures between preceramic RC 711 and the two alumina powders are shown in Figure 50 and 51. Mullite formation was confirmed in both systems, due to the high reactivity of both the transitional form of alumina powders employed (γ-alumina),[4, 26, 27, 29] with their comparatively small particle size (nm-sized or < 6 μm) and the silica deriving from the polymer-to-ceramic transformation of the polysiloxane. Indeed, the siloxane preceramic polymer decomposes during debinding, leaving behind the inorganic backbone, a highly reactive silica source,[26, 29] which starts to react with the alumina powders in both systems at a low firing temperature.

For the nanometre sized alumina filled system, pure mullite formation was observed (see Figure 50); the molecular reaction between the transformed silica source and the nm-powder started at 1300 °C and was complete within one hour of dwelling time. The mixture with micrometre sized alumina particles also reacted extensively to form mullite, starting equally at 1300 °C (see Figure 51). However, traces of alumina were still present, which thermally transformed from the initial γ-Al_2O_3 into θ-Al_2O_3 at the firing temperature in the 1200 – 1400 °C range, if previously suspended in the polysiloxane matrix. θ-Al_2O_3 formed according to the transformation sequence of alumina: $\gamma \rightarrow \delta \rightarrow \theta \rightarrow \alpha$ with progressive dehydration before the corundum phase forms.[153] The presence of θ-alumina, despite being well above its stability range of 1100 °C,[153] could be attributed to the known stabilisation reaction between hydroxyl groups of alumina powders and a silicon-containing precursor surrounding the alumina surface,[154] which, in this case, is represented by the siloxane preceramic polymer. If no such silicon precursor is present, the γ-Al_2O_3 transforms into the expected α-Al_2O_3 at the mullite formation temperature of 1300 °C (see Figure 51).

In addition to the traces of residual alumina, some cristobalite was also detected in the samples containing the micro-sized powders when the system was heated to 1400 °C. The higher firing temperature caused the crystallisation of the previously amorphous residual silica phase, indicating that the reaction was incomplete. Since the formation of mullite in the system containing the micro-sized particles started at the same temperature (1300 °C) as in the formulation containing the nano-sized ones, we can observe that the reactivity of the participants was high in both cases. However, the micro-sized alumina particles were evidently too large for a complete reaction with the silica source, and were therefore left partially unreacted at the surface of the structures (see later in Figures 55,56), along with residual silica. This excess silica, which is detrimental to the properties of the component since it generates cristobalite, was eliminated by changing the ratio between the preceramic RC 711 and the micro-sized alumina powder (see Table 12). The XRD data for this adjusted formulation fired at 1400 °C, reported in Figure 51, indicates the formation of a large amount

of mullite with no residual crystalline phase. Furthermore, the amount of residual alumina phase seems not to have increased in terms of the sample produced using a stoichiometric ratio among the reactants, suggesting that the change in formulation did not modify the portion of reacted mullite. Additional work to further increase the purity of the phase assemblage in the heat treated component produced starting from the stoichiometric formulation is currently being carried out, including firing for longer times at 1400 °C or at higher temperature.
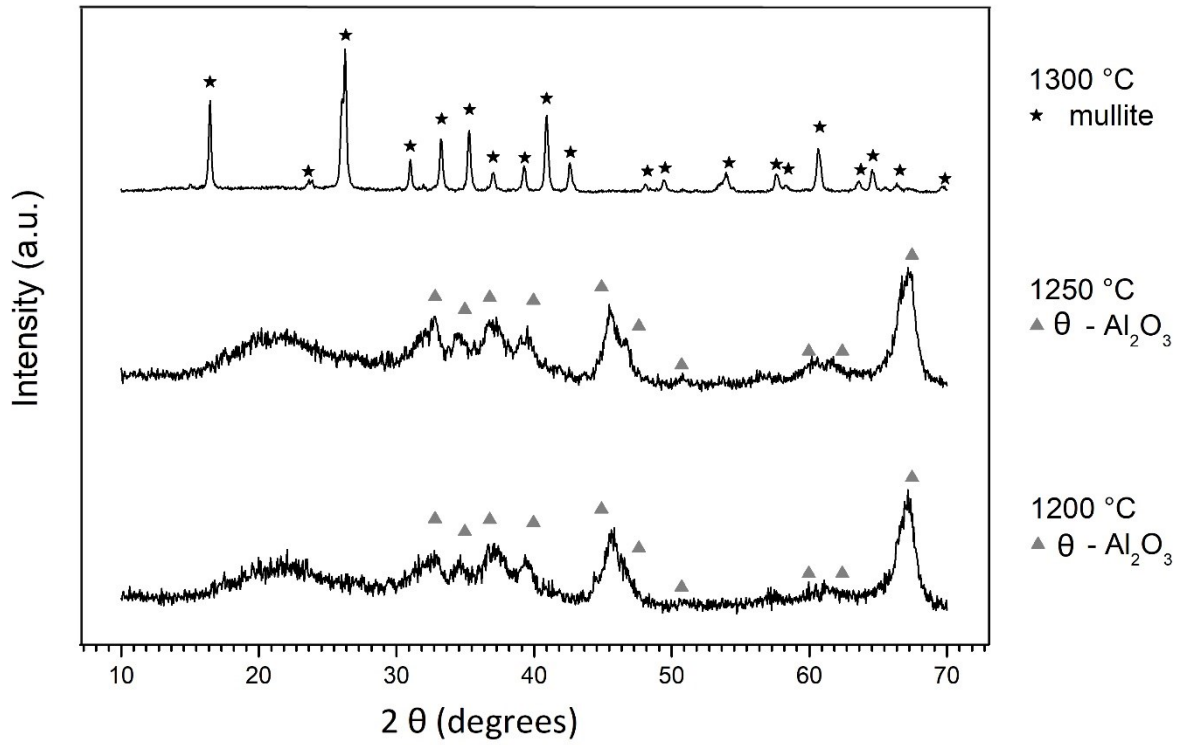
Figure 50 XRD analysis of RC 711 printing resin filled with nano-size alumina powders, heat treated at 1200-1300 °C.
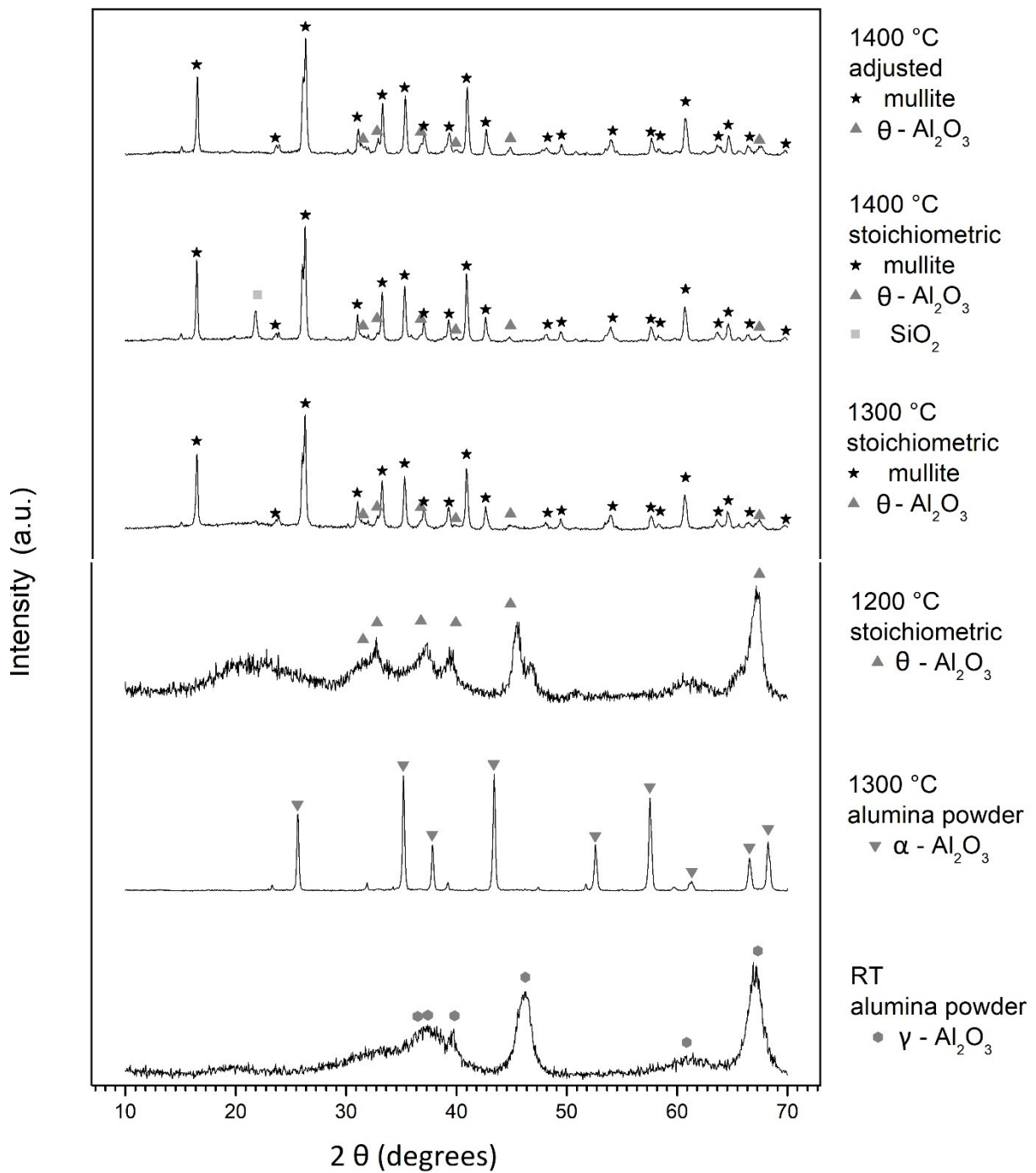
Figure 51 XRD analysis of RC 711 printing resin filled with micro-size alumina powders, heat treated at 1200-1400 °C.

6.4 Initial Printing Tests

The same illumination test using a model star shape, which was done to characterize the reactivity of the photosensitive RC 711 with different amounts of Irg 819 (see Tbale 1), was also performed for the mullite printing mixtures. It confirmed a very fast curing of the RC 7111 with a minimum exposure time of 2 s to build the star shape, with no photoabsorber present, despite the addition of alumina particles in the system. Equally, the printing tests of the complex porous structures (Figure 52) proved a very low necessary exposure time of only 6 s at a set layer height of 25 μm and with photoabsorber for control of z-resolution in the system. This exposure time falls in the range of those of the physical preceramic polymer blends (see Figure 16) and within the previously determined viable exposure time of 1 – 20 s, to produce centimetre sized components with DLP in a reasonable time period.

Initial printing tests with stochiometric mixtures of RC 711 and both alumina powders are shown in Figure 52. During 3D printing, the photosensitive polysiloxane develops the acrylate network and traps the alumina particles within the structures. A constant viscosity of the mixtures was observed during printing and this, along with the measured weight loss which coincides with the theoretical calculations, confirms that the alumina particles do not separate during the fabrication, and therefore the same amount is present in both the polymerized structure and the liquid mixtures. Although it is remarkable that the formulation containing the nano-sized alumina was able to be printed at all, considering that it had a content of only 14 wt% photosensitive polymer (see Table 12), the resolution of the manufactured part was very poor, displaying a weakly connected soft and fragile structure (see Figure 52A). After firing at 1300 °C to develop mullite, the printed component developed major cracks (Figure 52B). The large amount of solvent in the formulation (74 wt%), which is necessary to obtain a suitably low viscosity for processing, led to a system with only 15 % ceramic yield, which was not enough to prevent crack formation and structural collapse due to large shrinkage. Conversely, the system containing the micro-sized alumina powder required only one third of the solvent amount to reach suitable viscosity for printing due to the lower surface area of the reactive filler particles (Table 12). The larger amount of photosensitive RC 711 and the lower solvent content enabled the printing of well defined, accurate structures, and no cracks or structural collapse were observed after firing and mullite formation (see Figure 52C,D).
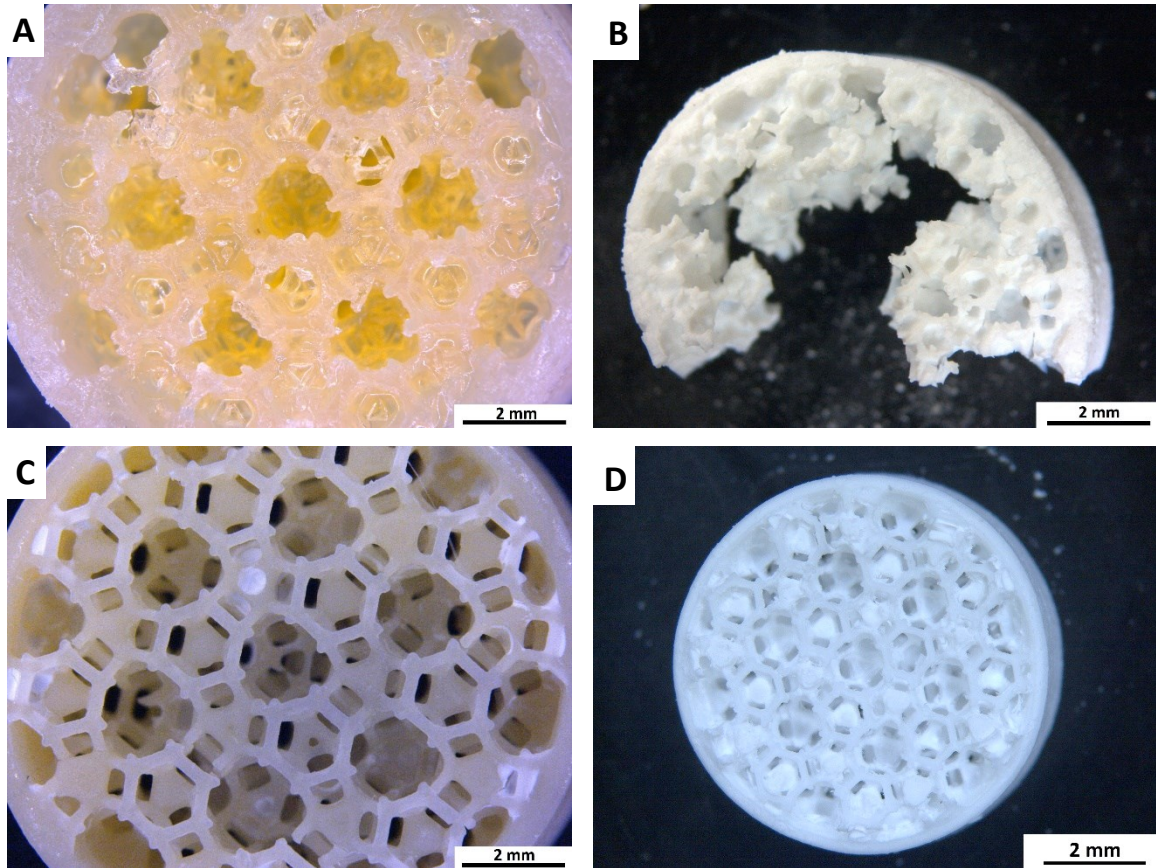
Figure 52 Ceramic filter structure fabricated with mixtures of RC 711 with nano-sized alumina before (A) and after (B) sintering at 1300 °C and with micro-sized alumina before (C) and after (D) sintering at 1300 °C (stoichiometric silica/alumina ratio (A-D)).

Although the nano-sized alumina powder allowed complete mullite formation at 1300 °C to be obtained (see Figure 50), this formulation was not optimal for printing and subsequent firing. These processing steps proved to be unproblematic for the formulation containing the micro-sized alumina particles, although the incompleteness of the reaction (in the adopted firing conditions) led to the development of a modified formulation. Subsequent experiments were carried out using micro-sized alumina powder in the adjusted ratio of RC 711/alumina = 0.85, which was determined by considering the ceramic yield of the polysiloxane, the stoichiometry of mullite and the XRD confirmation of the absence of cristobalite (see Figure 51).

6.5 Fabrication of Complex Mullite Architectures

Complex ceramic structures were printed via Digital Light Processing, forming a silica-free, mullite composition. Both porous and bulk samples were manufactured and transformed into mullite at 1300 °C, with no formation of cracks even in samples several millimetres in dimension despite the relatively low ceramic yield of the printing formulation (Figure 53).
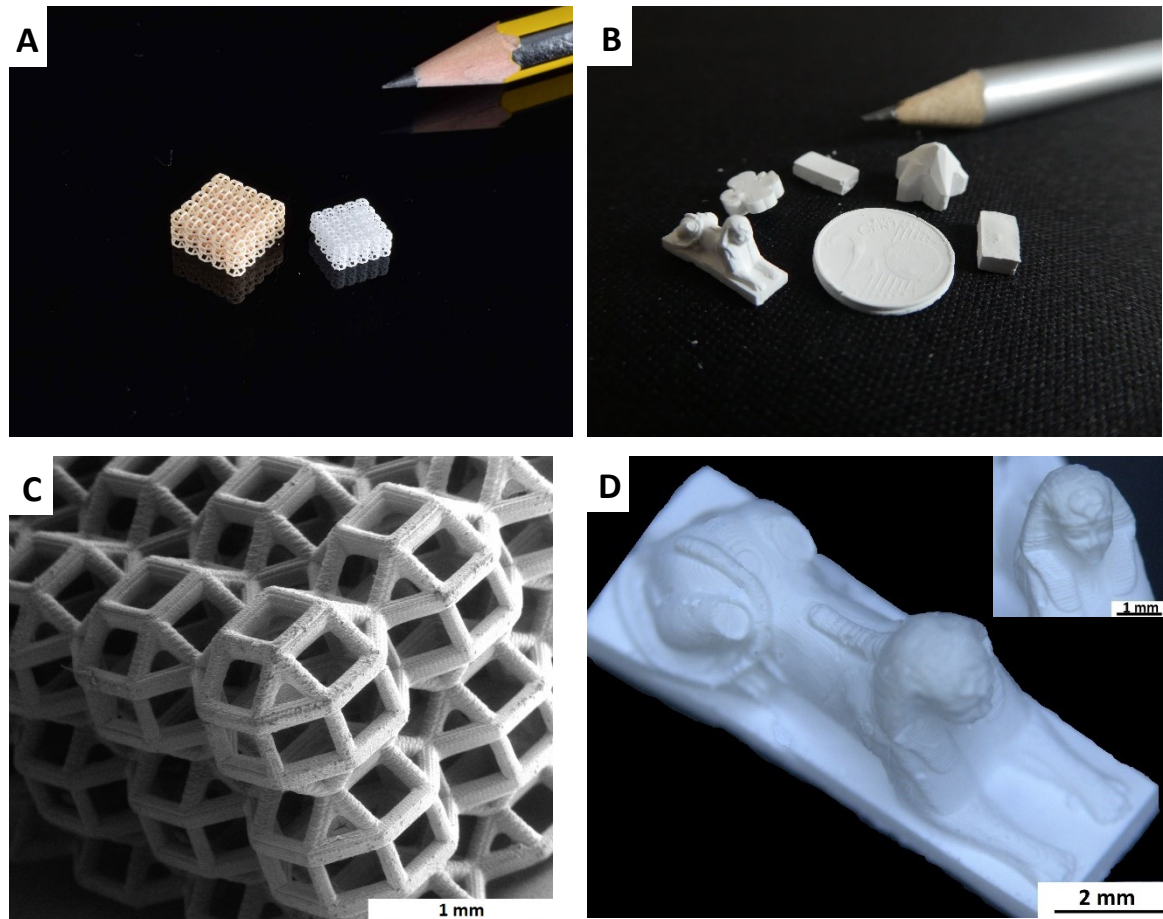
Figure 53 Images showing a complex (rhombi-cuboctahedron) porous structure before (A, left) and after (A,C) sintering, and bulk parts (after sintering (B,D)). Note: the coin in Figure 53B was manufactured by soft-lithography.

Figure 54 shows the SEM images of a highly complex porous structure, consisting of a collection of rhombi-cuboctahedron cells with eight equilateral triangles and eighteen squares, as printed and after its conversion to mullite ceramic. The structure presents an exact replica of the original stl-file, with no loss in resolution. The small difference in the refractive index between alumina and polymers generally diminishes the interactions between the light and the ceramic particles.[9, 15, 17, 20] Light scattering and absorption phenomena, which accompany the shaping via stereolithography of ceramic materials from particle filled resins, are therefore limited and seem to have no influence in this work. The struts are perfectly resolved with no rounded edges, and the discrete layers in z-

direction are visible in the printed structure due to the stepwise printing of slices in stereolithography (see Figure 55A,B). Additionally, there is no sign of delamination between the printed layers either before or after firing. After the heat treatment, the isotropic homogenous linear shrinkage of 36 % led to no observable deformation, and resulted in a complete retention of shape during the formation of the mullite phase (see Figure 54C,D). It is evident that 21 % of photosensitive polysiloxane was sufficient to print a highly complex structure and form a network which was both stable enough to retain the trapped alumina particles and strong enough to sustain the subsequent handling. Ceramic strut sizes as small as 160 μm were produced and maintained their shape completely during the complete heat treatment, which included debinding, the preceramic polymer transformation into silica, the chemical reaction between the silica matrix and entrapped alumina particles to develop the mullite phase and the densification of the crystalline ceramic material during sintering.
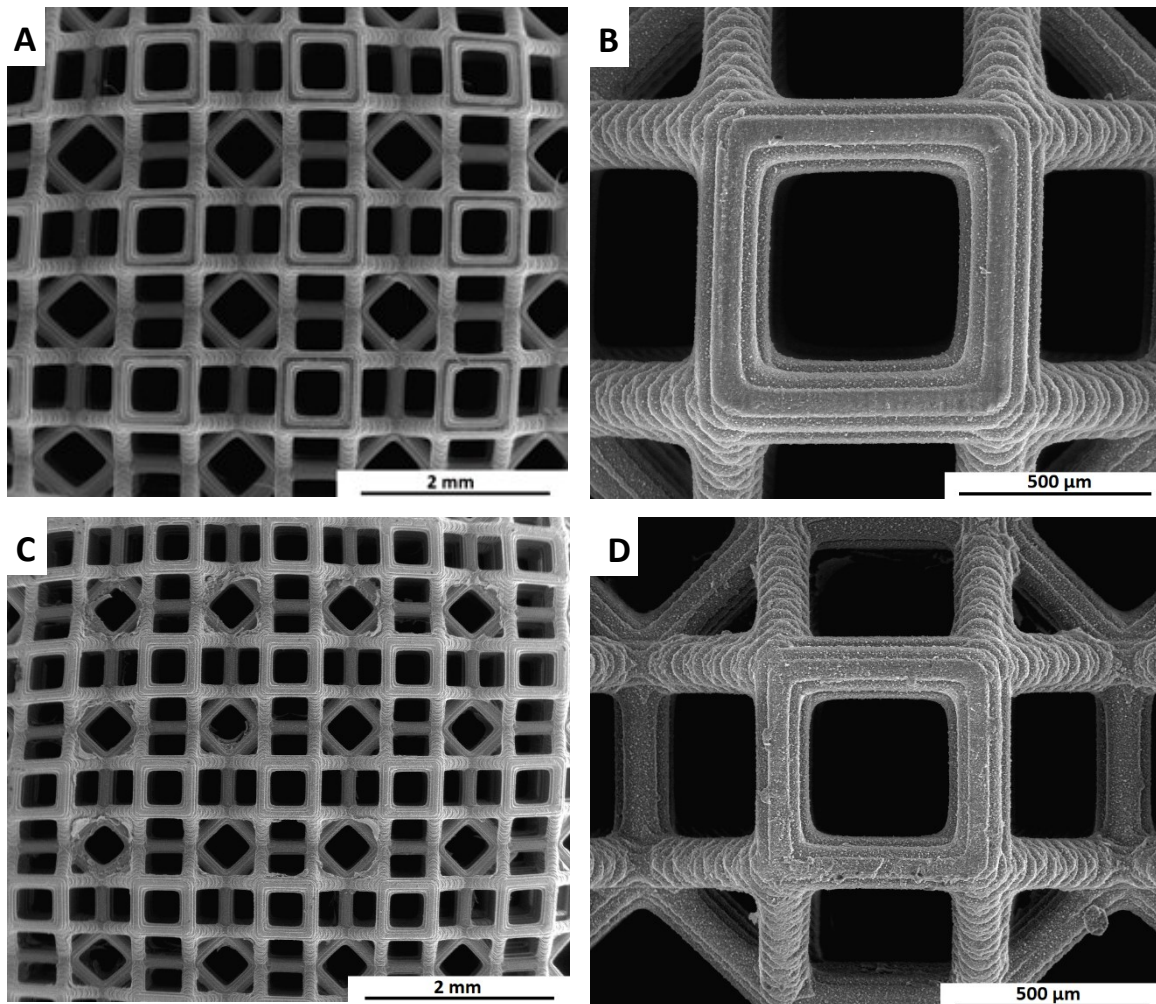
Figure 54 SEM pictures of a structure printed with the phase-optimised mixture of polysiloxane/micro-sized alumina, before (A,B) and after (C,D) sintering at 1300 °C (images taken at same magnification).

Apart from the stepwise slices in z-direction due to the manufacturing conditions and the absence of surface cracks (see Figure 54A,B), the SEM analysis of the printed struts at a higher magnification

(Figure 55A,B) shows the presence of some particles at the surface of the printed part. During UV exposure, the polysiloxane crosslinks, and builds a solid polymeric network in the desired shape while also trapping the alumina powders, which are partially incorporated at the surface of the strut due to their relatively large micrometre size. Likewise, particles are also observed in a similar size, shape and position at the surface of the struts after sintering at 1300 °C (see Figure 55C,D). The SEM analysis of the fracture surface of a 3D printed sample fired at 1300 °C (see Figure 55E,F) highlights the absence of internal cracks and the porosity within the mullite ceramic, as well as the lack of distinguishable particles within the dense struts. The elimination of the organic part of the acrylic preceramic polymer, and the reaction-sintering with the alumina particles, led to a dense and homogenous internal mullite structure, with a measured density of 3.1 g/cm^3, close to the theoretical density of 3.16 g/cm^3 of 3Al2O3·2SiO2mullite ceramics.[155]

Preliminary mechanical tests carried out on the dense and crack-free rhombi-cuboctahedron cell structures (Figure 54C) indicate a compression strength of 1.8 ± 0.3 MPa for samples with a total porosity of 90 vol%, which is greater than the previously reported values for highly porous cellular mullite ceramics.[139, 145]
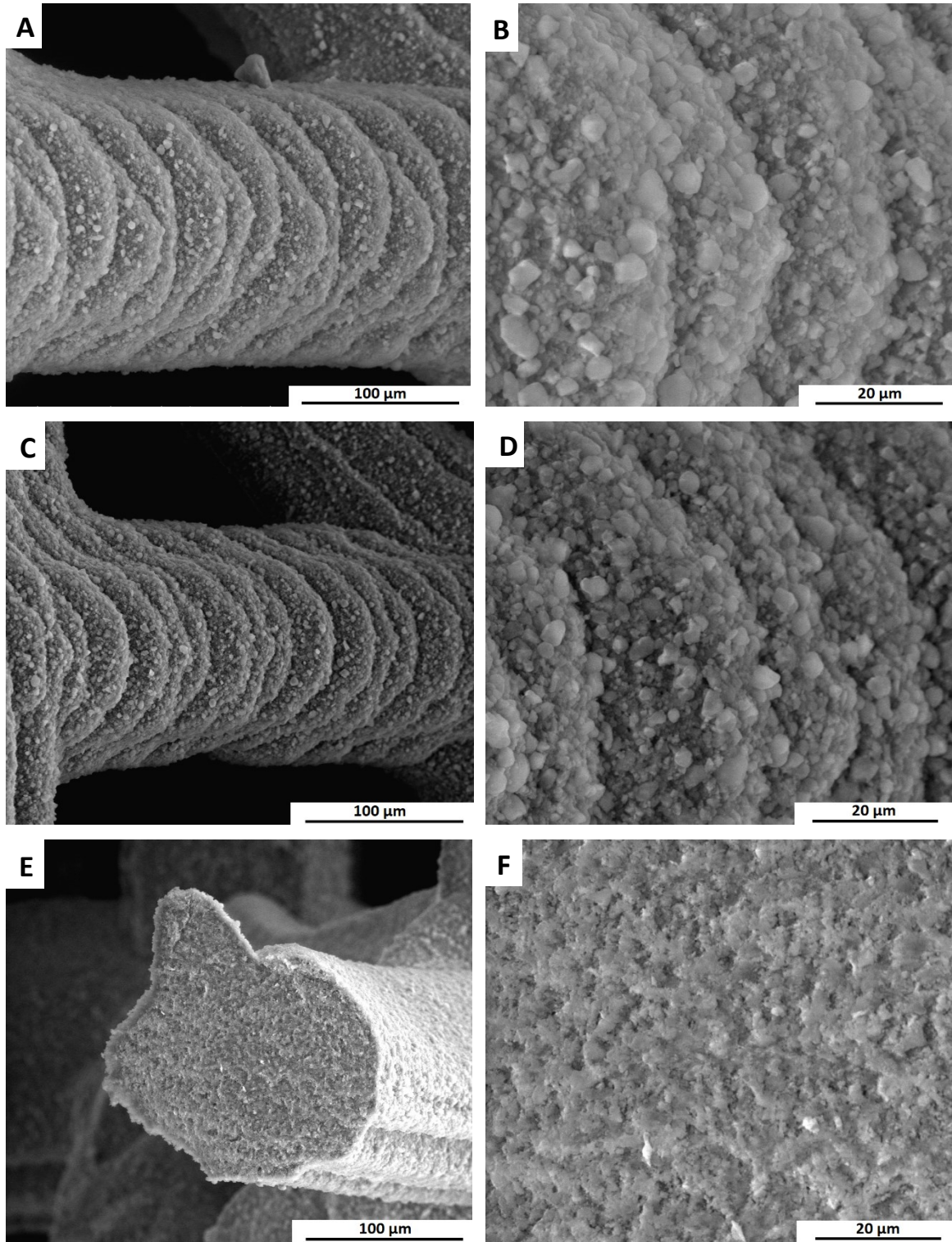
Figure 55 SEM images of a mullite structure produced with the optimised polysiloxane/micro-alumina formulation; comparison of the strut surface before (A,B) and after (C,D) firing at 1300 °C and image of a dense and non-porous mullite fracture surface (E,F) fired at 1300 °C, taken at same magnification.

6.6   Unreacted Alumina Particles at Structure Surface

Since the size, shape and position of the starting alumina particles observed in the UV-cured sample (Figure 55B) is very similar to those of the particles visible in the fired ceramic struts (Figure 55D), it seems that unreacted alumina particles remain mainly at the surface of the component after mullite formation. Since the overall dimensions of those particles are only a few micrometres, the composition of the particle itself was unable to be verified without also measuring some of the surrounding and underlying ceramic material. Therefore, EDX analysis was used investigate the composition of an area (30 x 35 μm^2) of ceramic material located at the surface (Figure 55D) and inside the cross-section of the dense strut (Figure 55F). The results of the analysis at both spots, which was performed on an equally sized area and under the same measuring conditions, are shown in Figure 56. With the exception of some carbon contamination, the ceramic material at both spots consists solely of the elements oxygen, aluminium and silicon, with more silicon inside the strut volume (Figure 56A) than at the strut surface (Figure 56B). The elemental analysis, compared to the nominal composition of mullite ($3Al_2O_3 \cdot 2SiO_2$), is shown in Table 13.
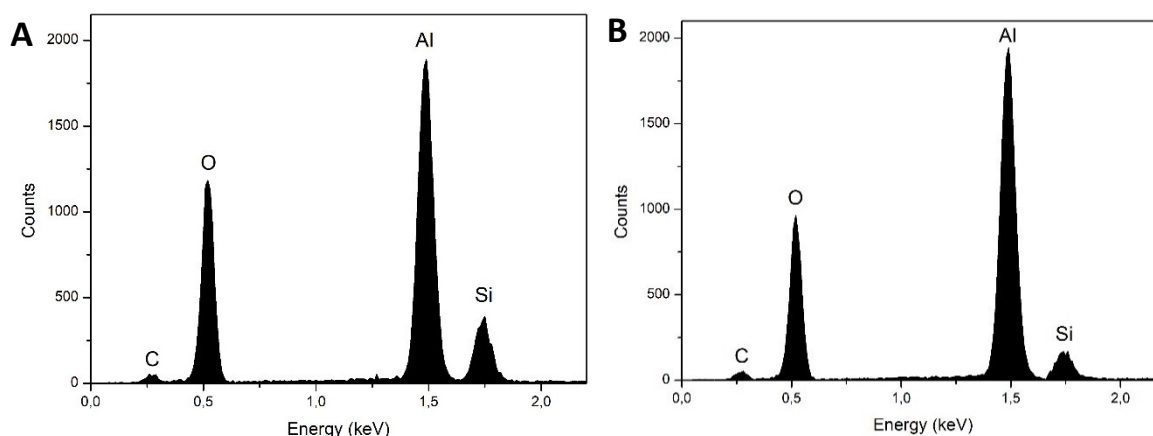
Figure 56 EDX analysis of an area located inside the strut cross-section (Figure 55F) and at the strut surface (Figure 55D).

Table 13 Elemental analysis of spots located in the strut cross-section (Figure 56A) and at the strut surface (Figure 56B), compared to the nominal mullite composition ($3Al_2O_3 \cdot 2SiO_2$).

Element	Strut cross-section (mol%)	Strut surface (mol%)	Mullite (mol%)
O	60.4	57.6	61.9
Al	31.1	37.5	28.6
Si	8.5	4.9	9.5
Ratio Si/Al	0.273	0.131	0.332

It can be observed that, while the elemental composition within the volume of the 3D printed and the sintered struts correlate reasonably well with the nominal mullite composition, the amount of silicon at the strut surface is only half of that within the cross-section. Therefore, when also considering the observation of a homogenous fracture surface (Figure 55F) without the presence of coarse particles, we can posit that the unreacted alumina, found by XRD analysis (Figure 51), is mainly attributable to the presence of alumina particles at the surface of the printed struts, which do not react during sintering. While inside the volume of the material, the reactive alumina particles are surrounded by a siloxane UV-crosslinked matrix, while the ones at the surface are only partially trapped inside the polymeric matrix (see Figure 55B) and therefore do not react (see Figure 55D).

6.7   Conclusion

Mullite ceramic structures were developed by additive manufacturing, by using a photoreactive siloxane containing nano- and micro-sized alumina particles and by firing at a temperature range of 1300-1400 °C. Mullite formed from the reaction between the alumina particles and the silica, originating from the decomposition of the polysiloxane. When nano-sized alumina was used, phase pure mullite formed at 1300 °C, while micro-sized particles did not completely react after firing at 1400 °C for 1 hour.

When processing the developed formulations via Digital Light Processing, the suspensions containing nano-sized particles required a large amount of solvent, giving a low ceramic yield and producing a soft and weak polymerised acrylate-network, with poor printing resolution, crack development and collapse of the structure during firing. The use of micro-sized alumina powders enabled dense and crack-free bulk as well as porous components with highly complex architecture to be manufactured. Because of the incomplete reaction in the case of micro-sized alumina, the printing formulation was adjusted to eliminate any trace of residual cristobalite from the ceramic after the heat treatment, leading to some residual alumina at the surface of the fired parts.

The printed porous ceramic components had a total porosity of 90 vol% and a compression strength of 1.8 ± 0.3 MPa. The relatively high compressive strength of the produced cellular structure, the virtually limitless possibility of shaping via DLP the developed formulation into components with highly complex architectures, where the porosity, cell distribution, size and shape can easily be adjusted and optimized according to a simple modification of the stl-file, and the properties of mullite ceramics;[123, 125, 126] all these aspects create the possibility to produce ceramic structures at low processing temperatures suitable for advanced filter applications,[126-128] such as the structure shown in Figure 57.
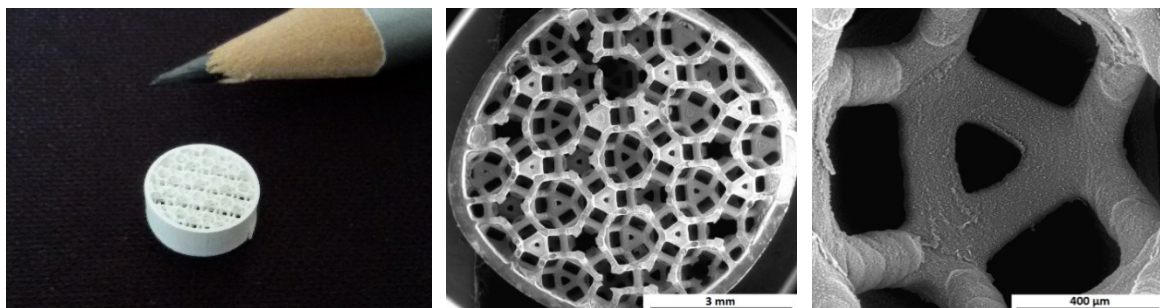
Figure 57 Mullite-based ceramic filter structure fabricated via DLP printing of a photosensitive polysiloxane containing micro-sized reactive alumina particles.

7   Summary and Future Work

A photosensitive polysiloxane was used throughout the whole work to fabricate different ceramic structures across different length scales. Complementary approaches, both at the material level and with the production processes, have been applied to alter material properties, like ceramic yield, shrinkage, resolution or free-carbon content (chapter 3), to achieve different structural dimensions and resolutions (chapter 3 and 4), to fabricate multi-scale ceramics (chapter 5) and to take advantage of the multi-functional properties of preceramic polymers by combining shaping with the simultaneous production of a new desired ceramic phase (chapter 6).

For these purposes, the photosensitive polysiloxane was combined with other high ceramic yield polysiloxanes in a physical blend to reduce the amount of decomposed material during debinding and therefore the shrinkage of the component. The physical blends made it possible to produce highly complex and dense, pure SiOC ceramic structures via DLP printing, enclosing a whole range of ceramic yields, shrinkages, different carbon contents and final feature size, which pushes the resolution limit of 3D stereolithography technology. At the same time, even by incorporating non-photosensitive preceramic polymers in the printing resin, which basically dilutes the photocurable material in the printing solution, no decrease in structural complexity and resolution during printing arouse. The disadvantages of structuring ceramics via stereolithography, due to light absorption and scattering from glass and ceramic particles,[1, 9, 14, 15] were completely avoided by using preceramic polymers to build SiOC structures, which is a phase only obtainable by the molecular route.[38, 40, 43] Large scale structures have been printed and their linear shrinkage behaviour overall and in the unit elements analysed. It was shown that the shrinkage of a ceramic lattice material is not a straight-forward approach and has to be considered when creating parts, as aspect ratios are changing during pyrolysis. The same material was used to fabricate equally complex structure at an entirely different scale via 2PL, with features sizes ranging in the hundreds of nanometres. Dense, ceramic structures with unprecedented complexity at this scale were fabricated with homogenous shrinkage on top of support pillars. The hybridisation of both printing techniques combined the achievements accomplished with the separated fabrication processes, producing free-standing and easily to handle cm-sized SiOC ceramics with 3D structured sub-µm features, the latter only achievable through 2PL printing. Furthermore, the produced chemical composition of the ceramic material itself was changed by adding active alumina fillers, which react with the silica source formed by the decomposition of the polysiloxane at high temperature in air and formed mullite ceramic. The photosensitive polysiloxane was therefore used in a multi-faceted way, where it was possible to achieve a new chemical composition at the same time as the structuring step, eliminating the two-step process where the desired glass or ceramic composition needs to be created before shaping.

The in-situ reaction with the silica source developed the new chemical composition, mullite, within the predetermined, printed shape.

Highly complex ceramic structures have been fabricated via lithography based additive manufacturing with structural dimensions from nm (2PL) to cm (DLP). All fabricated structures showed no sign of delamination and an isotropic shrinkage after heat treatment, where pore and crack-free ceramic structures with dense struts were obtained.

7.1   The Photosensitive Material

This work was mainly based on the photosensitive properties of the RC 711 siloxane preceramic polymer. It is a highly acrylated polysiloxane which is both printable at the macro-scale via DLP and the micro-scale via 2PL. This in itself is noteworthy, since it's not a given that a material processable via DLP/SLA printing can also be processed via 2-photon-lithography, as is not the case for modified-MK (see chapter 5.4). The high amount of acrylate groups in the preceramic polymer chain of RC 711 made this material highly effective in both lithography-based technologies. Remarkable low exposure doses were needed, which made it feasible to achieve minimal exposure times of only 3.5 s in DLP and writing speeds up to 5000 µm/s in 2PL, which is comparable to standard polymeric photocurable materials for both printing technologies. Moreover, a strong polymerised network formed upon light exposure, providing no limitation in shape complexity and size of the realised structures at both implemented length scales. Furthermore, since it is possible to process RC 711 with both lithography-based technologies, a complete combination via hybrid additive manufacturing proved to be successful both in the printed and in the pyrolysed state.

The high shrinkage of RC 711 is, from an engineering standpoint, a downside of using this particular photocurable polysiloxane, as 93 % of the material is eliminated during pyrolysis in nitrogen to produce a SiOC material, and 68 % during sintering in air to transform the material into SiO_2. The 70 % linear shrinkage during the transformation into SiOC ceramic certainly doesn't install confidence in using this material for engineering applications. However, it should be noted that, notwithstanding that large shrinkage, the developed SiOC structures completely maintained their shape, exhibited homogenous, isotropic shrinkage, dense struts and no defect formation at all, such as micro-cracks, porosity or delamination upon pyrolysis (see Figure 21,23-25). Using RC 711 can very well be of advantage in producing ceramic parts, where fine feature details are especially important, as the resolution after pyrolysis is greatly enhanced exactly because of the linear shrinkage being larger than 70 %. In this way, SiOC ceramic structures can be manufactured from RC 711 which show feature sizes well below the resolution limit of any available DLP printing equipment. At the same time, the shrinkage can be significantly decreased, to as low as 42 %, by simply mixing RC 711 with other high ceramic yield polysiloxanes (Silres 601 and H44) without losing any resolution or achievable complexity during printing (see Figure 22).

As far as even smaller dimensions are concerned, below the µm-level in 2PL printing, the high shrinkage of RC 711 makes it actually possible to achieve comparable resolutions in the manufactured micro-SiOC structures to those of polymer structures printed from a standard polymer photoresist developed from Nanoscribe itself, possessing an optimised reflection index. Equipped with a supporting base, homogenous shrinkage with no structural deformation can be realised in SiOC

structures, even when such a high shrinkage is occurring. Complex ceramic micro-structures with dense struts can be produced which have much better mechanical, thermal or chemical properties as polymers, and surpass other existing ceramic microstructures in their complexity[49, 64, 65, 88] and mechanical strength.[83, 85, 91-93]

Focusing on the production of new ceramic phases by placing active fillers in the photosensitive RC 711, the low ceramic yield of only 32 % in air allows for an increased amount of RC 711 inside the printing resins, while maintaining the predetermined molar ratios. To develop specific ceramic phases a certain ratio between the fillers and the polysiloxanes, the source of silica, has to be maintained according to the stoichiometry of the desired new phase, as has been done in the preparation of mullite with RC 711 and active alumina fillers. By using a polysiloxane with a low ceramic yield, a higher volume fraction of it has to be placed in the printing resin, than if a polysiloxane with a high ceramic yield would have been used. Since RC 711 is not only added as a source of liquid silica, but also due to its photosensitive properties to accomplish the shaping via DLP printing, a larger amount of it will increase the photosensitivity of the printing slurry, thereby favourably reducing the fabrication times. The larger fraction of acrylates in the mixture can form a strong and rigid network upon photopolymerisation, which decreases the necessary size (and number) of self-sustaining struts and increases the achievable complexity and overall size of the printable structure.

7.2 Size, Scale and Resolution

By using two different lithography-based additive manufacturing techniques, structures of entirely different sizes and scales were fabricated. Printing of polysiloxanes with DLP allowed for the realisation of structures as tall as 6 cm (see Figure 26), while the pyrolysed SiOC structures exhibited features as small as 30 µm (small struts in cube illustrated in Figure 15), spanning a feasible size-range from micrometres to several centimetres. 2PL on the other hand, starts at the micrometre scale and reaches down to the hundreds of nanometres, as structures as tall as 100 µm, the operational limit of 2PL, and as wide as 250 x 300 µm^2 (see Figure 35) were printed with small scale features as small as 800 nm (see Figure 43). Both techniques allowed for the production of highly complex structures, which were geometrically exactly the same, but in a completely different size scale. Taking note of the scale bars in Figure 58, this point is demonstrated by showing images of the same diamond structure from polysiloxane material as tall as 12 x 12 x 12 mm^3 and as small as 24 x 24 x 24 µm^3 fabricated by DLP and 2PL respectively. It shows that the diamond node, printed via DLP, is 50 times larger than the entire diamond structure fabricated by 2PL.
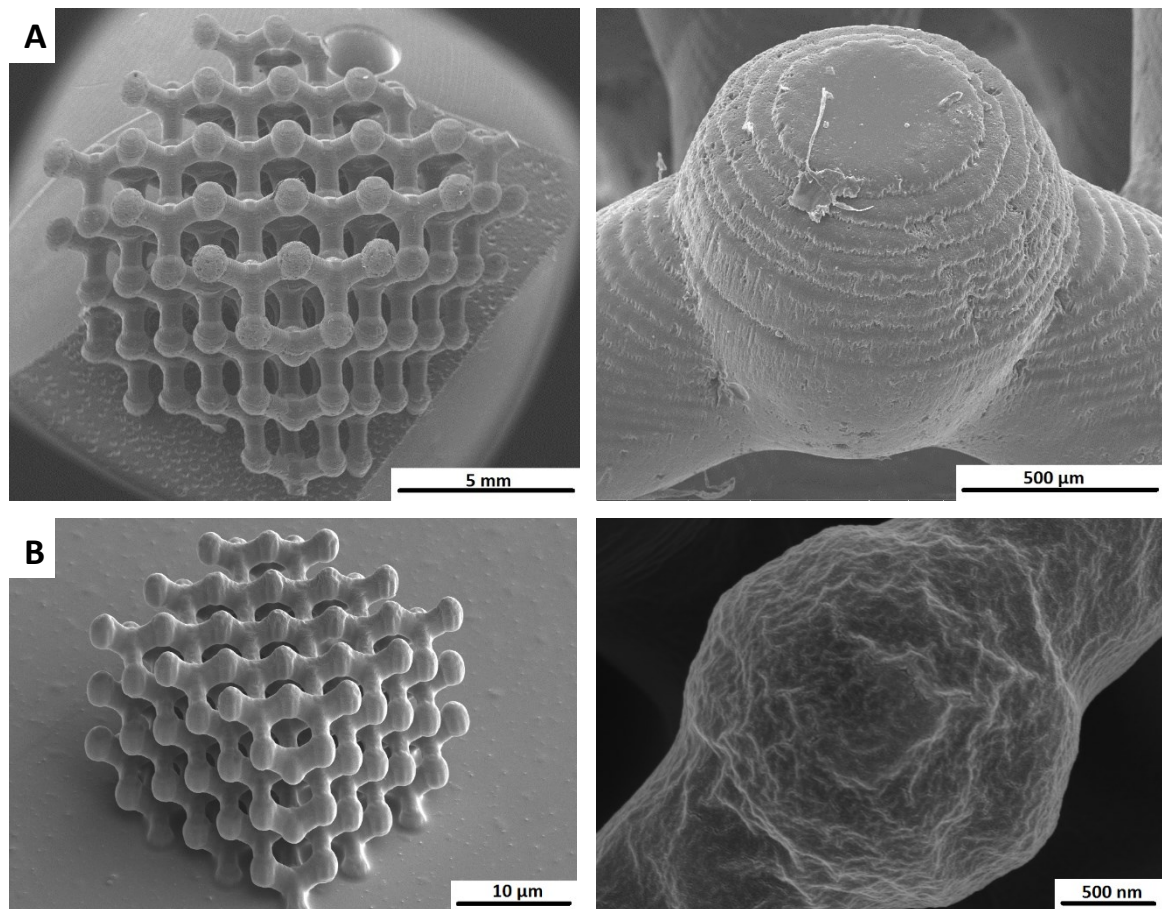
Figure 58 Polysiloxane diamond structures at different scales; physical blend RC 711/H44 = 5/5 printed via DLP (A) and RC 711 printed via 2PL (B).

Ceramic SiOC structures were created with geometries up to the cm-range (DLP) or structural features down to the sub µm-scale (2PL). The hybridisation of the two technologies permitted to extend both printing ranges, combining the macro-dimensional printing with nm-sized elements. The advantages of DLP printing, listed in Table 14, were combined with the nm-resolution limit offered by 2PL. The limitations of both printing technologies were removed, since not only the resolution limit of DLP/STL fabrication was exceeded, but the structures, fabricated via 2PL, were removed from the up-to-now unavoidable glass substrate, from which they would be not detachable, and printed on preceramic components previously structured in any configuration.

Table 14 Comparison of advantages and disadvantages DLP/STL and 2PL printing includes.

DLP/STL	2PL
+ macro components (cm sized)	+ resolution limit (nm)
+ free standing component	– micro components (µm)
+ easy handling	– attached to glass substrate
– resolution limit (~ 50 µm)	– not detachable

The shrinkage values of the different SiOC physical blends, reported in Figure 19B, were measured for all materials by means of the cubic structure shown in Figure 15. Chapter 3.2 already reported that in printing the same material via DLP, different shrinkages of the overall sample and their structural elements occurs. The shrinkage, although homogenously in nature, changes the aspect ratio of the elements due to their different geometrical arrangements and therefore constraints. It was also shown for both DLP and 2PL printing that different structures, although printed with the same material, exhibit different shrinkages (summarised in Table S13), which clearly demonstrates that the shrinkage is not only dependent on the material but also on the structural configuration in both printing techniques. Furthermore, the analysis of the Kelvin cell structure (5 x 5 x 5 cells), printed with both lithography-based processes with pure RC 711 and subsequently pyrolysed, reveals a higher shrinkage of 67 % for DLP printed macro-sample than the 51 % shrinkage for 2PL printed micro-sample. This additional difference in shrinkage of the same material, printed in the same structural configuration, is probably due to the constrained pyrolysis condition in the micro-structure, which are not free sliding, but are attached to the glass substrate. Although the support pillars allow for a homogenous shrinkage of the structure on top by disconnecting them from the unshrinking glass support, the overall condition through pyrolysis still seems to be under additional

constraint, resulting in a 16 % lower shrinkage of 2PL printed RC 711 Kelvin cell structure in opposition to the same structure printed via DLP. This constrained shrinking condition is removed in the case of the hybrid woodpile structures, where the micro-woodpile fabricated via 2PL was printed on top of the DLP macro-woodpile fabricated using the same material, with no un-shrinking glass substrate present. Both macro- and micro-structures exhibit now the same shrinkage behaviour, producing a hybrid structure capable of homogeneous shrinkage upon pyrolysis (see Figure 48B). This demonstrates that the shrinkage is apparently depending on the ceramic yield of the material and the structural configuration of the component, but not on the lithography-based printing technique employed to print said structure.

7.3 Extending the Range of Processable Materials

The photosensitive polysiloxane was combined with two high ceramic yield polysiloxane materials, of different carbon content, to produce SiOC ceramic structure, as well as with alumina nano- and micro-particles to produce mullite ceramics.

The compatible, high ceramic yield polysiloxanes were chosen from a randomly available collection of commercially available preceramic polysiloxanes. Seven high ceramic yield preceramic polymers were used for testing, and only combinations with RC 711 were produced, which was also selected from five different photosensitive preceramic polymers, which resulted in the development of three stable solutions, two of them maintaining their printed shape after pyrolysis. Likewise, combinations were tested with only a number of solvents, which were by no means complete, to reach solutions without phase separation. A higher availability of primary and secondary preceramic polymers and compatible solvents will more than likely lead to more stable solutions, which can be used to fabricate further physical printing blends with different features (e.g. even higher ceramic yield). By using different secondary preceramic polymers, containing methyl, phenyl, vinyl, propyl etc. side groups, a broad spectrum of different molar compositions can be obtained; e.g. polymethylsiloxane MK or Silres 610 possess only 28.6 mol% carbon compared to 76.4 mol% C of polyphenylsiloxane Silres 601.[45] Due the difference in chemical composition, since the Si:C ratio depends on the organic side groups whereas the Si:O is kept constant at 1:1.5 in polysiloxanes,[45] potentially different functional properties e.g. electrical conductivity, mechanical properties or chemical durability can be achieved.[37, 44, 47] The range of possible ceramic yield, shrinkage, resolution and amount of free carbon in the system can therefore be further extended, leaving more freedom to choose the desired properties of the blend. The widening of the range of preceramic polymers that can be employed for additive manufacturing, using this approach and different combinations of preceramic polymers and solvents could be the goal of further work.

Different from the random selection of available preceramic polysiloxanes with high ceramic yield, alumina powders were specifically added to produce a particular desired material composition. While mullite has been produced from a reaction of the RC 711 derived SiO_2 with the added alumina powders, other glass or ceramic phases from the reaction of filler material with polymer derived silica source upon heating have already been investigated to from oxide systems (mullite, zircon, cordierite, fosterite, yttrium-silicates) or oxynitride ceramics (SiAlONs, YSiONs).[55] Different active filler materials can also be added to RC 711, forming a stable solution with appropriate solvents. This will further extend the range of achievable materials to include other silicate ceramics, glasses and glass-ceramics. All these potential material compositions would take advantage of the multifunctionality of the photosensitive polysiloxane, the processability via DLP and its transformation

into SiOC or SiO_2 phase upon treatment in nitrogen or air, respectively. It would also be interesting to explore if powder filled RC 711 is likewise printable with 2PL. Instead of adding silica nanoparticles to reduce the shrinkage of micro-structures,[65] alumina nanoparticles could for example be added to see if they can be incorporated in the polymerised structures via 2PL printing and transformed into dense, mullite micro-structures, in the same way as for DLP processing (see chapter 6).

The successful integration of DLP and 2PL printing was shown in the hybrid additive manufacturing processing of polysiloxanes. A hybrid structure, scaling across several length scales, from overall cm-dimensions to nm-range feature sizes, can be accomplished by combining those two lithography-based processes. The precise positioning of parts fabricated using those two technologies and the stable adhesion of the materials, with no sign of delamination, has been shown. The same temperature treatment and necessary heating atmosphere, N_2, allowed the conversion of the polysiloxane structures into SiOC ceramics. By using the same material, RC 711, for both printing processes, a homogenous shrinkage across the entire structure was obtained. First explorations into the concept of using multi-materials in this hybrid process, as has been carried out in other hybridisation processes combining two additive manufacturing technologies,[108-110, 112, 115] proved a stable combination of two different polysiloxane materials, modified-MK with RC 711, in the printed state. Just as other examples of multi-material structures, challenges occur if those materials have to undergo an additional heat treatment. For the production of ceramic materials, this includes the need of matching sintering behaviour (heating schedule, final temperature, atmosphere), shrinkage and coefficient of thermal expansion to avoid critical internal stresses during cooling, and avoiding chemical interactions between the two different materials.[111, 115, 120] Figure 47 highlights the difficulties in printing and pyrolysing two materials, which are the same in nature being both polysiloxane preceramic polymers producing SiOC ceramic, but exhibit different shrinkage behaviour. The materials selection in producing ceramics is therefore restricted to two materials, where above mentioned characteristics can be satisfied and they can be printed with DLP and/or 2PL printing techniques. Therefore, the physical blends developed in chapter 3.1 cannot be unrestrictedly used, without compensating for shrinkage mismatch, as the blends firstly exhibit a drying shrinkage (see Figure 19B) and secondly cannot be printed via 2PL (see chapter 4.7). Differently, pure RC 711 represents an ideal candidate to fabricate multi-scale ceramic structures via hybridisation of lithography-based additive manufacturing technology, as it has a negligible polymerisation shrinkage, can be printed with both DLP and 2PL and allows for the printing of almost every imaginable, complex structure (see Figure 35). Although possible combinations with other materials could only be verified in the printed state, but not up to now extended to pyrolysed multi-materials, compatible materials, meeting the above-mentioned characteristics, could be explored in future works.

Supplementary Information

Table S1 List of used chemicals.

Photosensitive preceramic polymers	TEGO RC 711 (Evonik Industries, Germany)
	UV Poly 110 and UV Poly 204 with their respective catalysts UV CATA 102 and 211 (Bluestar Silicones, France)
	Si-vinile-EQ (EEMS.LLC, USA)
	AB 108972 (abcr GmbH, Germany)
Preceramic polymers	MK, Silres 601, Silres 610, H44 H62C (Wacker Chemie AG, Germany)
	Dow Corning 3074, DOW 217 (Dow Corning, USA)
Photosensitive polymers	PEGDA (Sigma Aldrich)
	Green Resin (Robofactory, Italy)
Solvents	Dowanol, phenoxyethanol, benzylalcohol, toluene, isopropanol, hydroxyethyl methacrylate, dimethylsulfoxid, divinylbenzene, cyclohexanone, diphenylether, ethanol
Photoinitiators and absorber	Irgacure 819 (Ciba Specialty Chemicals, Switzerland)
	Camphorquinone and ethyl 4-(dimethylamino)benzoate (Sigma-Aldrich)
	4,4'-Bis(diethylamino)benzophenone (BDEBP) (Sigma Aldrich)
	E133 (Squires Kitchen, England)
Glass and Ceramic powders	Puralox TH 100/150 (SASOL, Germany) mean particle size = 2–6 µm
	Aluminium oxide C (Degussa, Germany) mean particle size = 15 nm, specific surface area = 100 m^2/g
Catalyst	Geniosil GF91 (Wacker Chemie AG, Germany)

Table S 2 Stl-files of all printed structures with dimensions and origin of the design.

A) Chapter 3.1 Achieving Variable Properties in SiOC Ceramic through Physical Blend Formulation
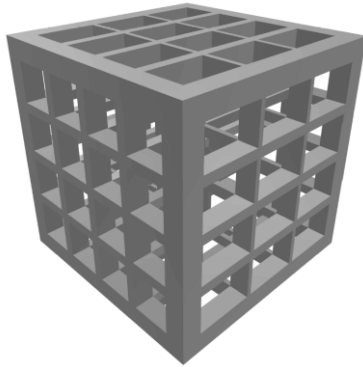
Model cube structure

4.5 x 4.5 x 4.5 mm^3
Strut Ø: 0.1 mm (smallest)
Origin: UniPD
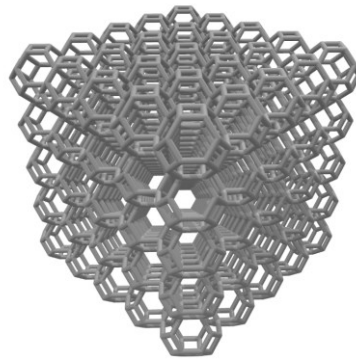
Kelvin cell structure
(5 x 5 x 5 cells)

19.5 x 19.5 x 19.5 mm^3
Strut Ø: 0.39 mm
Origin: UniPD
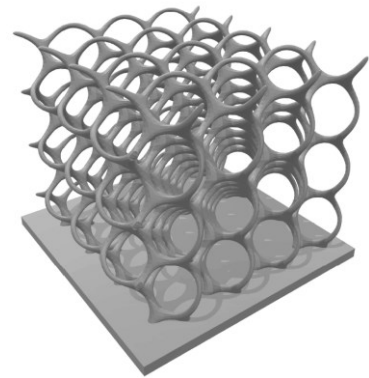
MS-Gitter structure

15 x 15 x 15 mm^3
Strut Ø: ~ 0.3 mm
Origin: Lithoz GmbH

B) Chapter 3.2 Analysis of Multi-Scale Sinter- and Mechanical Properties of SiOC Trusses
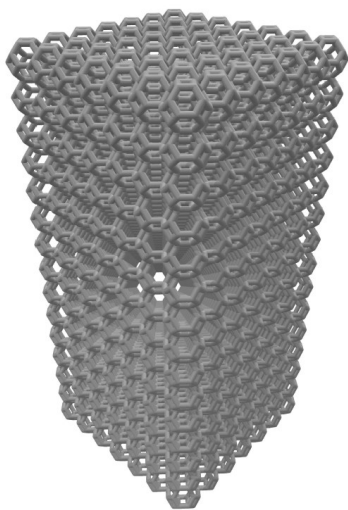
Kelvin cell structure
(7 x 7 x 15 cells)
30 x 30 x 63 mm^3
Strut Ø: 0.6 and 0.7 mm
Origin:
University of Applied Sciences
of Southern Switzerland
(SUPSI)

Octet cell structure
(7 x 7 x 15 cells)
30 x 30 x 63 mm^3
Strut Ø: 0.34 mm
Origin: UniPD
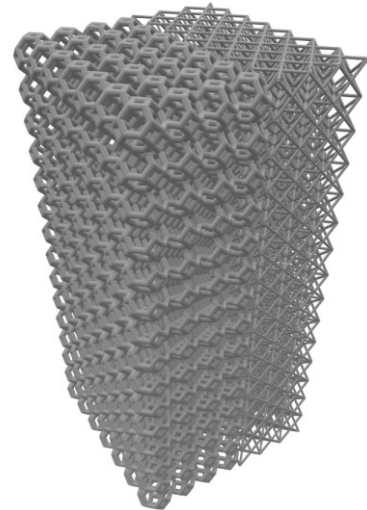
Hybrid structure
(7 x 7 x 15 cells)
30 x 30 x 63 mm^3
Strut Ø: 0.7 and 0.34 mm
Origin: CalTech
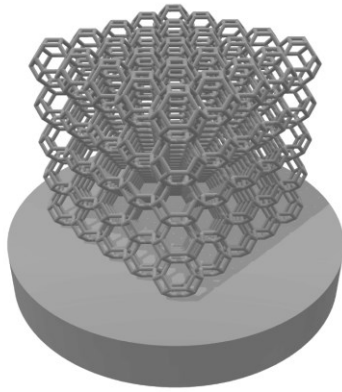
Kelvin cell structure
(5 x 5 x 5 cells)
30 x 30 x 30 μm^3
Strut Ø: 0.6 μm
Origin: UniPD
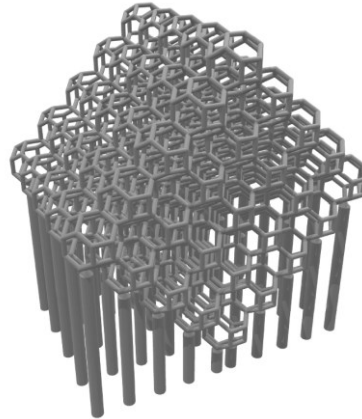
Kelvin cell structure
(5 x 5 x 5 cells)
With support structures
30 x 30 x 30 μm^3
Strut Ø: 0.6 μm
Origin: UniPD
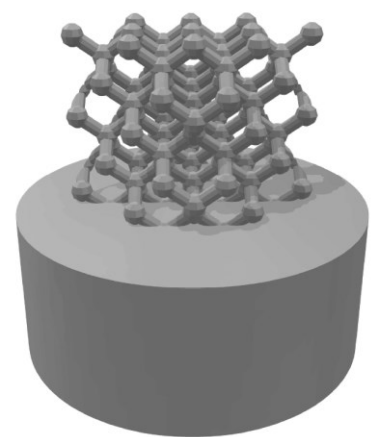
Diamond structure

32 x 32 x 32 μm^3
Node Ø: 3.7 μm
Origin: UniPD

Colloseum of Rome
305 x 255 x 40 μm^3
Origin: Thingiverse.com
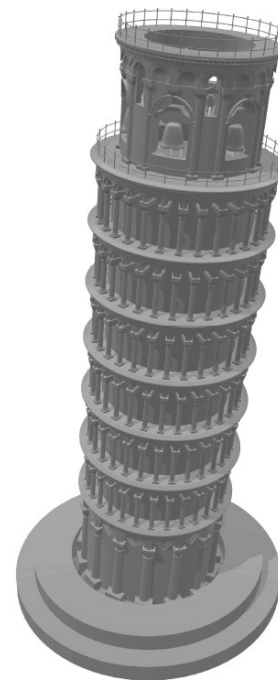
Pisa Tower
25 x 25 x 100 μm^3
Origin: Thingiverse.com
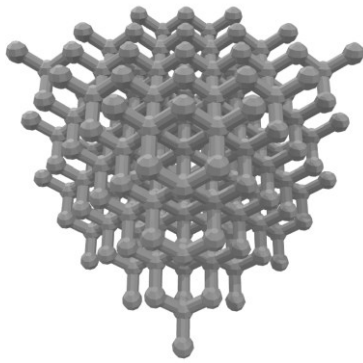
Diamond structure
23 x 23 x 23 μm^3
Node Ø: 2.1 μm
Origin: UniPD
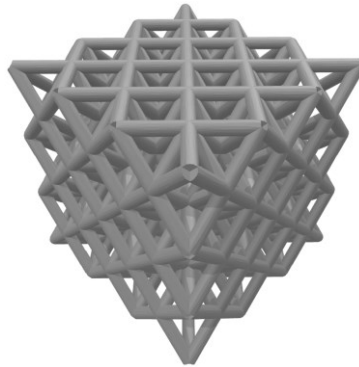
Octet structure
12.5 x 12.5 x 12.5 μm^3
Strut Ø: 0.7 μm
Origin: UniPD

D) Chapter 5 Hybridisation of Lithography-based Technologies for the Fabrication of Multiscale SiOC Ceramic Components

---
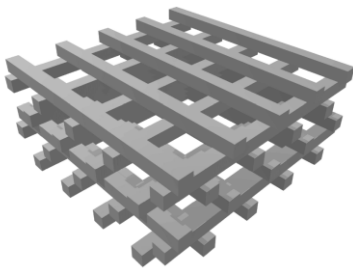
Woodpile structure
2.25 x 2.25 x 1.00 mm^3
Strut Ø: 1.25 mm
Origin: UniPD
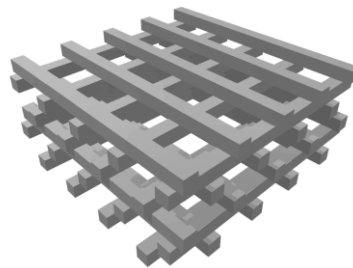
Woodpile structure
90 x 90 x 40 μm^3
Strut Ø: 5 μm
Origin: UniPD

E) Chapter 6 Exploitation of Multi-Functionality of Preceramic Polymers: Mullite Structures from Alumina Filled Polysiloxane

---
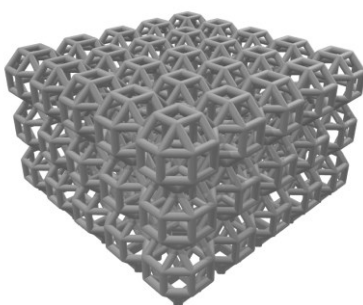
Rhombicuboctahedrons structure
10.25 x 10.25 x 6.40 mm^3
Strut Ø: 0.5 mm
Origin: Lithoz GmbH
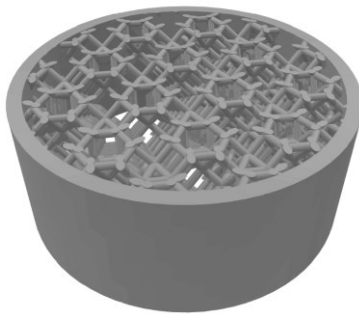
Filter structure

12 x 12 x 7.7 mm^3
Strut Ø: 0.5 mm
Origin: Lithoz GmbH

Sphinx

100 x 32 x 43 mm^3
Origin: myminifactory.com
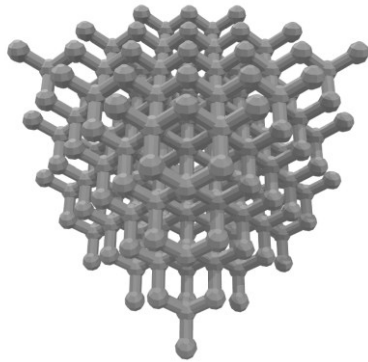
Diamond structure
12.7 x 12.7 x 12.7 mm^3
Node Ø: 1.2 mm
Origin: UniPD
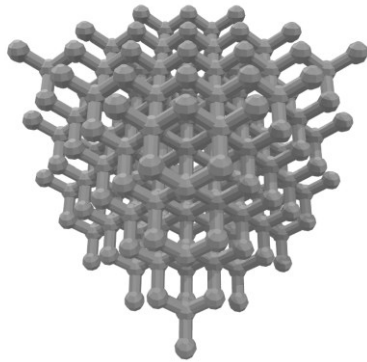
Diamond structure
23 x 23 x 23 μm^3
Node Ø: 2.1 μm
Origin: UniPD

Table S3 Cleaning Tests of physical blend mixtures conducted with RC 711/Silres 601 = 3/7 specifying the used solvent, if it was suitable for cleaning, method of drying since evaporation temperature of some cleaning solvents exceeded room temperature, formation of cracks during cleaning and overall appearance of sample surface.

Material	Cleaning	Drying	Micro- or macro-crack formation	Appearance
Manual	No	Air	No	Fluid layer remains
		Paper	No	Fibres from paper remain
Ethanol	No			
Isopropanol	No			
Heptane	No			
Acetone	Yes	RT	Yes	
Toluene	Yes	RT	Yes	
Cyclohexanone	Yes	60 °C	Yes	
Divinylbenzene	Yes	60 °C	Yes	
		Heptane	Yes	
		Isopropanol	Yes	
Dowanol	Yes	60 °C	Cube no star ~	Indentations and "octopus" patterning effect
Benzylalcohol	Yes	RT	Yes	
		60 °C	Cube no star ~	Indentations and "octopus" patterning effect
		Toluene	Yes	
		Isopropanol	Yes	
		Heptane	Micro-cracks	Indentations and "octopus" patterning effect;
		Isopropanol	Micro-cracks	Indentations and "octopus" patterning effect;
Phenoxy-ethanol	Yes	60 °C	Cube no star ~	Indentations and "octopus" patterning effect
		Heptane	Micro-cracks	Indentations and "octopus" patterning effect
		Isopropanol	Micro-cracks	Indentations and "octopus" patterning effect
Diphenylether	Yes	60 °C	No	Clean surface
		Isopropanol	Yes	Small indentations and "octopus" patterning effect
Mixture + extra Toluene	Maybe	Air	No	Smooth fluid layer on top remains
		UV	No	Smooth fluid layer on top remains

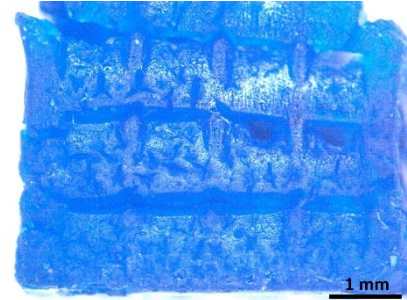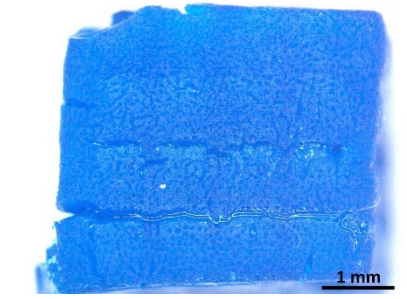*Table S4 Exemplary images of cleaning tests specifying appearance descriptions used in Table S3.*
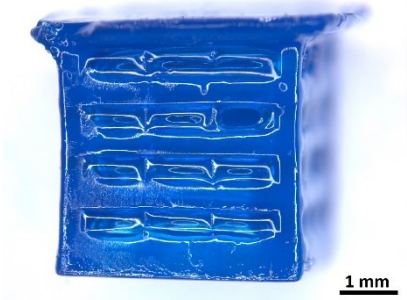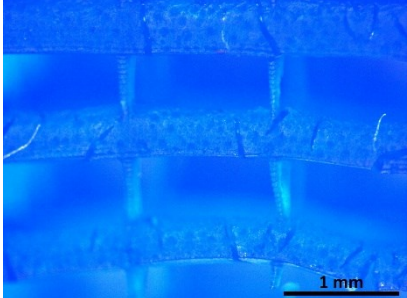
Cleaning solvent	Appearance	Image
Mixture + Toluene	Fluid layer remains on top of printed surface	
Divinylbenzene	Macro-crack formation	
Benzylalcohol	Micro-cracks; Indentations and "octopus" patterning effect	

Table S5 Drop Tests with available photoinitiators, in their already optimised concentration, to determine their effectiveness in investigating the min. exp. time.

Photosensitive material	Photoinitiator	Min. exp. time (s)
RC 711	2 wt% Irg 819	1
RC 711	0.25 wt % Ethyl-4-dimethylamin-benzo-ate and 1 wt% Camphorquinone	2
RC 711	2 wt% Irg 651	-
RC 711/DOW 217 = 1/1	2 wt% Irg 819	3
RC 711/DOW 217 = 1/1	0.25 wt % Ethyl-4-dimethylamin-benzo-ate and 1 wt% Camphorquinone	20
PEGDA	2 wt % Irg 819	2
PEGDA	5 wt% Erythrosin B	> 2 min

Table S6 Molar composition (SiO_2, SiC, C) of the used poylsiloxanes Silres 601 and H44.[45]

Polymer	SiO_2 (mol%)	SiC (mol%)	C (mol%)	Amount of side group
Silres 601	18.3	5.3	76.4	$(C_6H_5)_{0.9}$
H44	21.4	6.5	72.1	$(C_6H_5)_{0.62}(CH_3)_{0.31}$

Table S7 Optimisation of photoabsorber in blends of RC 711/Silres 601 (upper row) and RC 711/H44 (lower row = 5/5; amount of E133 is according to RC 711 content; scale bars = 0.5 mm.

0.5 wt% E133	1 wt%	1.25 wt%	1.5 wt% E133
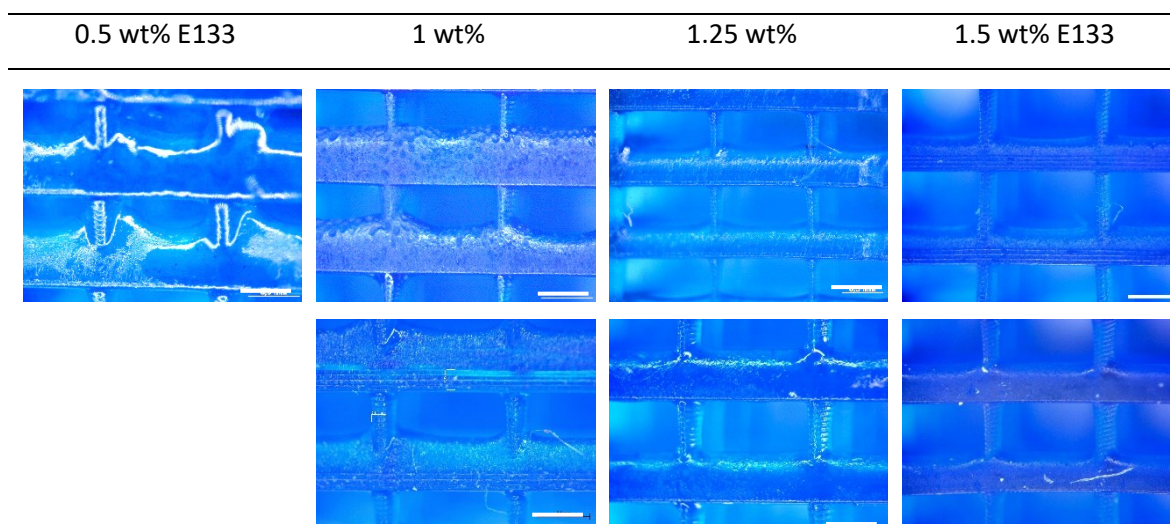
Table S8 Model cubes printed with all different blend mixtures (9/1 – 3/7) with 0.75 wt% E133 according to preceramic siloxane content (RC 711 + Silres 601/H44) show no overexposure, confirming the appropriate photoabsorber amount to reach desired penetration depth of light; upper row: blends containing Silres 601, lower row: blends containing H44; scale bars = 0.5 mm.
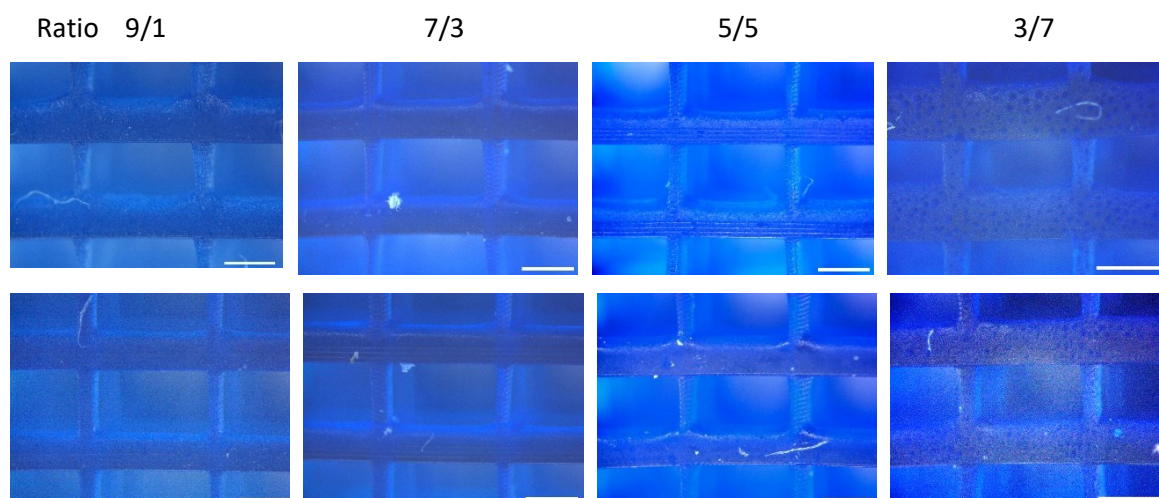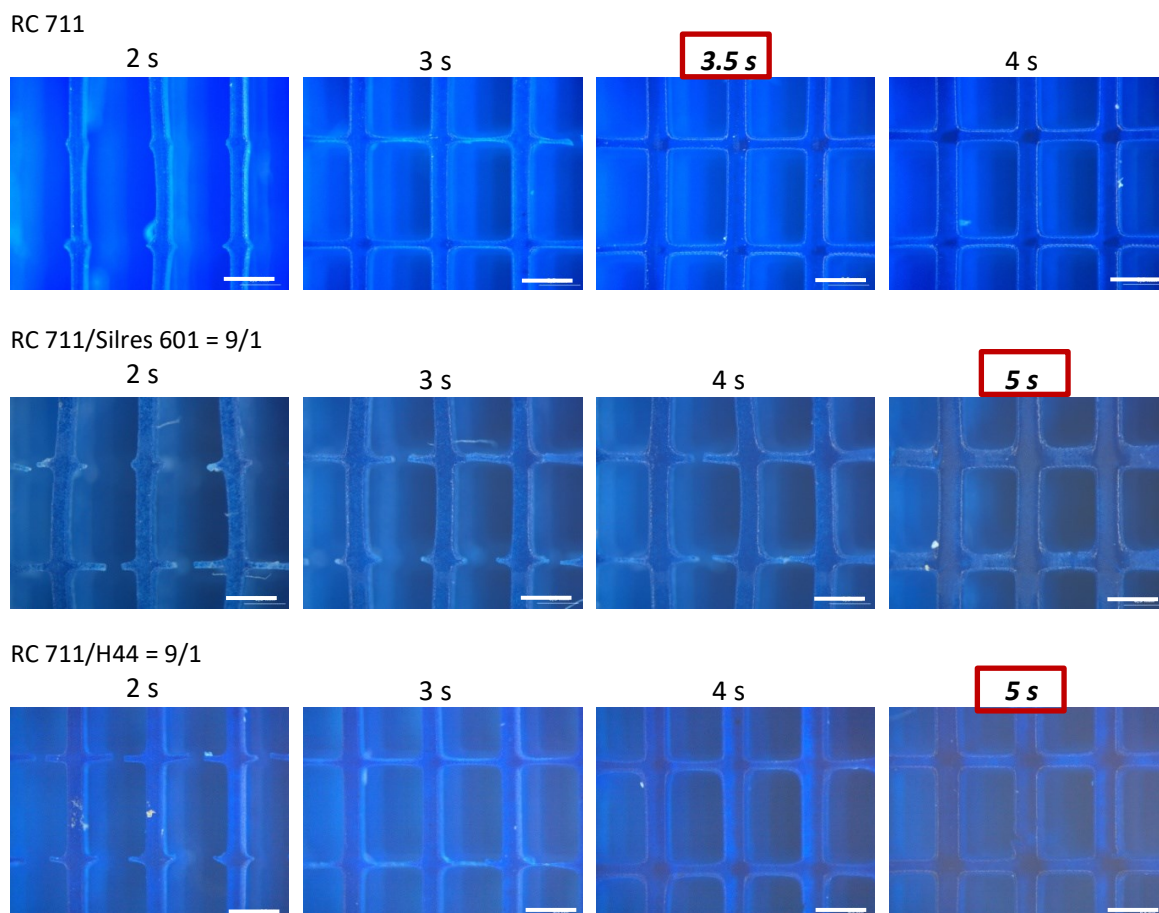

| Ratio 9/1 | 7/3 | 5/5 | 3/7 |

Table S9 Optimisation of exposure time for all blend configuration; scale bars = 0.5 mm.

RC 711

| 2 s | 3 s | **3.5 s** | 4 s |

RC 711/Silres 601 = 9/1

| 2 s | 3 s | 4 s | **5 s** |

RC 711/H44 = 9/1

| 2 s | 3 s | 4 s | **5 s** |

RC 711/Silres 601 = 7/3

| 3 s | 4 s | **5 s** |
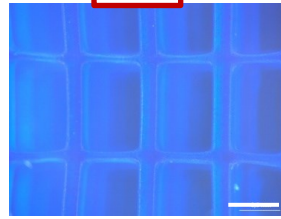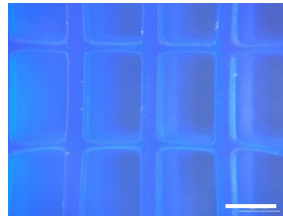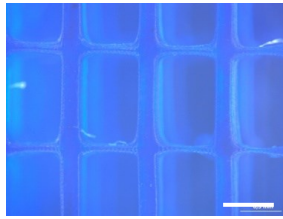
RC 711/H44 = 7/3

| 4 s | 5 s | **6 s** | 7 s |
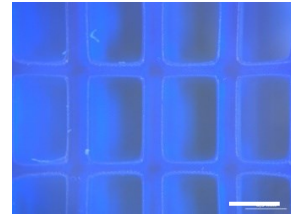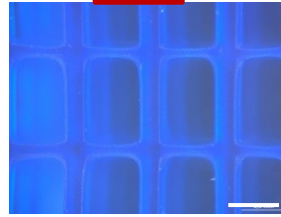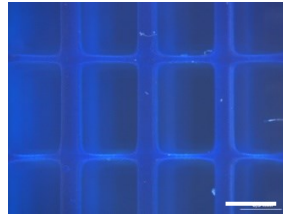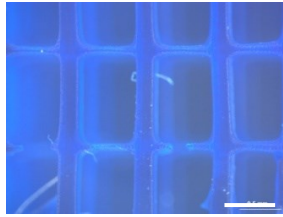
RC 711/Silres 601 = 5/5

| 4 s | 5 s | 6 s | **7 s** |
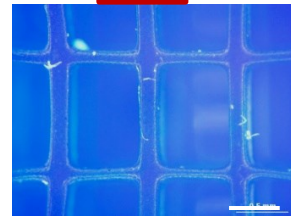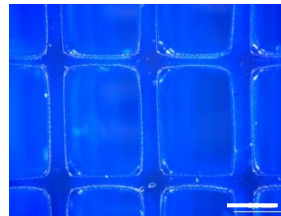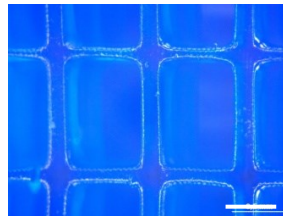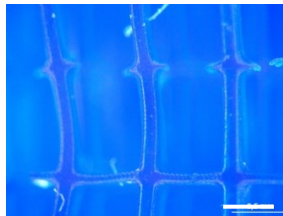
RC 711/H44 = 5/5

| 4 s | 5 s | 6 s | **7 s** |
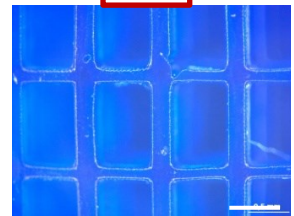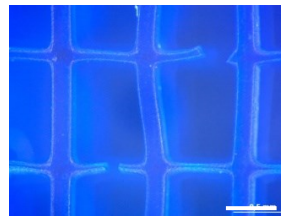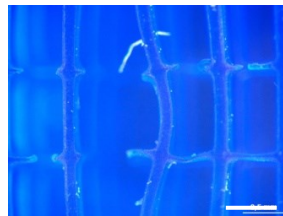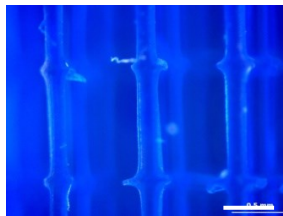
RC 711/Silres 601 = 3/7

| 13 s | **14 s** | 15 s |
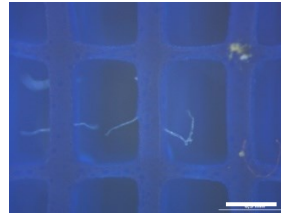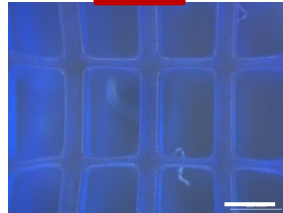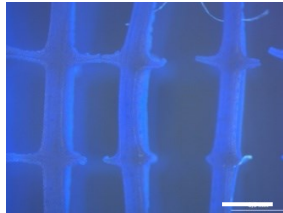
RC 711/H44 = 3/7

| 10 s | 11 s | 12 s | **13 s** |
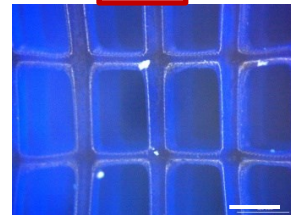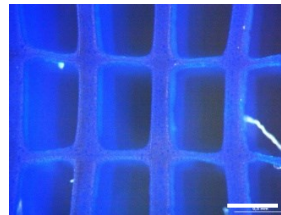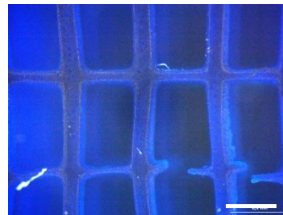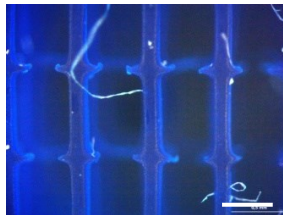
Table S 10 Display of type of strut failure in Kelvin 1,2 and octet structures with the respective mechanical strength of the individual struts.

		Kelvin 1 Strength (GPa)	Kelvin 2 Strength (GPa	octet Strength (GPa
node intact		0.43	0.87	1.76
		0.40	0.65	1.87
		0.45	0.34	1.61
			0.58	2.10
			0.53	2.21
				2.04
	average	0.42 ± 0.02	0.59 ± 0.17	1.93 ± 0.20
node partially removed		0.41	0.63	1.43
		0.35	0.46	2.32
		0.70	0.41	1.78
		0.37	0.54	2.20
		0.85	0.42	
		0.38		
		0.37		
	average	0.49 ± 0.18	0.49 ± 0.08	1.93 ± 0.35

Table S11 Image sequence of 2PL printing process taken from video of fabrication.
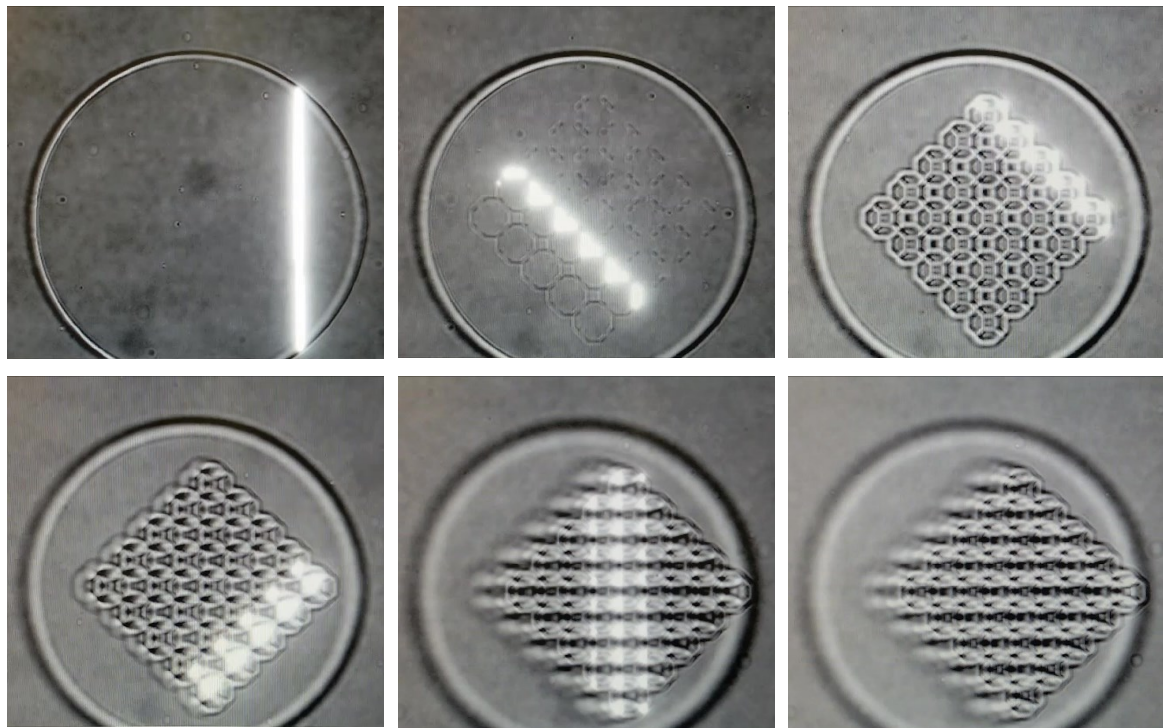
Table S12 Image sequence taken from compression test of pyrolysed RC 711 Kelvin cell structure.
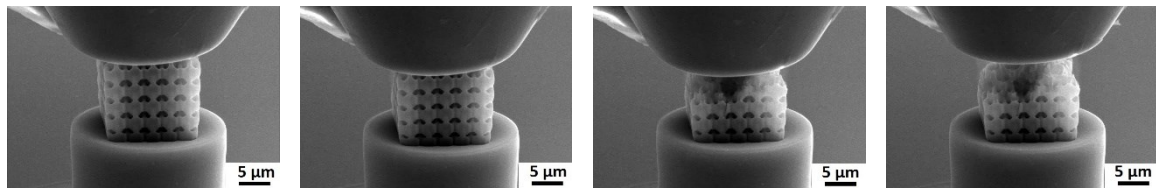
Table S13 Overview of shrinkages of different structures fabricated via DLP and 2PL process.

	DLP (RC 711/H44 = 5/5)	DLP (RC 711)	2PL (RC 711)
Kelvin cell (5 x 5 x 5 cells)	50.1 %	67.4 %	51 %
Octet	48.6 %	-	48 %
Cube	51.4 %	70.1	-
Woodpile	-	-	54 %
Diamond	-	-	56 %
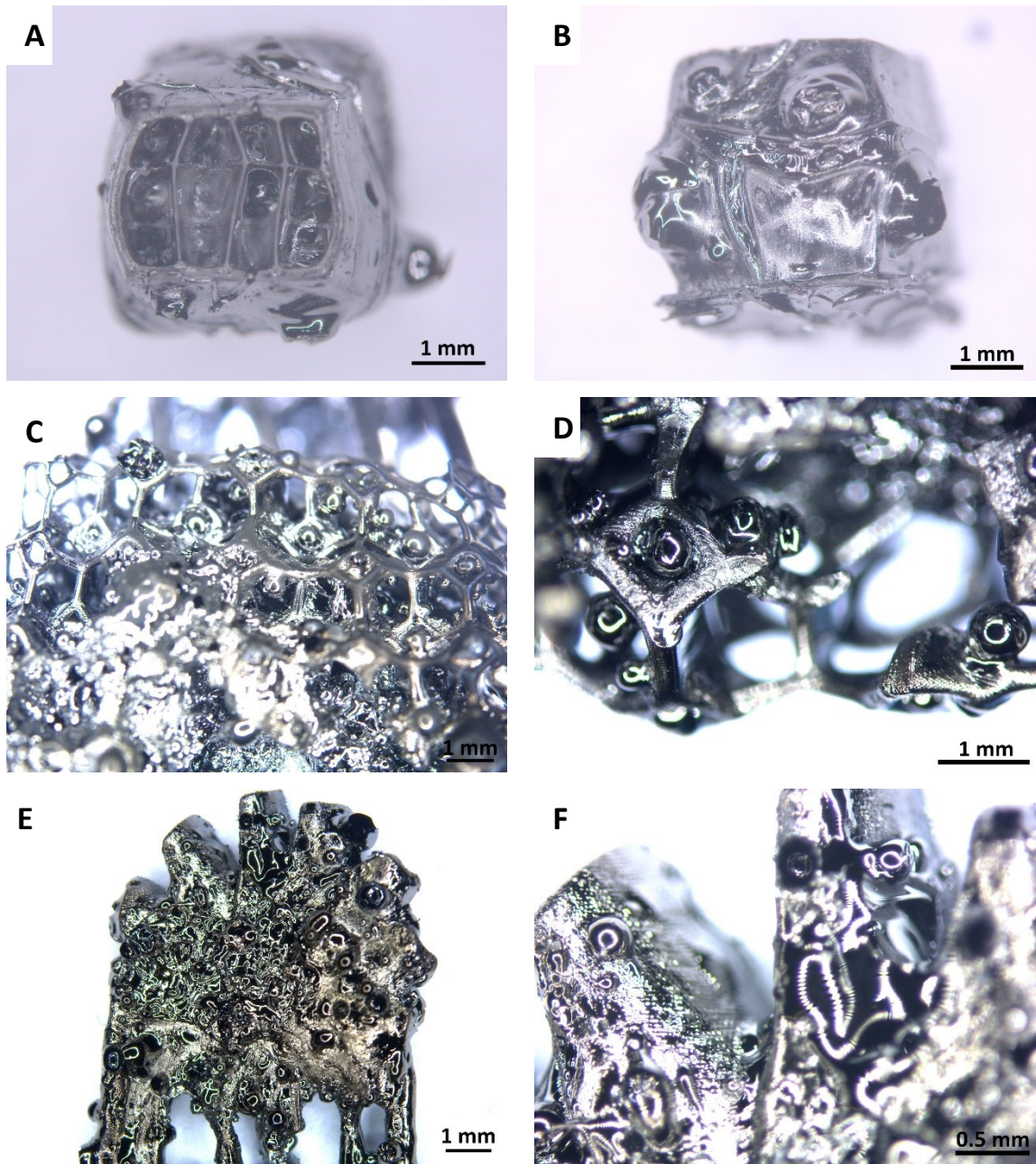
Figure S1 Examples of pyrolysed structures printed with RC 711/DOW 217 = 5/5 showing the bubble formation and loss of shape the use of DOW 217 includes; cube top view (A), side view (B); Kelvin cell structure (C,D); turbine (E,F).
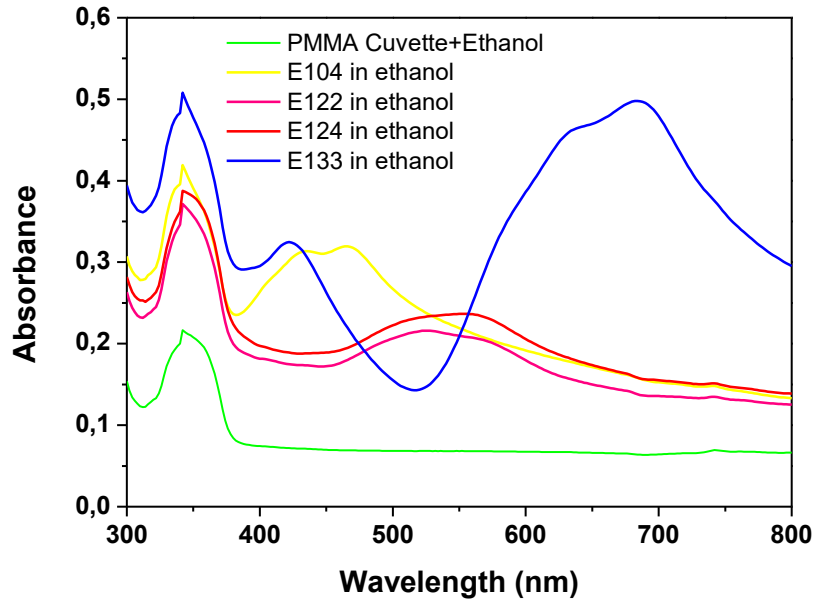
Figure S2 Absorbance spectra of different available photoabsorbers; E133 was selected due to its reactivity in the targeted wavelength of 400-500 nm, corresponding to the operational wavelength of the DLP printer.
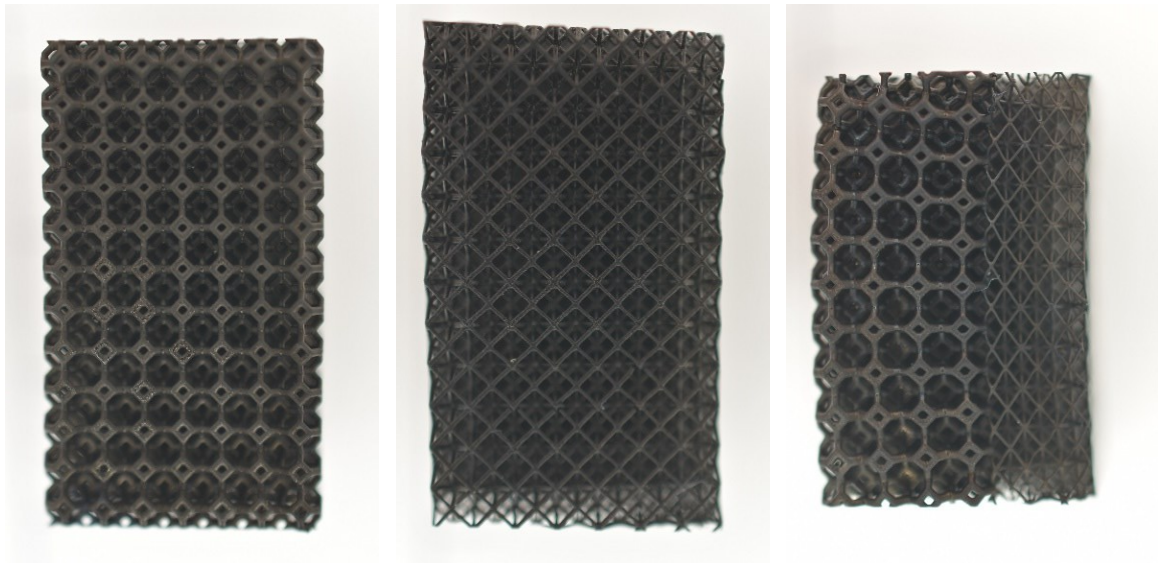
Figure S 3 Kelvin, octet and hybrid structure with cut surface area for mechanical compression test. Note that a larger part of the hybrid structure was cut to remove much of the bended part while preserving the middle part with limited bending.
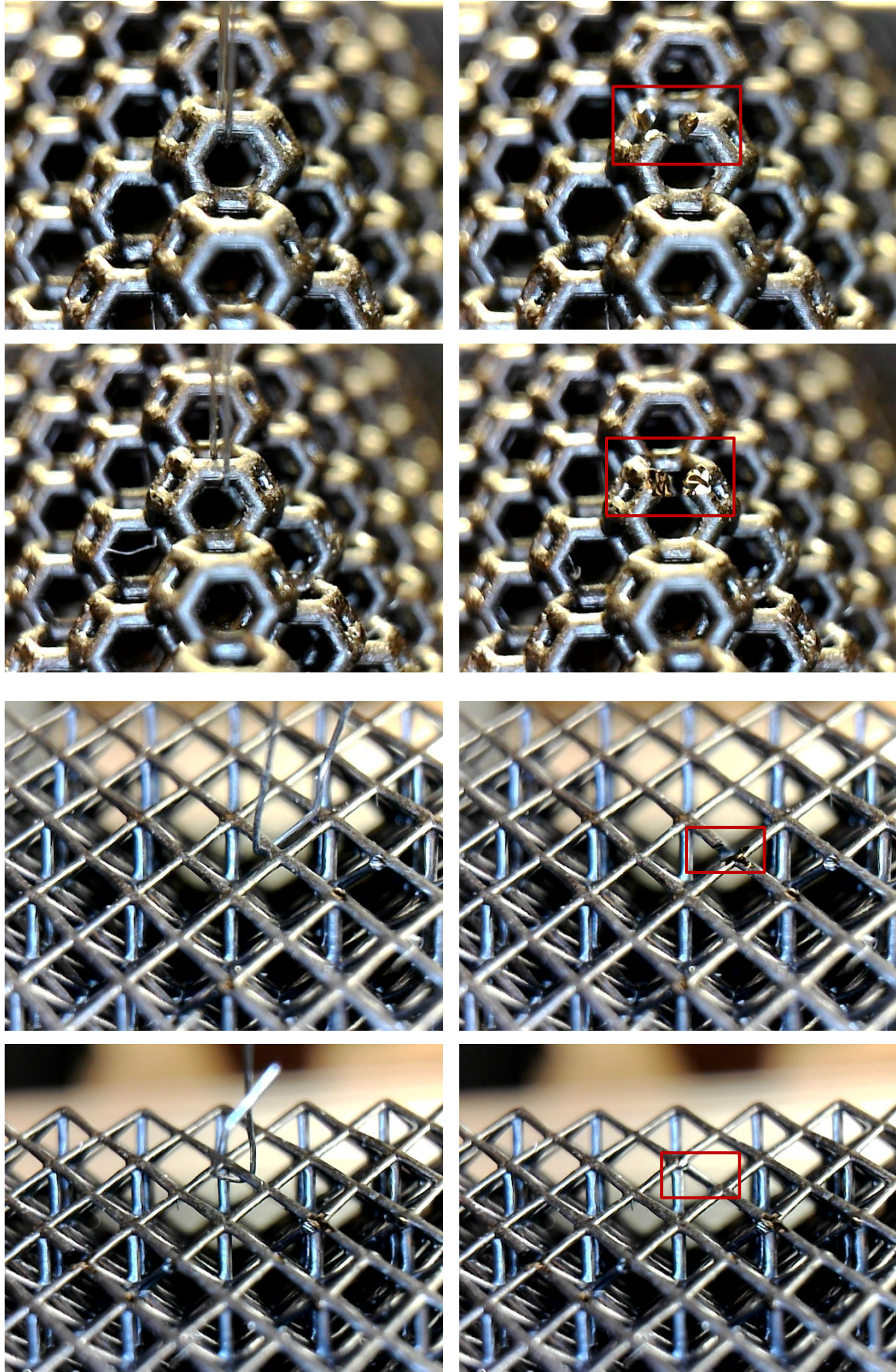
Figure S 4 Images extracted from video files taken during the strut failure experiments.
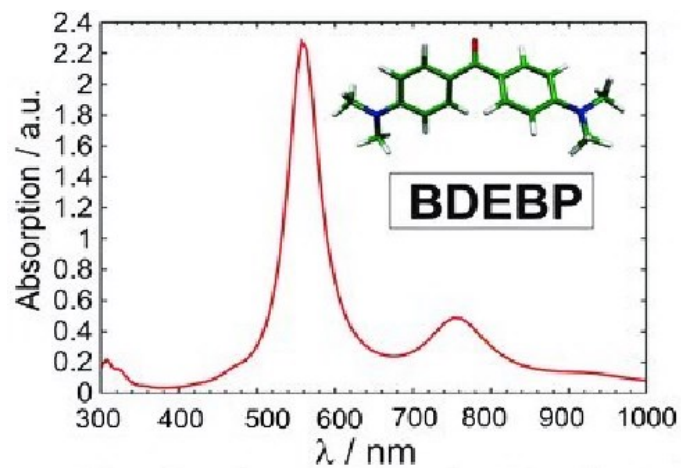
Figure S5 2-Photon absorption spectrum of BDEBP.[90]
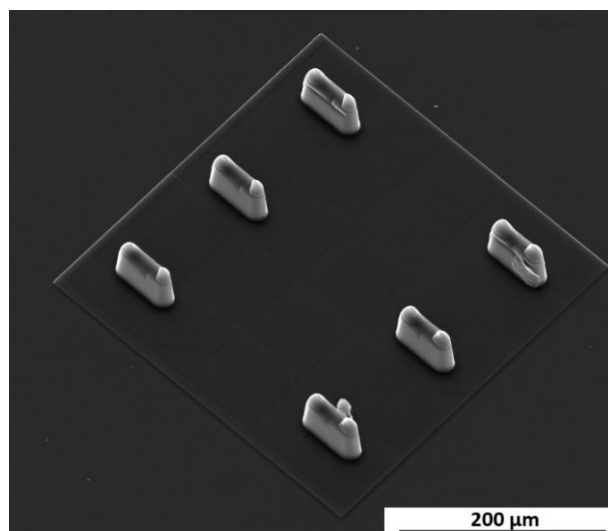
Figure S6 Simple pillars, fabricated with the preceramic polymer RC 711 with scan speeds up to 50000 µm/s.
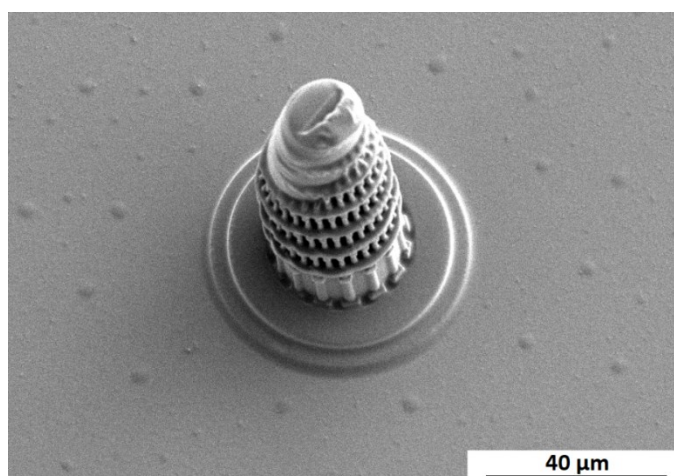
Figure S7 Pisa Tower, printed with RC 711 in standard configuration, shows the shadowing effect of already polymerised, dense material to the laser.
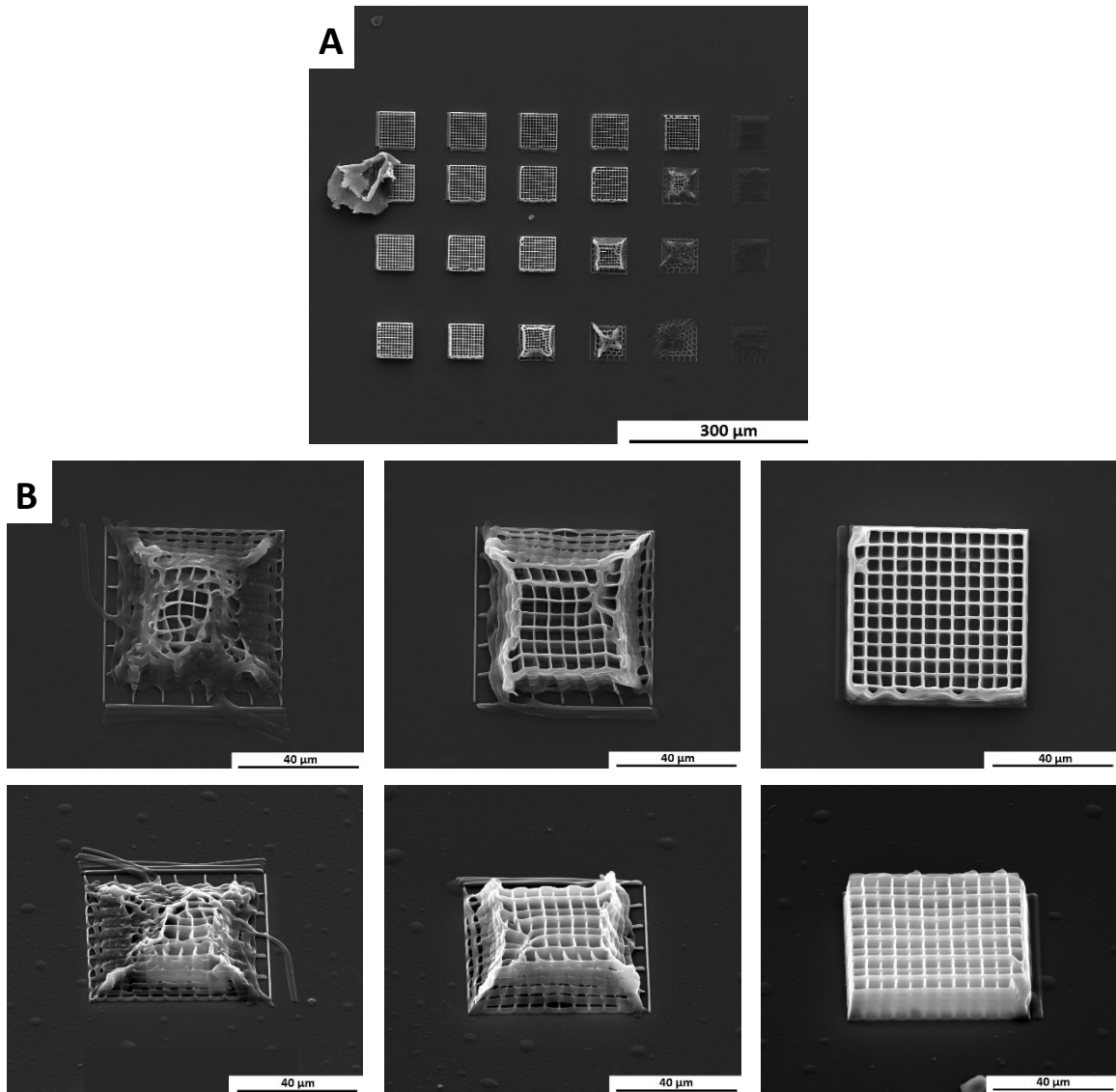
Figure S8 Dose matrix (A) and some magnifications (B) of woodpiles fabricated with the preceramic polymer.
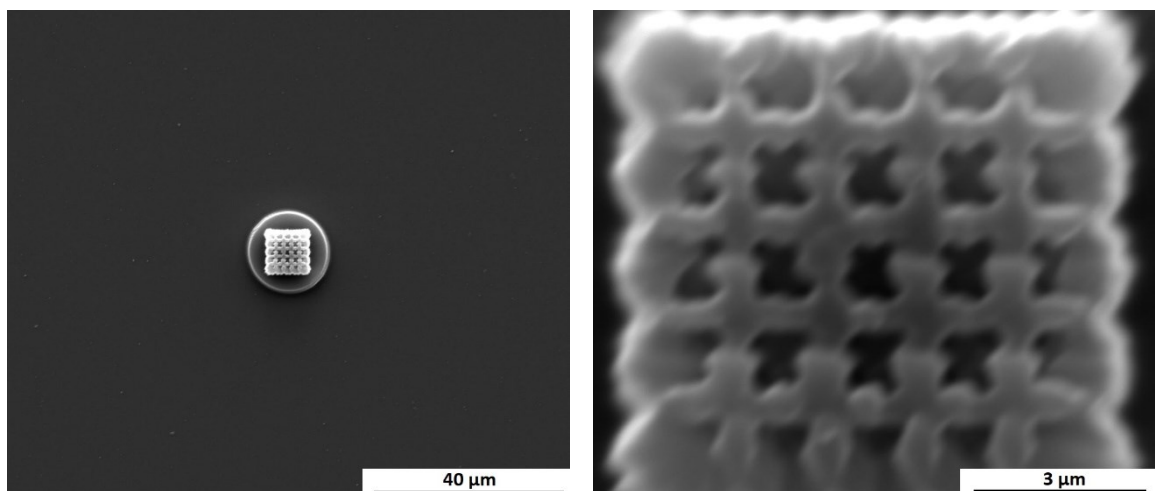
Figure S9 Kelvin cell with a scaling of 0.5 fails to show the distinct features of the Kelvin cell, making the scaling too small to resolve the small struts in the Kelvin cell structure during printing.
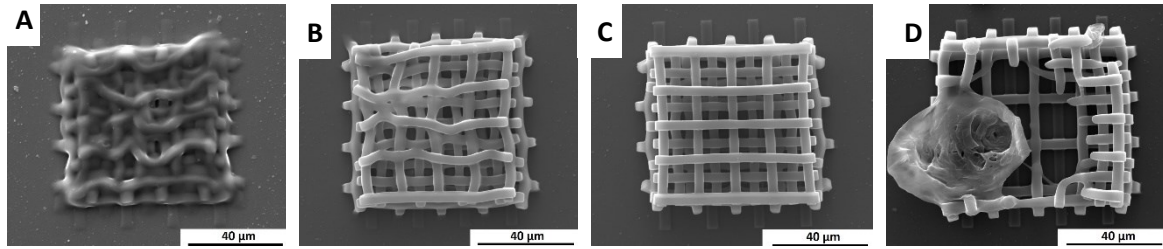
Figure S10 Optimisation of exposure dose for physical blend RC 711/H44 = 5/5 with 2PL printing; woodpile structures are printed at constant writing speed of 4000 µm/s, laser power of 0.7 and power scaling of 60 % (A), 80 % (B), 100 % (C) and laser power 0.8 power scaling 100 % (D).
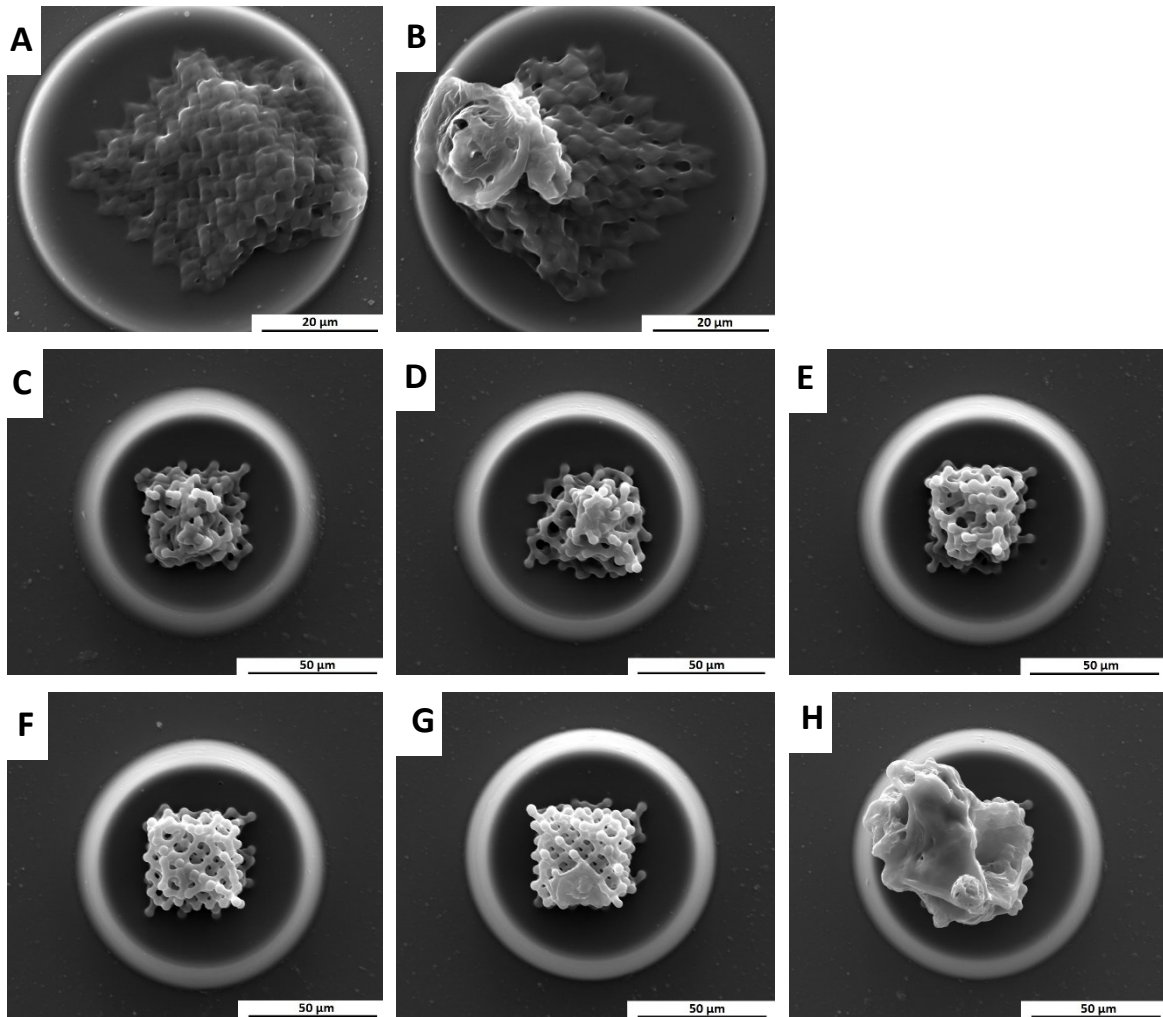
Figure S11 Attempts to print with 2PL the Kelvin cell (A,B) and diamond (C-H) structure with physical blend RC 711/H44 = 5/5; Kelvin cell: laser power: 0.9, writing speed 4000 µm/s and power scaling 80 % (A) and 90 % (B) show underdeveloped structure (A) and underdeveloped and at the same time exploded structure (B); Diamond: laser power: 0.8, writing speed 2000 µm/s, increasing power scaling from 55−80 % (C-H) in 5 % increments show underdeveloped structures (C-F) and exploded structures (G-H).
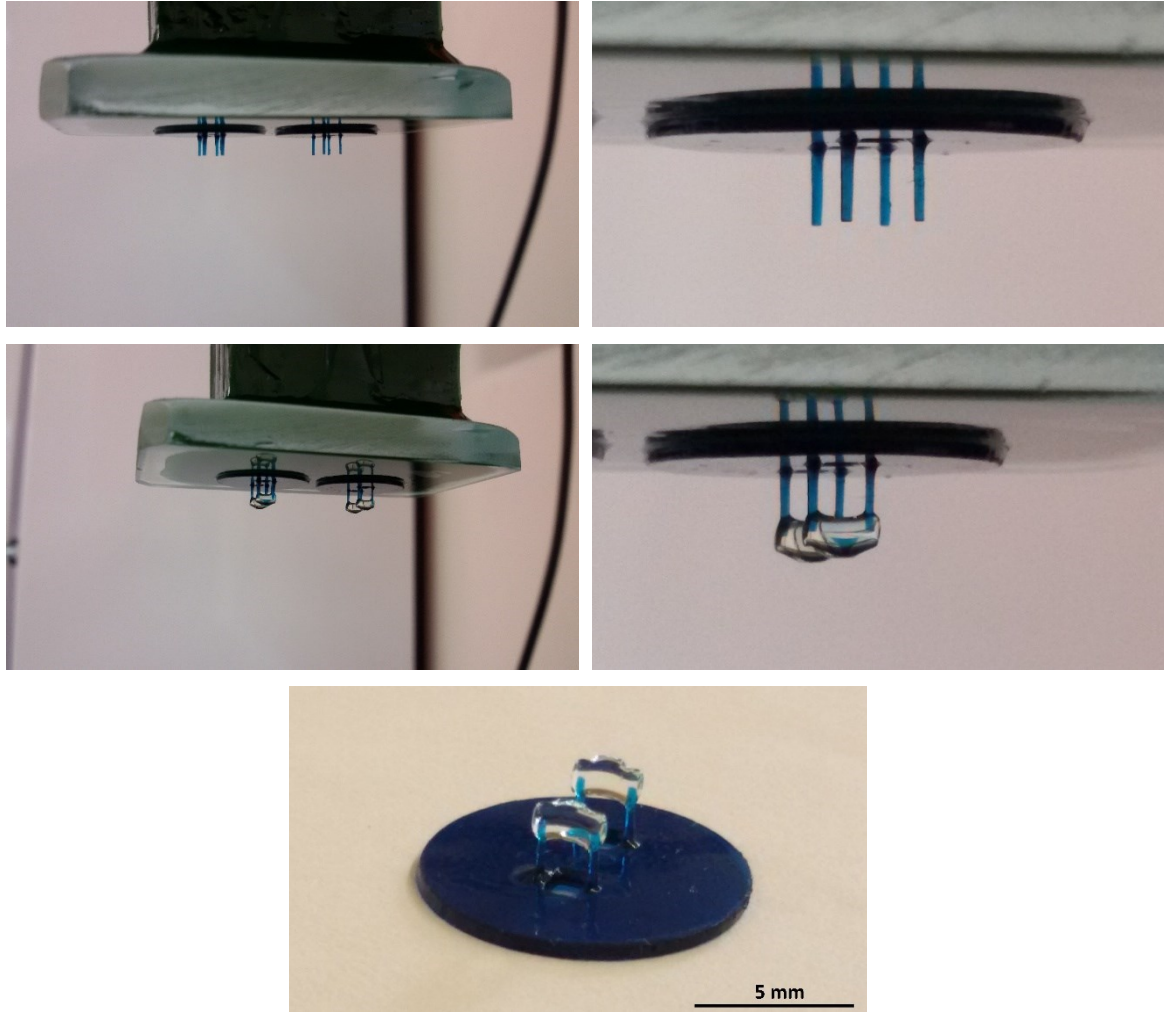
Figure S12 Hybrid multi-material fabrication; production of muscle structure printed with RC 711 (bottom base and pillars) and biodegradable, acrylate modified-Pullulan hydrogel (top channel) by a two-step printing process via DLP.

List of References

[1] N. Travitzky, A. Bonet, B. Dermeik, T. Fey, I. Filbert-Demut, L. Schlier, T. Schlordt, P. Greil, Additive Manufacturing of Ceramic-Based Materials, Advanced Engineering Materials 16(6) (2014) 729-754.

[2] J. Panetta, Q. Zhou, L. Malomo, N. Pietroni, P. Cignoni, D. Zorin, Elastic textures for additive fabrication, ACM Trans. Graph. 34(4) (2015) 1-12.

[3] J.R. Raney, J.A. Lewis, Printing mesoscale architectures, MRS Bulletin 40(11) (2015) 943-950.

[4] A. Zocca, P. Colombo, C.M. Gomes, J. Günster, Additive Manufacturing of Ceramics: Issues, Potentialities, and Opportunities, Journal of the American Ceramic Society 98(7) (2015) 1983-2001.

[5] G. Diego, Ottimizzazione di una macchina per additive manufacturing, Ingegneria meccanica, Svizzera Italiana, 2015.

[6] F. Doreau, C. Chaput, T. Chartier, Stereolithography for Manufacturing Ceramic Parts, Advanced Engineering Materials 2(8) (2000) 493-496.

[7] L. Overmeyer, A. Neumeister, R. Kling, Direct precision manufacturing of three-dimensional components using organically modified ceramics, CIRP Annals - Manufacturing Technology 60(1) (2011) 267-270.

[8] E. Zanchetta, M. Cattaldo, G. Franchin, M. Schwentenwein, J. Homa, G. Brusatin, P. Colombo, Stereolithography of SiOC Ceramic Microcomponents, Advanced Materials 28(2) (2016) 370-376.

[9] J.W. Halloran, Ceramic Stereolithography: Additive Manufacturing for Ceramics by Photopolymerization, Annual Review of Materials Research 46(1) (2016) 19-40.

[10] Formlabs, 3D Printing Technology Comparison: SLA vs. DLP, 2017. https://formlabs.com/blog/3d-printing-technology-comparison-sla-dlp/. (Accessed 18.07. 2018).

[11] S. Martínez-Crespiera, E. Ionescu, M. Schlosser, K. Flittner, G. Mistura, R. Riedel, H.F. Schlaak, Fabrication of silicon oxycarbide-based microcomponents via photolithographic and soft lithography approaches, Sensors and Actuators A: Physical 169(1) (2011) 242-249.

[12] M. Schulz, Polymer derived ceramics in MEMS/NEMS - A review on production processes and application, Advances in Applied Ceramics 108(8) (2009) 454-460.

[13] H.H. Yayue Pan, Jie Xu, Alan Feinerman, Study of separation force in constrained surface projection stereolithography, Rapid Prototyping Journal 23(2) (2017) 353-361.

[14] J.H. Jang, S. Wang, S.M. Pilgrim, W.A. Schulze, Preparation and characterization of barium titanate suspensions for stereolithography, Journal of the American Ceramic Society 83(7) (2000) 1804-1806.

[15] J.W. Halloran, V. Tomeckova, S. Gentry, S. Das, P. Cilino, D. Yuan, R. Guo, A. Rudraraju, P. Shao, T. Wu, T.R. Alabi, W. Baker, D. Legdzina, D. Wolski, W.R. Zimbeck, D. Long, Photopolymerization of powder suspensions for shaping ceramics, Journal of the European Ceramic Society 31(14) (2011) 2613-2619.

[16] C. Provin, S. Monneret, H. Le Gall, S. Corbel, Three-Dimensional Ceramic Microcomponents Made Using Microstereolithography, Advanced Materials 15(12) (2003) 994-997.

[17] M. L. Griffith, J. Halloran, Ultraviolet curable ceramic suspensions for stereolithography of ceramics, American Society of Mechanical Engineers1994.

[18] Y. De Hazan, J. Heinecke, A. Weber, T. Graule, High solids loading ceramic colloidal dispersions in UV curable media via comb-polyelectrolyte surfactants, Journal of Colloid and Interface Science 337(1) (2009) 66-74.

[19] M. Wozniak, T. Graule, Y. de Hazan, D. Kata, J. Lis, Highly loaded UV curable nanosilica dispersions for rapid prototyping applications, Journal of the European Ceramic Society 29(11) (2009) 2259-2265.

[20] Y. de Hazan, D. Penner, SiC and SiOC ceramic articles produced by stereolithography of acrylate modified polycarbosilane systems, Journal of the European Ceramic Society 37(16) (2017) 5205-5212.

[21] W.L. Wang, C.M. Cheah, J.Y.H. Fuh, L. Lu, Influence of process parameters on stereolithography part shrinkage, Materials & Design 17(4) (1996) 205-213.

[22] R. Jayne, T. Stark, J. Reeves, D. Bishop, A. White, Dynamic Actuation of Soft 3D Micromechanical Structures Using Micro-Electromechanical Systems (MEMS), Advanced Materials Technologies 3(3) (2018) 1700293.

[23] R. Bekenstein, Y. Kabessa, Y. Sharabi, O. Tal, N. Engheta, G. Eisenstein, A.J. Agranat, M. Segev, Control of light by curved space in nanophotonic structures, Nature Photonics 11(10) (2017) 664-670.

[24] P.-A. Blanche, M. Neifeld, N. Peyghambarian, A 100,000 Scale Factor Radar Range, Scientific Reports 7(1) (2017) 17767.

[25] T. Frenzel, M. Kadic, M. Wegener, Three-dimensional mechanical metamaterials with a twist, Science 358(6366) (2017) 1072-1074.

[26] S. Thiele, K. Arzenbacher, T. Gissibl, H. Giessen, A.M. Herkommer, 3D-printed eagle eye: Compound microlens system for foveated imaging, Science Advances 3(2) (2017).

[27] C.M. Soukoulis, M. Wegener, Past achievements and future challenges in the development of three-dimensional photonic metamaterials, Nature Photonics 5 (2011) 523.

[28] T. Ergin, N. Stenger, P. Brenner, J.B. Pendry, M. Wegener, Three-Dimensional Invisibility Cloak at Optical Wavelengths, Science 328(5976) (2010) 337-339.

[29] M. Kadic, T. Frenzel, M. Wegener, When size matters, Nature Physics 14 (2017) 8.

[30] A. Ovsianikov, B.N. Chichkov, Two-Photon Polymerization – High Resolution 3D Laser Technology and Its Applications, in: A. Korkin, F. Rosei (Eds.), Nanoelectronics and Photonics: From Atoms to Materials, Devices, and Architectures, Springer New York, New York, NY, 2008, pp. 427-446.

[31] H.S. K. König, M. Afshar, M. Klötzer, D. Feili, and M. Straub, Nanoprocessing using near-infrared sub-15 femtosecond laser microscopes, in: O.A. König K (Ed.), Optically Induced Nanostructures: Biomedical and Technical Applications, De Gruyter, Berlin, 2015.

[32] S. Maruo, O. Nakamura, S. Kawata, Three-dimensional microfabrication with two-photon-absorbed photopolymerization, Opt. Lett. 22(2) (1997) 132-134.

[33] M. Deubel, G. von Freymann, M. Wegener, S. Pereira, K. Busch, C.M. Soukoulis, Direct laser writing of three-dimensional photonic-crystal templates for telecommunications, Nature Materials 3 (2004) 444.

[34] F. Joachim, W. Martin, Three-dimensional optical laser lithography beyond the diffraction limit, Laser & Photonics Reviews 7(1) (2013) 22-44.

[35] M. Wegener, 3D Optical Laser Lithography, Springer Netherlands, Dordrecht, 2017, pp. 143-148.

[36] T. Michael, H. Martin, Three-dimensional laser lithography, Optik & Photonik 6(4) (2011) 36-39.

[37] P. Colombo, G. Mera, R. Riedel, G.D. Sorarù, Polymer-Derived Ceramics: 40 Years of Research and Innovation in Advanced Ceramics, Journal of the American Ceramic Society 93(7) (2010) 1805-1837.

[38] A. Zocca, C.M. Gomes, A. Staude, E. Bernardo, J. Günster, P. Colombo, SiOC ceramics with ordered porosity by 3D-printing of a preceramic polymer, Journal of Materials Research 28(17) (2013) 2243-2252.

[39] R. Harshe, C. Balan, R. Riedel, Amorphous Si(Al)OC ceramic from polysiloxanes: Bulk ceramic processing, crystallization behavior and applications, Journal of the European Ceramic Society 24(12) (2004) 3471-3482.

[40] Z.C. Eckel, C. Zhou, J.H. Martin, A.J. Jacobsen, W.B. Carter, T.A. Schaedler, Additive manufacturing of polymer-derived ceramics, Science 351(6268) (2016) 58-62.

[41] Y. Blum, G.D. Sorarù, A.P. Ramaswamy, D. Hui, S.M. Carturan, Controlled mesoporosity in SiOC via chemically bonded polymeric "spacers", Journal of the American Ceramic Society 96(9) (2013) 2785-2792.

[42] P. Greil, Polymer Derived Engineering Ceramics, Advanced Engineering Materials 2(6) (2000) 339-348.

[43] R. Riedel, G. Mera, R. Hauser, A. Klonczynski, Silicon-based polymer-derived ceramics: Synthesis properties and applications-A review, Nippon Seramikkusu Kyokai Gakujutsu Ronbunshi/Journal of the Ceramic Society of Japan 114(1330) (2006) 425-444.

[44] G.D. Soraru, G. D'Andrea, R. Campostrini, F. Babonneau, G. Mariotto, Structural characterization and high-temperature behavior of silicon oxycarbide glasses prepared from sol-gel precursors containing Si-H bonds, Journal of the American Ceramic Society 78(2) (1995) 379-387.

[45] M. Scheffler, T. Gambaryan-Roisman, T. Takahashi, J. Kaschta, H. Muenstedt, P. Buhler, P. Greil, Pyrolytic decomposition of preceramic organo polysiloxanes, Ceramic Transactions(USA) 115 (2000) 239-250.

[46] R. Zhuo, P. Colombo, C. Pantano, E.A. Vogler, Silicon oxycarbide glasses for blood-contact applications, Acta Biomaterialia 1(5) (2005) 583-589.

[47] Y.D. Blum, D.B. MacQueen, H.J. Kleebe, Synthesis and characterization of carbon-enriched silicon oxycarbides, Journal of the European Ceramic Society 25(2-3 SPEC. ISS.) (2005) 143-149.

[48] Y.D. Blum, K.B. Schwartz, R.M. Laine, Preceramic polymer pyrolysis, Journal of Materials Science 24(5) (1989) 1707-1718.

[49] S. Park, D.H. Lee, H.I. Ryoo, T.W. Lim, D.Y. Yang, D.P. Kim, Fabrication of three-dimensional SiC ceramic microstructures with near-zero shrinkage via dual crosslinking induced stereolithography, Chemical Communications (32) (2009) 4880-4882.

[50] a. K J Wynne, R.W. Rice, Ceramics Via Polymer Pyrolysis, Annual Review of Materials Science 14(1) (1984) 297-334.

[51] R. Brezny, D.J. Green, C.Q. Dam, Evaluation of Strut Strength in Open-Cell Ceramics, Journal of the American Ceramic Society 72(6) (1989) 885-889.

[52] P. Greil, Active-Filler-Controlled Pyrolysis of Preceramic Polymers, Journal of the American Ceramic Society 78(4) (1995) 835-848.

[53] P. Greil, Near Net Shape Manufacturing of Polymer Derived Ceramics, Key Engineering Materials 132-136 (1997) 1981-1984.

[54] M. Seibold, P. Greil, Thermodynamics and microstructural development of ceramic composite formation by active filler-controlled pyrolysis (AFCOP), Journal of the European Ceramic Society 11(2) (1993) 105-113.

[55] P. Colombo, E. Bernardo, G. Parcianello, Multifunctional advanced ceramics from preceramic polymers and nano-sized active fillers, Journal of the European Ceramic Society 33(3) (2013) 453-469.

[56] P. Colombo, J. Schmidt, G. Franchin, A. Zocca, J. Günster, Additive manufacturing techniques for fabricating complex ceramic components from preceramic polymers, American Ceramic Society Bulletin 96(3) (2017) 16-23.

[57] J. Schmidt, P. Colombo, Digital light processing of ceramic components from polysiloxanes, Journal of the European Ceramic Society 38(1) (2018) 57-66.

[58] Wacker GmbH, Technical data sheet for SILRES® H44, in: www.wacker.com (Ed.) Germany, 2014.

[59] Y.H. Li, X.D. Li, D.P. Kim, Chemical development of preceramic polyvinylsilazane photoresist for ceramic patterning, Journal of Electroceramics 23(2-4) (2009) 133-136.

[60] Starfire Systems, POLYMER-TO-CERAMIC™ TECHNOLOGY, 2010-2017. http://www.starfiresystems.com/data-sheets.html. (Accessed 29.05. 2017).

[61] T.-H. Yoon, S.-H. Park, K.-I. Min, X. Zhang, S.J. Haswell, D.-P. Kim, Novel inorganic polymer derived microreactors for organic microchemistry applications, Lab on a Chip 8(9) (2008) 1454-1459.

[62] L.-A. Liew, R.A. Saravanan, V.M. Bright, M.L. Dunn, J.W. Daily, R. Raj, Processing and characterization of silicon carbon-nitride ceramics: application of electrical properties towards MEMS thermal actuators, Sensors and Actuators A: Physical 103(1–2) (2003) 171-181.

[63] T.-H. Yoon, L.-Y. Hong, D.-P. Kim, Fabrication of SiC-based Ceramic Microstructures from Preceramic Polymers with Sacrificial Templates and Softlithography Techniques, in: M. Wang (Ed.), Lithography, InTech, Rijeka, 2010, p. Ch. 21.

[64] Y.-H. Li, K.-D. Ahn, D.-P. Kim, Synthesis and properties of UV curable polyvinylsilazane as a precursor for micro-structuring, Polymers for Advanced Technologies 26(3) (2015) 245-249.

[65] T.A. Pham, D.P. Kim, T.W. Lim, S.H. Park, D.Y. Yang, K.S. Lee, Three-dimensional SiCN ceramic microstructures via nano-stereolithography of inorganic polymer photoresists, Advanced Functional Materials 16(9) (2006) 1235-1241.

[66] S.K. Reddy, N.B. Cramer, A.K. O' Brien, T. Cross, R. Raj, C.N. Bowman, Rate mechanisms of a novel thiol-ene photopolymerization reaction, Macromolecular Symposia 206(1) (2004) 361-374.

[67] V. Tomeckova, J.W. Halloran, Cure depth for photopolymerization of ceramic suspensions, Journal of the European Ceramic Society 30(15) (2010) 3023-3033.

[68] Sicherheitsdatenblatt diphenylether, in: A. Aesar (Ed.) 2015.

[69] IFA (Institut für Arbeitsschutz der Deutschen Gesetzlichen Unfallversicherung) GESTIS-Stoffdatenbank http://gestis.itrust.de/nxt/gateway.dll/gestis_de/000000.xml?f=templates$fn=default.htm$vid=gestisdeu:sdbdeu$3.0. (Accessed 07/02 2018).

[70] T. Chartier, C. Dupas, M. Lasgorceix, J. Brie, E. Champion, N. Delhote, C. Chaput, Additive manufacturing to produce complex 3D ceramic parts, Journal of Ceramic Science and Technology 6(2) (2015) 95-104.

[71] B. Wiedemann, K.H. Dusel, J. Eschl, Investigation into the influence of material and process on part distortion, Rapid Prototyping Journal 1(3) (1995) 17-22.

[72] G.D. Quinn, Fractography of Ceramics and Glasses, National Institute of Standards and Technology 2016.

[73] J. Schmidt, N. Brodnik, P. Colombo, K.T. Faber, Analysis of Multi-scale Mechanical Properties of Ceramic Trusses Prepared from Preceramic Polymers, manuscript in process.

[74] H.X. Zhu, J.F. Knott, N.J. Mills, Analysis of the elastic properties of open-cell foams with tetrakaidecahedral cells, Journal of the Mechanics and Physics of Solids 45(3) (1997) 319-343.

[75] V.S. Deshpande, N.A. Fleck, M.F. Ashby, Effective properties of the octet-truss lattice material, Journal of the Mechanics and Physics of Solids 49(8) (2001) 1747-1769.

[76] ASTM International, ASTM C1684-18, Standard Test Method for Flexural Strength of Advanced Ceramics at Ambient Temperature—Cylindrical Rod Strength, West Conshohocken, PA, 2018.

[77] L.J. Gibson, M.F. Ashby, Cellular Solids: Structure and Properties, 2nd ed., Cambridge University Press, Cambridge, 1997.

[78] M. Scheffler, P. Colombo, Cellular Ceramics: Structure, Manufacturing, Properties and Applications, Wiley-VCH Verlag, Weinheim, 2006.

[79] P. Colombo, J.R. Hellmann, D.L. Shelleman, Thermal Shock Behavior of Silicon Oxycarbide Foams, Journal of the American Ceramic Society 85(9) (2002) 2306-2312.

[80] N.A. Fleck, V.S. Deshpande, M.F. Ashby, Micro-architectured materials: past, present and future, Proceedings of the Royal Society A: Mathematical, Physical and Engineering Science 466(2121) (2010) 2495-2516.

[81] J. Christensen, M. Kadic, O. Kraft, M. Wegener, Vibrant times for mechanical metamaterials, MRS Communications 5(3) (2015) 453-462.

[82] T.A. Schaedler, A.J. Jacobsen, A. Torrents, A.E. Sorensen, J. Lian, J.R. Greer, L. Valdevit, W.B. Carter, Ultralight Metallic Microlattices, Science 334(6058) (2011) 962-965.

[83] L.R. Meza, S. Das, J.R. Greer, Strong, lightweight, and recoverable three-dimensional ceramic nanolattices, Science 345(6202) (2014) 1322-1326.

[84] L. Brigo, J. Schmidt, A. Gandin, N. Michieli, P. Colombo, G. Brusatin, 3D Nanofabrication of SiOC Ceramic Structures, Advanced Science (2018) 1800937.

[85] J. Bauer, A. Schroer, R. Schwaiger, O. Kraft, Approaching theoretical strength in glassy carbon nanolattices, Nat Mater 15(4) (2016) 438-443.

[86] D. Jang, L.R. Meza, F. Greer, J.R. Greer, Fabrication and deformation of three-dimensional hollow ceramic nanostructures, Nat Mater 12(10) (2013) 893-898.

[87] L.R. Meza, J.R. Greer, Mechanical characterization of hollow ceramic nanolattices, Journal of Materials Science 49(6) (2014) 2496-2508.

[88] L.T. Woo, S. Yong, Y. Dong-Yol, P.T. Anh, K. Dong-Pyo, Y. Byeong-Il, L. Kwang-Sup, P.S. Hu, Net Shape Manufacturing of Three-Dimensional SiCN Ceramic Microstructures Using an Isotropic Shrinkage Method by Introducing Shrinkage Guiders, International Journal of Applied Ceramic Technology 5(3) (2008) 258-264.

[89] M. Wilhelm, C. Soltmann, D. Koch, G. Grathwohl, Ceramers—functional materials for adsorption techniques, Journal of the European Ceramic Society 25(2-3) (2005) 271-276.

[90] B. Harke, W. Dallari, G. Grancini, D. Fazzi, F. Brandi, A. Petrozza, A. Diaspro, Polymerization Inhibition by Triplet State Absorption for Nanoscale Lithography, Advanced Materials (Deerfield Beach, Fla.) 25(6) (2013) 904-909.

[91] J. Bauer, S. Hengsbach, I. Tesari, R. Schwaiger, O. Kraft, High-strength cellular ceramic composites with 3D microarchitecture, Proceedings of the National Academy of Sciences of the United States of America 111(7) (2014) 2453-2458.

[92] L. Dong, V. Deshpande, H. Wadley, Mechanical response of Ti–6Al–4V octet-truss lattice structures, International Journal of Solids and Structures 60-61 (2015) 107-124.

[93] A. Jacobsen, S. Mahoney, W. Carter, S. Nutt, Vitreous Carbon Micro-Lattice Structures, 49 (2011) 1025-1032.

[94] S. Shin, S. Kucheyev, M. Worsley, A. Hamza, Mechanical deformation of carbon-nanotube-based aerogels, 50 (2012) 5340-5342.

[95] A.A. Griffith, The Phenomena of Rupture and Flow in Solids, Philosophical Transactions of the Royal Society of London. Series A, Containing Papers of a Mathematical or Physical Character 221 (1921) 163-198.

[96] I.T. Yusuf, Y.A. Jimoh, W.A. Salami, An appropriate relationship between flexural strength and compressive strength of palm kernel shell concrete, Alexandria Engineering Journal 55(2) (2016) 1553-1562.

[97] J. Schmidt, L. Brigo, M. Schwentenwein, P. Colombo, G. Brusatin, Multiscale ceramic components from preceramic polymers by hybridization of vat polymerization-based technologies, submitted to Journal of ACS Applied Materials & Interfaces.

[98] H.-B. Sun, T. Kawakami, Y. Xu, J.-Y. Ye, S. Matuso, H. Misawa, M. Miwa, R. Kaneko, Real three-dimensional microstructures fabricated by photopolymerization of resins through two-photon absorption, Opt. Lett. 25(15) (2000) 1110-1112.

[99] J. Serbin, A. Ovsianikov, B. Chichkov, Fabrication of woodpile structures by two-photon polymerization and investigation of their optical properties, Opt. Express 12(21) (2004) 5221-5228.

[100] A. Doraiswamy, C. Jin, R.J. Narayan, P. Mageswaran, P. Mente, R. Modi, R. Auyeung, D.B. Chrisey, A. Ovsianikov, B. Chichkov, Two photon induced polymerization of organic–inorganic hybrid biomaterials for microstructured medical devices, Acta Biomaterialia 2(3) (2006) 267-275.

[101] A. Ostendorf, B. N. Chichkov, Two-photon polymerization: A new approach to micromachining, 40 (2006) 72-80.

[102] R.J. Narayan, A. Doraiswamy, D.B. Chrisey, B.N. Chichkov, Medical prototyping using two photon polymerization, Materials Today 13(12) (2010) 42-48.

[103] H.-B. Sun, T. Suwa, K. Takada, R.P. Zaccaria, M.-S. Kim, K.-S. Lee, S. Kawata, Shape precompensation in two-photon laser nanowriting of photonic lattices, Applied Physics Letters 85(17) (2004) 3708-3710.

[104] M.P. Sealy, G. Madireddy, R.E. Williams, P. Rao, M. Toursangsaraki, Hybrid Processes in Additive Manufacturing, Journal of Manufacturing Science and Engineering 140(6) (2018) 060801-060801-13.

[105] A.N.M.A. Tomal, S. Tanveer, K. Md. Raisuddin, Improvement of Dimensional Accuracy of 3-D Printed Parts using an Additive/Subtractive Based Hybrid Prototyping Approach, IOP Conference Series: Materials Science and Engineering 260(1) (2017) 012031.

[106] J.M. Flynn, A. Shokrani, S.T. Newman, V. Dhokia, Hybrid additive and subtractive machine tools – Research and industrial developments, International Journal of Machine Tools and Manufacture 101 (2016) 79-101.

[107] W.-S. Chu, C.-S. Kim, H.-T. Lee, J.-O. Choi, J.-I. Park, J.-H. Song, K.-H. Jang, S.-H. Ahn, Hybrid manufacturing in micro/nano scale: A Review, International Journal of Precision Engineering and Manufacturing-Green Technology 1(1) (2014) 75-92.

[108] I. Staude, M. Decker, M. Ventura, C. Jagadish, D. Neshev, M. Gu, Y. Kivshar, Hybrid High-Resolution Three-Dimensional Nanofabrication for Metamaterials and Nanoplasmonics (Adv. Mater. 9/2013), Advanced Materials 25(9) (2013) 1259-1259.

[109] J. Li, T. Wasley, T.T. Nguyen, V.D. Ta, J.D. Shephard, J. Stringer, P. Smith, E. Esenturk, C. Connaughton, R. Kay, Hybrid additive manufacturing of 3D electronic systems, Journal of Micromechanics and Microengineering 26(10) (2016) 105005.

[110] J.A. Palmer, D. Davis, B.D. Chavez, P. Gallegos, R.B. Wicker, F. Medina, Rapid Prototyping of High Density Circuitry, Rapid Prototyping & Manufacturing 313 (2004).

[111] K.B. Perez, C.B. Williams, Combining additive manufacturing and direct write for integrated electronics - A review, 24th International SFF Symposium - An Additive Manufacturing Conference, SFF 2013, 2013, pp. 962-979.

[112] F. Medina, A. Lopes, A. Inamdar, R. Hennessey, J.Palmer, B. Chavez, D. Davis, P. Gallegos, R. Wicker, Hybrid Manufacturing: Integrating Direct Write and Stereolithography, Solid Freeform Fabrication Symposium (2005).

[113] A. Seidel, A. Straubel, T. Finaske, T. Maiwald, S. Polenz, M. Albert, J. Näsström, A. Marquardt, M. Riede, E. Lopez, F. Brueckner, E. Beyer, C. Leyens, Added value by hybrid additive manufacturing and advanced manufacturing approaches, Journal of Laser Applications 30(3) (2018).

[114] Y.-P. Qian, J.-H. Huang, H.-O. Zhang, G.-L. Wang, Direct rapid high-temperature alloy prototyping by hybrid plasma-laser technology, Journal of Materials Processing Technology 208(1) (2008) 99-104.

[115] K.B. Perez, C.B. Williams, Design considerations for hybridizing additive manufacturing and direct write technologies, Proceedings of the ASME Design Engineering Technical Conference, 4 (2014).

[116] Z. Zhu, V. Dhokia, A. Nassehi, S.T. Newman, Investigation of part distortions as a result of hybrid manufacturing, Robot. Comput.-Integr. Manuf. 37(C) (2016) 23-32.

[117] M. Merklein, D. Junker, A. Schaub, F. Neubauer, Hybrid Additive Manufacturing Technologies – An Analysis Regarding Potentials and Applications, Physics Procedia 83 (2016) 549-559.

[118] L. Chong, S. Ramakrishna, S. Singh, A review of digital manufacturing-based hybrid additive manufacturing processes, The International Journal of Advanced Manufacturing Technology 95(5) (2018) 2281-2300.

[119] M. Ashby, Designing hybrid materials, Materials selection in mechanical design, Butterworth-Heinemann, Amsterdam, 2004, pp. 339-377.

[120] U. Scheithauer, S. Weingarten, R. Johne, E. Schwarzer, J. Abel, H.-J. Richter, T. Moritz, A. Michaelis, Ceramic-Based 4D Components: Additive Manufacturing (AM) of Ceramic-Based Functionally Graded Materials (FGM) by Thermoplastic 3D Printing (T3DP), Materials 10(12) (2017) 1368.

[121] J. Schmidt, A.A. Altun, M. Schwentenwein, P. Colombo, Complex mullite structures fabricated via Digital Light Processing of a preceramic polysiloxane with active alumina fillers, Journal of the European Ceramic Society (2018) accepted.

[122] H. Schneider, K. Okada, J.A. Pask, Mullite and mullite ceramics, Chichester, 1994.

[123] D.J. Duval, S.H. Risbud, J.F. Shackelford, Mullite, in: J.F. Shackelford, R.H. Doremus (Eds.), Ceramic and Glass Materials: Structure, Properties and Processing, Springer US, Boston, MA, 2008, pp. 27-39.

[124] H. Schneider, J. Schreuer, B. Hildmann, Structure and properties of mullite—A review, Journal of the European Ceramic Society 28(2) (2008) 329-344.

[125] E. Bernardo, P. Colombo, E. Pippel, J. Woltersdorf, Novel Mullite Synthesis Based on Alumina Nanoparticles and a Preceramic Polymer, Journal of the American Ceramic Society 89(5) (2006) 1577-1583.

[126] A.J. Pyzik, C.G. Li, New Design of a Ceramic Filter for Diesel Emission Control Applications, International Journal of Applied Ceramic Technology 2(6) (2005) 440-451.

[127] B.A. Latella, L. Henkel, E.G. Mehrtens, Permeability and high temperature strength of porous mullite-alumina ceramics for hot gas filtration, Journal of Materials Science 41(2) (2006) 423.

[128] C. Voigt, E. Jäckel, F. Taina, T. Zienert, A. Salomon, G. Wolf, C.G. Aneziris, P. Le Brun, Filtration Efficiency of Functionalized Ceramic Foam Filters for Aluminum Melt Filtration, Metallurgical and Materials Transactions B: Process Metallurgy and Materials Processing Science 48(1) (2017) 497-505.

[129] V. Viswabaskaran, F.D. Gnanam, M. Balasubramanian, Mullitisation behaviour of calcined clay-alumina mixtures, Ceramics International 29(5) (2003) 561-571.

[130] M.A. Sainz, F.J. Serrano, J.M. Amigo, J. Bastida, A. Caballero, XRD microstructural analysis of mullites obtained from kaolinite–alumina mixtures, Journal of the European Ceramic Society 20(4) (2000) 403-412.

[131] W.-C. WEI, J.W. HALLORAN, Transformation Kinetics of Diphasic Aluminosilicate Gels, Journal of the American Ceramic Society 71(7) (1988) 581-587.

[132] D.X. Li, W.J. Thomson, Mullite Formation from Nonstoichiometric Diphasic Precursors, Journal of the American Ceramic Society 74(10) (1991) 2382-2387.

[133] A. Taylor, D. Holland, The chemical synthesis and crystallization sequence of mullite, Journal of Non-Crystalline Solids 152(1) (1993) 1-17.

[134] H. Schneider, D. Voll, B. Saruhan, J. Sanz, G. Schrader, C. Rüscher, A. Mosset, Synthesis and structural characterization of non-crystalline mullite precursors, Journal of Non-Crystalline Solids 178 (1994) 262-271.

[135] D. Amutharani, F.D. Gnanam, Low temperature pressureless sintering of sol-gel derived mullite, Materials Science and Engineering: A 264(1) (1999) 254-261.

[136] K.J.D. MacKenzie, R.H. Meinhold, J.E. Patterson, H. Schneider, M. Schmücker, D. Voll, Structural evolution in gel-derived mullite precursors, Journal of the European Ceramic Society 16(12) (1996) 1299-1308.

[137] H. Ivankovic, E. Tkalcec, R. Nass, H. Schmidt, Correlation of the precursor type with densification behavior and microstructure of sintered mullite ceramics, Journal of the European Ceramic Society 23(2) (2003) 283-292.

[138] E. Tkalcec, H. Ivankovic, R. Nass, H. Schmidt, Crystallization kinetics of mullite formation in diphasic gels containing different alumina components, Journal of the European Ceramic Society 23(9) (2003) 1465-1475.

[139] S. Ding, Y.-P. Zeng, D. Jiang, Fabrication of Mullite Ceramics With Ultrahigh Porosity by Gel Freeze Drying, Journal of the American Ceramic Society 90(7) (2007) 2276-2279.

[140] S.P. Chaudhuri, S.K. Patra, Preparation and characterisation of transition metal ion doped mullite, British Ceramic Transactions 96(3) (1997) 105-111.

[141] Y. Hirata, I.A. Aksay, R. Kurita, S. Hori, H. Kaji, Processing of Mullite Powders Processed by CVD, in: S. Somiya, R.F. Davies, J.A. Pask (Eds.), Ceramic Transactions Mullite and Mullite Matrix Composites, American Ceramic Society, Westerville, OH, 1990, pp. 119–26.

[142] M. Bartsch, B. Saruhan, M. Schmücker, H. Schneider, Novel Low-Temperature Processing Route of Dense Mullite Ceramics by Reaction Sintering of Amorphous SiO_2-Coated γ-Al_2O_3 Particle Nanocomposites, Journal of the American Ceramic Society 82(6) (1999) 1388-1392.

[143] M.D. Sacks, Y.-J. Lin, G.W. Scheiffele, K. Wang, N. Bozkurt, Effect of Seeding on Phase Development, Densification Behavior, and Microstmcture Evolution in Mullite Fabricated from Microcomposite Particles, Journal of the American Ceramic Society 78(11) (1995) 2897-2906.

[144] M.D. Sacks, K. Wang, G.W. Scheiffele, N. Bozkurt, Effect of Composition on Mullitization Behavior of α-Alumina/Silica Microcomposite Powders, Journal of the American Ceramic Society 80(3) (1997) 663-672.

[145] T. Konegger, R. Felzmann, B. Achleitner, D. Brouczek, Mullite-based cellular ceramics obtained by a combination of direct foaming and reaction bonding, Ceramics International 41(7) (2015) 8630-8636.

[146] Y.-W. Kim, H.-D. Kim, C.B. Park, Processing of Microcellular Mullite, Journal of the American Ceramic Society 88(12) (2005) 3311-3315.

[147] F. Griggio, E. Bernardo, P. Colombo, G.L. Messing, Kinetic Studies of Mullite Synthesis from Alumina Nanoparticles and a Preceramic Polymer, Journal of the American Ceramic Society 91(8) (2008) 2529-2533.

[148] G. Parcianello, E. Bernardo, P. Colombo, Mullite/zirconia nanocomposites from a preceramic polymer and nanosized fillers, Journal of the American Ceramic Society 94(5) (2011) 1357-1362.

[149] E. Bernardo, P. Colombo, Advanced oxide ceramics from a preceramic polymer and fillers, Soft Materials 4(2-4) (2006) 175-185.

[150] E. Bernardo, P. Colombo, S. Hampshire, Advanced ceramics from a preceramic polymer and nano-fillers, Journal of the European Ceramic Society 29(5) (2009) 843-849.

[151] R. Riedel, L. Toma, C. Fasel, G. Miehe, Polymer-derived mullite–SiC-based nanocomposites, Journal of the European Ceramic Society 29(14) (2009) 3079-3090.

[152] G.A.F. Machado, R.M. Rocha, A.H.A. Bressiani, Composites obtained from alumina and polymer derived ceramic, Materials Science Forum, 2018, pp. 141-146.

[153] Z. Lodziana, K. Parlinski, Dynamical stability of the alpha and theta phases of alumina, Physical Review B Condensed Matter 67(17) (2003) 174106.

[154] B. Beguin, E. Garbowski, M. Primet, Stabilization of alumina toward thermal sintering by silicon addition, Journal of Catalysis 127(2) (1991) 595-604.

[155] W. Kollenberg, Technische Keramik: Grundlagen-Werkstoffe-Verfahrenstechnik, Vulkan-Verlag GmbH, Essen, Germany, 2004.